

# Three-Nucleon Forces: Implementation and Applications to Atomic Nuclei and Dense Matter

Kai Hebeler<sup>a,b</sup>

<sup>a</sup>Technische Universität Darmstadt, 64289 Darmstadt, Germany

<sup>b</sup>ExtreMe Matter Institute EMMI, GSI Helmholtzzentrum für Schwerionenforschung GmbH, 64291 Darmstadt, Germany

---

## Abstract

Recent advances in nuclear structure theory have significantly enlarged the accessible part of the nuclear landscape via *ab initio* many-body calculations. These developments open new ways for microscopic studies of light, medium-mass and heavy nuclei as well as nuclear matter and represent an important step toward a systematic and comprehensive understanding of atomic nuclei across the nuclear chart. While remarkable agreement has been found between different many-body methods for a given nuclear Hamiltonian, the comparison with experiment and the understanding of theoretical uncertainties are still important open questions. The observed discrepancies to experiment indicate deficiencies in presently used nuclear interactions and operators. Chiral effective field theory (EFT) allows to systematically derive contributions to nucleon-nucleon (NN), three-nucleon (3N) and higher-body interactions including estimates of theoretical uncertainties. While the treatment of NN interactions in many-body calculations is well established, the calculation of 3N interactions and their incorporation in *ab initio* frameworks is still a frontier.

This work reviews in detail recent and current developments on the derivation and implementation of improved 3N interactions and provides a comprehensive introduction to fundamental methods for their practical calculation and representation. We further give an overview of novel and established methods that facilitate the inclusion and treatment of 3N interactions in *ab initio* nuclear structure frameworks and present a selection of the latest calculations of atomic nuclei as well as nuclear matter based on state-of-the-art nuclear NN and 3N interactions derived within chiral EFT. Finally, we discuss ongoing efforts, open questions and future directions.

---

## Contents

<b>Symbols and Notation</b>	<b>3</b>
<b>1 Introduction and Overview</b>	<b>4</b>
<b>2 Nuclear interactions and chiral effective field theory</b>	<b>9</b>
2.1 Chiral expansion of nuclear forces . . . . .	9
2.2 A brief history of chiral EFT NN interactions . . . . .	13
2.3 Chiral EFT three-nucleon interactions and fitting strategies . . . . .	14
2.3.1 Fits of 3N interactions based on fixed NN interactions ( $\Delta$ -less) . . . . .	15
2.3.2 Fits of $\Delta$ -full 3N interactions . . . . .	20
2.3.3 Simultaneous fits of NN and 3N interactions . . . . .	21
2.3.4 Bayesian parameter estimation . . . . .	24
2.4 EFT uncertainty quantification . . . . .	25

---

Email address: [kai.hebeler@physik.tu-darmstadt.de](mailto:kai.hebeler@physik.tu-darmstadt.de) (Kai Hebeler)

<b>3</b>	<b>Representation and calculation of 3N interactions</b>	<b>28</b>
3.1	Definition of coordinates . . . . .	28
3.2	Momentum basis representation of three-nucleon forces . . . . .	31
3.3	Partial-wave decomposition of local 3N interactions . . . . .	32
3.4	Generalization to spin- and isospin-dependent 3N interactions . . . . .	34
3.5	Decomposition of 3N interactions and antisymmetrization . . . . .	37
3.6	Example: Calculation of two-pion exchange 3N interactions . . . . .	41
3.7	Regularization of 3N interactions . . . . .	42
3.7.1	Nonlocal momentum-space regularization . . . . .	44
3.7.2	Local momentum-space regularization . . . . .	45
3.7.3	Semilocal momentum-space regularization . . . . .	47
3.7.4	Local coordinate-space regularization . . . . .	48
3.7.5	Semilocal coordinate-space regularization . . . . .	51
3.8	Visualization and comparison of matrix elements . . . . .	54
3.9	Transformation of matrix elements to harmonic oscillator basis . . . . .	57
<b>4</b>	<b>Incorporation of 3N interactions in many-body frameworks</b>	<b>59</b>
4.1	Partial-wave convergence of 3N interaction in dense matter . . . . .	60
4.2	SRG evolution in momentum basis . . . . .	64
4.2.1	Flow equations . . . . .	64
4.2.2	Application to state-of-the-art chiral NN and 3N interactions . . . . .	69
4.3	Normal ordering of 3N interactions . . . . .	73
4.3.1	Normal ordering in nuclear matter . . . . .	77
4.3.2	Normal ordering in finite nuclei . . . . .	82
4.4	Application of 3N interactions without partial-wave decomposition . . . . .	86
<b>5</b>	<b>Applications to nuclei and matter</b>	<b>91</b>
5.1	SRG evolution of 3N interactions versus low-resolution fits . . . . .	91
5.2	Nuclear matter based on consistently SRG-evolved 3N interactions . . . . .	93
5.3	Ground-state energies of nuclei . . . . .	94
5.4	Charge radii of nuclei . . . . .	97
5.5	Spectra of nuclei . . . . .	100
5.6	Electromagnetic response of nuclei and neutron distributions . . . . .	101
5.7	Beta decay transitions . . . . .	103
5.8	Three-body scattering cross sections . . . . .	105
5.9	Nuclear equation of state and astrophysical applications . . . . .	107
<b>6</b>	<b>Summary and outlook</b>	<b>115</b>
6.1	Present status and achievements . . . . .	115
6.2	Open questions and future directions . . . . .	116
<b>A</b>	<b>Normalization convention of momentum basis states</b>	<b>122</b>
<b>B</b>	<b>Integral for partial-wave decomposition of local 3N interactions</b>	<b>124</b>
<b>C</b>	<b>Partial-wave matrix elements of permutation operator <math>P_{123}</math></b>	<b>125</b>
<b>D</b>	<b>Normal-ordered effective interactions for nuclear matter</b>	<b>127</b>
<b>E</b>	<b>List of three-body configurations</b>	<b>131</b>
	<b>References</b>	<b>132</b>

## List of Symbols and Abbreviations

$\hbar = c = 1 = \hbar c = 197.326 \text{ MeV fm}$	unit system		
<i>Momenta (see Table 2 for details):</i>			
$\hat{\mathbf{a}} = \mathbf{a}/ \mathbf{a}  = \mathbf{a}/a$	unit vector		
$\mathbf{k}_i$	single-particle momentum of particle $i$		
$\mathbf{k}(\mathbf{k}')$	initial (final) state momentum		
$\mathbf{Q}_i = \mathbf{k}'_i - \mathbf{k}_i$	momentum transfer		
$\mathbf{p}, \mathbf{q}$	Jacobi momenta		
<i>Angular momentum coupling coefficients (using the conventions of Ref. [1]):</i>			
$C_{j_1 m_1 j_2 m_2}^{j_3 m_3} = \langle j_1 m_1 j_2 m_2   (j_1 j_2) j_3 m_3 \rangle$	Clebsch-Gordan coefficients		
$\left\{ \begin{matrix} j_1 & j_2 & j_3 \\ j_4 & j_5 & j_6 \end{matrix} \right\}$	6j symbols		
$\left\{ \begin{matrix} j_1 & j_2 & j_3 \\ j_4 & j_5 & j_6 \\ j_7 & j_8 & j_9 \end{matrix} \right\}$	9j symbols		
$Y_{lm}(\hat{\mathbf{a}}) = \langle \hat{\mathbf{a}}   lm \rangle, Y_{lm}^*(\hat{\mathbf{a}}) = \langle lm   \hat{\mathbf{a}} \rangle = (-1)^m Y_{l-m}(\hat{\mathbf{a}})$	spherical harmonics		
$\mathcal{Y}_{l_1 l_2}^{l_3 m_3}(\hat{\mathbf{a}}, \hat{\mathbf{b}}) = \sum_{m_1, m_2} C_{l_1 m_1 l_2 m_2}^{l_3 m_3} Y_{l_1 m_1}(\hat{\mathbf{a}}) Y_{l_2 m_2}(\hat{\mathbf{b}})$	coupled spherical harmonics		
<i>Three-body partial-wave states:</i>			
$ pq\alpha\rangle =  pq; [(LS)J(ls)j]\mathcal{J}(Tt)\mathcal{T}\rangle$	states in $Jj$ -coupling scheme		
$ pq\beta\rangle =  pq; [(LL)\mathcal{L}(Ss)S]\mathcal{J}(Tt)\mathcal{T}\rangle$	states in $LS$ -coupling scheme		
$L, S, J, T$	two-body quantum numbers: relative orbital angular momentum, spin, total relative angular momentum and isospin of the particles with Jacobi momentum $p$		
$l, s = \frac{1}{2}, j, t = \frac{1}{2}$	orbital angular momentum, spin, total angular momentum and isospin of the particle with Jacobi momentum $q$		
$\mathcal{L}, \mathcal{S}, \mathcal{J}, \mathcal{T}$	three-body quantum numbers: total orbital angular momentum, spin, angular momentum and isospin		
<i>Abbreviations:</i>			
NN	nucleon-nucleon	3N	three-nucleon
EFT	effective field theory	LEC	low-energy coupling
LO	leading order	NLO	next-to-LO
N <sup>2</sup> LO	next-to-next-to-LO	N <sup>3</sup> LO	next-to-next-to-next-to-LO
MS	momentum space	CS	coordinate space
PNM	pure neutron matter	SNM	symmetric nuclear matter
RG	renormalization group	SRG	similarity renormalization group
IM-SRG	in-medium SRG	MR-IM-SRG	multi-reference IM-SRG
NCSM	no-core shell model	IT-NCSM	importance-truncated NSCM
CC	coupled cluster	QMC	quantum Monte Carlo
MBPT	many-body perturbation theory	BMBPT	Bogoliubov-MBPT
SCGF	self-consistent Green's function	GSCGF	Gorkov-SCGF
HO	harmonic oscillator	QCD	quantum chromodynamics

## 1. Introduction and Overview

One of the central goals of *ab initio* nuclear theory is the microscopic understanding of the structure of atomic nuclei and dense matter starting from the properties of the fundamental degrees of freedom and their interactions. According to our present understanding, at the most fundamental level the strong interaction is governed by the quark-gluon dynamics described by quantum chromodynamics (QCD). However, even though it is now possible to correctly predict properties of single-nucleon states via Lattice QCD [2–4], the accurate and realistic description of multi-nucleon systems directly based on QCD has so far remained an elusive goal [5–14]. An alternative path from the principles of QCD to low-energy nuclear structure observables consists in employing low-energy effective theories and quantum many-body methods (see Figure 1). The fundamental principle of any effective low-energy description is based on the fact that details at small distance scales are not resolved when a physical system is probed at low energies. This makes it possible to introduce low-energy degrees of freedom that encapsulate the complex high-energy dynamics.

The radius of an average atomic nucleus is of the order of a few femtometers ( $1 \text{ fm} = 10^{-15} \text{ m}$ ). Hence, the uncertainty principle implies typical momenta in nuclei to be on the order of the pion mass  $m_\pi \approx 135 \text{ MeV}$ . At this scale the relevant degrees of freedom are not quarks and gluons but colorless hadrons, like neutrons, protons and pions. Chiral effective field theory (EFT) allows to systematically derive contributions to interactions between nucleons within a given power counting expansion scheme [15–17], which are parametrized in terms of long-range pion exchange contributions and short-range couplings (see Section 2). These contributions include nucleon-nucleon (NN), three-nucleon (3N) and even higher-body interactions. The presence of three- and higher-body nuclear interactions is a natural consequence of the composite nature of nucleons since for any non-elementary particle its constituents can be distorted by the presence of external forces. This phenomenon is well known in classical systems consisting of extended objects interacting via gravitational or electromagnetic interactions. For example, the orbit of a satellite around the earth is affected by the location of the moon due to the induced tides on earth, which in turn affect the gravitational force between earth and the satellite. If earth, moon and the satellite are all parametrized as point particles, such an effect can only be described via three-body forces. In the case of the gravitational force such effects are typically rather small. In contrast, for nuclear systems 3N contributions play a central role for, e.g., the

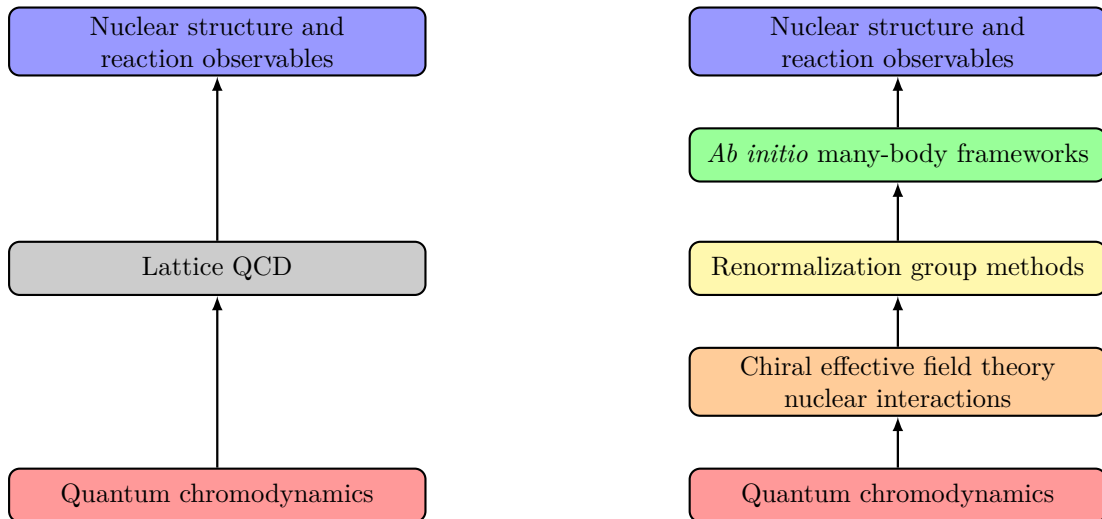


Figure 1: Two different paths from quantum chromodynamics (QCD), the fundamental theory of the strong interaction, to low-energy nuclear structure observables. The left panel shows the direct approach from first principles, by explicitly simulating the quark-gluon dynamics on a discrete lattice and extracting single- and multi-nucleon observables from such calculations. The right panel shows the path based on low-energy effective degrees of freedom, i.e., neutrons, protons and pions. The nuclear interaction between neutrons and protons is constrained by the symmetries and the symmetry-breaking patterns of QCD. The resulting chiral EFT interactions represent the microscopic input for *ab initio* many-body frameworks.



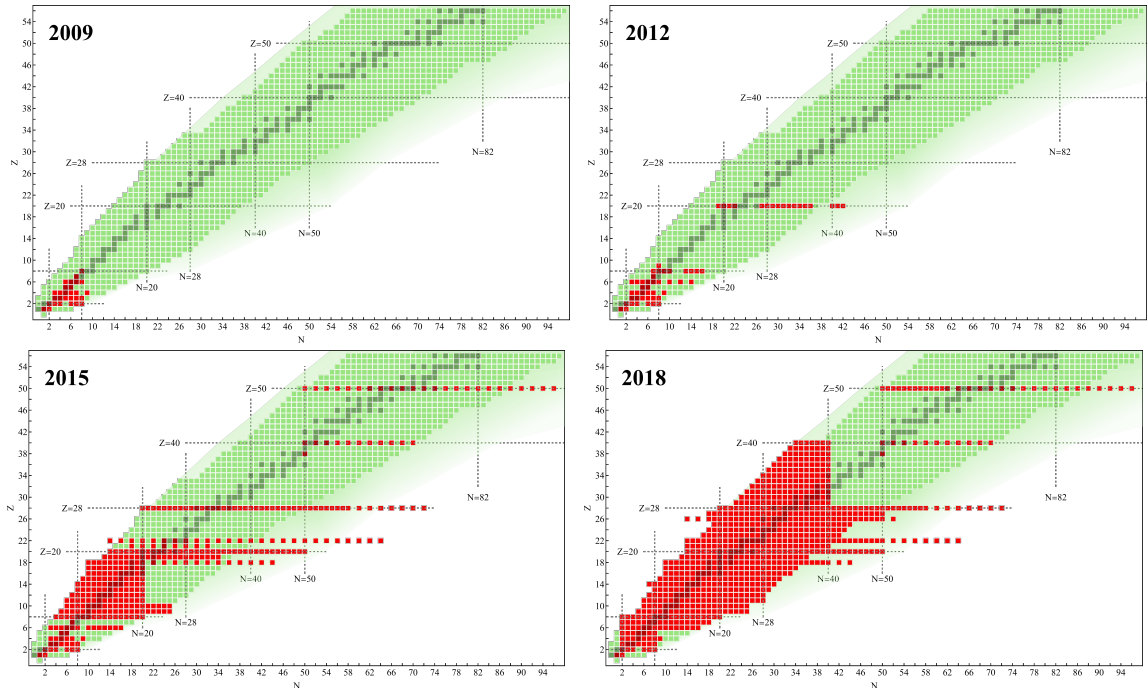


Figure 2: Illustration of the scope of *ab initio* many-body calculations of nuclei from the year 2009 (upper left) to 2018 (lower right) using NN and 3N interactions. Studied nuclei are highlighted in red. The figures include calculations for which converged results with respect to the basis size have been achieved. Credits to Heiko Hergert for providing the figures, see also Ref. [18].

shell structure of atomic nuclei, the bulk properties of nuclear matter and the evolution of systems toward the limits of stability (see Section 5).

The interactions derived within chiral EFT represent the fundamental microscopic input for *ab initio* many-body frameworks. In the following we consider all frameworks as “*ab initio*” which only use free-space nuclear interactions as basic input and can be systematically improved such that in the limit of infinite basis size and infinite order in the many-body expansion one can in principle recover results of exact calculations (see Table 1). In Figure 2 we illustrate the part of the nuclear chart studied within such approaches in the years 2009, 2012, 2015 and 2018 [18, 19]. Evidently, in recent years there has been a dramatic increase in the scope of such *ab initio* frameworks. These advances were driven by developments in different sectors (see also the right panel of Figure 1):

1. *Nuclear interactions*: The predictive power of nuclear many-body calculations is naturally limited by the quality of the employed nuclear interactions. Even results of virtually exact calculations can only be as good as the underlying input. During the recent years several new families of interactions have been derived at different orders in the chiral expansion. These efforts include the exploration of various different regularization schemes and fitting strategies for the short-range low-energy couplings as well as the investigation of different methods for estimating uncertainties due to neglected higher-order terms of the chiral expansion. Most of these investigations are still ongoing. In Section 2 we give a more detailed overview of these developments.

2. *Renormalization Group methods*: Renormalization Group (RG) techniques allow to systematically decouple low- and high-momentum components of nuclear interactions while preserving low-energy observables [20]. Such RG transformations to lower resolution scales help to reduce the scheme dependence of nuclear interactions, offer new tools to assess many-body uncertainties by studying residual resolution scale dependencies, and, most importantly for practical calculations, can dramatically improve the convergence of many-body calculations and generate much less correlated wave functions. This improved perturbativeness is in particular key for all many-body frameworks based on harmonic oscillator basis expansions (see

*atomic nuclei*

<b>method</b>	<b>type/representation</b>	<b>mass*</b>	
Faddeev(-Yakubovsky) equations	momentum/coordinate space basis	3-5	[25–33]
hyperspherical harmonics (HH)	momentum/coordinate space basis	3-6	[34–38]
no-core shell model (NCSM)	harmonic oscillator configuration basis	$\lesssim 12$	[39–46]
quantum Monte Carlo (QMC)	eucl. time prop. in coordinate basis	$\lesssim 16$	[47–55]
importance-truncated NCSM (IT-NCSM)	harmonic oscillator configuration basis	$\lesssim 25$	[56–60]
lattice EFT	eucl. time prop. on a discrete lattice	$\lesssim 28$	[61–74]
valence-shell diagonalization	harmonic oscillator configuration basis	$\lesssim 100$	[75–83]
in-medium SRG (IM-SRG)	harmonic oscillator configuration basis	$\lesssim 100$	[18, 24, 84–93]
coupled cluster (CC)	harmonic oscillator configuration basis	$\lesssim 100$	[58, 93–106]
self-consistent Green’s function (SCGF)	harmonic oscillator configuration basis	$\lesssim 100$	[107–114]
many-body perturbation theory (MBPT)	harmonic oscillator configuration basis	$\lesssim 100$	[23, 115–120]

\*The given mass number limits include constraints from limitations regarding the storage of three-body matrix elements, which currently prevent converged results for systems beyond the mass number regime  $A \approx 100$ .

*infinite nuclear matter*

<b>method</b>	<b>type/representation</b>	
many-body perturbation theory	momentum basis	[121–130]
self-consistent Green’s function	momentum basis	[111, 131, 132]
diagrammatic hole-line expansion	momentum basis	[133–137]
coupled cluster	momentum basis on a discrete lattice	[94, 138–142]
quantum Monte Carlo	eucl. time prop. in coordinate space	[49, 143–146]
lattice EFT	eucl. time prop. on a discrete lattice	[147]

Table 1: Summary of different microscopic many-body frameworks for atomic nuclei and matter including selected developments and applications based on NN and 3N interactions derived within chiral effective field theory.

Table 1). In fact, many of the calculations illustrated in Figure 2 have only been possible thanks to the use of low-resolution interactions obtained within the Similarity Renormalization Group (SRG) [21, 22] (see also Section 4.2).

3. *Improved and novel many-body frameworks:* Advances in many-body theory have led to various new improved frameworks that allow to study nuclear matter as well as nuclei in different regions of the nuclear chart. In Table 1 we give an overview of currently used and actively developed many-body frameworks for atomic nuclei and nuclear matter. Each of the listed methods has its own benefits and drawbacks, determined by factors like the required computational resources, the scaling behavior as a function of mass number, the nature and level of many-body truncations, the flexibility regarding which nuclear interactions can be used, as well as the accessibility of different observables of closed- and/or open-shell systems. The availability of various different methods offers new possibilities for cross-benchmarks and for studying in detail the validity of different many-body truncations for a given Hamiltonian. In particular, given that various frameworks generally can differ quite substantially in terms of computational cost, it is now possible to test novel nuclear interactions in an efficient and reliable way by using computationally inexpensive methods and by validating the results for a few systems using more precise and costly methods. Furthermore there are active ongoing efforts to combine the advantages of different methods by developing mixed and hybrid methods (see, e.g., Refs. [23, 24]).

4. *Increased computational resources:* Finally, advances in the hardware equipment of present high-performance computer clusters contributed to the increased scope of present many-body calculations. These developments include improved floating point performance as well as the availability of large-memory machines, which are in particular key for handling matrix elements of 3N interactions (see Section 4).

We stress that Figure 2 illustrates only the scope of converged many-body calculations without quantifying the degree of agreement with experimental data. Typically, results based on present nuclear interactions

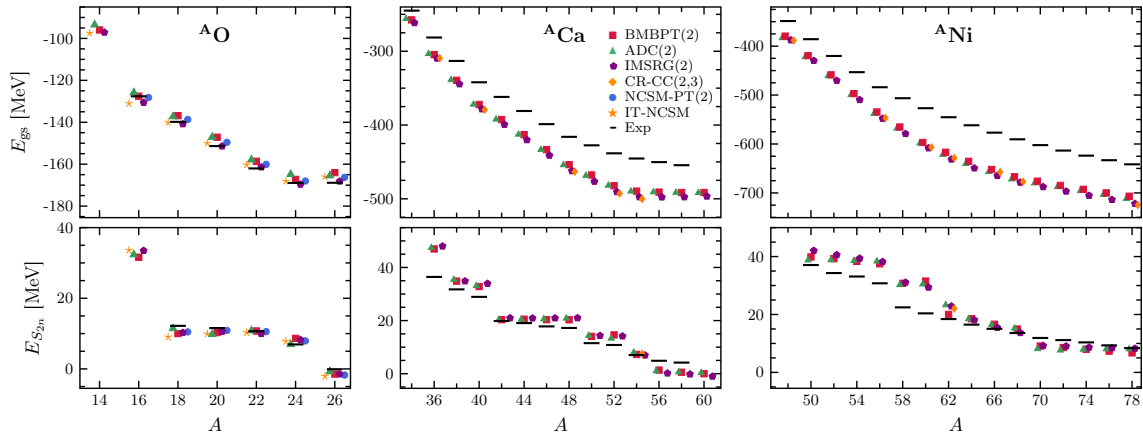


Figure 3: Ground-state energies (top) and two-neutron separation energies (bottom) for nuclei of the oxygen, calcium and nickel isotopic chains. Shown are results of second-order BMBPT (■), perturbatively-improved no-core shell model (NCSM-PT) (●), IT-NCSM (★), Gorkov-SCGF (GSCGF-ADC(2)) (▲), MR-IM-SRG (◆) and coupled cluster (CR-CC) (◇). Black lines show the experimental values [149].

Source: Figure taken from Ref. [117].

can lead to good agreement with experiment for specific observables (like, e.g., ground-state energies, excited states or charge radii) in a restricted area of the nuclear chart (see Section 5 for a detailed discussion). The agreement, however, generally depends on details of the nuclear forces and on the observables that have been included in the fitting process of the interaction (see Section 2). A typical example is shown in Figure 3, where we compare theoretical results for the ground-state energies and two-neutron separation energies of the oxygen (left panel), calcium (middle panel) and nickel (right panel) isotopic chain with experimental data [117]. All the calculations have been performed based on the same SRG-evolved NN plus 3N interaction [148]. While the results of the theoretical calculations show excellent agreement with experimental values for the oxygen chain (left panel), the agreement deteriorates significantly for isotopic chains of heavier elements. However, it is remarkable that the agreement between the predictions of different many-body methods is excellent for all shown nuclei, given that the many-body truncations are quite different in the various approaches. Based on these observations we can draw the following general conclusions:

- a) The agreement between the results of state-of-the-art many-body frameworks is excellent for a given low-resolution Hamiltonian. This implies that the many-body uncertainties are small for such interactions and possible disagreement with experimental results can be mainly attributed to deficiencies of currently used interactions and operators.
- b) The agreement between theoretical predictions and experimental results sensitively depends on the studied observable, the system under investigation and the details of the employed nuclear interactions. Presently, there exist no nuclear interactions that exhibit a systematic convergence pattern in the chiral expansion and are able to correctly predict simultaneously different few- and many-body observables of nuclei over the full range of mass number within theoretical uncertainties.

Clearly, these findings emphasize the urgent need for improved nuclear interactions which are able to correctly reproduce empirical properties of known atomic nuclei as well as nuclear matter and can be applied in a reliable and controlled way to systems in still unknown territory of the nuclear chart. While the implementation of NN interactions in a form suitable for application in many-body frameworks is straightforward and well established, the calculation of 3N interactions is much more intricate and still involves major challenges. This is true for both the conceptual development as well as their practical implementation. The present work provides a comprehensive introduction into methods for the practical implementation of 3N interactions and their incorporation in microscopic many-body calculations. Even though the techniques

presented in this work can be applied to arbitrary 3N interactions, in this work we will mainly focus on interactions derived within chiral effective field theory (EFT).

Specifically, in Section 2 we review recent efforts to derive NN plus 3N interactions within chiral EFT with a particular focus on 3N interactions and summarize different strategies to fit the unknown LECs. In Section 3 we discuss in detail how 3N interactions can be practically represented and computed in a form suitable for *ab initio* many-body frameworks. In addition, we summarize different currently employed regularization schemes and illustrate the degree of scheme dependence of these interactions. In Section 4 we present novel methods that help to simplify the incorporation and treatment of 3N interactions in practical calculations. In particular, we focus here on the SRG and normal ordering. In Section 5 we give a selection of state-of-the-art calculations of atomic nuclei and dense matter based on the most recent chiral EFT interactions. Finally, in Section 6 we conclude and give an outlook.

## 2. Nuclear interactions and chiral effective field theory

In this section we review recent developments and the current status of deriving NN, 3N and higher-body forces based on EFT principles. Compared to more phenomenological approaches EFT provides a framework that allows to derive contributions more systematically in a low-energy expansion scheme and to estimate theoretical uncertainties due to neglected higher-order terms. In this work we will not discuss the underlying concepts of chiral EFT, but rather focus on providing an overview of recent developments and strategies to derive novel and improved NN and 3N interactions for state-of-the-art calculations of atomic nuclei and nuclear matter, with a particular focus on 3N interactions. For details on the underlying concepts of chiral EFT to nuclear forces we refer the reader to Refs. [15–17, 150] and references therein. We also note that all “high precision” chiral interactions developed so far and discussed below are based on the power counting scheme originally suggested by Weinberg [151, 152]. There are ongoing discussions regarding alternative EFT expansion schemes [17] which involve the promotion of short-range couplings to lower orders in the chiral expansion for improved RG invariance (see, e.g., Refs. [17, 153–161]) and the perturbative many-body treatment of all interaction contributions beyond leading order in the chiral expansion (see, e.g., Ref. [162]). However, so far no interactions suitable for practical nuclear structure calculations have been developed within these alternative schemes. This is currently work in progress. We stress that the techniques discussed in Sections 3 and 4 on the calculation and treatment of 3N interactions for many-body calculations are general and can be applied to interactions derived in any power counting scheme and also to phenomenological 3N interactions.

### 2.1. Chiral expansion of nuclear forces

Chiral EFT represents a systematic framework to describe the strong interaction at momentum scales of the order of the pion mass  $Q \approx m_\pi$ , constrained by the symmetries and symmetry-breaking patterns of QCD. In chiral EFT the interaction between nucleons is parametrized in terms of long-range pion-exchange interactions and short-range contact interactions. These contributions to the nuclear interactions can be organized in a systematic expansion in powers of  $Q/\Lambda_b$ , where  $\Lambda_b$  denotes the breakdown scale of the EFT. The expansion of any effective theory is based on a separation of scales. Chiral EFT in particular exploits the mass separation between the lightest meson, the pion with  $m_\pi \approx 135$  MeV, and the next lightest meson, the  $\rho$  meson with  $m_\rho \approx 770$  MeV. This mass separation is rooted in the chiral symmetry breaking pattern of QCD which requires the existence of an unnaturally light Goldstone boson in the form of the pion. Since only pion contributions are treated explicitly in chiral EFT while the contributions from heavier mesons are captured implicitly in terms of short-range interactions, the breakdown scale is expected to be below the  $\rho$  mass and usually chosen to be around  $\Lambda_b \approx 500$  MeV. This results in an effective expansion parameter  $Q/\Lambda_b \approx \frac{1}{3}$ .

The values of the short-range interactions cannot be determined within the EFT but need to be fixed either based on the underlying theory, i.e., QCD, or by fitting them to observables. In the case of chiral EFT the short-range couplings entering the NN interactions are usually fit to elastic two-nucleon scattering cross sections and properties of the deuteron. In the future it might be possible to connect nuclear forces directly to the underlying theory through Lattice QCD [5, 9]. It is important, however, to keep in mind that nuclear forces are generally non-observable, and in particular the values of the short-range couplings are strongly scale and scheme dependent, which can be made manifest in RG frameworks [20] (see Section 4.2).

In Figure 4 we show the contributions to NN, 3N and 4N interactions from one- or multi-pion exchanges, which govern the long- and intermediate-range forces, as well as from short-range contact interactions at different orders in the chiral expansion. The short-range couplings are fit to low-energy data and thus capture all short-range effects relevant at low energies. The leading-order (LO) contributions were derived by Weinberg [151, 152]. These seminal works represent the foundation of the chiral expansion of nuclear forces that is still being used today. At LO the NN interaction consists of a long-range pion exchange interaction, which corresponds to the empirically well-known Yukawa interaction [163] and two short-range interactions parametrized by the coupling  $C_S$  and  $C_T$ . In the following years this framework was extended to higher orders in the expansion. At next-to-leading order (NLO) and next-to-next-to-leading order (N<sup>2</sup>LO)

	NN	3N	4N
LO $\mathcal{O}(Q^0/\Lambda^0)$	1990 [151,152] 2 	—	—
NLO $\mathcal{O}(Q^2/\Lambda^2)$	1992 [164,165] 7 	1992,1994 [166-169] —	—
N <sup>2</sup> LO $\mathcal{O}(Q^3/\Lambda^3)$	1992 [164,165] 0 	1994 [167,170] 2 	—
N <sup>3</sup> LO $\mathcal{O}(Q^4/\Lambda^4)$	2000–2002 [179-182] 12 	2008–2011 [183-185] 0 	2006 [186] 0 
N <sup>4</sup> LO $\mathcal{O}(Q^5/\Lambda^5)$	2015 [188,189] 0 	2011– [190-192] ? 	? 

Figure 4: Contributions to NN, 3N and 4N interactions in chiral EFT at different orders in the chiral expansion within Weinberg’s power counting without explicit  $\Delta$  degrees of freedom for intermediate states. Solid and dashed lines denote nucleon and pion propagators, respectively. In each panel we give the years when the terms were first derived, with corresponding references and the number of new couplings (in naive dimensional analysis) in the upper right corner. The low-energy coupling constants that enter the 3N interactions are highlighted by vertices of different colors and shapes. The following couplings show up first at N<sup>2</sup>LO: the long-range pion-nucleon couplings  $c_i$  (●), the intermediate-range coupling  $c_D$  (■) and the short-range 3N coupling  $c_E$  (◆). The 3N and 4N interactions at N<sup>3</sup>LO are parameter-free in the sense that they only depend on short-range couplings that appear already at lower orders, like, e.g., the leading-order NN couplings  $C_S$  and  $C_T$  (◆). The derivation of the 3N interactions at N<sup>4</sup>LO is still work in progress, in particular the short-range contributions (formally indicated by the couplings ●). Higher-order couplings that only enter NN interactions up to the shown orders are indicated by white vertices. See main text for details.

$2\pi$  exchange interactions and higher-order short-range couplings contribute to NN forces [164, 165]<sup>1</sup>. For 3N interactions it was shown that contributions at NLO cancel exactly [166–169], while the first nonvanishing contributions to 3N interactions appear at N<sup>2</sup>LO [167, 170]. The 3N interactions at this order include long-range two-pion exchange interactions  $V_{3N}^{2\pi}$ , an intermediate-range one-pion plus contact interaction  $V_{3N}^{1\pi}$  and a pure contact interaction  $V_{3N}^{\text{contact}}$  (see Figure 5). Since these 3N interactions play a central role in this work as well as in many recent and current nuclear structure studies, we discuss them in more detail now. The interactions are given by the following expressions [170]:

$$V_{3N}^{2\pi} = \frac{1}{2} \left( \frac{g_A}{2f_\pi} \right)^2 \sum_{i \neq j \neq k} \frac{(\boldsymbol{\sigma}_i \cdot \mathbf{Q}_i)(\boldsymbol{\sigma}_j \cdot \mathbf{Q}_j)}{(Q_i^2 + m_\pi^2)(Q_j^2 + m_\pi^2)} F_{ijk}^{\alpha\beta} \tau_i^\alpha \tau_j^\beta, \quad (1)$$

where  $\mathbf{Q}_i = \mathbf{k}'_i - \mathbf{k}_i$  denotes the momentum transfers, i.e., the difference between the initial and final single-particle momenta ( $\mathbf{k}_i$  and  $\mathbf{k}'_i$  respectively), with  $i, j$  and  $k = 1, 2, 3$ ,  $\sigma_i^a$  ( $\tau_i^a$ ) the Cartesian component  $a$  of the spin (isospin) operators of particle  $i$  and

$$F_{ijk}^{\alpha\beta} = \delta^{\alpha\beta} \left[ -\frac{4c_1 m_\pi^2}{f_\pi^2} + \frac{2c_3}{f_\pi^2} \mathbf{Q}_i \cdot \mathbf{Q}_j \right] + \sum_\gamma \frac{c_4}{f_\pi^2} \epsilon^{\alpha\beta\gamma} \tau_k^\gamma \boldsymbol{\sigma}_k \cdot (\mathbf{Q}_i \times \mathbf{Q}_j). \quad (2)$$

<sup>1</sup>We note that there exist different schemes to count contributions from relativistic corrections, indicated by the white circles in Figure 4 (see, e.g., Ref. [15]).

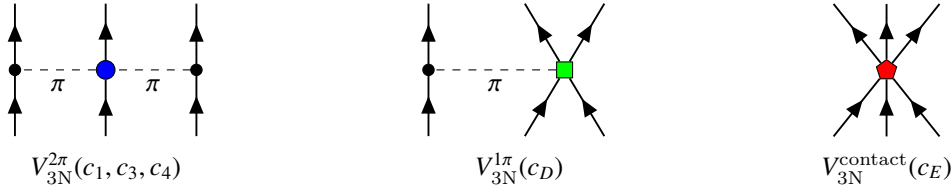


Figure 5: 3N interactions at  $N^2\text{LO}$  in the chiral expansion. The long-range pion-nucleon couplings  $c_i$  (●) also enter the NN interactions at this and higher orders and can hence be constrained by NN observables and  $\pi\text{N}$  scattering data. The short-range couplings  $c_D$  (■) and  $c_E$  (●) need to be fixed in three- or higher-body systems.

The  $1\pi$ -exchange and contact interactions are given respectively by

$$V_{3N}^{1\pi} = -\frac{g_A}{8f_\pi^2} \frac{c_D}{f_\pi^2 \Lambda_\chi} \sum_{i \neq j \neq k} \frac{\boldsymbol{\sigma}_j \cdot \mathbf{Q}_j}{Q_j^2 + m_\pi^2} (\boldsymbol{\tau}_i \cdot \boldsymbol{\tau}_j) (\boldsymbol{\sigma}_i \cdot \mathbf{Q}_j), \quad V_{3N}^{\text{contact}} = \frac{c_E}{2f_\pi^4 \Lambda_\chi} \sum_{j \neq k} (\boldsymbol{\tau}_j \cdot \boldsymbol{\tau}_k). \quad (3)$$

In Ref. [170] the values  $g_A = 1.29$ ,  $f_\pi = 92.4 \text{ MeV}$ ,  $m_\pi = 138 \text{ MeV}$  and  $\Lambda_\chi = 700 \text{ MeV}$  were chosen. Similarly to the LO one-pion exchange interactions, the long-range two-pion exchange contribution  $V_{3N}^{2\pi}$  resembles features of previously developed phenomenological 3N forces [171–173]. However, we stress that in contrast to these interactions, the  $V_{3N}^{2\pi}$  interactions formally do not contain any new parameters since the subleading pion-nucleon couplings  $c_1$ ,  $c_3$  and  $c_4$ , which characterize the strength of  $V_{3N}^{2\pi}$  (see Figure 5), also appear in the NN interaction at  $N^2\text{LO}$  (see Figure 4) and play also a key role in  $\pi$ -nucleon ( $\pi\text{N}$ ) scattering. In fact, currently the most robust extraction of the values of these long-range couplings was achieved based on the Roy-Steiner-equation analysis of  $\pi\text{N}$  scattering [174–176]. This demonstrates that contributions to NN and 3N interactions as well as terms determining the pion-nucleon scattering dynamics are treated on equal footing in chiral EFT, in contrast to most phenomenological approaches. The 3N interactions  $V_{3N}^{1\pi}$  and  $V_{3N}^{\text{contact}}$  on the other hand depend on two low-energy couplings  $c_D$  and  $c_E$  that encode pion interactions with short-range NN pairs and short-range three-body physics, respectively [167, 170]. These genuine three-body couplings do not appear in NN interactions and hence need to be fixed in few- or many-body systems (see Section 2.3).

Even though nuclear forces are not observable, there are natural sizes of two- and many-body-force contributions that are made manifest in the EFT power counting (see Figure 4) and which explain the phenomenological hierarchy of contributions from NN and many-body forces to observables, i.e., schematically  $V_{\text{NN}} > V_{3\text{N}} > V_{4\text{N}}$  [15, 16]. Although it might be tempting to neglect contributions from 3N interactions in cases when calculations based on only NN forces already provide a good description of experimental data (see, e.g., Ref. [140]), EFT power counting dictates the inclusion of all many-body forces up to a given order. In fact, explicit calculations show that 3N forces typically provide important contributions in nuclei and matter [178] (see also Sections 2.3 and 5).

The evaluation of the contributions to NN interactions at next-to-next-to-next-to-leading-order ( $N^3\text{LO}$ ) is quite involved as they include two-loop pion contributions, three-pion exchange contributions as well as

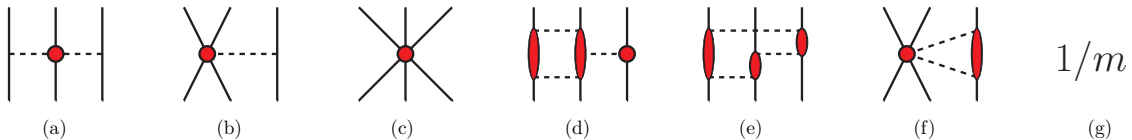


Figure 6: Different topologies contributing to chiral 3N interactions up to  $N^3\text{LO}$  (and  $N^4\text{LO}$ ). Nucleons and pions are represented by solid and dashed lines, respectively. The vertices denote the amplitudes of the corresponding interaction. Specifically, the individual diagrams are: (a)  $2\pi$  exchange, (b)  $1\pi$ -contact, (c) pure contact, (d)  $2\pi$ - $1\pi$  exchange, (e) ring contributions, (f)  $2\pi$ -contact and (g) relativistic corrections.

Source: Figure taken from Ref. [177].



	NN	3N
LO $\mathcal{O}(Q^0/\Lambda^0)$	—	—
NLO $\mathcal{O}(Q^2/\Lambda^2)$		
N <sup>2</sup> LO $\mathcal{O}(Q^3/\Lambda^3)$		
N <sup>3</sup> LO $\mathcal{O}(Q^4/\Lambda^4)$		

Figure 7: Additional diagrams contributing to NN and 3N interactions at different orders in  $\Delta$ -full chiral EFT compared to the terms shown in Figure 4. Double solid lines denote intermediate states of the  $\Delta$  resonance. We use the same notation as in Figure 4.

relativistic corrections [179–182]. The 3N interactions at this order also include many new structures as shown in Figure 6, but are predicted in a parameter-free way since they only depend on the leading NN contact interactions proportional to the LECs  $C_S$  and  $C_T$  [183–185] (see the  $2\pi$ -contact contributions (f) and the relativistic corrections (g) in Figure 6). In addition, the first nonvanishing contributions to 4N interactions appear at this order [186], which are also predicted in a parameter-free way. Remarkably, for systems consisting of only neutrons, the N<sup>2</sup>LO 3N interactions  $V_{3N}^{1\pi}$  and  $V_{3N}^{\text{contact}}$  do not contribute for unregularized or nonlocally regularized interactions [122] (see Section 3.7 for details). Therefore, chiral EFT predicts all three-neutron and four-neutron forces up to N<sup>3</sup>LO.

Due to the involved analytical structure of the 3N interactions at N<sup>3</sup>LO the implementation has only been completed relatively recently [130, 177, 187]. However, the development and implementation of optimized regularization schemes is still work in progress (see Section 3.7). The practical calculation of all topologies shown in Figure 6 in a form suitable for few- and many-body calculations is a nontrivial task but is key for improved many-body calculations and a systematic investigation of chiral power counting in the 3N sector. Due to the large amounts of required computational resources using traditional methods, the available 3N matrix elements were at first restricted to small basis spaces [187], insufficient for converged many-body calculations. In Section 3 we discuss in detail a more efficient method for decomposing 3N forces in a momentum partial-wave basis [177]. The new framework makes explicit use of the fact that all unregularized contributions to chiral 3N forces are either local, i.e., they depend only on momentum transfers, or they contain only polynomial nonlocal terms (see Section 3.3). These new developments allow to calculate matrix elements of all N<sup>3</sup>LO 3N contributions for large basis spaces, opening the way to *ab initio* studies of nuclei and nucleonic matter.

Recently the derivation of the NN contributions has been extended to N<sup>4</sup>LO [188, 189]. The corresponding 3N contributions at this order have been worked out for the long- and intermediate-range parts [190–192], while the derivation of all short-range parts is still work in progress. In contrast to the N<sup>3</sup>LO contributions new short-range couplings appear at this order and need to be fixed based on properties of few- or many-body systems, in addition to the couplings  $c_D$  and  $c_E$ . The 4N contributions at N<sup>4</sup>LO have not been worked out yet.

All the discussed developments above were performed in the so-called  $\Delta$ -less chiral EFT formulation. Since it is known that the  $\Delta$  resonance of the nucleon at the excitation energy of  $\Delta = m_\Delta - m_N \approx 300$  MeV plays an important role in nucleon scattering, it is argued that the chiral EFT expansion might be more



efficient and exhibit a faster converging pattern by treating the  $\Delta$  explicitly in intermediate states rather than implicitly in low-energy couplings. By introducing this new degree of freedom an additional small energy scale appears in the EFT expansion and the power counting has to be adjusted. As a consequence additional diagrams with new couplings appear at different orders, while a specific types of diagrams in the  $\Delta$ -less formulation get promoted to lower orders (see Figure 7). In particular, if Ref. [193] it was shown that the contributions from intermediate  $\Delta$  excitations expanded in powers of  $1/\Delta$  can be absorbed via a shift in the couplings in  $\Delta$ -less EFT. The  $\Delta$  contributions in the subleading pion-nucleon couplings take the following form:  $c_3^\Delta = -2c_4^\Delta = -4h_A^2/(9\Delta)$ , with the  $\pi N\Delta$  axial coupling  $h_A$ . Comparing the values of these shifts with the typical numerical values of the  $c_i$  couplings in  $\Delta$ -less EFT demonstrates that indeed a significant part of the  $c_i$  contributions can be attributed to the  $\Delta$  resonance [193].

The first additional contributions to NN and 3N interactions in  $\Delta$ -full theory show up at NLO [167, 194–196]. These diagrams can all be interpreted as promoted diagrams at N<sup>2</sup>LO and N<sup>3</sup>LO in Figure 4 by replacing the subleading couplings  $c_i$  by intermediate  $\Delta$  resonance states. The fact that 3N interactions already contribute at NLO in this EFT indicates that the effects of 3N interactions might be formally underestimated in  $\Delta$ -less theory and that 3N contributions get enhanced due to unnaturally large LEC values and might also lead to a slower convergence of the expansion series. At N<sup>2</sup>LO various new NN contributions appear [193] while no new 3N contributions are generated [196]. This implies that up to N<sup>2</sup>LO the 3N interaction topologies are identical to those of  $\Delta$ -less EFT, apart from a reshuffling of some contributions to NLO. Finally, the derivation of contributions at N<sup>3</sup>LO is still work in progress. In the case of 3N interactions the long-range contributions have been developed [197] while the intermediate-range and short-range parts are still under development.

In the next subsections we will give an overview of recent developments of new interactions within these two chiral EFT formulations for many-body calculations. An important open question concerns how to fit the NN and 3N LECs up to a given order. In particular, given that several low-energy couplings appear on equal footing in NN and many-body forces, it may be beneficial to fit several different two- and few-body observables simultaneously within theoretical uncertainties or to also include information beyond few-nucleon systems in the fits. In the following we will summarize recent explorations of these different strategies and briefly discuss advantages and disadvantages of each approach.

## 2.2. A brief history of chiral EFT NN interactions

The first “high-precision” NN interactions derived within chiral EFT including contributions up to N<sup>3</sup>LO were constructed in the years 2002 to 2005 in Refs. [29, 198] and [199]. The low-energy couplings of these two families of interactions were fitted to neutron-proton and proton-proton scattering phase shifts and the resulting interactions were provided in a partial-wave decomposed form, suitable for applications in many-body frameworks. Even though both interactions are derived within the same power counting framework they differ in several ways, particularly in the choice of regularization (see discussion in Ref. [29] for details). The accuracy of the reproduction of NN scattering phase shifts of the interaction presented in Ref. [199] was comparable to the best available phenomenological NN interactions at this time up to laboratory energies of about 290 MeV. These features made this force the interaction of choice for many-body calculations in the following years.

It took about 10 years until the next generation of NN interactions was developed. First, the NN interaction “N<sup>2</sup>LO<sub>opt</sub>” was constructed [140] by fitting the LECs up to N<sup>2</sup>LO to phase shifts up to 125 MeV using the automated derivative-free POUNDERS method [200] for the  $\chi^2$  minimization. First calculations of few-body systems based on only NN interactions showed remarkable agreement with experimental results, suggesting that the missing 3N contributions might be small. However, explicit calculations including 3N interactions showed that they provide significant contributions [201]. Within the same year another novel chiral EFT NN interaction up to N<sup>2</sup>LO was developed [50, 51]. In contrast to the previous chiral EFT interactions this interaction was local, including the choice for the regulator (see also Section 3.3), which made this force particularly suitable for Quantum Monte Carlo applications [47]. Following these developments, another “minimally nonlocal” interaction was developed in 2015 [202] and later reduced to a fully local potential in 2016 by discarding the nonlocal terms [203]. These forces contain contributions from the  $\Delta$  degree of freedom to  $2\pi$  exchange interactions up to N<sup>2</sup>LO.

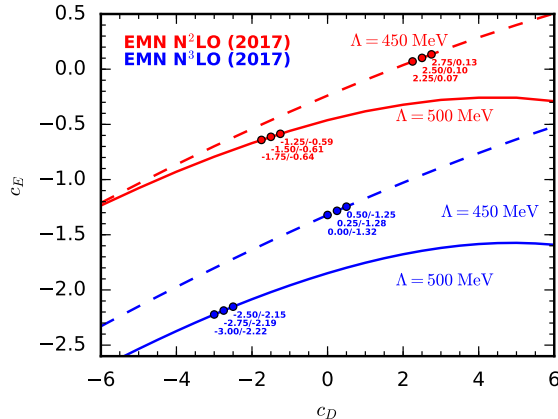


Figure 8: Three-nucleon couplings  $c_D$  and  $c_E$ , fit to the  ${}^3\text{H}$  binding energy using the NN potentials of Ref. [188] with  $\Lambda = 450\text{ MeV}$  (dashed) and  $\Lambda = 500\text{ MeV}$  (solid line) at  $\text{N}^2\text{LO}$  (red) and  $\text{N}^3\text{LO}$  (blue), combined with consistent 3N interactions at these orders using  $\Lambda = \Lambda_{\text{NN}, 3\text{N}}$ .

Source: Figure taken from Ref. [130].

In 2014 a new NN interaction including contributions up to  $\text{N}^3\text{LO}$  was presented [204]. One new feature of this interaction compared to its predecessor published in Ref. [29] was the use of a local coordinate-space regulator (see Section 3.7) for the long-range parts of the interaction, similar to the interactions of Refs. [50, 51]. It was argued that this choice of regulator reduces finite cutoff artifacts and preserves the analytic structure of the scattering amplitude (see Ref. [204] for details). In addition, a novel method for quantifying theoretical uncertainties due to the truncation of the chiral expansion was proposed. The same year contributions at  $\text{N}^4\text{LO}$  were included for the first time [189], while it was shown that long-range parameter-free terms at this order lead to a significant improvement of the reproduction of scattering phase shifts. The interactions were made available for different cutoff scales and at different orders in the chiral expansion, allowing for a more systematic study of the theoretical uncertainties of many-body observables. In 2017 a second set of NN interactions up to  $\text{N}^4\text{LO}$  was presented [188]. Similarly to the potential of Ref. [189] a whole set of interactions with different regularization cutoff scales and chiral orders were provided. On the other hand, a nonlocal momentum regulator was used like in Ref. [199]. Finally, in 2018 a local momentum-space regularized  $\text{N}^4\text{LO}$  interaction was presented [205]. This new interaction combines the advantages of the previously developed interaction of Ref. [204] with simplified calculations of many-body forces and current operators in the novel regularization scheme (see Section 3.7 for details). In addition, it was demonstrated that the removal of redundant short-range couplings leads to simplified fits of scattering observables and softer interactions. Finally, in Ref. [142] a nuclear NN interaction (plus 3N interaction) with explicit contributions from the  $\Delta$  isobar was constructed. Interactions at different orders up to  $\text{N}^2\text{LO}$  were fitted to NN scattering phase shifts and by using the pion-nucleon LECs from the Roy-Steiner analysis of  $\pi\text{N}$  scattering phase shifts [174, 175]. Calculations of heavier nuclei as well as matter based on these interactions at  $\text{N}^2\text{LO}$ , plus corresponding 3N interactions (see Section 2.3.2), showed remarkable agreement with experimental results, which might be an indication for an improved and more natural convergence of the chiral expansion (see Section 2.1).

### 2.3. Chiral EFT three-nucleon interactions and fitting strategies

Parallel to the developments of new NN interactions as outlined in the previous section first steps toward simultaneous fits of NN and 3N interactions up to a given order in the chiral expansion were achieved [141, 206]. While the determination of the 3N-interaction LECs is effectively a two-parameter problem (determination of  $c_D$  and  $c_E$ ), a simultaneous fit of all LECs in NN and 3N interactions is obviously of much higher complexity due to the large number of parameters. We will first discuss different strategies that have been pursued in recent years to determine the values for  $c_D$  and  $c_E$  for a given NN interaction

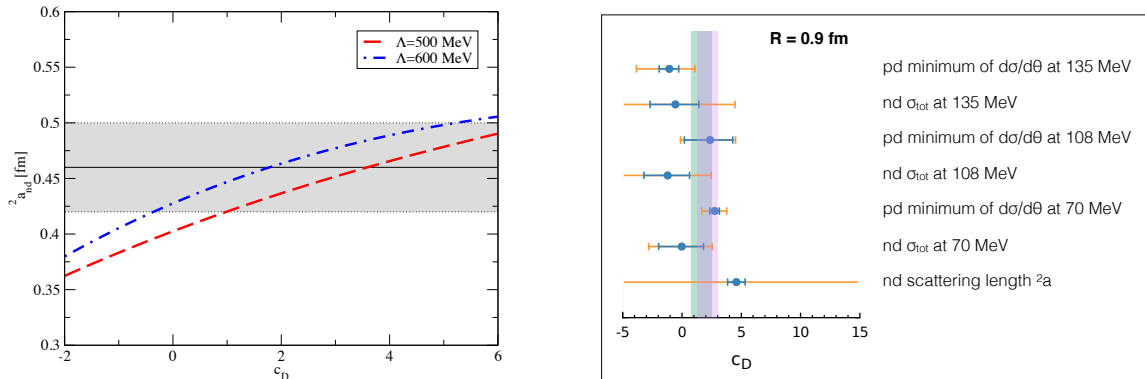


Figure 9: Left: Neutron-deuteron scattering length  $^2a_{nd}$  as function of the LEC  $c_D$ . The relation between  $c_D$  and  $c_E$  has been determined by fits of the  $^3\text{H}$  binding energy based on the NN interactions of Ref. [198] for two different cutoff values. The shaded band indicates the uncertainty of the experimental scattering length. Right: Determination of the LEC  $c_D$  from the differential cross section in elastic pd scattering, total nd cross section and the nd doublet scattering length  $^2a$  for the cutoff choice of  $R = 0.9$  fm of the interactions at N<sup>2</sup>LO of Ref. [33]. The smaller (blue) error bars correspond to the experimental uncertainty while the larger (orange) error bars also take into account the theoretical uncertainty estimated as described in Ref. [204]. The pink (green) bands show the results from a combined fit to all observables (to observables up to  $E = 108$  MeV). *Source:* Left figure taken from Ref. [170] and right figure adapted from Ref. [33].

based on few-body observables (see also Ref. [207]) and then discuss the simultaneous construction of NN and 3N interactions.

### 2.3.1. Fits of 3N interactions based on fixed NN interactions ( $\Delta$ -less)

One of the most natural observables for constraining the LECs of 3N interactions is the binding energy of 3N systems. In fact, for most 3N interactions developed in recent years the three-body ground-state energy has been used as one of the fitting observables. Calculations based on only NN interactions typically lead to a reasonable agreement with the experimental ground-state energies of  $^3\text{H}$  and  $^3\text{He}$  ( $E_{^3\text{H}} = -8.482$  MeV and  $E_{^3\text{He}} = -7.781$  MeV [149]), with a total net effect of 3N interactions typically of the order of 1 MeV or less. Due to subtleties connected to the precise treatment and infrared regularization of the Coulomb interaction for calculations of  $^3\text{He}$ , usually the 3N couplings are fitted to the ground-state energy of  $^3\text{H}$ . Such fits provide a relation between the two couplings, i.e., formally a function of the form  $c_E(c_D)$ . Figure 8 shows an example of such relations for interactions at N<sup>2</sup>LO and N<sup>3</sup>LO for the recently developed NN interactions of Ref. [188]. It can be argued if the perfect reproduction of the experimental ground-state energy is useful, given that the interactions contain inherent uncertainties due to truncation effects of neglected higher order terms of the chiral expansion. It might be more natural and meaningful to take into account these uncertainties at a given order in the chiral expansion by fitting the LECs to some range around the experimental value. Such a fit would result in a correlation band between  $c_D$  and  $c_E$  instead of a correlation line. Such a strategy would allow to investigate to what degree fits to different observables are consistent at a given order in the chiral expansion. Work along these directions is currently in progress. For the full determination of both 3N couplings,  $c_D$  and  $c_E$ , a second few-body observable is needed. Ideally both observables should be as uncorrelated as possible. Examples of quantities that exhibit significant correlations are the binding energy of  $^3\text{He}/^3\text{H}$  and  $^4\text{He}$  (“Tjon line” [208, 209]) or between  $^3\text{He}/^3\text{H}$  binding energy and the neutron-deuteron (nd) scattering length (“Phillips line” [210]). The correlation manifests itself in the form of a mild sensitivity of the results for the correlated observables as a function of the remaining coupling constant.

In the left panel of Figure 9 we show as an example the results for the nd-scattering length as a function of the LEC  $c_D$  after the  $c_E$  coupling has been fixed to the experimental  $^3\text{H}$  binding energy for each value of  $c_D$  [170]. The results show that the nd scattering length is rather insensitive to  $c_D$  since the theoretical results are compatible with the experimental constraints over a wide range of  $c_D$  values. In addition, minor variations of the cutoff, regularization schemes and inclusion of higher-order terms tend to lead to significant changes in the values of the extracted LECs. This makes it hard or even impossible to extract tight and

robust constraints on this LEC from a fit to the scattering length alone. One possibility to improve such a fit is to include additional scattering observables and perform a global fit. An example of such an analysis is shown in the right panel of Figure 9. The figure shows the constraints on  $c_D$  resulting from the reproduction of the proton-deuteron differential cross section data at  $E = 70$  and 135 MeV based on interactions at N<sup>2</sup>LO of Refs. [189, 204] (see Ref. [33] for details). Such a more global analysis allows to improve the significance and robustness of a fit based on three-body scattering observables.

Another three-body scattering observable sensitive to 3N interaction contributions is connected to the long-standing “A<sub>y</sub> puzzle” [26, 211]. This puzzle refers to the observed large discrepancy between theoretical predictions and experimental measurements of a particular polarization observable, the so called vector analyzing power, in elastic nucleon-deuteron scattering in the region of its maximum around the center-of-mass angle  $\Theta_{cm} \approx 120^\circ$  and for incoming nucleon energies below  $E \approx 20$  MeV [26, 212, 213]. So far, no satisfactory resolution of this puzzle has been found. However, it should be emphasized that the low-energy vector analysing power is a fine-tuned observable which is very sensitive to changes in  $^3P_j$  NN force components [187]. Thus, it is not obvious if the observed discrepancies can be mainly attributed to deficiencies of presently used NN interaction or to genuine three-body effects (see also Figure 65).

In Figure 10 we show as another example the results of 3N interaction fits using quantum Monte-Carlo methods to the binding energy of  $^4\text{He}$  and the spin-orbit splitting in the  $n\alpha$   $P$ -wave phase shifts, i.e., a five-body scattering observable [52]. These calculations are based on the NN interactions presented in Refs. [50, 51] and use a purely local coordinate-space regularization scheme (see Section 3.7 for details). These calculations demonstrate that the employed NN and 3N interactions derived from chiral EFT up to N<sup>2</sup>LO are capable of correctly predicting  $n\alpha$  scattering phase shifts and properties of light nuclei within theoretical uncertainties. The inclusion of  $n\alpha$  scattering phase shifts in the fitting process was triggered by the inability of previous phenomenological 3N interactions like the Urbana IX interaction [214] to correctly describe the spin-orbit splitting in neutron-rich systems, which in turn motivated the inclusion of three-pion exchange diagrams in the Illinois 3N models [215]. Since the  $n\alpha$  scattering phase shifts are sensitive to three-neutron forces, this strategy might constrain this part of the 3N interactions and lead to a better agreement in neutron-rich systems. In addition, the results of Ref. [52] investigated the impact of the Fierz-ambiguity on observables when using local regulators (see Section 3.7.4 and also Ref. [216]) and showed that the fitted NN plus 3N interactions lead to pure neutron matter results in good agreement with other works [178].

For comparison to the results shown in Figure 9 we show in Figure 11 3N fits based on observables that are less correlated, in this case the  $^3\text{H}$  binding energy and the  $\beta$  decay half-life of  $^3\text{H}$ . The latter observable was first suggested in Ref. [217] in the year 2006 as a suitable observable to constrain 3N forces, while it was first implemented in Ref. [148] three years later. Such fits based on electroweak reactions take advantage of one of the key strengths of chiral EFT, that nuclear interactions and nuclear currents are derived from the same Lagrangian and hence contain the same low-energy couplings. In particular, for the calculations in Ref. [148] and later in Refs. [37, 218, 219] the dependence of the axial two-body current on the 3N coupling  $c_D$  was exploited<sup>2</sup>. This dependence leads a strong sensitivity in the predictions of the  $^3\text{H}$  half-life, which can be measured quite accurately [221]. The two panels of Figure 11 show the ratio of the theoretical and experimental values of the reduced Gamow-Teller transition matrix elements for different interactions as a function of  $c_D$  (see also Section 5.7). The shaded region indicates the experimental uncertainty of the transition matrix element (see Refs. [148, 219] for details). Of course, the specific values of  $c_D$  that are consistent with the experimental value sensitively depend on the employed NN interactions. However, it is generally true that the sensitivity of the  $^3\text{H}$  half-life on the 3N coupling is much stronger than for more correlated observables like in Figure 9 and hence in principle allows for tighter constraints on this coupling.

However, we note that contributions from the leading one-body currents already contribute about 98% of the total transition strength for the shown NN interaction in Figure 11, which implies that the 3N coupling  $c_D$  is effectively fitted to a 2% discrepancy to experimental values. In addition, such fits based on electroweak currents involve additional sources of uncertainty that are not present in pure nuclear structure calculations. These uncertainties concern the way the nuclear current operators are regularized. The right panel of

---

<sup>2</sup>We note that in all original publications an incorrect factor of  $-4$  was included in the coefficient multiplying the coupling  $c_D$  in the nuclear current [220]. This error was corrected later in all those references.

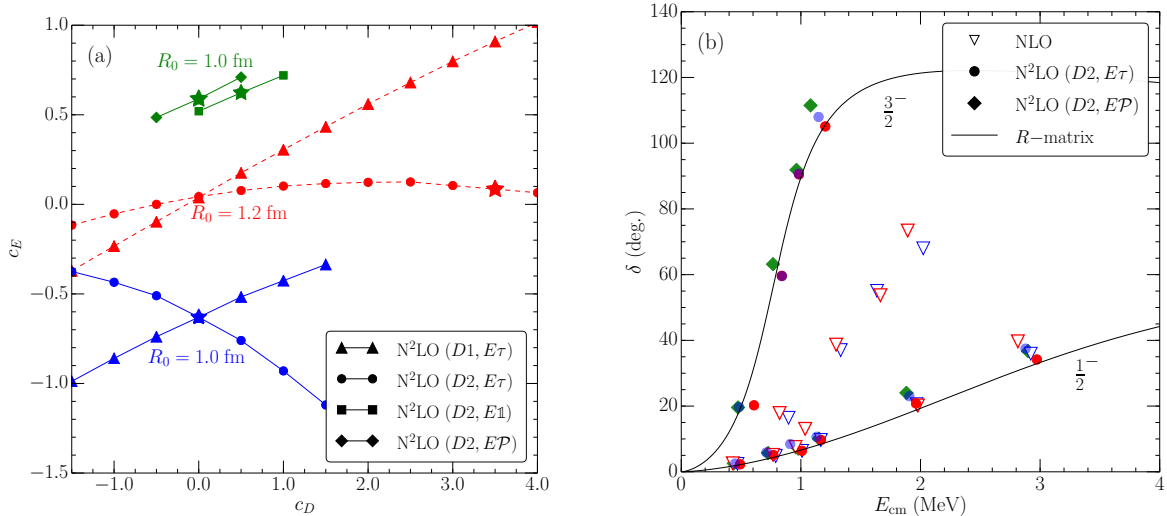


Figure 10: Left: Coupling values for  $c_E$  and  $c_D$  obtained by fits to the  ${}^4\text{He}$  binding energy using different operator forms and different cutoff values  $R_0$  (see Ref. [52] for details). The stars in the left panel indicate the values of  $c_D$  and  $c_E$  that simultaneously fit the experimental binding energy of  ${}^4\text{He}$  and the  $n\alpha$   $P$ -wave phase shifts (see right panel). Right:  $P$ -wave  $n\alpha$  elastic scattering phase shifts compared with an  $R$ -matrix analysis of experimental data. The same color coding as in the left panel has been used. Colors correspond to the left panel. *Source:* Figures taken from Ref. [52].

Figure 11 shows that a variation in the current cutoff scale can lead to a strong variation of the extracted  $c_D$  values. These results indicate that the uncertainties of the LECs due to the regulator dependence of the nuclear forces and currents can lead to significant uncertainties for nuclear structure observables. The observed dependence may also be related to possible inconsistencies in the power counting in the currents due to the non-trivial enhancement of some contributions [158]. In order to systematically reduce these uncertainties more detailed studies are required to find a consistent way of regularizing nuclear interactions and currents ensuring also the validity of the continuity equation. In Ref. [222] it was shown that the currents and interactions indeed fulfill the continuity equation at the operator level, i.e., for infinite cutoffs. Generalizing this analysis to regularized matrix elements will provide additional nontrivial constraints for a consistent way of regularizing electroweak currents.

In Ref. [123] another set of few-body observables was used to fit the 3N interactions, the  ${}^3\text{H}$  binding energy and the charge radius of  ${}^4\text{He}$ . The main focus of this work was to explore properties of symmetric nuclear matter (see also Section 5.1) based on NN plus 3N interactions which are only constrained by two- and few-body physics. The historical route to heavy nuclei is through infinite nuclear matter, a theoretical uniform limit that first turns off the Coulomb interaction, which otherwise drives heavier stable nuclei toward an imbalance of neutrons over protons and eventually, instability. However, predicting nuclear matter based on microscopic nuclear forces has proved to be an elusive target for a long time. In particular, few-body fits have not sufficiently constrained 3N interactions around saturation density such that nuclear matter calculations are predictive. Nuclear matter saturation is very delicate, with the binding energy resulting from cancellations of much larger potential and kinetic energy contributions. When a quantitative reproduction of empirical saturation properties was obtained, it was imposed by hand through the adjustment of short-range three-body forces (see, e.g., Refs. [225, 226]).

It is not unnatural to expect a correlation between theoretical predictions for heavier nuclei and nuclear matter. Naively, one might be tempted to expect that nuclear interactions that predict a saturation point in good agreement with the empirical saturation point  $E/A = -16$  MeV and  $n_0 = 0.16$  fm $^{-3}$  should also lead to a reasonably realistic descriptions of heavier nuclei. In Ref. [123] the nuclear matter many-body calculations were simplified by an RG evolution of the NN interaction to lower resolution scales [20] (see also Section 4.2). Given that at the time of that work no consistent evolution of 3N interactions in momentum

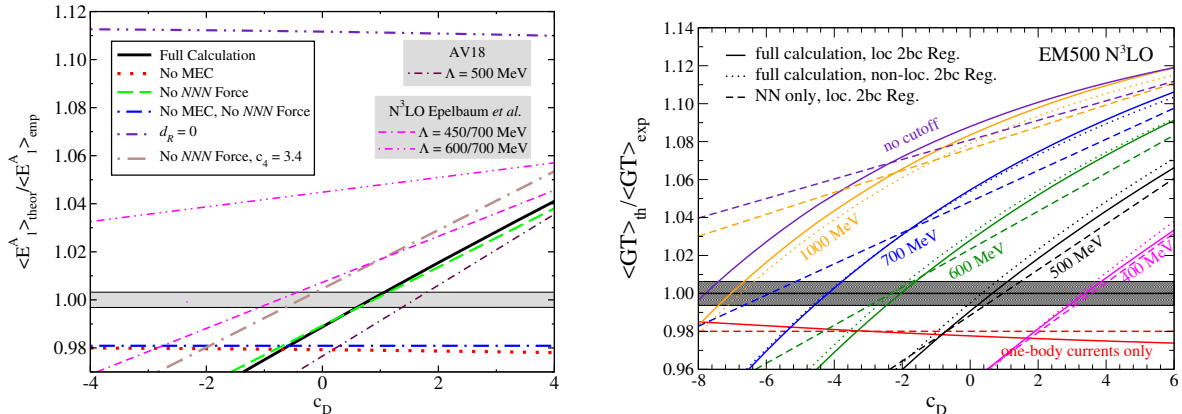


Figure 11: Ratio of calculated and experimental Gamow-Teller matrix elements as a function of  $c_D$ , while the width of the shaded bands denotes the  $2\sigma$  experimental uncertainty. Left: Results based on the NN interaction of Refs. [29, 199, 223] plus local 3N interactions [224]. Right: Results for different cutoff values and regulators in the two-body currents, using the NN interaction of Ref. [199]. The solid (dotted) lines show results for nuclear wave functions including contributions from 3N forces at N<sup>2</sup>LO for a local (a nonlocal regulator in the two-body currents).

Source: Left figure taken from Ref. [148] and right figure taken from Ref. [219].

space was possible yet, a hybrid approach for the determination of the 3N interactions was employed instead. While the NN interaction of Ref. [199] was SRG-evolved to lower resolution scales  $\lambda_{\text{SRG}}$ , the 3N interactions were fitted to the  ${}^3\text{H}$  binding energy and  ${}^4\text{He}$  charge radius at each resolution scale with a fixed cutoff scale  $\Lambda_{3\text{N}}$ . This strategy is implicitly based on the assumption that the  $c_i$  coefficients of the long-range two-pion-exchange part are not modified by the RG and the N<sup>2</sup>LO 3N interactions serve as a truncated “basis” for low-momentum 3N interactions. In Section 5.1 we compare this approach to calculations based on consistently-evolved NN plus 3N interactions and present the new results based on the framework presented in Section 4.2.

The left panel of Figure 12 shows the results for symmetric nuclear matter energy per particle as a function of the Fermi momentum  $k_F$  with  $n = 2k_F^3/(3\pi^2)$  and in particular illustrates the role and importance of 3N interactions for saturation when using low-resolution NN interactions. While calculations based on only NN interactions do not exhibit saturation in the shown density region (dashed lines), the inclusion of contributions from 3N interactions lead to saturation properties in reasonable agreement with the empirical region (gray rectangle) even though the 3N interactions have been fit to only few-body systems. The right panel shows the detailed results for the saturation points of different NN plus 3N interactions at different orders in the many-body expansion (see Ref. [130] for details), while the results based on the forces derived in Ref. [123] are indicated by the labels  $\lambda_{\text{SRG}}/\Lambda_{3\text{N}}$ . Evidently, there is a pronounced linear correlation between the density and energy similar to the “Coester line” [229]. In contrast to the original Coester line with NN potentials only, however, the green band encompassing all shown theoretical saturation points overlaps with the empirical saturation region because of the inclusion of 3N forces.

Furthermore, a systematic trend toward higher saturation densities and larger binding energies was found with decreasing NN resolution scale  $\lambda_{\text{SRG}}$ . This trend translates in a systematic way to the ground-state energies and radii of finite nuclei over a wide mass range, from  ${}^4\text{He}$  to much heavier nuclei up to  ${}^{78}\text{Ni}$  as shown in Figure 13. Remarkably, all calculated ground-state energies based on the “1.8/2.0” interaction are in very good agreement with experiment, except for the neutron-rich oxygen isotopes  ${}^{22,24}\text{O}$ . The other three shown interactions follow the same pattern but are shifted by as much as 1.5 MeV/A in the case of the “2.0/2.0 (PWA)” interaction (see Ref. [123] for details). The experimental charge radii are enclosed by the “2.2/2.0” and “2.0/2.0 (PWA)” results, but the trend observed for the closed-shell nuclei studied in detail already above appears to hold at least up to  ${}^{78}\text{Ni}$ . That is, radii with “1.8/2.0” to “2.2/2.0” are too small, but “2.0/2.0 (PWA)” gives slightly too large radii. As in the case of ground-state energies, the radius systematics is similar for all Hamiltonians, with mainly only a constant shift for the different interactions. This behavior



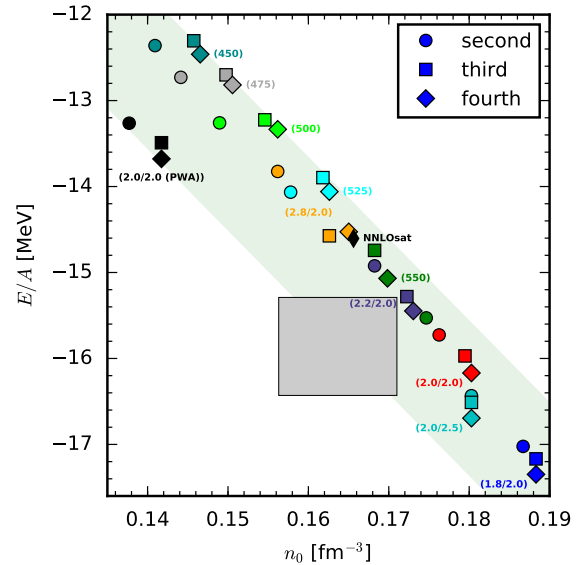
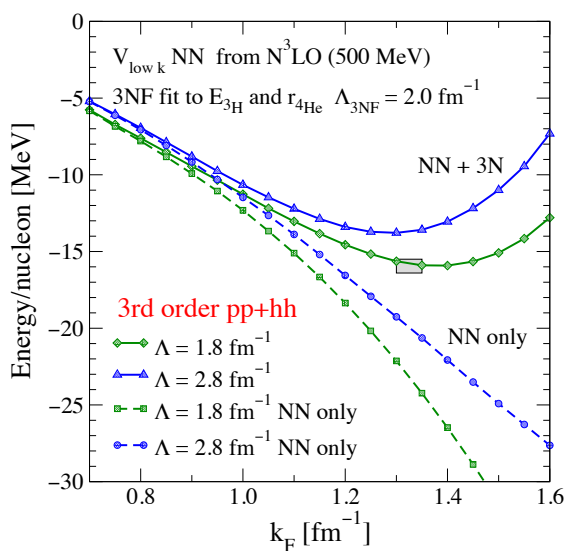


Figure 12: Left: Symmetric nuclear matter energy per particle as a function of the Fermi momentum  $k_F$  including contributions up to third-order particle-particle/hole-hole correlations, based on evolved  $N^3$ LO NN potentials (NN-only, dashed lines) and NN+3N contributions, fit to  $E_{3H}$  and  $r_{4He}$  ( $\Lambda_{3NF} = 2.0 \text{ fm}^{-1}$ ) (solid lines). Theoretical uncertainties are estimated by the cutoff variation  $\Lambda = 1.8\text{--}2.8 \text{ fm}^{-1}$ . Right: Saturation density  $n_0$  and saturation energy  $E/A$  for the interactions of Ref. [123] (labeled by the NN resolution scale and 3N cutoff scales  $\lambda_{SRG}/\Lambda_{3N}$ , see also Table 7), the interactions of Ref. [206], given by the cutoff scale of the NN and 3N interactions, and the interaction  $N^2LO_{\text{sat}}$  of Ref. [141] (black diamond).  
 Source: Left figure taken from Ref. [123] and right figure taken from Ref. [130].

for the ground-state energy and charge radii is clearly reminiscent of the Coester-like line for the saturation points of the four Hamiltonians considered, as shown in the right panel of Figure 12. However, the reason why in particular interaction “1.8/2.0” leads to such an excellent agreement with experimental ground-state energies remains an open question. Nevertheless, thanks to these promising results for heavier nuclei this set of interactions has been used quite intensively in recent years in *ab initio* studies of medium-mass nuclei. We will present a selection of these results in more detail in Section 5.

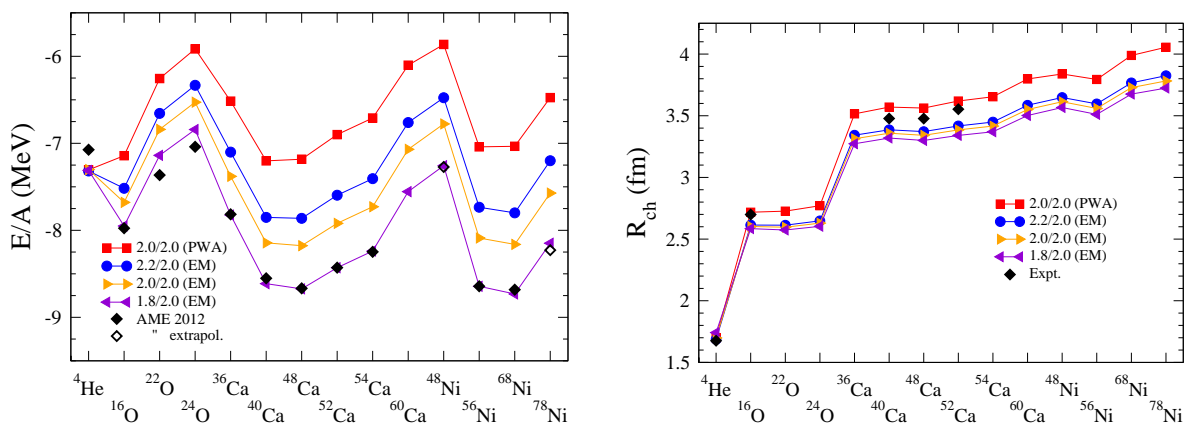


Figure 13: Systematics of the energy per nucleon (left)  $E/A$  and charge radii (right)  $R_{\text{ch}}$  of closed-shell nuclei from  ${}^4\text{He}$  to  ${}^{78}\text{Ni}$  calculated with the IM-SRG for four resolution scales given in the legend. The energy results are compared against experimental ground-state energies from the atomic mass evaluation (AME) 2012 [149] (extrapolated for  ${}^{48,78}\text{Ni}$ ), while the results for the radii are compared against experimental charge radii [227] where available.  
 Source: Figures taken from Ref. [228].

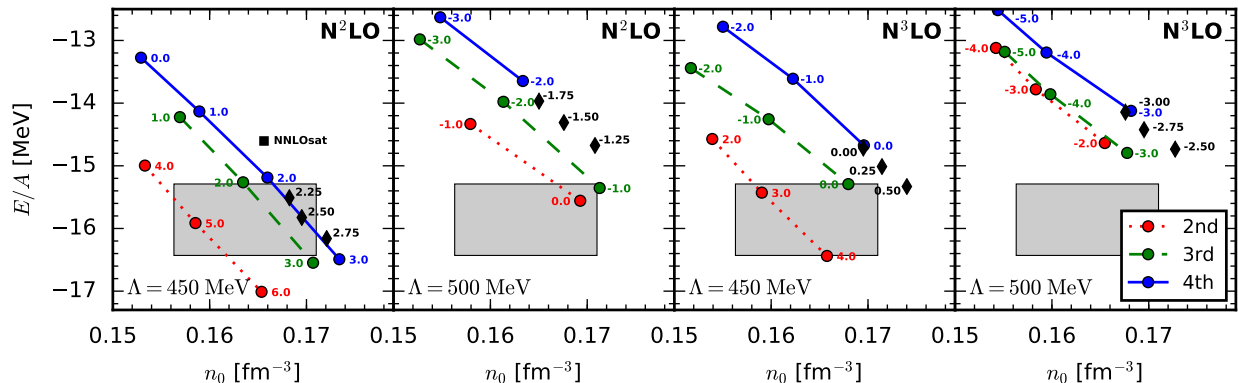


Figure 14: Saturation density and energy of symmetric nuclear matter at 2nd, 3rd and 4th order in MBPT for the NN and 3N interactions at  $N^2\text{LO}$  and  $N^3\text{LO}$ . The points indicate different values of  $c_D$ , while the red-dotted, green-dashed, and blue-solid lines correspond to calculations at different orders. The left (right) two panels are for  $N^2\text{LO}$  ( $N^3\text{LO}$ ) interactions with  $\Lambda = 450$  and  $500$  MeV [188]. The diamonds in each panel represent the calculations with the best simultaneous reproduction of both saturation density and energy at fourth order.

Source: Figure taken from Ref. [130].

The results discussed above highlight the importance of realistic saturation properties of infinite matter for nuclear forces, even though a deeper and more quantitative understanding of the connection between properties of matter and finite nuclei is still lacking. This suggests that it might be useful to include information about saturation properties in the construction of the interactions. However, the explicit incorporation of nuclear matter properties in the fit process of nuclear forces has not been achieved until recently [130]. In Figure 14 we show results for the saturation point based on NN interactions of Ref. [188] at  $N^2\text{LO}$  and  $N^3\text{LO}$  as a function of the LEC  $c_D$  (annotated numbers of the data points), while the relation between  $c_D$  and  $c_E$  was determined via the  $^3\text{H}$  binding energy (see Figure 8). Note that for such fits to nuclear matter properties effectively two LECs are fitted to three observables,  $E_{^3\text{H}}$ , the saturation energy  $E(n_0)/A$ , and the saturation density  $n_0$ . Hence it is *a priori* not obvious that a reasonable simultaneous reproduction of all observables can be achieved. Remarkably, for the shown cases in Figure 14 a reasonable reproduction can be achieved for all four interactions. These best fits are indicated by the black diamonds in each panel. In Section 5 we will present first results for finite nuclei based on these interactions.

Finally, properties of light and medium-mass nuclei have also been investigated based on chiral NN and 3N interactions using Lattice EFT methods [63, 70–72]. For these studies the relation between the couplings  $c_D$  and  $c_E$  was fixed via the  $^3\text{H}$  binding energy [64], while the value for  $c_D$  could only be constrained to the regime  $c_D \sim \mathcal{O}(1)$  using the spin-doublet nucleon-deuteron scattering phase shifts [65]. For the practical calculations, like those of the Hoyle state in  $^{12}\text{C}$  [67], the authors set  $c_D = 0$ , while they studied the sensitivity of the results to changes  $c_D \pm 1$ . Generally, the effects of this modification were found to be minor [230]. In Ref. [70] results for nuclei up to  $^{28}\text{Si}$  were presented based on NN and 3N interactions up to  $N^2\text{LO}$  and using a low cutoff scale. For heavier systems,  $A \geq 16$ , a significant overbinding was observed which was attributed to too attractive 3N interactions at this order and for the employed low cutoff scale, which in turn leads to the formation of alpha clusters on single lattice points. The addition of a single empirical repulsive 4N interaction allowed to fix this overbinding effect. This additional interaction was argued to mimic the effects of higher-order interactions that should become particularly important when using low resolution interactions, similar to those generated by SRG transformations (see Section 4.2).

### 2.3.2. Fits of $\Delta$ -full 3N interactions

In Ref. [142] NN and 3N interactions were constructed with and without explicit inclusion of the  $\Delta$ -isobar degree of freedom up to  $N^2\text{LO}$ , following exactly the same fitting protocol for both formulations. The 3N LECs were fitted to the binding energy and point-proton radius of  $^4\text{He}$ , respectively. Based on



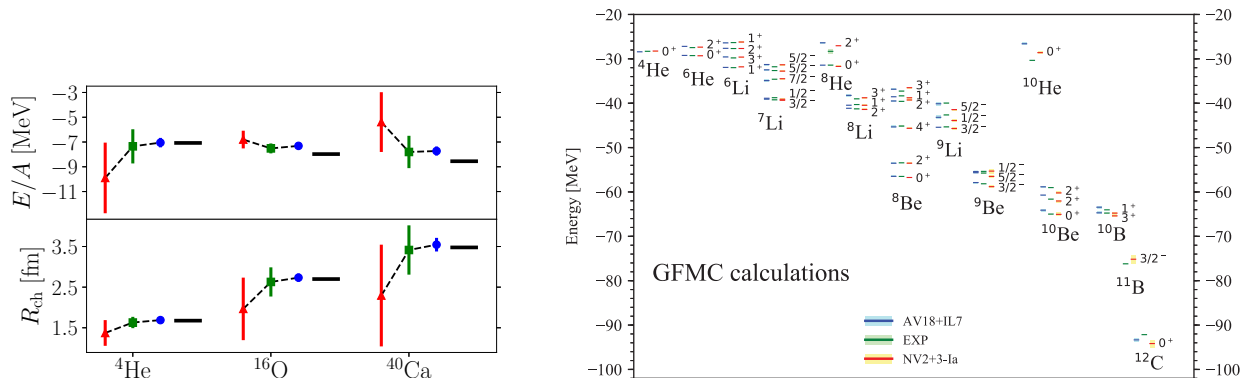


Figure 15: Left: Ground-state energy per nucleon and charge radii of selected nuclei based on the  $\Delta$ -full interactions of Ref. [142] at LO (red triangle), NLO (green square), and  $\text{N}^2\text{LO}$  (blue circle). The black bars show the experimental data. Error bars are estimated from the order-by-order EFT truncation errors following Ref. [204] (see also Section 2.4). Right: Energy spectra of selected nuclei obtained with the interaction of Ref. [54] compared to experimental data [232]. *Source:* Left figure taken from Ref. [142] and right figure taken from Ref. [54].

these interactions, properties of medium-mass nuclei and also matter were investigated, which in particular allowed to study in detail the differences between  $\Delta$ -less and  $\Delta$ -full nuclear interactions. While the results for radii and binding energies turn out to be in remarkable agreement with experiment based on the  $\Delta$ -full interaction (see left panel of Figure 15), the  $\Delta$ -less interactions produce nuclei that are not bound with respect to breakup into  $\alpha$  particles. In addition, the saturation properties of symmetric nuclear matter are also significantly improved for the  $\Delta$ -full interaction.

In Ref. [54] 3N interactions within  $\Delta$ -full chiral EFT were fitted to the ground-state energy of  ${}^3\text{H}$  and the central value of the neutron-deuteron scattering length  ${}^2a_{nd}$  based on the NN interactions presented in Ref. [203]. Even though these two observables exhibit a strong correlation (see Section 2.3.1) these fits lead to a good reproduction of ground state states and excited states of light nuclei up to  $A = 12$  (see right panel of Figure 15). The agreement with experiment is of the same quality as calculations based on the phenomenological Argonne v18 interaction, augmented with 3N interactions that were fit to observables of nuclei beyond  $A = 3$ . In Ref. [137] the 3N LECs  $c_D$  and  $c_E$  were fitted to properties of symmetric nuclear matter based on the same local NN interaction of Ref. [203]. The obtained values for the LECs differ quite significantly from the values found in Ref. [54]. Some of the difference can most likely be attributed to the approximate treatment of the angular dependence of the momentum transfer in the local regulator during the incorporation of the 3N interactions in the many-body calculations via normal-ordering (see discussions in Section 4.3.1 and also Ref. [231]).

### 2.3.3. Simultaneous fits of NN and 3N interactions

For all fits discussed in the previous section, the determination of the 3N coupling constants amounts to an optimization problem in a two-dimensional parameter space since all LECs in the NN interaction have been fixed using two-nucleon observables plus pion-nucleon data. Furthermore, in cases when only two few-body observables are used, the fitting problem of the 3N interactions has by construction a unique solution if theoretical and experimental uncertainties are neglected. If more observables are considered (as, e.g., in the right panel of Figure 9) some kind of  $\chi^2$  minimization can be employed to find the optimal values for the LECs  $c_D$  and  $c_E$ .

However, within chiral EFT all contributions to NN and 3N interactions are derived on equal footing at each order in the chiral expansion and thus depend on the same LECs. Hence it can be argued that it might be more natural and consistent to determine the LECs of NN and 3N interactions as well as the underlying couplings of  $\pi\text{N}$  scattering simultaneously instead of sequentially up to a given order. Of course, such a simultaneous fit is much more challenging since the number of couplings and hence the dimension of the parameter space for the optimization process obviously increases significantly. For example, the

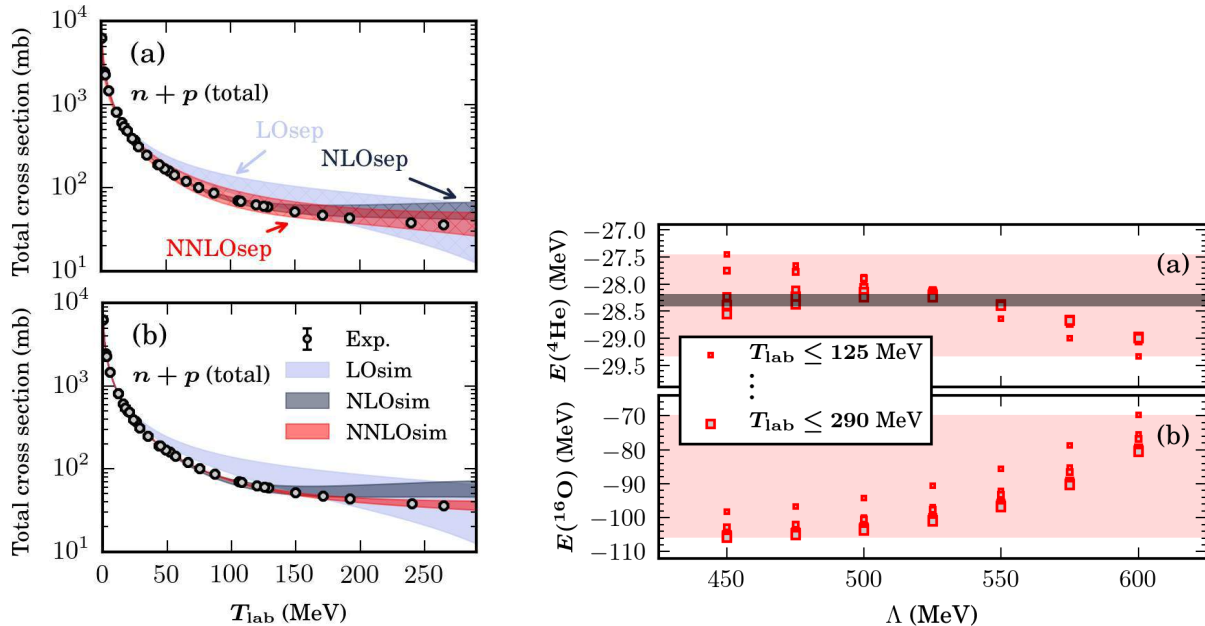


Figure 16: Left: Comparison between neutron-proton total cross section for the sequentially optimized interactions ((a), upper panel) and the simultaneously-optimized interactions ((b), lower panel) at LO, NLO and  $N^2$ LO. The bands show the total uncertainties, including statistical and model uncertainties. Right: Ground-state energies of (a)  ${}^4\text{He}$  and (b)  ${}^{16}\text{O}$  using different optimization parameters for the maximal kinetic energy  $T_{\text{lab}}$  and regularization cutoff scales  $\Lambda$  for the interaction  $N^2\text{LO}_{\text{sim}}$ . For reference, the experimental binding energies are  $E({}^4\text{He}) \approx -28.3\text{MeV}$ , indicated by the gray band in the upper panel and  $E({}^{16}\text{O}) \approx -127\text{MeV}$ , which is not visible on the shown scale.

Source: Figures adapted from Ref. [206].

NN interactions derived within Weinberg’s power counting scheme (see Section 2.1) in naive dimensional analysis contain 2,7,0,12,0 new unknown short-range couplings at LO, NLO,  $N^2$ LO,  $N^3$ LO and  $N^4$ LO respectively [205] (see also Figure 4), while 3N interactions contain 2 new couplings at  $N^2$ LO and the terms at  $N^3$ LO are predicted in a parameter free way<sup>3</sup>. The precise number of new 3N LECs at  $N^4$ LO is still unknown. That means the parameter space dimension involving 3N couplings increases from 2 to 11 at  $N^2$ LO and from 2 to 23 at  $N^3$ LO for simultaneous fits of NN and 3N interactions, which requires powerful and efficient few-body and optimization frameworks.

In Ref. [206] a first automated optimization framework for NN and 3N interactions was presented using scattering and bound-state observables in the pion-nucleon, nucleon-nucleon, and few-nucleon sectors. The framework allows to perform parameter optimizations in large spaces, study correlations between the different parameters and perform a statistical analysis of systematic uncertainties. Furthermore it is possible to in- and exclude observables and adapt the weighting of scattering observables at different energies in a straightforward and flexible way. The framework was used to construct a set of NN plus 3N interactions at different orders in the chiral expansion and using different regularization scales. In particular, the effects of a simultaneous fit of NN and 3N couplings compared to a sequential treatment was investigated. The left panel of Figure 16 shows the uncertainty bands for the total neutron-proton cross sections at different orders for these two approaches. While the results for the sequential fit (upper panel) show no clear sign of convergence with increasing chiral order, the simultaneous fits lead to a reproduction of the scattering observables with systematically reduced uncertainty bands toward higher orders. The right panel of the figure shows the predictions for the ground-state energies of  ${}^4\text{He}$  and  ${}^{16}\text{O}$  based on the derived potentials

<sup>3</sup>Note that in Ref. [205] it was shown that the number of LECs in NN interaction terms at  $N^3$ LO can be reduced by three due to the presence of redundant couplings.

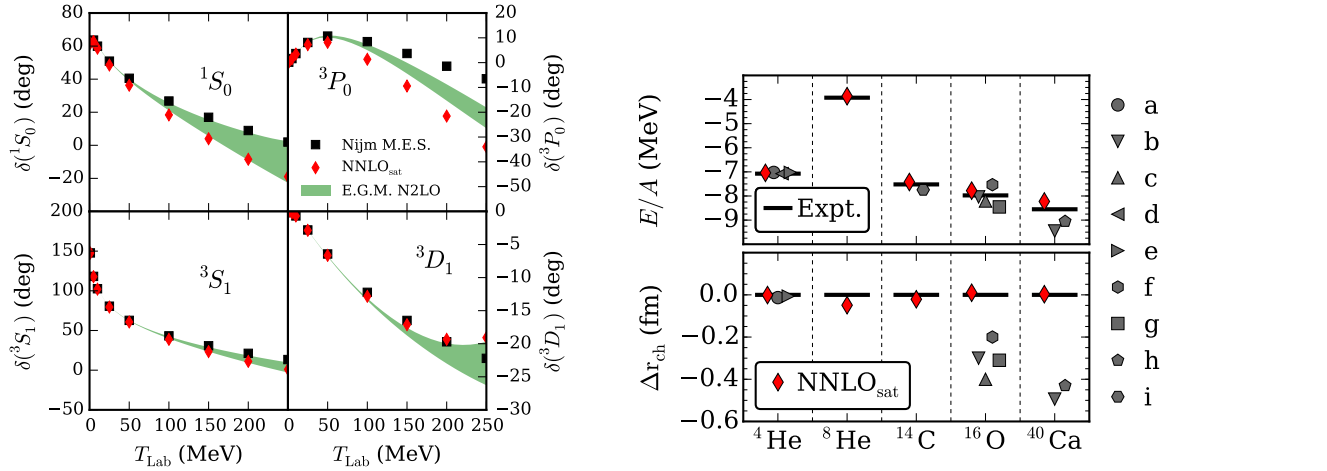


Figure 17: Left: Neutron-proton scattering phase shifts obtained from the interaction  $N^2LO_{\text{sat}}$  (red diamonds) compared to the Nijmegen phase shift analysis (black squares). The green bands shows the results of the  $N^2LO$  interactions of Ref. [233] for comparison. Right: Ground-state energies per nucleon (top panel), and differences between computed and experimental charge radii (bottom panel) for selected nuclei computed with different chiral interactions. *Source:* Figures taken from Ref. [141].

at  $N^2LO$  for different cutoff scales and different values of  $T_{\text{lab}}^{\text{max}}$ , which controls the upper energy limit of the included NN scattering observables in the fit (see Ref. [206] for details). While the energy variation for all considered potentials is only about 2 MeV for  ${}^4\text{He}$ , it increases significantly to about 35 MeV for  ${}^{16}\text{O}$ . In addition, the obtained energy range for  ${}^{16}\text{O}$  does not include the experimental value  $E \approx 127$  MeV (not visible in the shown figure). These results raise some fundamental questions concerning the size of theoretical uncertainties and the predictive power for many-body observables when the underlying nuclear interactions are only constrained by two- and few-nucleon observables.

The traditional paradigm for the construction of NN and 3N interactions has been to determine short-range couplings in the lightest systems in which they contribute. According to this approach the 3N couplings  $c_D$  and  $c_E$  should be determined based on three-body observables. This approach has several advantages:

1. Uncertainties of the many-body calculations are minimized since few-body systems can be solved exactly up to numerical uncertainties.
2. Effects from four- and even higher-body forces can be cleanly disentangled as they do not contribute in three-body systems.
3. For few-body systems it is possible to include nuclear structure as well as scattering observables in the fitting process.

However, this strategy also has practical disadvantages, in particular for applications to medium-mass or even heavier systems. For example, for interactions such as those used in Figures 12, 13 and 16, the calculation of many-body systems like  ${}^{16}\text{O}$  involves a significant extrapolation in particle number from the systems that have been used to fit the underlying interactions and the system under investigation. It is *a priori* not obvious how sensitive many-body observables are to small changes in interactions when fitted only to few-body systems. This question is particularly relevant since fits of LECs up to a given chiral order generally involve inherent uncertainties due to truncation effects of the chiral expansion. In order to avoid such an extrapolation, it might be more efficient and stable to include information about heavier systems in the construction of the interactions. By using properties of the heaviest nuclei of interest as anchor points the extrapolation problem can be effectively changed into an interpolation problem, which mathematically is typically much better behaved.

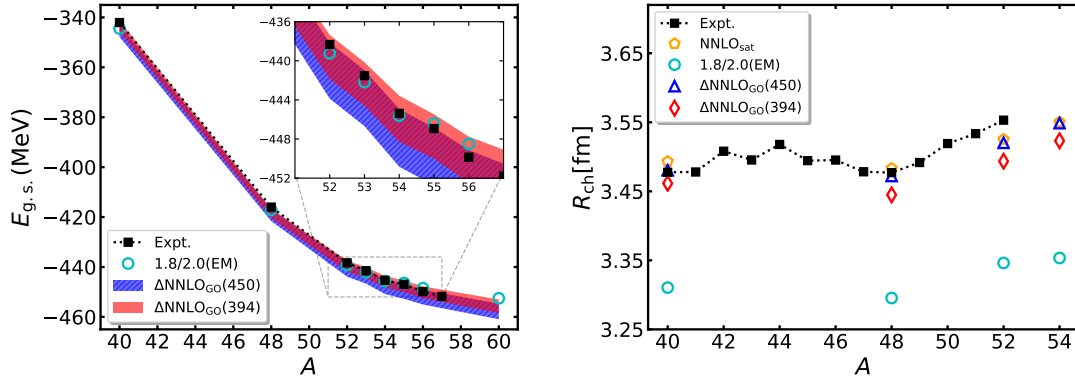


Figure 18: Left: Ground-state energies of calcium isotopes based on the interactions “ $\Delta N^2 LO_{GO}$ ” and “1.8/2.0” compared to experimental values [234]. Right: Charge radii of calcium isotopes based on the same interactions plus “ $N^2 LO_{sat}$ ” compared to experimental values [104].

Source: Figures taken from Ref. [235].

A first interaction, “ $N^2 LO_{sat}$ ”, following this strategy was presented in Ref. [141]. For the practical fit of the NN and 3N LECs the automated optimization framework of Ref. [206] was employed. Again, all LECs were fitted simultaneously while binding energies and charge radii of  ${}^3\text{H}$ ,  ${}^3\text{He}$ ,  ${}^{14}\text{C}$ , and  ${}^{16,22,24,25}\text{O}$  were included in the optimization. The implementation of such an optimization including many-body calculations requires significant computational optimizations in order to make such calculations feasible. The maximum energy for the NN scattering observables had to be limited to 35 MeV in order find a reasonable simultaneous reproduction of experimental scattering phase shifts as well as many-body observables. The detailed theoretical results for scattering phase shifts and many-body observables are shown in Figure 17. We note that the results for  ${}^{40}\text{Ca}$  are also in good agreement with experiment even though the fit included only information up to oxygen. In addition, the saturation properties of symmetric nuclear matter based on  $N^2 LO_{sat}$  are in reasonable agreement with the empirical constraints (see Figure 12).

Very recently, the novel interactions “ $\Delta N^2 LO_{GO}$ ” were presented in Ref. [235]. In contrast to “ $N^2 LO_{sat}$ ” these interactions are based on a chiral EFT formulation with explicit  $\Delta$  degrees. The LECs of the NN and 3N interactions were fitted simultaneously to the NN scattering data, bound state properties of  $A = 2, 3$  and 4 nucleon systems as well as nuclear matter, while the long-range pion-nucleon couplings were taken from the Roy-Steiner analysis of Refs. [174, 175]. The new interactions exhibit a significantly improved reproduction of experimental NN scattering data up to laboratory energies of about 125 MeV compared to the interaction “ $N^2 LO_{sat}$ ”. Furthermore, first results for medium-mass and heavy nuclei up to  $A = 132$  indicate that the new interactions are able to reproduce experimental ground-state energies to a similar degree as the “1.8/2.0” interaction of Ref. [123], but shows a significantly improved description of experimental charge radii (see Figure 18). However, still, they also fail to reproduce the rapid increase of the charge radii toward neutron-rich isotopes (see also Ref. [104]). These promising first results could be an indication that interactions based on a  $\Delta$ -full EFT formulation might be capable of correctly reproducing different observables of nuclei over a wide range of the nuclear chart already at order  $N^2 LO$ . However, further investigations are needed before definite conclusions can be drawn.

#### 2.3.4. Bayesian parameter estimation

The fits of NN and 3N interactions discussed in the previous sections were all based on some kind of  $\chi^2$  minimization procedures. That means the set of low-energy couplings of the interactions are determined such that a given objective function, which encodes the deviation between some given input data and their theoretical predictions, gets minimized. Recently, alternative strategies for estimating the couplings based on Bayesian statistics were proposed [238, 239]. Instead of extracting specific values for each of the couplings, such a framework allows to determine posterior probability distributions for each coupling (see Figure 19),

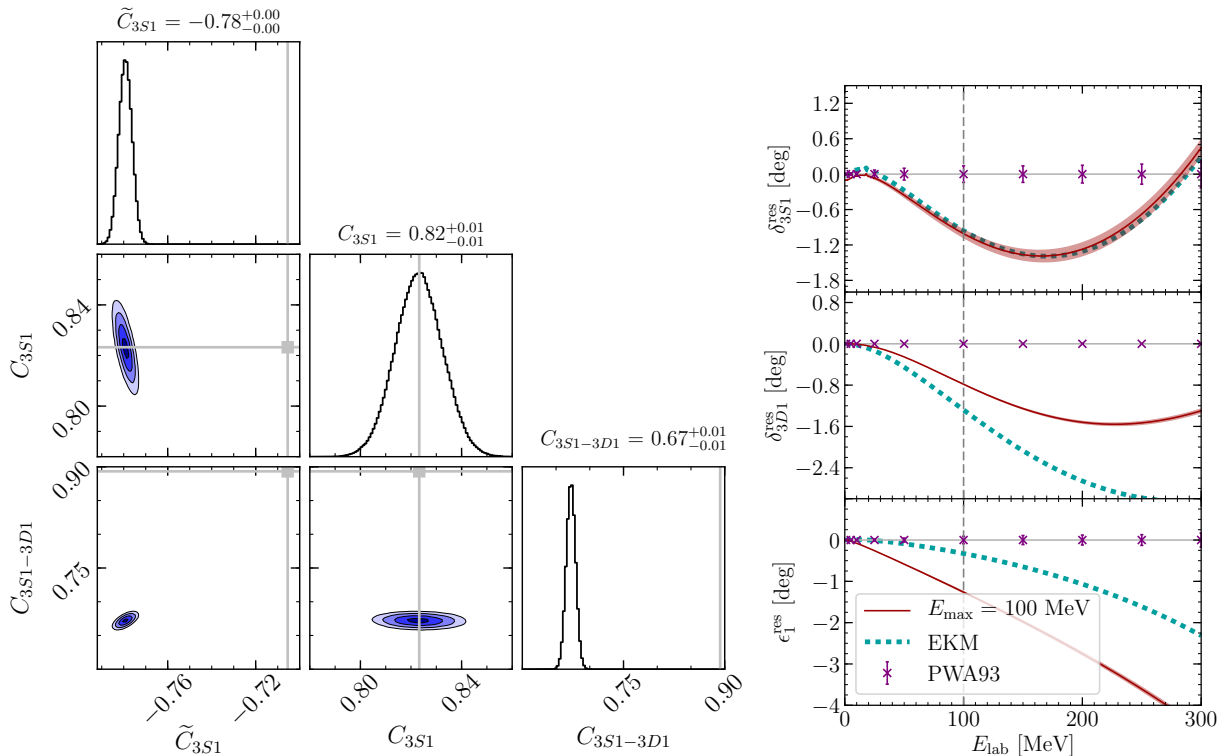


Figure 19: Left: Posterior distribution functions for the NLO fit in the  $^3S_1$  channel to the np phase shifts with  $E_{\max} = 100$  MeV. The values of the EKM NN interactions of Ref. [204] are denoted by the gray squares and lines. Right: The red band shows the propagated prediction for the deviation of the phase shifts and mixing angle to the partial-wave analysis of Ref. [236]. The cyan dotted line shows the EKM result. *Source:* Figure taken from Ref. [237].

opens ways to systematically study correlations between different couplings and observables and to naturally incorporate statistical and systematic uncertainties in the analysis. Furthermore, the determination of the parameters can be guided by theoretical expectations, such as naturalness, through the specification of Bayesian priors, which allows to avoid problems connected to the overfitting of parameters. In Ref. [237] the framework was first applied to the NN interactions of Ref. [204] and two major issues could be identified as part of the analysis. First, indications for degenerate couplings were found, which were also validated and fixed in Ref. [205]. Furthermore, the incorporation of correlations between observables in different kinematical regimes via Gaussian processes was discussed (see also Ref. [239]) and the stability of the extraction with respect to the inclusion of data at higher energies was investigated.

#### 2.4. EFT uncertainty quantification

One of the key benefits of calculations based on nuclear forces derived within a systematic EFT expansion is the possibility to estimate theoretical uncertainties of results due to neglected interaction contributions at higher orders. Calculations performed at different orders in the EFT expansion provide expansion coefficients for observables and allow to study the convergence of the EFT expansion, which can in turn be used to estimate the size of the unknown higher order terms. To be specific, let us consider an observable at a typical momentum scale  $p$ , for example, a scattering cross section at a given energy. Then this observable is expected to take the following form within the EFT expansion [242]:

$$X(p) = X_{\text{ref}}(p) \sum_{n=0}^{\infty} c_n(p) Q^n. \quad (4)$$

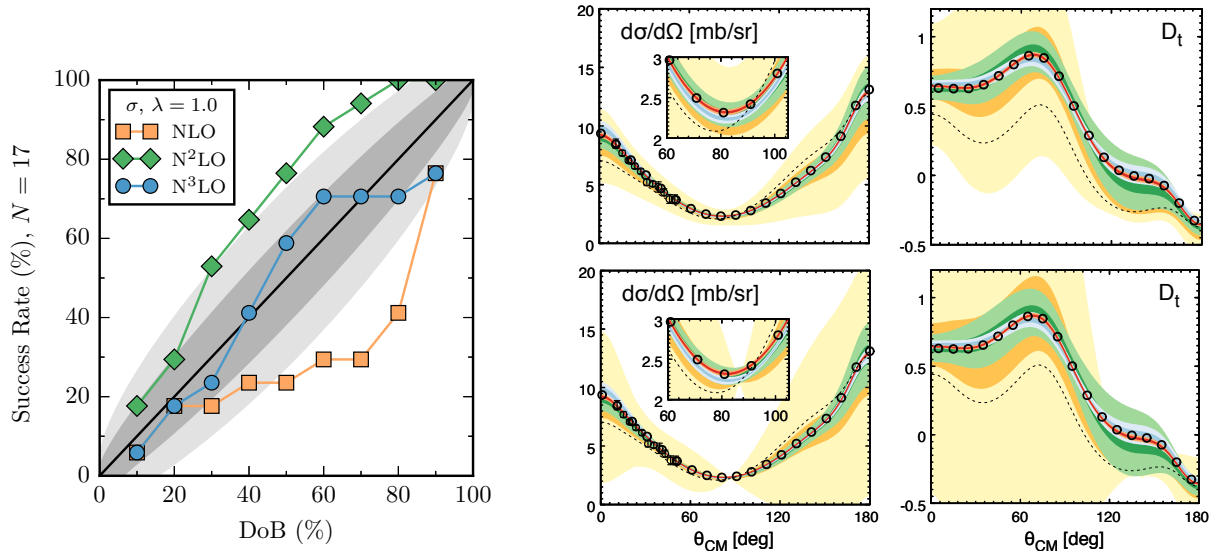


Figure 20: Left: Consistency plot for the total np scattering cross section at different orders in the chiral expansion and based on the NN interactions of Ref. [204]. The degree-of-beliefs (DoBs) were determined at energies  $E_{\text{lab}} = 20, 40, \dots, 340$  MeV. Right: Estimated theoretical uncertainty for the chiral EFT results for np differential cross section (left) and polarization transfer coefficient  $D_t$  (right) at laboratory energy of  $E_{\text{lab}} = 143$  MeV. The top and bottom rows correspond to different Bayesian models. The light- (dark-) shaded yellow, green, blue and red bands show the 95% (68%) DoB intervals at NLO,  $N^2\text{LO}$ ,  $N^3\text{LO}$  and  $N^4\text{LO}$ , respectively. Dashed lines show the LO predictions. Open circles refer to the results of the Nijmegen partial-wave analysis [236].

Source: Left figure taken from Ref. [240] and right figure adapted from Ref. [241].

Here  $X_{\text{ref}}$  is a natural size of the considered observable and defines the scale of the observable. The parameter  $Q$  is the expansion coefficient with  $Q = p/\Lambda$ , where  $\Lambda$  is the breakdown scale of the EFT. The coefficients  $c_n$  are dimensionless quantities which in general also depend on the momentum scale  $p$ , but are expected to be of order one since the scaling factor  $X_{\text{ref}}$  has been factored out. Some coefficients can also vanish due to symmetry reasons. If the series is truncated at order  $k$  then the truncation error is given by (see Ref. [242]):

$$\Delta X^{(k)}(p) = \Delta_k X_{\text{ref}}(p) = X_{\text{ref}}(p) \sum_{n=k+1}^{\infty} c_n(p) Q^n. \quad (5)$$

Different strategies have been developed to obtain an estimate for  $\Delta X^{(k)}(p)$  for chiral EFT given information on the size of the computed coefficients  $c_0, c_1, \dots, c_k$ . In Ref. [204] a conservative prescription for the estimate was proposed which at  $N^3\text{LO}$  takes the following form:

$$\Delta X^{N^3\text{LO}}(p) = \max\left(Q^5 |X^{\text{LO}}(p)|, Q^3 |X^{\text{LO}}(p) - X^{N^{\text{LO}}}(p)|, Q^2 |X^{N^{\text{LO}}}(p) - X^{N^2\text{LO}}(p)|, Q |X^{N^2\text{LO}}(p) - X^{N^3\text{LO}}(p)|\right). \quad (6)$$

The corresponding uncertainties at other orders follow accordingly. This estimate is based on the assumption that all coefficients  $c_n$  are of the same order of magnitude, which in turn allows to estimate the contributions at order  $n$  as the leading order result  $X_{\text{ref}} c_0$  times the factors  $Q^n$ . In particular, the differences of results at successive orders provide various ways to estimate the leading order term in Eq. (5), for example:

$$Q^3 (X^{N^{\text{LO}}}(p) - X^{\text{LO}}(p)) = X_{\text{ref}}(p) c_2(p) Q^5 \approx X_{\text{ref}}(p) c_5(p) Q^5 \approx \Delta X^{N^3\text{LO}}(p). \quad (7)$$

The maximum of all available differences represents a conservative estimate for the truncation error and leads to Eq. (6). It should be noted, however, that this prescription is also based on the assumption that the leading order result  $X^{\text{LO}}(p)$  already provides a reasonable description of a given observable. If that is not

the case the first term in Eq. (6) will typically dominate the uncertainty bands and the resulting estimates will not necessarily be reasonable (see, e.g., Ref. [243]).

Another drawback of the strategy above is that it does not provide a statistical interpretation of uncertainty estimates. A more systematic and quantitative determination of truncation errors can be achieved by employing Bayesian frameworks instead [241, 242, 244, 245]. Such Bayesian analyses allow to extract statistical degree-of-belief (DoB) intervals based on results up to a given order (see Figure 20), to study the consistency of a chosen breakdown scale  $\Lambda$  (see, e.g. Ref. [240]) and also to explore the parameter estimation of the LECs in EFTs (see Refs. [237, 238, 240] and Section 2.3.4). First Bayesian analyses of various NN and nucleon-deuteron scattering observables found that uncertainties based on the Eq. (6) were in good agreement with 68% DoB intervals for particular prior choices [240, 241].

The generalization and improvement of these Bayesian analyses is presently a very active field of research. Current work aims at improving the treatment of correlations between observables in different physical regimes via, e.g., Gaussian processes [245] or the extension of the analyses to heavier nuclei, including contributions from 3N interactions. One additional challenge when investigating bound-state observables of atomic nuclei is the question how to exactly determine the scale  $p$  in Eqs. (4) and (5) given that wave functions generally contain contributions from various different momentum scales (see, e.g., the discussion in Ref. [246]). Such global analyses will open new ways to benchmark NN and 3N interactions more systematically in different regimes of the nuclear chart, explore and test different fitting strategies for the LECs, benchmark various regularization schemes (see also Section 3.7) and isolate possible deficiencies of interactions regarding the description of specific observables of nuclei and matter (see also Section 5).



### 3. Representation and calculation of 3N interactions

In this section we give a comprehensive overview of fundamental techniques for the calculation of 3N interaction matrix elements in a partial-wave basis representation. Many state-of-the-art few- and many-body frameworks in nuclear physics like, e.g., Faddeev(-Yakubovsky), hyperspherical harmonics, no-core shell model, valence-shell diagonalization, in-medium similarity renormalization group, coupled cluster, self-consistent Greens-Function and many-body perturbation theory (see Table 1) are formulated in such a basis representation. That means the matrix elements obtained from the methods discussed in this section can be incorporated in a straightforward way in all these frameworks. On the other hand, frameworks based on Quantum Monte Carlo techniques or lattice effective field theory require different representations of 3N interactions.

Specifically, in this section we discuss in detail how to efficiently calculate and represent 3N interactions in a three-body partial-wave momentum representation. This basis representation has several conceptual advantages:

- The momentum representation does not contain an implicit infrared cutoff scale, in contrast to, e.g, a harmonic oscillator (HO) representation (see, e.g., Refs. [247, 248]). This ensures that the long-range part of the interactions is fully captured in this representation.
- The ultraviolet cutoff scale of the momentum representation can be specified explicitly by appropriate choices of the discrete momentum meshes. Note that the ultraviolet momentum cutoff scale can vary significantly, depending of the specific choice of regularization scheme and cutoff scale (see Section 3.7).
- The transformation from a momentum basis to a HO partial-wave representation can be performed in a straightforward and numerically stable way (see Section 3.9), whereas the inverse transformation is problematic since a large number of HO states is required to represent a plane-wave state. This implies that a momentum representation allows to apply the same interactions to few- and many-body frameworks that are formulated directly in the momentum basis (like, e.g, the Faddeev(-Yakubovsky) equations or MBPT for nuclear matter) as well as to frameworks for medium-mass nuclei, which are typically formulated in a HO representation (see Table 1).

#### 3.1. Definition of coordinates

We consider a system of three interacting point particles with mass  $m_1$ ,  $m_2$  and  $m_3$  located at the coordinates  $\mathbf{x}_1$ ,  $\mathbf{x}_2$  and  $\mathbf{x}_3$ . Starting from these single-particle coordinates we can introduce relative coordinates via the following definitions [25, 249]:

$$\begin{aligned}
 \mathbf{r}_{\{12\}} &= \mathbf{x}_1 - \mathbf{x}_2 \\
 \mathbf{R}_{\{12\}} &= \frac{m_1 \mathbf{x}_1 + m_2 \mathbf{x}_2}{m_1 + m_2} \\
 \mathbf{s}_{\{12\}} &= \mathbf{x}_3 - \mathbf{R}_{\{12\}} \\
 \mathbf{R}_{3N} &= \frac{1}{M} (m_1 \mathbf{x}_1 + m_2 \mathbf{x}_2 + m_3 \mathbf{x}_3),
 \end{aligned} \tag{8}$$

with the total mass  $M = m_1 + m_2 + m_3$ . Here,  $\mathbf{r}_{\{12\}}$  represents the relative distance between particle 1 and 2, and  $\mathbf{R}_{\{12\}}$  is the two-body center-of-mass coordinate of the subsystem consisting of particles 1 and 2, indicated in the following by the index {12}. Of course, this choice is only one possible alternative. The choices {31} and {23} are equally valid and are discussed in more detail below. The second relative coordinate  $\mathbf{s}_{\{12\}}$  is defined by the distance of the third particle to the center-of-mass coordinate of subsystem {12}. These definitions can be generalized straightforwardly to arbitrary particle numbers [25]. Parametrizing three particles in terms of relative coordinates  $\mathbf{r}_{\{12\}}$  and  $\mathbf{s}_{\{12\}}$  instead of single-particle coordinates  $\mathbf{x}_1$ ,  $\mathbf{x}_2$  and  $\mathbf{x}_3$  allows to explicitly factor out the total center-of-mass coordinate  $\mathbf{R}_{3N}$ . Thanks to this factorization the total number of coordinates required for the description of translational invariant system can be reduced from 3 to 2, which is of crucial importance for the practical representation of 3N interactions.



Accordingly, in a momentum representation the three particles can be characterized by three single-particle momenta  $\mathbf{k}_1$ ,  $\mathbf{k}_2$  and  $\mathbf{k}_3$  or by the corresponding relative and total center-of-mass momenta:

$$\begin{aligned}\mathbf{p}_{\{12\}} &= \frac{m_2\mathbf{k}_1 - m_1\mathbf{k}_2}{m_1 + m_2} \\ \mathbf{P}_{\{12\}} &= \mathbf{k}_1 + \mathbf{k}_2 \\ \mathbf{q}_{\{12\}} &= \frac{1}{M}[(m_1 + m_2)\mathbf{k}_3 - m_3\mathbf{P}_{\{12\}}] \\ \mathbf{P}_{3N} &= \mathbf{k}_1 + \mathbf{k}_2 + \mathbf{k}_3.\end{aligned}\tag{9}$$

The relative momenta  $\mathbf{p}$  and  $\mathbf{q}$  are also called Jacobi momenta. The kinetic energy of the system can then be expressed in terms of single-particle momenta or Jacobi momenta:

$$T = \sum_{i=1}^3 \frac{\mathbf{k}_i^2}{2m_i} = \frac{\mathbf{P}_{3N}^2}{2M} + \frac{\mathbf{p}_{\{12\}}^2}{2\mu_1} + \frac{\mathbf{q}_{\{12\}}^2}{2\mu_2},\tag{10}$$

with the reduced masses

$$\frac{1}{\mu_1} = \frac{1}{m_1} + \frac{1}{m_2}, \quad \frac{1}{\mu_2} = \frac{1}{m_1 + m_2} + \frac{1}{m_3}.\tag{11}$$

Corresponding relations can be derived in the basis representations  $\{31\}$  and  $\{23\}$  (see Figure 21). Since each choice of variables represents a complete basis to describe the relative motion of the three particles, the different variables are all related by linear transformations. These relations can be derived straightforwardly and are summarized in Table 2 for the case of equal masses,  $m_1 = m_2 = m_3$ .

The different basis representations are related by a cyclic (or anticyclic) permutation of particles. Let us consider a generic three-body state  $|abc\rangle$  with some arbitrary single-particle quantum numbers  $a$ ,  $b$  and  $c$ . Now consider the following permutation operators

$$P_{123} = P_{12}P_{23} \quad \text{and} \quad P_{132} = P_{13}P_{23},\tag{12}$$

where  $P_{ij}$  are the two-body transposition operators that exchange the labels of particles  $i$  and  $j$ , e.g.:

$$P_{12}|abc\rangle = |bac\rangle, \quad P_{13}|abc\rangle = |cba\rangle, \quad \text{etc.}\tag{13}$$

It is easy to verify that the following relations hold:

$$P_{123}|abc\rangle = P_{12}P_{23}|abc\rangle = P_{12}|acb\rangle = |cab\rangle,\tag{14}$$

$$P_{132}|abc\rangle = P_{13}P_{23}|abc\rangle = P_{13}|acb\rangle = |bca\rangle = P_{123}^{-1}|abc\rangle.\tag{15}$$

That means  $P_{123}$  ( $P_{132}$ ) represent the cyclic (anticyclic) permutation operators for three-body states. These operators play a key role for the treatment of 3N interactions as we will discuss in detail the following sections.

If we now consider specifically a three-body state in a momentum representation, we can parametrize it via the single-particle momenta in the form  $|\mathbf{k}_1\mathbf{k}_2\mathbf{k}_3\rangle$  or in a relative momentum representation  $|\mathbf{p}\mathbf{q}\mathbf{P}_{3N}\rangle_{\{ab\}}$ . Here the total three-body momentum  $\mathbf{P}_{3N}$  is identical for all basis representations  $\{ab\}$  and just characterizes boosts of the three-body system. As we will discuss in more detail in Section 3.2, microscopic nuclear forces do not depend on the three-body center-of-mass momentum. This implies that the entire structure of 3N interactions is encoded in their dependence on the Jacobi momenta  $\mathbf{p}$  and  $\mathbf{q}$ . For that reason, we suppress in the following the center-of-mass quantum number  $\mathbf{P}_{3N}$  in the three-body states and write them in the form  $|\mathbf{p}\mathbf{q}\rangle_{\{ab\}}$ , while we choose the following normalization convention (see also Appendix A):

$${}_{\{ab\}}\langle\mathbf{p}'\mathbf{q}'|\mathbf{p}\mathbf{q}\rangle_{\{ab\}} = (2\pi)^6\delta(\mathbf{p}' - \mathbf{p})\delta(\mathbf{q}' - \mathbf{q}), \quad \int \frac{d\mathbf{p}}{(2\pi)^3} \frac{d\mathbf{q}}{(2\pi)^3} |\mathbf{p}\mathbf{q}\rangle_{\{ab\}} {}_{\{ab\}}\langle\mathbf{p}\mathbf{q}| = 1.\tag{16}$$

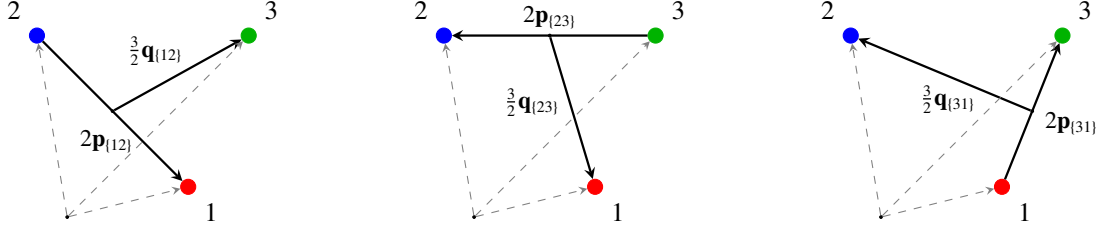


Figure 21: Definition of the three-body Jacobi momenta  $\mathbf{p}$  and  $\mathbf{q}$  in the representations  $\{12\}$  (left),  $\{23\}$  (center) and  $\{31\}$  (right) for equal masses ( $m_1 = m_2 = m_3$ ). The dashed arrows denote the single-particle momenta  $\mathbf{k}_1$ ,  $\mathbf{k}_2$  and  $\mathbf{k}_3$ . The relations between the momenta in the different representations are summarized in Table 2.

	$\mathbf{k}_i$	$\{12\}$	$\{23\}$	$\{31\}$
$\mathbf{p}_{\{12\}}$	$\frac{1}{2}(\mathbf{k}_1 - \mathbf{k}_2)$	$\mathbf{p}_{\{12\}}$	$-\frac{1}{2}\mathbf{p}_{\{23\}} + \frac{3}{4}\mathbf{q}_{\{23\}}$	$-\frac{1}{2}\mathbf{p}_{\{31\}} - \frac{3}{4}\mathbf{q}_{\{31\}}$
$\mathbf{q}_{\{12\}}$	$\frac{2}{3}[\mathbf{k}_3 - \frac{1}{2}(\mathbf{k}_1 + \mathbf{k}_2)]$	$\mathbf{q}_{\{12\}}$	$-\mathbf{p}_{\{23\}} - \frac{1}{2}\mathbf{q}_{\{23\}}$	$\mathbf{p}_{\{31\}} - \frac{1}{2}\mathbf{q}_{\{31\}}$
$\mathbf{p}_{\{23\}}$	$\frac{1}{2}(\mathbf{k}_2 - \mathbf{k}_3)$	$-\frac{1}{2}\mathbf{p}_{\{12\}} - \frac{3}{4}\mathbf{q}_{\{12\}}$	$\mathbf{p}_{\{23\}}$	$-\frac{1}{2}\mathbf{p}_{\{31\}} + \frac{3}{4}\mathbf{q}_{\{31\}}$
$\mathbf{q}_{\{23\}}$	$\frac{2}{3}[\mathbf{k}_1 - \frac{1}{2}(\mathbf{k}_2 + \mathbf{k}_3)]$	$\mathbf{p}_{\{12\}} - \frac{1}{2}\mathbf{q}_{\{12\}}$	$\mathbf{q}_{\{23\}}$	$-\mathbf{p}_{\{31\}} - \frac{1}{2}\mathbf{q}_{\{31\}}$
$\mathbf{p}_{\{31\}}$	$\frac{1}{2}(\mathbf{k}_3 - \mathbf{k}_1)$	$-\frac{1}{2}\mathbf{p}_{\{12\}} + \frac{3}{4}\mathbf{q}_{\{12\}}$	$-\frac{1}{2}\mathbf{p}_{\{23\}} - \frac{3}{4}\mathbf{q}_{\{23\}}$	$\mathbf{p}_{\{31\}}$
$\mathbf{q}_{\{31\}}$	$\frac{2}{3}[\mathbf{k}_2 - \frac{1}{2}(\mathbf{k}_3 + \mathbf{k}_1)]$	$-\mathbf{p}_{\{12\}} - \frac{1}{2}\mathbf{q}_{\{12\}}$	$\mathbf{p}_{\{23\}} - \frac{1}{2}\mathbf{q}_{\{23\}}$	$\mathbf{q}_{\{31\}}$
$\mathbf{k}_1$	$\mathbf{k}_1$	$\mathbf{p}_{\{12\}} - \frac{1}{2}\mathbf{q}_{\{12\}} + \frac{1}{3}\mathbf{P}_{3N}$	$\mathbf{q}_{\{23\}} + \frac{1}{3}\mathbf{P}_{3N}$	$-\mathbf{p}_{\{31\}} - \frac{1}{2}\mathbf{q}_{\{31\}} + \frac{1}{3}\mathbf{P}_{3N}$
$\mathbf{k}_2$	$\mathbf{k}_2$	$-\mathbf{p}_{\{12\}} - \frac{1}{2}\mathbf{q}_{\{12\}} + \frac{1}{3}\mathbf{P}_{3N}$	$\mathbf{p}_{\{23\}} - \frac{1}{2}\mathbf{q}_{\{23\}} + \frac{1}{3}\mathbf{P}_{3N}$	$\mathbf{q}_{\{31\}} + \frac{1}{3}\mathbf{P}_{3N}$
$\mathbf{k}_3$	$\mathbf{k}_3$	$\mathbf{q}_{\{12\}} + \frac{1}{3}\mathbf{P}_{3N}$	$-\mathbf{p}_{\{23\}} - \frac{1}{2}\mathbf{q}_{\{23\}} + \frac{1}{3}\mathbf{P}_{3N}$	$\mathbf{p}_{\{31\}} - \frac{1}{2}\mathbf{q}_{\{31\}} + \frac{1}{3}\mathbf{P}_{3N}$

Table 2: Relations between the single-particle momenta  $\mathbf{k}_i$  and the Jacobi momenta  $\mathbf{p}$  and  $\mathbf{q}$  for a three-body system with equal masses in the different representations  $\{12\}$ ,  $\{31\}$  and  $\{23\}$  (see Figure 21).

Since the representations  $\{12\}$  and  $\{23\}$  are related by the transformations (see Table 2)

$$\mathbf{k}_1 \rightarrow \mathbf{k}_2, \quad \mathbf{k}_2 \rightarrow \mathbf{k}_3, \quad \mathbf{k}_3 \rightarrow \mathbf{k}_1. \quad (17)$$

the following relations hold:

$$|\mathbf{p}\mathbf{q}\rangle_{\{23\}} = P_{123} |\mathbf{p}\mathbf{q}\rangle_{\{12\}}, \quad |\mathbf{p}\mathbf{q}\rangle_{\{31\}} = P_{123} |\mathbf{p}\mathbf{q}\rangle_{\{23\}} \quad \text{and} \quad |\mathbf{p}\mathbf{q}\rangle_{\{12\}} = P_{123} |\mathbf{p}\mathbf{q}\rangle_{\{31\}}. \quad (18)$$

Hence, the momentum matrix elements of the permutation operator can be expressed as (see Table 2):

$$\begin{aligned} {}_{\{12\}}\langle \mathbf{p}'\mathbf{q}' | P_{123} |\mathbf{p}\mathbf{q}\rangle_{\{12\}} &= {}_{\{12\}}\langle \mathbf{p}'\mathbf{q}' | \mathbf{p}\mathbf{q}\rangle_{\{23\}} \\ &= (2\pi)^6 \delta(\mathbf{p}'_{\{12\}} + \frac{1}{2}\mathbf{p}_{\{23\}} - \frac{3}{4}\mathbf{q}_{\{23\}}) \delta(\mathbf{q}'_{\{12\}} + \mathbf{p}_{\{23\}} + \frac{1}{2}\mathbf{q}_{\{23\}}) \end{aligned} \quad (19a)$$

$$= (2\pi)^6 \delta(\mathbf{p}_{\{23\}} + \frac{1}{2}\mathbf{q}_{\{23\}} + \mathbf{q}'_{\{12\}}) \delta(\mathbf{p}'_{\{12\}} - \frac{1}{2}\mathbf{q}'_{\{12\}} - \mathbf{q}_{\{23\}}) \quad (19b)$$

$$= (2\pi)^6 \delta(\mathbf{p}_{\{23\}} + \frac{1}{2}\mathbf{p}'_{\{12\}} + \frac{3}{4}\mathbf{q}'_{\{12\}}) \delta(\mathbf{q}_{\{23\}} - \mathbf{p}'_{\{12\}} + \frac{1}{2}\mathbf{q}'_{\{12\}}). \quad (19c)$$

From Eq. (18) it follows immediately that

$${}_{\{12\}}\langle \mathbf{p}'\mathbf{q}' | \mathbf{p}\mathbf{q}\rangle_{\{23\}} = {}_{\{23\}}\langle \mathbf{p}'\mathbf{q}' | \mathbf{p}\mathbf{q}\rangle_{\{31\}} = {}_{\{31\}}\langle \mathbf{p}'\mathbf{q}' | \mathbf{p}\mathbf{q}\rangle_{\{12\}}, \quad (20)$$

and, consequently, the representation of the permutation operator is identical in all basis representations:

$$\langle \mathbf{p}' \mathbf{q}' | P_{123} | \mathbf{p} \mathbf{q} \rangle = {}_{\{ab\}} \langle \mathbf{p}' \mathbf{q}' | P_{123} | \mathbf{p} \mathbf{q} \rangle_{\{ab\}}. \quad (21)$$

The corresponding relations to Eq. (18) for the bra states can be derived by using the relations

$${}_{\{12\}} \langle \mathbf{p}' \mathbf{q}' | \mathbf{p} \mathbf{q} \rangle_{\{12\}} = {}_{\{12\}} \langle \mathbf{p}' \mathbf{q}' | P_{123}^{-1} P_{123} | \mathbf{p} \mathbf{q} \rangle_{\{12\}} = {}_{\{12\}} \langle \mathbf{p}' \mathbf{q}' | P_{123}^{-1} | \mathbf{p} \mathbf{q} \rangle_{\{23\}}. \quad (22)$$

Hence:

$${}_{\{23\}} \langle \mathbf{p} \mathbf{q} | = {}_{\{12\}} \langle \mathbf{p} \mathbf{q} | P_{123}^{-1}, \quad (23)$$

and accordingly:

$${}_{\{31\}} \langle \mathbf{p} \mathbf{q} | = {}_{\{23\}} \langle \mathbf{p} \mathbf{q} | P_{123}^{-1}, \quad {}_{\{12\}} \langle \mathbf{p} \mathbf{q} | = {}_{\{31\}} \langle \mathbf{p} \mathbf{q} | P_{123}^{-1}. \quad (24)$$

In Section 3.5 the matrix elements of the permutation operator for particles with spin and isospin are evaluated explicitly in a partial-wave representation. These elements are a key quantity for the representation of 3N interactions and three-body wave functions as well as for the implementation of the SRG flow equations for NN and 3N interactions.

### 3.2. Momentum basis representation of three-nucleon forces

Now we discuss how to represent 3N interactions in a momentum plane wave basis. To this end, we first neglect spin and isospin degrees of freedom of the nucleons in order to simplify the notation and discussion. We will discuss the general case including all internal degrees of freedom in Section 3.3.

For spinless particles the matrix elements of a general three-body operator  $\hat{O}$  have the following form:

$$\langle \mathbf{k}'_1 \mathbf{k}'_2 \mathbf{k}'_3 | \hat{O} | \mathbf{k}_1 \mathbf{k}_2 \mathbf{k}_3 \rangle, \quad (25)$$

where  $\mathbf{k}_i$  ( $\mathbf{k}'_i$ ) are the single-particle momenta in the initial (final) state. The computation of these matrix elements is a highly nontrivial task, given that they depend on six vector variables. For our purposes, however, we can simplify the task considerably since microscopic free-space 3N interactions have the following symmetry properties:

- *conservation* of the center-of-mass momentum, i.e.,  $\mathbf{P}_{3N} = \sum_{i=1}^3 \mathbf{k}_i = \sum_{i=1}^3 \mathbf{k}'_i$ ,
- *independence* on  $\mathbf{P}_{3N}$  (Galilean invariance),
- *rotational invariance*, i.e., the interaction transforms like a scalar under spatial rotations.

The first two symmetries follow from the basic symmetries of QCD in the non-relativistic limit, while the third symmetry holds since there is no preferred direction in the absence of external fields. In the following we will study the representation of such an interaction,  $V_{3N}$ , for the case of equal masses,  $m_1 = m_2 = m_3$ . This is an excellent approximation for practical calculations, given that the relative mass difference of the proton and neutron is smaller than one per mille. For 3N interactions the matrix elements in Eq. (25) can be significantly simplified by using a representation in terms of Jacobi momenta and explicitly factorizing out the trivial dependence on the center-of-mass motion:

$${}_{\{ab\}} \langle \mathbf{p}' \mathbf{q}' \mathbf{P}'_{3N} | V_{3N} | \mathbf{p} \mathbf{q} \mathbf{P}_{3N} \rangle_{\{ab\}} = {}_{\{ab\}} \langle \mathbf{p}' \mathbf{q}' | V_{3N} | \mathbf{p} \mathbf{q} \rangle_{\{ab\}} \delta(\mathbf{P}'_{3N} - \mathbf{P}_{3N}), \quad (26)$$

where  $\{ab\}$  represents one of the three basis choices  $\{12\}$ ,  $\{31\}$  or  $\{23\}$ . This factorization drastically reduces the complexity of 3N interaction matrix elements as the number of vector variables gets reduced from 6 to 4. Instead of computing matrix elements  ${}_{\{ab\}} \langle \mathbf{p}' \mathbf{q}' | V_{3N} | \mathbf{p} \mathbf{q} \rangle_{\{ab\}}$  directly in the vector representation, for practical applications it is usually most convenient and efficient to compute the matrix elements in a partial-wave

representation<sup>4</sup>. For such a representation the angular dependence of the Jacobi vectors is expanded in terms of spherical harmonics. Specifically, we define (see also Appendix A):

$${}_{\{ab\}}\langle \mathbf{p}'\mathbf{q}' | pq(L) \mathcal{L} \mathcal{M}_{\mathcal{L}} \rangle_{\{ab\}} \equiv (2\pi)^3 \frac{\delta(p-p')}{pp'} \frac{\delta(q-q')}{qq'} \mathcal{Y}_{Ll}^{\mathcal{L}\mathcal{M}_{\mathcal{L}}}(\hat{\mathbf{p}}', \hat{\mathbf{q}}') \quad (27)$$

with

$$\mathcal{Y}_{l_a l_b}^{lm}(\hat{\mathbf{a}}, \hat{\mathbf{b}}) = \sum_{m_a, m_b} C_{l_a m_a l_b m_b}^{lm} Y_{l_a m_a}(\hat{\mathbf{a}}) Y_{l_b m_b}(\hat{\mathbf{b}}). \quad (28)$$

Here all momenta are defined in a chosen representation  $\{ab\}$ , while  $L$  denotes the relative angular momentum corresponding to momentum  $\mathbf{p}'$  and  $l$  denotes the angular momentum corresponding to momentum  $\mathbf{q}'$ . From Eqs. (16) and (27) follows:

$$\langle p'q'(L'l') \mathcal{L}' \mathcal{M}'_{\mathcal{L}'} | pq(L) \mathcal{L} \mathcal{M}_{\mathcal{L}} \rangle = \frac{\delta(p'-p)}{pp'} \frac{\delta(q'-q)}{qq'} \delta_{LL'} \delta_{ll'} \delta_{\mathcal{L}\mathcal{L}'} \delta_{\mathcal{M}_{\mathcal{L}}\mathcal{M}'_{\mathcal{L}'}}. \quad (29)$$

In Eqs. (27) and (29) we couple both angular momenta to the total angular momentum  $\mathcal{L}$ , which is a conserved quantum number in the absence of spin degrees of freedom. Since free-space 3N interactions are invariant under spatial rotations the resulting matrix elements are proportional to  $\delta_{\mathcal{L}\mathcal{L}'} \delta_{\mathcal{M}_{\mathcal{L}}\mathcal{M}'_{\mathcal{L}'}}$  and independent of the quantum number  $\mathcal{M}_{\mathcal{L}}$ . Using Eq. (27) we obtain the following relation for the partial-wave matrix elements of 3N interactions for spinless particles:

$${}_{\{ab\}}\langle p'q'(L'l') \mathcal{L}' | V_{3N} | pq(L) \mathcal{L} \rangle_{\{ab\}} = \frac{1}{(2\pi)^6} \frac{1}{2\mathcal{L}+1} \sum_{\mathcal{M}_{\mathcal{L}}} \int d\hat{\mathbf{p}} d\hat{\mathbf{q}} d\hat{\mathbf{p}}' d\hat{\mathbf{q}}' \mathcal{Y}_{L'l'}^{*\mathcal{L}\mathcal{M}_{\mathcal{L}}}(\hat{\mathbf{p}}', \hat{\mathbf{q}}') {}_{\{ab\}}\langle \mathbf{p}'\mathbf{q}' | V_{3N} | \mathbf{p}\mathbf{q} \rangle_{\{ab\}} \mathcal{Y}_{Ll}^{\mathcal{L}\mathcal{M}_{\mathcal{L}}}(\hat{\mathbf{p}}, \hat{\mathbf{q}}). \quad (30)$$

It is convenient to parametrize the partial-wave decomposition of 3N interactions in the form of the following function:

$$F_{LlL'l'}^{m_l m_l' m_l' m_l'}(p, q, p', q') = \frac{1}{(2\pi)^6} \int d\hat{\mathbf{p}}' d\hat{\mathbf{q}}' d\hat{\mathbf{p}} d\hat{\mathbf{q}} Y_{L'l'}^*(\hat{\mathbf{p}}') Y_{l'm_l'}(\hat{\mathbf{q}}') Y_{Lm_l}(\hat{\mathbf{p}}) Y_{lm_l}(\hat{\mathbf{q}}) V_{3N}(\mathbf{p}, \mathbf{q}, \mathbf{p}', \mathbf{q}') \quad (31)$$

for fixed values of  $p = |\mathbf{p}|, q = |\mathbf{q}|, p' = |\mathbf{p}'|, q' = |\mathbf{q}'|$  and the angular momentum quantum numbers. Apart from some additional straightforward extensions this function will also be the key quantity for the general case of spin- and isospin-dependent interactions (see Section 3.4). Equation (31) shows that for each value of momenta and orbital quantum numbers an 8-dimensional angular integral needs to be computed. By using rotational symmetries of the interaction, it is possible to reduce the dimensionality of the angular integrals from 8 to 5. Traditional methods have been based on an explicit discretization and numerical evaluation of these 5 integrals [250, 251]. Due to the large number of external quantum numbers and momentum mesh points such algorithms require a huge amount of computational resources for calculating all matrix elements necessary for many-body studies. As a result, the number of matrix elements of chiral N<sup>3</sup>LO interactions have been insufficient for studies of nuclei as well as matter and were limited to three-body systems [252, 253], while scattering calculations were limited to low energies [254]. In the following sections we will discuss an improved framework that allows to compute matrix elements much more efficiently, which in turn makes it possible to reach basis sizes sufficient for large-scale many-body calculations.

### 3.3. Partial-wave decomposition of local 3N interactions

As shown in Section 3.2, a general translationally invariant 3N interaction depends on the four Jacobi momenta  $\mathbf{p}, \mathbf{q}, \mathbf{p}'$  and  $\mathbf{q}'$ . However, in addition to the two properties discussed in Section 3.2, most contributions to 3N interactions have an additional property, *locality*, which can be used to further simplify the calculations.

<sup>4</sup>In Section 4.4 we discuss a novel approach that allows to evaluate matrix elements in an efficient way in this vector representation of Eq. (25) for calculations of nuclear matter.



Figure 22: Examples of a local (left) and a nonlocal (right) contribution to an NN interaction in coordinate representation. The dashed line in the left panel indicates an instantaneously exchanged pion, i.e., both single-particle coordinates are the same before and after the interaction and the interaction is therefore local. In the right panel we show a contact interaction that is regularized via a regulator of the form  $f_\Lambda(\mathbf{p}^2)f_\Lambda(\mathbf{p}'^2)$  (see Eq. (37) and also Section 3.7). This regularization induces a nonlocality, i.e.,  $\mathbf{x}_i \neq \mathbf{x}'_i$ .

The concept of locality is illustrated most naturally in coordinate space. For this consider first a free-space two-body nucleon-nucleon interaction. Following the arguments of the previous sections it is easy to show that a Galilean-invariant NN interaction can be written in the following form

$$\langle \mathbf{k}'_1 \mathbf{k}'_2 | V_{\text{NN}} | \mathbf{k}_1 \mathbf{k}_2 \rangle = \langle \mathbf{p}' | V_{\text{NN}} | \mathbf{p} \rangle \delta(\mathbf{P}'_{(12)} - \mathbf{P}_{(12)}), \quad (32)$$

with  $\mathbf{p} = \mathbf{p}_{(12)}$  and  $\mathbf{p}' = \mathbf{p}'_{(12)}$ . Let us analyze such interactions in coordinate space. To this end, we consider two particles located at the coordinates  $\mathbf{x}_1$  and  $\mathbf{x}_2$  when they interact via the exchange of a meson. Here it is important to note that we work in a non-relativistic limit and neglect any retardation effects, which means that the interaction is instantaneous. In this case the center-of-mass coordinate of the two particles before and after the interaction process is identical,  $\mathbf{R}_{(12)} = \mathbf{R}'_{(12)}$ , and the interaction can only depend on the relative distance  $\mathbf{r} \equiv \mathbf{r}_{(12)} = \mathbf{r}'_{(12)} \equiv \mathbf{r}'$  (see also Figure 22):

$$\langle \mathbf{x}'_1 \mathbf{x}'_2 | V_{\text{NN}}^{\text{local}} | \mathbf{x}_1 \mathbf{x}_2 \rangle = \langle \mathbf{r}' | V_{\text{NN}} | \mathbf{r} \rangle \delta(\mathbf{r}' - \mathbf{r}) \delta(\mathbf{R}'_{(12)} - \mathbf{R}_{(12)}) = V_{\text{NN}}^{\text{local}}(\mathbf{r}) \delta(\mathbf{r}' - \mathbf{r}) \delta(\mathbf{R}'_{(12)} - \mathbf{R}_{(12)}). \quad (33)$$

This is the definition of a *local* NN interaction<sup>5</sup>. Fourier transform to momentum space of such an interaction leads to:

$$\begin{aligned} \langle \mathbf{k}'_1 \mathbf{k}'_2 | V_{\text{NN}}^{\text{local}} | \mathbf{k}_1 \mathbf{k}_2 \rangle &= \int d\mathbf{x}_1 d\mathbf{x}_2 d\mathbf{x}'_1 d\mathbf{x}'_2 e^{-i(\mathbf{k}'_1 \cdot \mathbf{x}'_1 + \mathbf{k}'_2 \cdot \mathbf{x}'_2 - \mathbf{k}_1 \cdot \mathbf{x}_1 - \mathbf{k}_2 \cdot \mathbf{x}_2)} \langle \mathbf{x}'_1 \mathbf{x}'_2 | V_{\text{NN}}^{\text{local}} | \mathbf{x}_1 \mathbf{x}_2 \rangle \\ &= \int d\mathbf{x}_1 d\mathbf{x}_2 e^{-i(\mathbf{k}'_1 - \mathbf{k}_1) \cdot \mathbf{x}_1 - i(\mathbf{k}'_2 - \mathbf{k}_2) \cdot \mathbf{x}_2} V_{\text{NN}}^{\text{local}}(\mathbf{r}) \\ &= \int d\mathbf{r} d\mathbf{R}_{(12)} e^{-i(\mathbf{p}' - \mathbf{p}) \cdot \mathbf{r} - i(\mathbf{P}'_{(12)} - \mathbf{P}_{(12)}) \cdot \mathbf{R}_{(12)}} V_{\text{NN}}^{\text{local}}(\mathbf{r}). \end{aligned} \quad (35)$$

This implies that the interaction depends in momentum space only on *differences of Jacobi momenta*, i.e., on momentum transfers (see Eq. (32)):

$$\langle \mathbf{p}' | V_{\text{NN}}^{\text{local}} | \mathbf{p} \rangle = \int d\mathbf{r} e^{-i(\mathbf{p}' - \mathbf{p}) \cdot \mathbf{r}} V_{\text{NN}}^{\text{local}}(\mathbf{r}) = V_{\text{NN}}^{\text{local}}(\mathbf{p}' - \mathbf{p}). \quad (36)$$

Examples of local interactions are the instantaneous meson exchanges and (unregularized) contact interactions (see left panel of Figure 22).

Let us consider in comparison a local interaction that is regularized via a cutoff function  $f_\Lambda$  in the following way:

$$\langle \mathbf{p}' | V_{\text{NN}}^{\text{reg}} | \mathbf{p} \rangle = f_\Lambda(\mathbf{p}') V_{\text{NN}}^{\text{local}}(\mathbf{p}' - \mathbf{p}) f_\Lambda(\mathbf{p}). \quad (37)$$

<sup>5</sup>We note that the antisymmetrization of the interaction leads to an exchange term with interchanged coordinates  $\mathbf{x}'_1 \leftrightarrow \mathbf{x}'_2$  in the final state, i.e.,  $\mathbf{r}_{(12)} = -\mathbf{r}'_{(12)}$ :

$$\langle \mathbf{x}'_1 \mathbf{x}'_2 | V_{\text{NN}}^{\text{ex}} | \mathbf{x}_1 \mathbf{x}_2 \rangle = V_{\text{NN}}(\mathbf{r}) \delta(\mathbf{r}' + \mathbf{r}) \delta(\mathbf{R}'_{(12)} - \mathbf{R}_{(12)}). \quad (34)$$

This regularization has been extensively used for chiral EFT NN interactions (see Section 3.7.1). The resulting regularized interaction obviously does not only depend on the momentum difference,  $\mathbf{p}' - \mathbf{p}$ , but rather on the individual momenta  $\mathbf{p}$  and  $\mathbf{p}'$ , which implies in coordinate space  $\mathbf{x}_i \neq \mathbf{x}'_i$ . Such an interaction is *nonlocal* (see right panel of Figure 22).

The arguments above can be extended straightforwardly to 3N interactions. Specifically, this implies that local 3N forces only depend on the difference of the two Jacobi momenta:

$$V_{3N}^{\text{local}} = V_{3N}^{\text{local}}(\mathbf{p}' - \mathbf{p}, \mathbf{q}' - \mathbf{q}) \equiv V_{3N}^{\text{local}}(\tilde{\mathbf{p}}, \tilde{\mathbf{q}}). \quad (38)$$

Using the rotational symmetry of the potential  $V_{3N}^{\text{local}}$  we can write the 3N interaction as a function of only three independent variables:

$$V_{3N}^{\text{local}}(\tilde{\mathbf{p}}, \tilde{\mathbf{q}}) = V_{3N}^{\text{local}}(\tilde{p}, \tilde{q}, \cos \theta_{\tilde{\mathbf{p}}\tilde{\mathbf{q}}}), \quad (39)$$

where  $\cos \theta_{\tilde{\mathbf{p}}\tilde{\mathbf{q}}} = \frac{\tilde{\mathbf{p}} \cdot \tilde{\mathbf{q}}}{\tilde{p}\tilde{q}}$ ,  $\tilde{p} = |\tilde{\mathbf{p}}|$ ,  $\tilde{q} = |\tilde{\mathbf{q}}|$ . Note that this statement refers to unregularized forces. The regularization is discussed in detail in Section 3.7.

The relation (39) shows that the original eight-dimensional integral in Eq. (31) actually contains only three non-trivial integrations for local interactions, while the other five integrations are purely geometric. In fact, after employing some integral transformations they can all be performed analytically. The details of this calculation are presented in Appendix B. The final result for the function  $F$  defined in Eq. (31) can be written in the following form:

$$\begin{aligned} & F_{LL'L'}^{m_L m_L' m_L'}(p, q, p', q') \\ &= \delta_{m_L - m_L', m_L' - m_L} \frac{(-1)^{m_L + m_L'}}{(2\pi)^6} \frac{2(2\pi)^4}{pp'qq'} \sum_{\bar{l}=\max(|L'-L|, |L'-l|)}^{\min(L'+L, l'+l)} \frac{C_{L'-m_L', L m_L}^{\bar{l}-m_L'+m_L} C_{L'-m_L', l m_L}^{\bar{l}-m_L'+m_L}}{2\bar{l}+1} \\ &\times \int_{|p'-p|}^{p'+p} d\tilde{p} \tilde{p} \int_{|q'-q|}^{q'+q} d\tilde{q} \tilde{q} \mathcal{Y}_{L'L}^{\bar{l}0}(\widehat{\tilde{p}\mathbf{e}_z + \mathbf{p}, \tilde{\mathbf{p}}}) \Big|_{\phi_p=0, \hat{p}\cdot\mathbf{e}_z=\frac{p'^2-p^2-\tilde{p}^2}{2\tilde{p}p}} \mathcal{Y}_{L'L}^{\bar{l}0}(\widehat{\tilde{q}\mathbf{e}_z + \mathbf{q}, \tilde{\mathbf{q}}}) \Big|_{\phi_q=0, \hat{q}\cdot\mathbf{e}_z=\frac{q'^2-q^2-\tilde{q}^2}{2\tilde{q}q}} \\ &\times \int_{-1}^1 d \cos \theta_{\tilde{\mathbf{p}}\tilde{\mathbf{q}}} P_{\bar{l}}(\cos \theta_{\tilde{\mathbf{p}}\tilde{\mathbf{q}}}) V_{3N}^{\text{local}}(\tilde{q}, \tilde{p}, \cos \theta_{\tilde{\mathbf{p}}\tilde{\mathbf{q}}}). \end{aligned} \quad (40)$$

This reduction from a five-dimensional numerical integral to a three-dimensional one represents a dramatic difference for practical calculations. In the next chapter we discuss in more detail the corresponding speedup factors for the calculation of matrix elements and the connected increase in accessible basis sizes. In essence, this new framework allows to compute matrix elements of 3N interactions at N<sup>2</sup>LO about 1000 more efficiently than the traditional approach for typical basis sizes and discrete momentum mesh systems.

#### 3.4. Generalization to spin- and isospin-dependent 3N interactions

Realistic nuclear forces also depend on the spin and isospin quantum numbers of the nucleons. In this section we generalize the arguments of the previous sections to a general spin- and isospin-dependent local 3N interaction. For this we choose the standard  $Jj$ -coupled three-body partial-wave basis of the form [25]:

$$\begin{aligned} |pq\alpha\rangle_{\{ab\}} &\equiv |pq; [(LS)J(l_s)j] \mathcal{J} \mathcal{M}_{\mathcal{J}}(Tt) \mathcal{T} \mathcal{M}_{\mathcal{T}}\rangle_{\{ab\}} \\ &= \sum_{M_L, M_S, M_J, m_l, m_s, m_j} C_{JM_J m_j}^{\mathcal{J} M_{\mathcal{J}}} C_{LM_L S M_S}^{JM_J} C_{lm_l s m_s}^{j m_j} \sum_{M_T, m_t} C_{TM_T m_t}^{\mathcal{T} M_{\mathcal{T}}} |pq; LM_L S M_S l m_l s m_s\rangle_{\{ab\}} |TM_T m_t\rangle_{\{ab\}}, \end{aligned} \quad (41)$$

where  $L, S, J$  and  $T$  denote the relative orbital angular momentum, two-body spin, total angular momentum and total isospin of particles  $a$  and  $b$  with Jacobi momentum  $p$ . The quantum numbers  $l, s = \frac{1}{2}, j$  and  $t = \frac{1}{2}$  label the orbital angular momentum, spin, total angular momentum and isospin of the remaining particle relative to the center-of-mass of the pair with relative momentum  $p$  (see Section 3.1). The quantum numbers  $\mathcal{J}$  and  $\mathcal{T}$  define the total three-body angular momentum and isospin. The orbital angular momentum partial-wave states are normalized like in Eq. (27). Hence, we immediately obtain the following normalization for

		$J_{\max} = 5$		$J_{\max} = 6$		$J_{\max} = 7$		$J_{\max} = 8$	
$\mathcal{J}$	$\mathcal{T}$	$N_\alpha$	$\dim(V_{3N})$	$N_\alpha$	$\dim(V_{3N})$	$N_\alpha$	$\dim(V_{3N})$	$N_\alpha$	$\dim(V_{3N})$
$\frac{1}{2}$	$\frac{1}{2}$	42	$7 \times 10^8$	50	$1 \times 10^9$	58	$1 \times 10^9$	66	$2 \times 10^9$
$\frac{3}{2}$	$\frac{1}{2}$	78	$2 \times 10^9$	94	$3 \times 10^9$	110	$5 \times 10^9$	126	$6 \times 10^9$
$\frac{5}{2}$	$\frac{1}{2}$	106	$4 \times 10^9$	130	$7 \times 10^9$	154	$9 \times 10^9$	178	$1 \times 10^{10}$
$\frac{7}{2}$	$\frac{1}{2}$	126	$6 \times 10^9$	158	$1 \times 10^{10}$	190	$1 \times 10^{10}$	222	$2 \times 10^{10}$
$\frac{9}{2}$	$\frac{1}{2}$	138	$7 \times 10^9$	178	$1 \times 10^{10}$	218	$2 \times 10^{10}$	258	$3 \times 10^{10}$
$\frac{11}{2}$	$\frac{1}{2}$	142	$8 \times 10^9$	190	$1 \times 10^{10}$	238	$2 \times 10^{10}$	286	$3 \times 10^{10}$
$\frac{1}{2}$	$\frac{3}{2}$	20	$2 \times 10^8$	26	$3 \times 10^8$	28	$3 \times 10^8$	34	$5 \times 10^8$
$\frac{3}{2}$	$\frac{3}{2}$	37	$5 \times 10^8$	49	$9 \times 10^8$	53	$1 \times 10^9$	65	$2 \times 10^9$
$\frac{5}{2}$	$\frac{3}{2}$	50	$1 \times 10^9$	68	$2 \times 10^9$	74	$2 \times 10^9$	92	$3 \times 10^9$
$\frac{7}{2}$	$\frac{3}{2}$	59	$1 \times 10^9$	83	$3 \times 10^9$	91	$3 \times 10^9$	115	$5 \times 10^9$
$\frac{9}{2}$	$\frac{3}{2}$	64	$2 \times 10^9$	94	$3 \times 10^9$	104	$4 \times 10^9$	134	$7 \times 10^9$
$\frac{11}{2}$	$\frac{3}{2}$	65	$2 \times 10^9$	101	$4 \times 10^9$	113	$5 \times 10^9$	149	$9 \times 10^9$

Table 3: Basis sizes and dimensions of 3N interaction matrix elements for the different three-body partial waves as a function of  $J_{\max}$ , the total angular momentum corresponding to the Jacobi momentum  $p$ . For the dimension estimates we have used a typical value for the number of mesh points for the two Jacobi momenta  $p$  and  $q$ ,  $N_p = N_q = 25$ .  $N_\alpha$  denotes the number of partial-wave channels in the  $JJ$ -coupled partial-wave basis defined in Eq. (41) for a given three-body channel  $\{\mathcal{J}, \mathcal{T}\}$ . All given values apply to both three-body parities  $\mathcal{P} = (-1)^{L+l}$ . Table E.9 shows explicitly the basis states for  $\mathcal{J} = \mathcal{T} = 1/2$  and  $\mathcal{P} = +1$ .

the partial-wave states (see Appendix A):

$${}_{\{ab\}}\langle p'q'\alpha' | pq\alpha \rangle_{\{ab\}} = \frac{\delta(p' - p)}{pp'} \frac{\delta(q' - q)}{qq'} \delta_{\alpha\alpha'}, \quad \int dp p^2 \int dq q^2 \sum_{\alpha} |pq\alpha\rangle_{\{ab\}} \langle pq\alpha|_{\{ab\}} = 1. \quad (42)$$

Note that, even though the basis states in Eq. (41) contain the quantum numbers  $\mathcal{M}_{\mathcal{J}}$  and  $\mathcal{M}_{\mathcal{T}}$ , the matrix elements of 3N interactions do not depend on them. Hence we omit these quantum numbers in the basis states in the following. That means the collective index  $\alpha$  in Eq. (41) defines a set of six quantum numbers  $\alpha = \{L, S, J, l, j, T\}$  for a given three-body partial wave specified by  $\{\mathcal{J}, \mathcal{T}, \mathcal{P}\}$ , where  $\mathcal{P}$  is the three-body parity  $\mathcal{P} = (-1)^{L+l}$ . The basis contains only states that are antisymmetric in subsystem  $\{ab\}$ , i.e., we require  $(-1)^{L+S+T} = -1$ . For illustration we list in Appendix E all configurations for the three-body channel with  $\mathcal{J} = \frac{1}{2}$ ,  $\mathcal{T} = \frac{1}{2}$  and  $\mathcal{P} = +1$  for  $J \leq 7$ .

In Table 3 we list typical basis sizes for the different three-body channels  $\{\mathcal{J}, \mathcal{T}, \mathcal{P}\}$  for practical calculations. Here we define the truncation by choosing a maximal value of the total two-body angular momentum  $J$ . Note that, as we will illustrate in Section 4.1, usually it is sufficient to include all partial waves up to the total three-body angular momentum  $\mathcal{J} = \frac{9}{2}$  and  $J_{\max} = 5$ . Typically, matrix elements beyond this truncation have only small effects on observables for finite nuclei and nuclear matter (see Section 4.1). However, the size of these contributions depends in general on the employed NN interaction and the regularization scheme (see Section 3.7).

Due to the explicit momentum dependence of spin-momentum operators, the relation for the fundamental function  $F$  in Eq. (31) needs to be generalized. This can be achieved in a straightforward way by factorizing out the momentum dependence of the spin operators. For illustration let us consider a simple operator of the form  $\boldsymbol{\sigma} \cdot \mathbf{a}$ , where  $\mathbf{a}$  represents one of the Jacobi momenta. First, we rewrite this scalar product in a spherical representation:

$$\boldsymbol{\sigma} \cdot \mathbf{a} = \sqrt{\frac{4\pi}{3}} a \sum_{\mu=-1}^1 Y_{1\mu}^*(\hat{\mathbf{a}}) \boldsymbol{\sigma} \cdot \mathbf{e}_{\mu}. \quad (43)$$

This factorization of the momentum dependence allows to combine the additional spherical harmonic func-

tion with those in Eq. (31) by using [1]:

$$Y_{lm}(\hat{\mathbf{a}})Y_{1\mu}(\hat{\mathbf{a}}) = \sum_{\bar{L}=|l-1|}^{l+1} \sqrt{\frac{3}{4\pi} \frac{2l+1}{2\bar{L}+1}} C_{l0\bar{L}}^{\bar{L}0} C_{lm1\mu}^{\bar{L}m+\mu} Y_{\bar{L}m+\mu}(\hat{\mathbf{a}}). \quad (44)$$

This strategy is completely general and can be used to reduce the expressions for arbitrary spin-dependent interactions to the expression for spin-independent interactions times some momentum-independent spin operators. This step has to be performed for each momentum vector in the spin-momentum operators. Obviously, the efficiency of the algorithm decreases with each additional sum over the quantum numbers  $\mu$  and  $\bar{L}$  in Eqs. (43) and (44). Note, however, that each of these sums contains only three terms at most.

In order to factorize the momentum, spin and isospin space, it is most convenient to perform the calculations of the matrix elements in an  $LS$ -coupled basis:

$$|pq\beta\rangle_{(ab)} \equiv |pq; [(Ll)\mathcal{L}(Ss)\mathcal{S}] \mathcal{J}(\mathcal{T}t)\mathcal{T}\rangle_{(ab)}, \quad (45)$$

and recouple only at the end to the  $Jj$ -coupled basis defined in Eq. (41). Here the quantum number  $\mathcal{L}$  denotes the total orbital angular momentum as in Eq. (27) and  $\mathcal{S}$  is the total three-body spin. Each time the factorization in Eq. (43) is applied, the spin matrix element acquires a dependence on the quantum number  $\mu$ . Consequently, the matrix element in spin space can be formally written in the form

$${}_{(ab)}\langle (Ss)\mathcal{S}\mathcal{M}_{\mathcal{S}} | \hat{O}_{\sigma}(\{\mu_i\}) | (S's')\mathcal{S}'\mathcal{M}_{\mathcal{S}'} \rangle_{(ab)}, \quad (46)$$

where the index  $i$  counts the number of momentum vectors in the spin operator. In the same way the function  $F$  in Eq. (31) becomes a function of the quantum numbers  $\mu_i$ , i.e., it takes the form  $F_{LL'L'}^{m_L m_{L'} m_{L'}' m_{\mu_i}}$ . To be explicit, if we consider, the case  $\mathbf{a} = \mathbf{p}$  in Eq. (43), the function  $F$  takes the form

$$F_{LL'L'}^{m_L m_{L'} m_{L'}' m_{\mu}}(p, q, p', q') = p \sum_{\bar{L}=|L-1|}^{L+1} \sqrt{\frac{2L+1}{2\bar{L}+1}} C_{L0\bar{L}}^{\bar{L}0} C_{Lm_L\mu}^{\bar{L}m_L+\mu} F_{LL'L'}^{m_L m_{L'} m_{L'}'}(p, q, p', q'), \quad (47)$$

where we included the factor  $\sqrt{\frac{4\pi}{3}}p$  from the spin operator factorization in Eq. (43) in this function.

For an efficient implementation it is important to note that all quantities that depend on the projection quantum numbers  $m$  and  $\mu$  are independent of the momenta. Hence, it is useful to factorize this dependence in the function  $F$ . Specifically, for the example shown in Eq. (47) we can write

$$F_{LL'L'}^{m_L m_{L'} m_{L'}' m_{\mu}}(p, q, p', q') \equiv \delta_{m_L - m_{L'}, m_{L'}' - m_{\mu}} (-1)^{m_L + m_{\mu}} \sum_{\bar{l}} C_{L' - m_{L'}' + m_L}^{\bar{l} - m_{L'}' + m_L} C_{L' - m_{\mu} m_{\mu}}^{\bar{l} - m_{\mu} + m_{\mu}} \sum_{\bar{L}} C_{L0\bar{L}}^{\bar{L}0} C_{Lm_L\mu}^{\bar{L}m_L+\mu} \tilde{F}_{LL'L'}^{\bar{L}}(p, q, p', q'). \quad (48)$$

For general interactions, the function  $\tilde{F}$  depends on multiple quantum numbers  $\bar{L}_i$ , hence the function takes formally the form  $\tilde{F}_{LL'L'}^{i(L_i)}(p, q, p', q')$ . Using this decomposition we can first precalculate all sums over the projection quantum numbers  $m$  and  $\mu_i$  and prestore the result in a function of the form  $A_{\beta\beta'}^{\bar{L}_i}$ , where  $\beta$  labels the  $LS$ -coupled partial-wave channels (see Eq. (45)). Then the final matrix element in  $LS$ -coupling can be calculated very efficiently via:

$${}_{(ab)}\langle p'q'\beta' | V_{3N} | pq\beta \rangle_{(ab)} = \sum_{\bar{l}} \sum_{\{\bar{L}_i\}} A_{\beta\beta'}^{\bar{l}(\bar{L}_i)} \tilde{F}_{LL'L'}^{\bar{l}(\bar{L}_i)}(p, q, p', q'), \quad (49)$$

where values of the quantum numbers  $L$ ,  $L'$ ,  $l$  and  $l'$  are specified by the  $LS$ -coupling partial-wave indices  $\beta$  and  $\beta'$ . Similar to the  $Jj$ -coupled basis, here the collective index  $\beta$  defines a set of six quantum numbers  $\beta = \{L, l, \mathcal{L}, S, \mathcal{S}, T\}$  for a given three-body partial wave  $\{\mathcal{J}, \mathcal{T}, \mathcal{P}\}$ . Finally, the recoupling to the  $Jj$ -basis is



achieved by applying the standard recoupling relation [1, 255]

$$|pq\alpha\rangle_{(ab)} = \sum_{\mathcal{L}, \mathcal{S}} \sqrt{\hat{\mathcal{L}}\hat{\mathcal{S}}\hat{j}} \left\{ \begin{array}{ccc} L & S & J \\ l & \frac{1}{2} & j \\ \mathcal{L} & \mathcal{S} & \mathcal{J} \end{array} \right\} |pq\beta\rangle_{(ab)}, \quad (50)$$

with  $\hat{a} = 2a + 1$  and the  $9j$ -symbol  $\{\dots\}$ . Note that by deriving Eq. (49) the original problem of numerically calculating a 5-dimensional integral for each matrix element as in Eq. (31) has been reduced to the evaluation of a few discrete sums. The calculation and prestorage of the matrix elements of  $\tilde{F}_{LL'L'}^{i(L_i)}(p, q, p', q')$  can be performed relatively efficiently since only three internal integrals have to be performed numerically. The exact speedup factor of the present method compared to the conventional approach of Refs. [250, 251] depends on the number of internal sums over  $\mu_i$  and  $L_i$ , i.e., on the specific form of the interaction. For example, the matrix elements of the chiral long-range interactions at N<sup>2</sup>LO proportional to the couplings  $c_1$  and  $c_3$  can be calculated with speedup factors of greater than 1000. In practical terms, that means that it is possible to calculate the matrix elements of all interaction terms up to N<sup>3</sup>LO on a local computer cluster for sufficiently large basis sizes needed for converged studies of few-nucleon scattering processes, light and medium mass nuclei and nuclear matter.

Despite the fact that the present algorithm makes explicit use of the local nature of the 3N interaction, it is also possible to treat polynomial nonlocal terms. This is of immediate practical importance since, e.g., the relativistic corrections to 3N interactions at N<sup>3</sup>LO have precisely this form [183, 184]. Consider, for example, a nonlocal momentum structure in the center-of-mass frame of the type

$$(\mathbf{k}_3 + \mathbf{k}'_3) \cdot (\mathbf{k}_3 - \mathbf{k}'_3) = (\mathbf{q}'_{[12]} + \mathbf{q}_{[12]}) \cdot (\mathbf{q}'_{[12]} - \mathbf{q}_{[12]}). \quad (51)$$

Such terms can be treated by factorizing the momentum dependence like in Eq. (43), for example:

$$\mathbf{q} \cdot \mathbf{q}' = qq' \frac{4\pi}{3} \sum_{\mu_1, \mu_2 = -1}^1 Y_{1\mu_1}^*(\hat{\mathbf{q}}) Y_{1\mu_2}^*(\hat{\mathbf{q}}') \mathbf{e}_{\mu_1} \cdot \mathbf{e}_{\mu_2}, \quad (52)$$

and then following exactly the steps after Eq. (43). Obviously, the algorithm becomes less efficient for nonlocal interactions, but this framework turns out to be still more efficient than the conventional approach for the relativistic corrections to chiral 3N interactions at N<sup>3</sup>LO.

### 3.5. Decomposition of 3N interactions and antisymmetrization

A local contribution to 3N interactions can generically be written in the form

$$V_{3N} = \sum_{i \neq j \neq k} f_Q(\mathbf{Q}_i, \mathbf{Q}_j, \mathbf{Q}_k) f_\sigma(\mathbf{Q}_i, \mathbf{Q}_j, \mathbf{Q}_k, \boldsymbol{\sigma}_i, \boldsymbol{\sigma}_j, \boldsymbol{\sigma}_k) f_\tau(\boldsymbol{\tau}_i, \boldsymbol{\tau}_j, \boldsymbol{\tau}_k), \quad (53)$$

with  $i, j, k \in \{1, 2, 3\}$ , the momentum transfers  $\mathbf{Q}_i = \mathbf{k}'_i - \mathbf{k}_i$  and spin (isospin) operators  $\boldsymbol{\sigma}_i$  ( $\boldsymbol{\tau}_i$ ) of particle  $i$ . The function  $f_Q$  includes all scalar momentum dependence,  $f_\sigma$  denotes the spin-momentum operators and  $f_\tau$  the isospin operators. Since the latter one is momentum independent it can be treated straightforwardly in the partial-wave decomposition. Here and in the following we focus only on the dynamical degrees of freedom of the particles and suppress all physical constants like, e.g.,  $g_A$  or  $m_\pi$ .

The interaction  $V_{3N}$  in Eq. (53) is by construction totally symmetric in all particle labels. In total there are six contributions, which are illustrated in Figure 23. It is important to note that we can always pick a subset of two terms which are not related by a cyclic or anticyclic permutation of the states, such that the remaining four diagrams can then be generated by the application of the 3-body permutation operators  $P_{123}$  and  $P_{132}$ . In order to illustrate this point let us make a particular choice and define  $V_{3N}^{(1)}$  to be those two diagrams in Figure 23 in which the central fermion line carries label “1”, i.e., diagrams (c) and (e). Note that this interaction term is by construction symmetric in particles 2 and 3, which follows directly from the total symmetry of  $V_{3N}$ . Then it is straightforward to show that the total interaction can be written in the

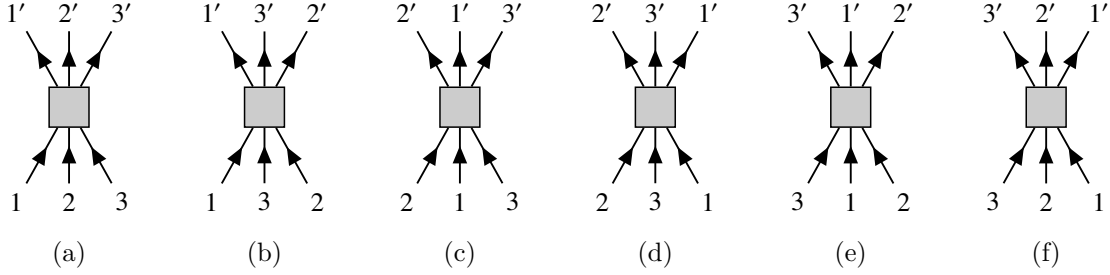


Figure 23: The six contributions to a general 3N interaction resulting from the sums over the particle indices in Eq. (53).

form

$$V_{3N} = V_{3N}^{(1)} + P_{123}^{-1} V_{3N}^{(1)} P_{123} + P_{132}^{-1} V_{3N}^{(1)} P_{132}. \quad (54)$$

The quantity  $V_{3N}^{(1)}$  is commonly called the *Faddeev component* of the interaction. To verify this relation note that the permutation operator  $P_{123}$  permutes the ket states cyclically and the inverse operator  $P_{123}^{-1}$  leads to a cyclic permutation of the bra states (see discussion after Eq. (17) in Section 3.1). Obviously, we could have chosen another subset of diagrams by selecting another particle label  $i$  or another fermion line. However, the chosen contributions will by construction always be symmetric in two particle labels  $j$  and  $k$ . For each possible choice we obtain a different decomposition of the 3N interaction in Eq. (54). The practical usefulness of this decomposition for our present purposes relies on the fact that it is sufficient to only compute  $V_{3N}^{(i)}$  explicitly for a chosen decomposition and to generate the other terms by the application of the permutation operators.

By employing the algorithm discussed in Section 3.3 we obtain as the final result the partial-wave matrix elements

$${}_{\{ab\}} \langle p' q' \alpha' | V_{3N}^{(i)} | p q \alpha \rangle_{\{ab\}} \quad (55)$$

for a given decomposition and in a specific basis representation  $\{ab\}$ . We emphasize that the specific values of the matrix elements depend on the choice of the decomposition Eq. (54) and on the chosen basis representation of the interaction. In this sense the matrix elements in Eq. (55) are scheme dependent and we cannot expect the results of independent implementations for a given interaction to agree. However, when computing expectation values of these interactions with respect to wave functions the results, of course, have to be unique and scheme independent.

In order to see that this is indeed the case consider the expectation value of the total 3N interaction  $V_{3N}$  with respect to a 3-body wave function  $\psi$ :

$$\langle V \rangle \equiv \langle \psi | V_{3N} | \psi \rangle, \quad (56)$$

using the normalization  $\langle \psi | \psi \rangle = 1$ . Since we consider nucleons as identical fermions the wave function is totally antisymmetric, i.e.,  $P_{ij} | \psi \rangle = - | \psi \rangle$  for two arbitrary particles  $i$  and  $j$ , with  $P_{ij}$  being the two-body transposition operators (see Section 3.1). Let us make the antisymmetry of the wave function explicit by inserting the three-body antisymmetrizer [249]:

$$\mathcal{A}_{123} = 1 - P_{12} - P_{13} - P_{23} + P_{123} + P_{132} = (1 - P_{ij})(1 + P_{123} + P_{132}), \quad (57)$$

where  $i$  and  $j$  are two arbitrary particle indices. Then the expectation value can be written in the form

$$\langle V \rangle = \frac{1}{36} \langle \psi | \mathcal{A}_{123} V_{3N} \mathcal{A}_{123} | \psi \rangle = \frac{1}{9} \langle \psi | (1 + P_{123} + P_{132}) V_{3N} (1 + P_{123} + P_{132}) | \psi \rangle. \quad (58)$$

The last identity follows directly from the antisymmetry of  $\psi$ , i.e.,  $(1 - P_{ij})/2 | \psi \rangle = | \psi \rangle$ . Now we insert the

decomposition from Eq. (54) and use the relations

$$P_{123}(1 + P_{123} + P_{132}) = P_{132}(1 + P_{123} + P_{132}) = (1 + P_{123} + P_{132}), \quad (59)$$

which follow directly from relations  $P_{123} = P_{132}^{-1} = P_{132}^2$  and  $P_{123}^3 = P_{132}^3 = 1$ . From Eq. (59) it follows that each term in the decomposition (54) gives the same contribution to the expectation value with the final result:

$$\langle V \rangle = \frac{1}{3} \langle \psi | (1 + P_{123} + P_{132}) V_{3N}^{(i)} (1 + P_{123} + P_{132}) | \psi \rangle. \quad (60)$$

The arguments above are independent of the specific choice of the decomposition and also on the chosen basis representation  $\{ab\}$ . In fact, the matrix elements of the *antisymmetrized* 3N interaction

$$\langle p' q' \alpha' | V_{3N}^{\text{as}} | p q \alpha \rangle = {}_{\{ab\}} \langle p' q' \alpha' | (1 + P_{123} + P_{132}) V_{3N}^{(i)} (1 + P_{123} + P_{132}) | p q \alpha \rangle_{\{ab\}} \quad (61)$$

are unique and scheme independent. Hence, in the following we can neglect the basis indices  $\{ab\}$  for the antisymmetrized interaction.

The practical computation of antisymmetrized matrix elements involves two steps: First, the calculation of the 3N interaction components defined in Eq. (54) and, second, the application of the permutation operators in Eq. (61). The latter operation is usually performed in a partial-wave representation by inserting a complete set of states, e.g.:

$${}_{\{ab\}} \langle p' q' \alpha' | P_{123} V_{3N}^{(i)} | p q \alpha \rangle_{\{ab\}} = \int d p'' p''^2 d q'' q''^2 \sum_{\alpha''} {}_{\{ab\}} \langle p' q' \alpha' | P_{123} | p'' q'' \alpha'' \rangle_{\{ab\}} {}_{\{ab\}} \langle p'' q'' \alpha'' | V_{3N}^{(i)} | p q \alpha \rangle_{\{ab\}}. \quad (62)$$

The matrix elements of the permutation operator  $P_{123}$  can be derived directly based on their definitions in momentum space, Eqs. (19a) to (19c), and by taking into account the spin- and isospin exchange parts. These definitions show that, in essence, the matrix elements  $\langle p' q' \alpha' | P_{123} | p q \alpha \rangle$  provide two relations of the four Jacobi momenta  $p, q, p'$  and  $q'$ , which depend in general on all angular momentum quantum numbers. There are different possible representations, for example:

1.  $p' = f_1(p, q), q' = f_2(p, q)$  (see Eq. (19a)),
2.  $p = f_1(q, q'), p' = f_2(q, q')$  (see Eq. (19b)),
3.  $p = f_1(p', q'), q = f_2(p', q')$  (see Eq. (19c)).

Note that we suppressed all angular, spin and isospin dependence in these schematic relations. The preferred choice depends on the context. For our purposes it is most convenient to choose option 3, because this choice makes it possible to implement products like  $P_{123} V_{3N}$  in Eq. (62) very efficiently as a matrix product as we will now demonstrate.

The definition of the partial-wave matrix elements of  $P_{123}$  follows from a generalization of Eqs. (20) and (21):

$$\langle p' q' \alpha' | P_{123} | p q \alpha \rangle = {}_{\{12\}} \langle p' q' \alpha' | p q \alpha \rangle_{\{23\}} = {}_{\{23\}} \langle p' q' \alpha' | p q \alpha \rangle_{\{31\}} = {}_{\{31\}} \langle p' q' \alpha' | p q \alpha \rangle_{\{12\}}. \quad (63)$$

The derivation of the explicit expression for the partial-wave matrix elements of the permutation operator is straightforward but somewhat tedious. The calculation is presented in detail in Appendix E. The final result

can be written in the following form:

$$\begin{aligned}
& {}_{\{ab\}}\langle p'q'\alpha'|P_{123}|pq\alpha\rangle_{\{ab\}} \\
&= \sum_{L,S} \sqrt{j\hat{j}\hat{j}'\hat{S}} \begin{Bmatrix} L & S & J \\ l & \frac{1}{2} & j \end{Bmatrix} \begin{Bmatrix} L' & S' & J' \\ l' & \frac{1}{2} & j' \end{Bmatrix} \\
&\times (-1)^S \sqrt{\hat{S}\hat{S}'} \begin{Bmatrix} \frac{1}{2} & \frac{1}{2} & S' \\ \frac{1}{2} & S & S \end{Bmatrix} (-1)^T \sqrt{\hat{T}\hat{T}'} \begin{Bmatrix} \frac{1}{2} & \frac{1}{2} & T' \\ \frac{1}{2} & T & T \end{Bmatrix} \\
&\times 8\pi^2 \int d\cos\theta_{\mathbf{p}'\mathbf{q}'} \frac{\delta(p-|\bar{\mathbf{p}}|)}{p^2} \frac{\delta(q-|\bar{\mathbf{q}}|)}{q^2} \sum_{M_L} \mathcal{Y}_{L'l'}^{*\mathcal{L}M_L}(\hat{\mathbf{p}}', \hat{\mathbf{q}}') \mathcal{Y}_{Ll}^{\mathcal{L}M_L}(\hat{\mathbf{p}}, \hat{\mathbf{q}}) \\
&\equiv \int d\cos\theta_{\mathbf{p}'\mathbf{q}'} G_{\alpha\alpha'}(p', q', \cos\theta_{\mathbf{p}'\mathbf{q}'}) \frac{\delta(p-|\bar{\mathbf{p}}|)}{p^2} \frac{\delta(q-|\bar{\mathbf{q}}|)}{q^2}, \tag{64}
\end{aligned}$$

with

$$\begin{aligned}
\bar{\mathbf{p}} &= \bar{\mathbf{p}}(p', q', \cos\theta_{\mathbf{p}'\mathbf{q}'}) = -\frac{1}{2}\mathbf{p}' - \frac{3}{4}\mathbf{q}', \\
\bar{\mathbf{q}} &= \bar{\mathbf{q}}(p', q', \cos\theta_{\mathbf{p}'\mathbf{q}'}) = \mathbf{p}' - \frac{1}{2}\mathbf{q}'. \tag{65}
\end{aligned}$$

In the last step in Eq. (64) we factorized the total matrix element into the radial delta functions and the geometric function  $G_{\alpha\alpha'}(p', q', \cos\theta_{\mathbf{p}'\mathbf{q}'})$ , which contains all the remaining terms (see also Ref. [25]). One of the main differences to other expressions (see, e.g., Refs. [25, 26]) is the fact that we directly perform the angular integrals in Eq. (64) without decomposing the angular dependence of the spherical harmonic functions any further. This implementation turns out to be numerically more efficient and, most importantly, very stable even for large values of angular momenta  $L$  and  $l$ .

We note that the partial-wave matrix elements of the anticyclic permutation operator  $P_{132} = P_{123}^{-1}$  with respect to antisymmetric states are also given by Eq. (64). However, applying the operator product  $P_{123}P_{132} = 1$  in this partial-wave representation to an operator or wave function  $\psi(p, q, \alpha) = \langle pq\alpha|\psi\rangle$  will generally *not* result in an identity:

$$\sum_{\alpha} \int dp' p'^2 dq' q'^2 dp'' p''^2 dq'' q''^2 \langle pq\alpha|P_{123}|p'q'\alpha'\rangle \langle p'q'\alpha''|P_{132}|p''q''\alpha''\rangle \langle p''q''\alpha''|\psi\rangle \neq \langle pq\alpha|\psi\rangle. \tag{66}$$

This is because the permutation operator generally couples states of different symmetries with respect to the exchange of particles. This can be seen by expressing the permutation operator in the following form (see Section 3.1 and also the discussion in Ref. [25]):

$$P_{132} = P_{13}P_{23} = P_{23}P_{12}P_{23}P_{23} = P_{23}P_{123}P_{23}, \tag{67}$$

and compute the following overlap matrix elements

$$\begin{aligned}
{}_{\{23\}}\langle p'q'\alpha'|P_{132}|pq\alpha\rangle_{\{23\}} &= {}_{\{23\}}\langle p'q'\alpha'|pq\alpha\rangle_{\{12\}} \\
&= {}_{\{23\}}\langle p'q'\alpha'|P_{23}P_{123}P_{23}|pq\alpha\rangle_{\{23\}} \\
&= {}_{\{23\}}\langle p'q'\alpha'|P_{123}|pq\alpha\rangle_{\{23\}} (-1)^{L+S+T} (-1)^{L'+S'+T'}. \tag{68}
\end{aligned}$$

If the initial and final states are antisymmetric with respect to the exchange of particles 2 and 3 (like all states in the definition of the basis in Eq. (41)) the phase factors cancel and we obtain  $\langle p'q'\alpha'|P_{123}|pq\alpha\rangle = \langle p'q'\alpha'|P_{132}|pq\alpha\rangle$ . However, in general there will be contributions from couplings to symmetric intermediate states when computing auxiliary quantities. When the operator is eventually applied to physical states, the symmetric contributions of the operator decouple and do not contribute to observables. However, for intermediate steps it is key to extend the basis state by “unphysical” states that are symmetric under

exchange of two particles. This point will become important for the regularization of 3N interactions (see Section 3.7.5).

For the practical evaluation of the radial delta functions in Eq. (64) we employ a method based on global splines, which was originally developed for solving the Faddeev equations for few-body systems [255]. This basic idea of this method is to construct continuous spline functions  $S_i(p)$  for some given mesh system  $\{p_i\}$  of size  $N_p$  such that the value of a function  $f$  at an arbitrary point  $p$  is given by the following global sum over all mesh points:

$$f(p) = \sum_{i=1}^{N_p} f(p_i) S_i(p). \quad (69)$$

The spline functions are constructed such that the interpolated function values agrees exactly with the original values  $f(p_i)$  at the mesh points. One possible parametrization of the spline functions  $S_i(p)$  is given in Ref. [255].

This interpolation method allows to express the product of the permutation operator with another operator in an elegant and efficient way as a matrix product. Consider as an example the product in Eq. (62), which can be written in the following form ( $x \equiv \cos \theta_{p'q'}$ ):

$$\begin{aligned} \langle p' q' \alpha' | P_{123} V_{3N}^{(i)} | p q \alpha \rangle &= \sum_{\alpha''} \int d p'' p''^2 d q'' q''^2 \langle p' q' \alpha' | P_{123} | p'' q'' \alpha'' \rangle \langle p'' q'' \alpha'' | V_{3N}^{(i)} | p q \alpha \rangle \\ &= \sum_{\alpha''} \int_{-1}^1 dx G_{\alpha' \alpha''}(p', q', x) \langle \bar{p} \bar{q} \alpha'' | V_{3N}^{(i)} | p q \alpha \rangle \\ &= \sum_{i, j, \alpha''} \int_{-1}^1 dx S_i(\bar{p}) S_j(\bar{q}) G_{\alpha' \alpha''}(p', q', x) \langle p_i'' q_j'' \alpha'' | V_{3N}^{(i)} | p q \alpha \rangle, \end{aligned} \quad (70)$$

where  $p_i''$  and  $q_j''$  are the mesh points of some chosen interpolation grid systems, and  $p = \bar{p}(p_i'', q_j'', x)$  and  $q = \bar{q}(p_i'', q_j'', x)$ , given in Eq. (65). Since for practical calculations all quantities need to be tabulated on a finite momentum mesh system anyway it is most natural to choose the same mesh system for the Jacobi momenta in the initial and final states in Eq. (70). This defines a common discrete matrix representation for all quantities in the chosen three-body basis. In particular, the permutation operator can be precalculated and prestored for each three-body partial wave by defining the discrete matrix of dimension  $N_p N_q N_\alpha$ :

$$\langle p_i' q_j' \alpha' | P_{123} | p_i q_j \alpha \rangle = \int_{-1}^1 dx S_i(\bar{p}) S_j(\bar{q}) G_{\alpha' \alpha}(p_i', q_j', x). \quad (71)$$

This matrix can then be applied to arbitrary operators in a three-body momentum representation via efficient BLAS (Basic Linear Algebra Subprograms) [256] matrix multiplication routines. For the application of  $P_{123}$  from the right hand side in Eq. (61) we just apply the transposed matrix.

### 3.6. Example: Calculation of two-pion exchange 3N interactions

In this section we illustrate the calculation of partial-wave 3N matrix elements using the algorithm discussed above by considering as an example the leading-order long-range 3N interactions in chiral EFT. At this point we neglect any regulators. We will discuss the regularization in detail in the next section.

Specifically, we consider the two-pion exchange interaction at N<sup>2</sup>LO proportional to the low-energy couplings  $c_1$  and  $c_3$ :

$$V_{3N} = \frac{1}{2} \left( \frac{g_A}{2f_\pi} \right)^2 \sum_{i \neq j \neq k} \frac{(\boldsymbol{\sigma}_i \cdot \mathbf{Q}_i)(\boldsymbol{\sigma}_j \cdot \mathbf{Q}_j)}{(\mathbf{Q}_i^2 + m_\pi^2)(\mathbf{Q}_j^2 + m_\pi^2)} \boldsymbol{\tau}_i \cdot \boldsymbol{\tau}_j \left[ -\frac{4c_1 m_\pi^2}{f_\pi^2} + \frac{2c_3}{f_\pi^2} \mathbf{Q}_i \cdot \mathbf{Q}_j \right], \quad (72)$$

where  $\mathbf{Q}_i$  denote as usual the momentum transfers,  $\mathbf{Q}_i = \mathbf{k}_i' - \mathbf{k}_i$  (with the single-particle momenta  $\mathbf{k}_i$ ). This interaction has a compact form but is nevertheless general enough to serve as an illustration of the efficient

framework discussed in Section 3.4 as this interaction contains all the fundamental complications of more intricate interactions like those at higher orders in chiral EFT.

As a first step we choose a particular subset of the six interaction terms (see Figure 23). Here we select again, without loss of generality, those two diagrams in which the central fermion line carries label “1”, again denoted by  $V_{3N}^{(1)}$  in the following. This uniquely defines the decomposition shown in Eq. (54) of the 3N interaction, where in the present example this interaction term takes the form

$$V_{3N}^{(1)} = \left( \frac{g_A}{2f_\pi} \right)^2 \frac{(\boldsymbol{\sigma}_2 \cdot \mathbf{Q}_2)(\boldsymbol{\sigma}_3 \cdot \mathbf{Q}_3)}{(\mathbf{Q}_2^2 + m_\pi^2)(\mathbf{Q}_3^2 + m_\pi^2)} \boldsymbol{\tau}_2 \cdot \boldsymbol{\tau}_3 \left[ -\frac{4c_1 m_\pi^2}{f_\pi^2} + \frac{2c_3}{f_\pi^2} \mathbf{Q}_2 \cdot \mathbf{Q}_3 \right]. \quad (73)$$

Note that this interaction term is, as discussed in the previous section, symmetric in particles 2 and 3. In fact, in the present case both terms are identical, so we just obtain a factor 2.

As a next step we choose one of the three basis representations for the Jacobi momenta (see Section 3.1). To be specific, we choose here the basis {23} (see Table 2), i.e.:

$$\mathbf{k}_1 = \mathbf{q}_{\{23\}} = \mathbf{q}, \quad \mathbf{k}_2 = \mathbf{p}_{\{23\}} - \frac{1}{2}\mathbf{q}_{\{23\}} = \mathbf{p} - \frac{1}{2}\mathbf{q}, \quad \mathbf{k}_3 = -\mathbf{p}_{\{23\}} - \frac{1}{2}\mathbf{q}_{\{23\}} = -\mathbf{p} - \frac{1}{2}\mathbf{q}, \quad (74)$$

where we have defined  $\mathbf{p}_{\{23\}} = \mathbf{p}$  and  $\mathbf{q}_{\{23\}} = \mathbf{q}$  for the sake of simplifying the notation for the rest of this section. Hence for the momentum transfers we obtain:

$$\mathbf{Q}_1 = \mathbf{k}'_1 - \mathbf{k}_1 = \tilde{\mathbf{q}}, \quad \mathbf{Q}_2 = \mathbf{k}'_2 - \mathbf{k}_2 = \tilde{\mathbf{p}} - \frac{1}{2}\tilde{\mathbf{q}}, \quad \mathbf{Q}_3 = \mathbf{k}'_3 - \mathbf{k}_3 = -\tilde{\mathbf{p}} - \frac{1}{2}\tilde{\mathbf{q}}, \quad (75)$$

with  $\tilde{\mathbf{p}} = \mathbf{p}' - \mathbf{p}$  and  $\tilde{\mathbf{q}} = \mathbf{q}' - \mathbf{q}$  like in Eq. (38). Now we can factorize the interaction into a momentum-dependent scalar function  $V_{3N}^{\text{local}}(\tilde{\mathbf{p}}, \tilde{\mathbf{q}})$  times spin- and isospin operators (see Eq. (53)):

$$V_{3N}^{(1)} = f_Q(\tilde{\mathbf{p}}, \tilde{\mathbf{q}}) f_\sigma(\mathbf{p}, \mathbf{q}, \mathbf{p}', \mathbf{q}') f_\tau, \quad (76)$$

with

$$f_Q(\tilde{\mathbf{p}}, \tilde{\mathbf{q}}) = \frac{1}{f_\pi^2} \left( \frac{g_A}{2f_\pi} \right)^2 \frac{-4c_1 m_\pi^2 + 2c_3 \mathbf{Q}_2 \cdot \mathbf{Q}_3}{(\mathbf{Q}_2^2 + m_\pi^2)(\mathbf{Q}_3^2 + m_\pi^2)}, \quad f_\sigma(\mathbf{p}, \mathbf{q}, \mathbf{p}', \mathbf{q}') = (\boldsymbol{\sigma}_2 \cdot \mathbf{Q}_2)(\boldsymbol{\sigma}_3 \cdot \mathbf{Q}_3), \quad f_\tau = \boldsymbol{\tau}_2 \cdot \boldsymbol{\tau}_3. \quad (77)$$

The function  $f_Q(\tilde{\mathbf{p}}, \tilde{\mathbf{q}})$  enters as the kernel in Eq. (40) after extending it by contributions from the momentum dependence of the spin operators  $f_\sigma$  as described in Section 3.4. Isospin operators like  $f_\tau$  can be treated very easily since they do not depend on any momenta and hence do not explicitly affect the partial-wave decomposition. For the spin operators we first expand the momentum dependence explicitly in terms of the Jacobi momenta

$$f_\sigma(\mathbf{p}, \mathbf{q}, \mathbf{p}', \mathbf{q}') = \left[ \boldsymbol{\sigma}_2 \cdot (\mathbf{p}' - \mathbf{p} - \frac{1}{2}\mathbf{q}' + \frac{1}{2}\mathbf{q}) \right] \left[ \boldsymbol{\sigma}_3 \cdot (-\mathbf{p}' + \mathbf{p} - \frac{1}{2}\mathbf{q}' + \frac{1}{2}\mathbf{q}) \right], \quad (78)$$

and then apply the factorizations shown in Eq. (43) and Eq. (44) to each of the terms. For example, for the contribution  $[\boldsymbol{\sigma}_2 \cdot (-\mathbf{p})][\boldsymbol{\sigma}_3 \cdot \mathbf{p}]$  the generalized function  $F$  needs to be extended twice by the quantum numbers of momentum  $\mathbf{p}$  in the way shown in Eq. (47). Accordingly, all the other remaining 15 terms in Eq. (78) can be treated. As a next step, we can calculate the function  $\tilde{F}_{LL'V}^{\tilde{L}_i}(p, q, p', q')$  as discussed in Section 3.4. The spherical components of the momentum-independent spin operators shown in Eq. (46) can either be prestored or directly computed on the fly. Combining all these results allows the calculation of the function  $A_{\beta\beta'}^{\tilde{L}_i}$  and eventually of the  $LS$ -coupled and  $Jj$ -coupled 3N interaction matrix elements (see Eqs. (49) and (50)).

### 3.7. Regularization of 3N interactions

The framework discussed in Section 3.3 allows to perform efficiently a partial-wave decomposition in momentum basis states for 3N interactions that are local or only contain polynomial nonlocal terms. How-

	momentum space	coordinate space
<b>nonlocal</b> <i>regulators:</i> long-range short-range  <i>regularization:</i>	<b>nonlocal MS</b> [170]  $f_\Lambda^{\text{long}}(\mathbf{p}, \mathbf{q}) = \exp[-((\mathbf{p}^2 + \frac{3}{4}\mathbf{q}^2)/\Lambda^2)^n]$ $f_\Lambda^{\text{short}}(\mathbf{p}, \mathbf{q}) = f_\Lambda^{\text{long}}(\mathbf{p}, \mathbf{q}) = f_R(\mathbf{p}, \mathbf{q})$  $\langle \mathbf{p}' \mathbf{q}'   V_{3N}^{\text{reg}}   \mathbf{p} \mathbf{q} \rangle = f_R(\mathbf{p}', \mathbf{q}') \langle \mathbf{p}' \mathbf{q}'   V_{3N}   \mathbf{p} \mathbf{q} \rangle f_R(\mathbf{p}, \mathbf{q})$	
<b>local</b> <i>regulators:</i> long-range short-range  <i>regularization:</i>	<b>local MS</b> [224]  $f_\Lambda^{\text{long}}(\mathbf{Q}_i) = \exp[-(\mathbf{Q}_i^2/\Lambda^2)^2]$ $f_\Lambda^{\text{short}}(\mathbf{Q}_i) = f_\Lambda^{\text{long}}(\mathbf{Q}_i) = f_\Lambda(\mathbf{Q}_i)$  $\langle \mathbf{p}' \mathbf{q}'   V_{3N}^{\text{reg}}   \mathbf{p} \mathbf{q} \rangle = \langle \mathbf{p}' \mathbf{q}'   V_{3N}   \mathbf{p} \mathbf{q} \rangle \prod_i f_R(\mathbf{Q}_i)$	<b>local CS</b> [52]  $f_R^{\text{long}}(\mathbf{r}) = 1 - \exp[-(r^2/R^2)^n]$ $f_R^{\text{short}}(\mathbf{r}) = \exp[-(r^2/R^2)^n]$  $V_{3N}^{\pi, \text{reg}}(\mathbf{r}_{ij}) = f_R^{\text{long}}(\mathbf{r}_{ij}) V_{3N}^\pi(\mathbf{r}_{ij})$ $V_{3N}^{\delta, \text{reg}}(\mathbf{r}_{ij}) = \alpha_n(R) f_R^{\text{short}}(\mathbf{r}_{ij})$
<b>semilocal</b> <i>regulators:</i> long-range short-range  <i>regularization:</i>	<b>semilocal MS</b> [241]  $f_\Lambda^{\text{long}}(\mathbf{Q}_i) = \exp[-(\mathbf{Q}_i^2 + m_\pi^2)/\Lambda^2]$ $f_\Lambda^{\text{short}}(\mathbf{p}) = \exp[-\mathbf{p}^2/\Lambda^2]$  $\langle \mathbf{p}' \mathbf{q}'   V_{3N}^{\pi, \text{reg}}   \mathbf{p} \mathbf{q} \rangle = \langle \mathbf{p}' \mathbf{q}'   V_{3N}   \mathbf{p} \mathbf{q} \rangle \prod_i f_R^{\text{long}}(\mathbf{Q}_i)$ $\langle \mathbf{p}' \mathbf{q}'   V_{3N}^{\delta, \text{reg}}   \mathbf{p} \mathbf{q} \rangle = f_\Lambda^{\text{short}}(\mathbf{p}'_\delta) \langle \mathbf{p}' \mathbf{q}'   V_{3N}^\delta   \mathbf{p} \mathbf{q} \rangle f_\Lambda^{\text{short}}(\mathbf{p}_\delta)$	<b>semilocal CS</b> [33]  $f_R^{\text{long}}(\mathbf{r}) = (1 - \exp[-r^2/R^2])^n$ $f_\Lambda^{\text{short}}(\mathbf{p}) = \exp[-\mathbf{p}^2/\Lambda^2]$  $V_{3N}^{\pi, \text{reg}}(\mathbf{r}_{ij}) = f_R^{\text{long}}(\mathbf{r}_{ij}) V_{3N}^\pi(\mathbf{r}_{ij}) \xrightarrow{\text{FT}} \langle \mathbf{p}' \mathbf{q}'   V_{3N}^{\pi, \text{reg}}   \mathbf{p} \mathbf{q} \rangle$ $\langle \mathbf{p}' \mathbf{q}'   V_{3N}^{\delta, \text{reg}}   \mathbf{p} \mathbf{q} \rangle = f_\Lambda^{\text{short}}(\mathbf{p}'_\delta) \langle \mathbf{p}' \mathbf{q}'   V_{3N}^\delta   \mathbf{p} \mathbf{q} \rangle f_\Lambda^{\text{short}}(\mathbf{p}_\delta)$

Table 4: Different regularization schemes for 3N interactions. We have suppressed all spin and isospin quantum numbers for the sake of simple notation. For all shown schemes only spin- and isospin-independent regulator functions have been applied so far. For each choice we list the reference in which the scheme was first proposed. We stress that a chosen regularization should be applied consistently to NN and 3N interactions.  $V_{3N}^\pi$  denotes the long-range part of a given interaction contribution, like pion-exchange interactions, whereas  $V_{3N}^\delta$  denotes the short-range contact contributions. The total unregularized and regularized interactions are then given by  $V_{3N} = V_{3N}^\pi V_{3N}^\delta$  and  $V_{3N}^{\text{reg}} = V_{3N}^{\pi, \text{reg}} V_{3N}^{\delta, \text{reg}}$ , respectively.  $\mathbf{p}_\delta$  denotes the momenta of the particles that interact via the short-range force  $V_{3N}^\delta$  (see also Figure 25),  $\alpha_n(R)$  is a normalization constant, and “FT” denotes the Fourier transform to momentum space.

ever, so far we have neglected the problem of regularizing the interaction. In general, all interactions for nuclear structure calculations are parametrized in terms effective low-energy degrees of freedom, i.e., neutrons, protons and pions (see Section 2). That means the description is, at least implicitly, based on some low-energy approximation of the underlying quark-gluon dynamics described by QCD. However, as with any low-energy effective theory, this description becomes inefficient beyond some ultraviolet momentum scale, or, equivalently, below a certain interparticle distance scale. The presence of this breakdown scale implies that the interaction matrix elements need to be regularized in order to separate the low-energy from the high-energy part. While the low-energy part is described in terms of the dynamics of the effective degrees of freedom, the contributions from high-energy physics is implicitly encoded in the low-energy couplings. In practice, the regularization is achieved by the multiplication of the interaction matrix elements with a regulator function  $f_\Lambda$  ( $f_R$ ), which suppresses the contributions beyond a momentum scale  $\Lambda$  (below a distance scale  $R$ ).

There are currently active ongoing discussions about over which range of values these scales should be varied and to which extent the effects from these variations can be absorbed in changes of the effective low-energy couplings. These questions are directly connected to fundamental questions regarding the power counting of the underlying chiral EFT and renormalizability. However, in this work we will not discuss these conceptual questions but refer the interested reader to, e.g., Ref. [17], for details. Instead, we will in the following discuss the practical implementation of different type of regularization schemes for 3N interactions. These are independent of any particular underlying power counting scheme.

The different regularization strategies can be characterized by the nature of the regulator function:



- First, we can categorize the regularization into a *momentum-space* or *coordinate-space* formulation. In the first case the regulator function is a general function of all Jacobi momenta in some chosen basis representation  $\{ab\}$ :

$$f_\Lambda = f_\Lambda(\mathbf{p}, \mathbf{q}, \mathbf{p}', \mathbf{q}'). \quad (79)$$

This regulator function is then applied as a simple multiplicative factor to leading-order 3N contributions (see, e.g. Eq. (54)):

$$V_{3N}^{\text{reg}} = V_{3N}^{\text{reg}}(\mathbf{p}, \mathbf{q}, \mathbf{p}', \mathbf{q}') f_\Lambda(\mathbf{p}, \mathbf{q}, \mathbf{p}', \mathbf{q}'). \quad (80)$$

For higher-order 3N contributions involving loop structures the regulator functions can in general also be applied to internal loop momenta.

Accordingly, in coordinate space the regulator function depends in general on all relative coordinates

$$f_R = f_R(\mathbf{r}, \mathbf{s}, \mathbf{r}', \mathbf{s}'). \quad (81)$$

In the present work we will not discuss methods to directly apply regulator functions in coordinate space since the calculation and decomposition of the 3N interactions is performed in momentum space. Instead, we perform a Fourier transform of the coordinate-space regulators shown in Eq. (81) to momentum space and apply them in the basis discussed in Section 3.4 via convolution integrals (see below for details).

- Second, the regulator function can be categorized into *local* and *nonlocal* regulator functions. According to the discussion in Section 3.3, in momentum space local regulator functions are functions of momentum transfers only, i.e., differences of Jacobi momenta:

$$f_\Lambda^{\text{local}} = f_\Lambda(\mathbf{p}' - \mathbf{p}, \mathbf{q}' - \mathbf{q}) = f_\Lambda(\tilde{\mathbf{p}}, \tilde{\mathbf{q}}), \quad (82)$$

while in coordinate space the regulator function is only a function of the relative distances  $\mathbf{r}' = \mathbf{r}$  and  $\mathbf{s} = \mathbf{s}'$ :

$$f_R^{\text{local}} = f_R(\mathbf{r}, \mathbf{s}). \quad (83)$$

Nonlocal regulator functions can depend on more general combinations of Jacobi coordinates. In practice also combinations of local and nonlocal regulator functions within one scheme have been applied to the short- and long-range contributions to 3N interactions (see Table 4).

Table 4 summarizes different regularization schemes for 3N interactions that have been developed and applied in recent years. Ideally, a chosen regularization prescription should be used consistently for NN and 3N interactions. In the following we discuss the different regularization schemes and their practical implementation in the partial-wave momentum basis defined in Section 3.3 in more detail.

### 3.7.1. Nonlocal momentum-space regularization

Nonlocal momentum regularizations were originally applied to the first generation of “high-precision” NN interactions developed within chiral EFT [29, 199, 257]. For these interactions the following regulator form was used:

$$V_{\text{NN}}^{\text{reg}} = f_\Lambda(\mathbf{p}') V_{\text{NN}}^{\text{reg}}(\mathbf{p}, \mathbf{p}') f_\Lambda(\mathbf{p}), \quad (84)$$

with

$$f_\Lambda(\mathbf{p}) = \exp[-(\mathbf{p}^2/\Lambda^2)^n] = f_\Lambda(p). \quad (85)$$

Here  $\Lambda$  is some chosen momentum cutoff scale,  $n$  some exponent and  $p = |\mathbf{p}|$ . This prescription is a natural choice in the sense that the square of the Jacobi momentum is proportional to the relative kinetic energy of the initial and final states and hence serves as a natural measure to characterize the high-energy part of the Hilbert space. In Ref. [170] a natural extension of this regulator to three-body interactions was proposed. From Eq. (10) it follows that the three-body intrinsic kinetic energy in the center-of-mass reference frame

for  $m = m_1 = m_2 = m_3$  takes the following form:

$$T_{\text{rel}} = \frac{1}{2m} \left[ \sum_{i=1}^3 \mathbf{k}_i^2 - \frac{1}{3} \left( \sum_{i=1}^3 \mathbf{k}_i \right)^2 \right] = \frac{1}{6m} \left[ (\mathbf{k}_2 - \mathbf{k}_1)^2 + (\mathbf{k}_3 - \mathbf{k}_2)^2 - (\mathbf{k}_1 - \mathbf{k}_3)^2 \right] = \frac{1}{m} \left[ \mathbf{p}_{\{ab\}}^2 + \frac{3}{4} \mathbf{q}_{\{ab\}}^2 \right], \quad (86)$$

for any basis representation  $\{ab\}$ . This leads to the following natural extension of Eq. (85) to the three-body case:

$$f_{\Lambda}(\mathbf{p}, \mathbf{q}) = \exp[-((\mathbf{p}^2 + \frac{3}{4}\mathbf{q}^2)/\Lambda^2)^n] = f_{\Lambda}(p, q), \quad (87)$$

with  $p = |\mathbf{p}|$  and  $q = |\mathbf{q}|$ . In this case, the regularization of the initial and final states again factorizes and the regularized interaction is given by:

$$V_{3N}^{\text{reg}} = f_{\Lambda}(p', q') V_{3N} f_{\Lambda}(p, q). \quad (88)$$

The choice in Eq. (87) is particularly convenient since this nonlocal regulator only depends on the absolute values of the Jacobi momenta. Consequently, the regulator does not affect the partial-wave decomposition and the regularized matrix elements can be obtained by a trivial multiplicative factor to the unregularized partial-wave matrix elements shown in Eq. (55):

$${}_{\{ab\}} \langle p' q' \alpha' | V_{3N}^{(i), \text{reg}} | p q \alpha \rangle_{\{ab\}} = f_{\Lambda}(p', q') {}_{\{ab\}} \langle p' q' \alpha' | V_{3N}^{(i)} | p q \alpha \rangle_{\{ab\}} f_{\Lambda}(p, q). \quad (89)$$

Since the expression for the relative kinetic energy Eq. (86) is identical in all basis representations  $\{ab\}$ , i.e., invariant under application of the permutation operators  $P_{123}$  and  $P_{132}$ , we can also equivalently apply the regulator functions to the antisymmetrized interaction defined in Eq. (61):

$$\langle p' q' \alpha' | V_{3N}^{\text{as, reg}} | p q \alpha \rangle = f_{\Lambda}(p', q') \langle p' q' \alpha' | V_{3N}^{\text{as}} | p q \alpha \rangle f_{\Lambda}(p, q), \quad (90)$$

i.e., the regularization commutes with the antisymmetrization operation for this type of regulator.

Applying the regulator on the operator level like in Eq. (88) or at the level of the partial-wave matrix elements as shown in Eqs. (89) and (90) all lead to identical results. This is a particular property of the specific regulator choice Eq. (87). This property has the great practical advantage that it is sufficient to explicitly calculate only unregularized matrix elements. The regulator functions, i.e., the values for the exponent  $n$  and the cutoff scale  $\Lambda$  in Eq. (87), can be specified at a later stage after the partial wave decomposition in a very flexible and convenient way.

### 3.7.2. Local momentum-space regularization

In contrast to the nonlocal regulator discussed in the previous section local regulators depend by definition on momentum transfers and hence also on the angles between Jacobi momenta. As a consequence, local regulators naturally couple different partial waves in the basis defined in Eq. (41), which makes it necessary to incorporate the regulators before the partial-wave decomposition. We start from a particular choice for the Faddeev component  $i$  and incorporate the regulator functions:

$$V_{3N}^{(i), \text{reg}} = V_{3N}^{(i)} \prod_{j=1}^{N_j} f_{\Lambda}(\mathbf{Q}_j), \quad (91)$$

where  $\mathbf{Q}_j = \mathbf{k}'_j - \mathbf{k}_j$  are the momentum transfers and the index  $j$  runs over one or multiple momentum transfer variables of a given 3N interaction. Typically, exponential forms were chosen for  $f_{\Lambda}$ , similarly to the nonlocal regulator Eq. (87). For example, in Ref. [224] the form  $f_{\Lambda}(\mathbf{Q}) = \exp[-(\mathbf{Q}^2/\Lambda^2)^2]$  and  $N_j = 2$  was used, and in Ref. [241] the regulator function  $f_{\Lambda}(\mathbf{Q}) = \exp[-(\mathbf{Q}^2 + m_{\pi}^2)/\Lambda^2]$  was applied to each long-range pion exchange interaction of a given diagram, where  $\mathbf{Q}_j$  is the momentum carried by the pion.

The regularized interaction defined in Eq. (91) can be straightforwardly decomposed in a partial-wave representation using the algorithm discussed in Section 3.3 since the regulator preserves the local nature of the interaction. Note, however, that the regularization in Eq. (91) does in general not commute with the

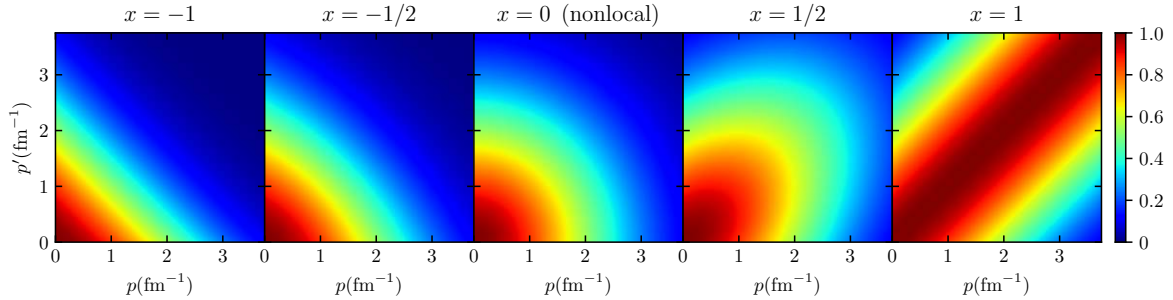


Figure 24: Phase-space weights of the local regulator function  $f_{\Lambda}^{\text{local}}(\mathbf{p}, \mathbf{p}') = \exp[-(\mathbf{p}' - \mathbf{p})^2/\Lambda^2] = \exp[-(p'^2 + p^2 - 2p'px)/\Lambda^2]$  with  $x = \cos \theta_{\mathbf{p}\mathbf{p}'}$  and  $\Lambda = 500$  MeV. The different panels show the phase-space contributions for different angles  $x$ . The case  $x = 0$ , i.e.,  $\theta_{\mathbf{p}\mathbf{p}'} = \frac{\pi}{2}$  (central panel), corresponds to the nonlocal regulator.

antisymmetrization operation, in contrast to the nonlocal regulator in Eq. (87). This leads to ambiguities regarding the choice of operators for the three-body interactions, which are absent for unregularized interactions or nonlocally regularized interactions using a function of the form Eq. (87). Consider as an example a pure contact interaction, which can be parametrized in terms of different spin-isospin operators:

$$\begin{aligned}
 V_{3N}^{\text{contact}} &= \sum_{i \neq j \neq k} \left[ \beta_1 + \beta_2 \boldsymbol{\sigma}_i \cdot \boldsymbol{\sigma}_j + \beta_3 \boldsymbol{\tau}_i \cdot \boldsymbol{\tau}_j + \beta_4 \boldsymbol{\sigma}_i \cdot \boldsymbol{\sigma}_j \boldsymbol{\tau}_i \cdot \boldsymbol{\tau}_j + \beta_5 \boldsymbol{\sigma}_i \cdot \boldsymbol{\sigma}_j \boldsymbol{\tau}_j \cdot \boldsymbol{\tau}_k + \beta_6 \left( (\boldsymbol{\sigma}_i \times \boldsymbol{\sigma}_j) \cdot \boldsymbol{\sigma}_k \right) \left( (\boldsymbol{\tau}_i \times \boldsymbol{\tau}_j) \cdot \boldsymbol{\tau}_k \right) \right] \\
 &= V_{3N}^{\beta_1} + V_{3N}^{\beta_2} + V_{3N}^{\beta_3} + V_{3N}^{\beta_4} + V_{3N}^{\beta_5} + V_{3N}^{\beta_6}.
 \end{aligned} \tag{92}$$

Antisymmetrization leads to the following relations:

$$\begin{aligned}
 \mathcal{A}_{123} V_{3N}^{\beta_2} &= \mathcal{A}_{123} V_{3N}^{\beta_3} = -\mathcal{A}_{123} V_{3N}^{\beta_1} \\
 \mathcal{A}_{123} V_{3N}^{\beta_4} &= -\mathcal{A}_{123} V_{3N}^{\beta_5} = -3 \mathcal{A}_{123} V_{3N}^{\beta_1} \\
 \mathcal{A}_{123} V_{3N}^{\beta_6} &= -12 \mathcal{A}_{123} V_{3N}^{\beta_1}.
 \end{aligned} \tag{93}$$

These relations imply that all operators are linearly dependent and it is hence sufficient to choose just one of the operators  $V_{3N}^{\beta_i}$  (see also discussion in Ref. [170]). By convention, the interaction  $V_{3N}^{\beta_3}$  is usually chosen to define the low-energy constant  $c_E$  (see Eq. (56)). However, for local regulators this symmetry, usually referred to as Fierz rearrangement freedom or Fierz symmetry, is generally not fulfilled anymore. This is in particular the case when the local regulator is not applied in a symmetric way to all momentum transfers in 3N interactions. In Ref. [258] the effects of this ambiguity in NN interactions was studied in few-body systems and neutron matter, whereas in Ref. [224] the effect of different coordinate choices in the local regulators for the 3N interactions was studied based on ground-state energies of  ${}^3\text{H}$ . Ref. [216] studied the impact of this ambiguity for local 3N interactions for nuclear matter. Generally, these ambiguities at a given order should be absorbable by operators at higher orders in the chiral expansion, but more detailed studies are needed to demonstrate this explicitly.

The local and nonlocal regulators discussed above can differ quite substantially, depending on the kinematical regime. We illustrate this in Figure 24 by showing the phase space contributions of a local regulator of form  $f_{\Lambda}^{\text{local}}(\mathbf{p}, \mathbf{p}') = \exp[-(\mathbf{p}' - \mathbf{p})^2/\Lambda^2] = f_{\Lambda}^{\text{local}}(p, p', \cos \theta_{\mathbf{p}\mathbf{p}'})$  for different angles  $\theta_{\mathbf{p}\mathbf{p}'}$  and for the cutoff scale  $\Lambda = 500$  MeV. Obviously, for  $\cos \theta_{\mathbf{p}\mathbf{p}'} = 0$ , i.e.,  $\theta_{\mathbf{p}\mathbf{p}'} = \pi/2$ , the local regulator agrees by construction with the nonlocal regulator defined in Eq. (85) with  $n = 1$ . Furthermore, in the kinematical regime with small  $x$  both regulators agree reasonably well. However, when both Jacobi momenta,  $\mathbf{p}$  and  $\mathbf{p}'$ , are getting close to being aligned or antialigned with each other, the regulators show significant differences. In particular for the case  $x = 1$ , i.e.,  $\mathbf{p} = \mathbf{p}'$  the local regulator exhibits a band diagonal structure and does not suppress contributions at large Jacobi momenta at all.

Besides such technical differences between local and nonlocal regulators, there are also conceptual dif-

ferences. In Ref. [204] it is argued that nonlocal cutoff functions of the form Eq. (85) lead to distortions of the analytic structure of the partial-wave scattering amplitude around the threshold since it affects the discontinuity across the left-hand cuts (see also discussion in Refs. [259, 260]). Local regulators, in contrast, can remove the short-range parts of the pion-exchange interactions and hence make an additional spectral function regularization obsolete. In addition, it is argued that locally regularized interactions lead to a better description of scattering phase shifts even at relatively high energies due to reduced finite-cutoff artifacts (see Refs. [204, 205] for details).

### 3.7.3. Semilocal momentum-space regularization

The semilocal regularization scheme first presented in Refs. [205, 241] combines features of the nonlocal and local regularizations discussed in the previous two sections. Specifically, in the semilocal regularization approach the long-range pion-exchange contributions are regularized via local regulator functions, whereas the short-range point couplings are regularized nonlocally (see also Ref. [261] for details). This has the practical advantage that the regularization of the short-range parts does not induce a coupling of partial waves and hence the low-energy couplings in the NN interaction can be fixed independently in different partial waves, e.g. by fitting them to extracted scattering phase shifts in the corresponding channel.

We illustrate the semilocal regularization by applying it to the 3N contributions at N<sup>2</sup>LO in chiral EFT for the interaction terms shown in Figure 25. The regularization of the purely long-range leading-order two-pion exchange contributions is formally identical to the local regularization of Ref. [224]. In diagram (a) of Figure 25 the pions carry the momenta  $\mathbf{Q}_1$  and  $\mathbf{Q}_3$ . Hence the regularized interaction is given by

$$V_{3N}^{c_i, \text{reg}}(\mathbf{Q}_1, \mathbf{Q}_3) = V_{3N}^{c_i}(\mathbf{Q}_1, \mathbf{Q}_3) f_{\Lambda}^{\text{long}}(\mathbf{Q}_1) f_{\Lambda}^{\text{long}}(\mathbf{Q}_3). \quad (94)$$

In Ref. [241] the particular form  $f_{\Lambda}^{\text{long}}(\mathbf{Q}) = \exp[-(\mathbf{Q}^2 + m_{\pi}^2)/\Lambda^2]$  was chosen (see also Table 4).

The intermediate-range diagram (b) in Figure 25, proportional to the coupling  $c_D$ , consists of a long-range pion-exchange part and short-range coupling. Here, the pion exchange is regularized via the local long-range regulator  $f_{\Lambda}^{\text{long}}$  (see above) and the short-range two-point coupling via a nonlocal regulator of the form  $f_{\Lambda}^{\text{short}} = \exp[-(\mathbf{p}_{\delta}^2/\Lambda^2)]$ , where the momenta  $\mathbf{p}_{\delta}$  ( $\mathbf{p}'_{\delta}$ ) are the initial (final) state relative momenta of the two particles interacting via the point coupling. For the practical calculation we choose a particular basis  $\{ab\}$ . In the present case it is most convenient to choose basis {23} since in this case the momentum  $\mathbf{p}_{\delta}$  is given by (see Table 2)

$$\mathbf{p}_{\delta} = \frac{\mathbf{k}_2 - \mathbf{k}_3}{2} = \mathbf{p}_{\{23\}}, \quad (95)$$

i.e., the argument of the regulator functions is independent of any angles. On the other hand, choosing another basis representation, e.g. {12}, leads to

$$\mathbf{p}_{\delta} = \frac{\mathbf{k}_2 - \mathbf{k}_3}{2} = -\mathbf{p}_{\{12\}} - \frac{3}{4}\mathbf{q}_{\{12\}}, \quad (96)$$

and the application of the nonlocal regulators obviously becomes much more intricate due to the dependence on the angle between the vectors  $\mathbf{p}_{\{12\}}$  and  $\mathbf{q}_{\{12\}}$ . Of course, both choices eventually lead to identical results for the antisymmetrized interaction.

That means in total we obtain for the regularized interaction:

$$V_{3N}^{c_D, \text{reg}}(\mathbf{Q}_1, \mathbf{p}_{\delta}, \mathbf{p}'_{\delta}) = V_{3N}^{c_D}(\mathbf{Q}_1) f_{\Lambda}^{\text{long}}(\mathbf{Q}_1) f_{\Lambda}^{\text{short}}(\mathbf{p}_{\delta}) f_{\Lambda}^{\text{short}}(\mathbf{p}'_{\delta}). \quad (97)$$

In Ref. [241] the regulator form was chosen to be  $f_{\Lambda}^{\text{short}}(\mathbf{p}) = \exp[-(\mathbf{p}^2/\Lambda^2)]$ .

The regularization of the purely short-range interaction, proportional to the coupling  $c_E$  (diagram (c) in Figure 25), reduces to the nonlocal regularization. Here all three particles participate in the short-range interaction, i.e.,

$$\mathbf{p}_{\delta}^2 = \frac{1}{6}[(\mathbf{k}_2 - \mathbf{k}_1)^2 + (\mathbf{k}_3 - \mathbf{k}_2)^2 + (\mathbf{k}_1 - \mathbf{k}_3)^2] = \mathbf{p}^2 + \frac{3}{4}\mathbf{q}^2, \quad (98)$$

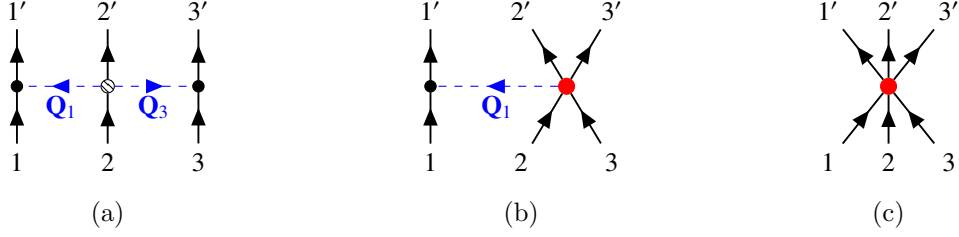


Figure 25: Semilocal momentum-space regularization of the 3N interactions at N<sup>2</sup>LO. The pion exchange contributions (blue) to all interactions are regularized locally via the long-range regulator  $f_R^{\text{long}}(\mathbf{Q}_i)$ , whereas the short-range parts (red) are regularized nonlocally by the regulator  $f_\Lambda^{\text{short}}(\mathbf{p}_\delta^2)$ . Here, the momentum  $\mathbf{p}_\delta$  denotes the momentum scale related to the relative kinetic energy in the initial and final states of those particles that interact via the short-range coupling, i.e., specifically, for diagram (b)  $\mathbf{p}_\delta^2 = ((\mathbf{k}_2 - \mathbf{k}_3)/2)^2$  and for diagram (c)  $\mathbf{p}_\delta^2 = \frac{1}{6}[(\mathbf{k}_2 - \mathbf{k}_1)^2 + (\mathbf{k}_3 - \mathbf{k}_2)^2 + (\mathbf{k}_1 - \mathbf{k}_3)^2] = \mathbf{p}^2 + \frac{3}{4}\mathbf{q}^2$ .

and for the regularized interaction we obtain:

$$V_{3N}^{cE,\text{reg}}(\mathbf{p}_\delta, \mathbf{p}'_\delta) = f_\Lambda^{\text{short}}(\mathbf{p}_\delta) V_{3N}^{cE} f_\Lambda^{\text{short}}(\mathbf{p}'_\delta). \quad (99)$$

In Ref. [241] a Gaussian form was chosen, i.e.:

$$f_\Lambda^{\text{short}}(\mathbf{p}_\delta) = \exp[-(\mathbf{p}^2 + \frac{3}{4}\mathbf{q}^2)/\Lambda^2] = f_\Lambda^{\text{short}}(p, q). \quad (100)$$

Since the argument does not depend on any angles between Jacobi momenta this regularization can directly be applied to the partial-wave matrix elements:

$${}_{(ab)}\langle p' q' \alpha' | V_{3N}^{cE,\text{reg}} | p q \alpha \rangle_{(ab)} = f_\Lambda^{\text{short}}(p', q') {}_{(ab)}\langle p' q' \alpha' | V_{3N}^{cE} | p q \alpha \rangle_{(ab)} f_\Lambda^{\text{short}}(p, q). \quad (101)$$

The regularization of the 3N contributions at N<sup>3</sup>LO that involve loop structures is more involved since the regulators can also be applied to internal momenta.

### 3.7.4. Local coordinate-space regularization

Local interactions formulated in coordinate space play a key role for Quantum Monte Carlo methods [47]. In recent years there has been significant progress toward incorporating chiral EFT interactions in these frameworks (see, e.g., Refs. [50, 51, 54, 146, 262]). Here we discuss strategies that allow to apply regulator functions defined in coordinate space, i.e.,  $f_R = f_R(\mathbf{r}, \mathbf{s}, \mathbf{r}', \mathbf{s}')$ , to matrix elements of 3N interactions. Generally there are two options to calculate regularized matrix elements  $\langle p' q' \alpha' | V_{3N}^{(i),\text{reg}} | p q \alpha \rangle$ :

1. Calculation of the Fourier transform of the regulator function  $f_R$  to momentum space and application of the regulator to the unregularized momentum-space partial-wave matrix elements of Eq. (54).
2. Computation of the coordinate-space partial-wave matrix elements of the regularized 3N interaction

$$V_{3N}^{\text{reg}} = V_{3N}(\mathbf{r}, \mathbf{s}, \mathbf{r}', \mathbf{s}') f_R(\mathbf{r}, \mathbf{s}, \mathbf{r}', \mathbf{s}'), \quad (102)$$

and Fourier transform of the result to momentum space. The Fourier transform of the chiral EFT 3N interactions at N<sup>2</sup>LO can be performed to a large extent analytically and can be expressed in terms of a few elementary functions which can be computed numerically in a straightforward way (see, e.g., appendix of Ref. [263]).

The second option has the advantage that the application of the regulator function is just a simple multiplicative operation. On the other hand, the expressions for various 3N contributions have so far only been derived in momentum space (see Ref. [183, 184]). In this sense the first option is more general and we will hence focus on this method in the following.

We consider a local interaction regularized by a local function in coordinate space. For the sake of simple notation we parametrize all quantities as a function of the interparticle distances  $\mathbf{r}_{ij} = \mathbf{x}_i - \mathbf{x}_j$  or the momentum transfers  $\mathbf{Q}_i = \mathbf{k}'_i - \mathbf{k}_i$ . In coordinate space the regularized Faddeev component is given by

$$V_{3N}^{(i),\text{reg}} = V_{3N}^{(i)}(\mathbf{r}_{12}, \mathbf{r}_{23})f_R(\mathbf{r}_{12}, \mathbf{r}_{23}). \quad (103)$$

Here we arbitrarily selected the two variables  $\mathbf{r}_{12}$  and  $\mathbf{r}_{23} = -\mathbf{r}_{32}$ . Since there are only two independent relative distance variables ( $\mathbf{r}_{12} + \mathbf{r}_{23} + \mathbf{r}_{31} = 0$ ) we could have equally well chosen any other two independent interparticle distance variables. The momentum-space representation of the regulator is then given by

$$\tilde{f}_R(\mathbf{Q}_1, \mathbf{Q}_3) = \int d\mathbf{r}_{12}d\mathbf{r}_{23} e^{-i\mathbf{Q}_1 \cdot \mathbf{r}_{12}} e^{-i\mathbf{Q}_3 \cdot \mathbf{r}_{23}} f_R(\mathbf{r}_{12}, \mathbf{r}_{23}), \quad (104)$$

or equivalently the coordinate-space representation by

$$f_R(\mathbf{r}_{12}, \mathbf{r}_{23}) = \int \frac{d\mathbf{Q}_1}{(2\pi)^3} \frac{d\mathbf{Q}_3}{(2\pi)^3} e^{i\mathbf{Q}_1 \cdot \mathbf{r}_{12}} e^{i\mathbf{Q}_3 \cdot \mathbf{r}_{23}} \tilde{f}_R(\mathbf{Q}_1, \mathbf{Q}_3). \quad (105)$$

The role of the regulator function  $f_R(\mathbf{r}_{12}, \mathbf{r}_{23})$  is to suppress contributions to the interaction at small interparticle distances, while leaving the interaction unchanged in the low-energy regime at large distances. Consequently the Fourier transform cannot be directly computed in the form given in Eq. (104) since the integration kernel is not suppressed at large interparticle distances. Instead we first need to subtract the identity:

$$\tilde{f}_R(\mathbf{Q}_1, \mathbf{Q}_3) = \int d\mathbf{r}_{12}d\mathbf{r}_{23} e^{-i\mathbf{Q}_1 \cdot \mathbf{r}_{12}} e^{-i\mathbf{Q}_3 \cdot \mathbf{r}_{23}} [f_R(\mathbf{r}_{12}, \mathbf{r}_{23}) - 1] + (2\pi)^6 \delta(\mathbf{Q}_1) \delta(\mathbf{Q}_3) = \tilde{f}_{R,\text{subtr}}(\mathbf{Q}_1, \mathbf{Q}_3) + (2\pi)^6 \delta(\mathbf{Q}_1) \delta(\mathbf{Q}_3). \quad (106)$$

Inserting the Fourier representation Eq. (104) and its inverse for the regulator and the interaction we obtain:

$$\begin{aligned} V_{3N}^{(i),\text{reg}}(\mathbf{Q}_1, \mathbf{Q}_3) &= \int d\mathbf{r}_{12}d\mathbf{r}_{23} e^{-i\mathbf{Q}_1 \cdot \mathbf{r}_{12}} e^{-i\mathbf{Q}_3 \cdot \mathbf{r}_{23}} V_{3N}^{(i)}(\mathbf{r}_{12}, \mathbf{r}_{23}) f_R(\mathbf{r}_{12}, \mathbf{r}_{23}) \\ &= \int \frac{d\tilde{\mathbf{Q}}_1}{(2\pi)^3} \frac{d\tilde{\mathbf{Q}}_3}{(2\pi)^3} V_{3N}^{(i)}(\tilde{\mathbf{Q}}_1, \tilde{\mathbf{Q}}_3) \tilde{f}_R(\mathbf{Q}_1 - \tilde{\mathbf{Q}}_1, \mathbf{Q}_3 - \tilde{\mathbf{Q}}_3) \end{aligned} \quad (107a)$$

$$= V_{3N}^{(i)}(\mathbf{Q}_1, \mathbf{Q}_3) + \int \frac{d\tilde{\mathbf{Q}}_1}{(2\pi)^3} \frac{d\tilde{\mathbf{Q}}_3}{(2\pi)^3} V_{3N}^{(i)}(\tilde{\mathbf{Q}}_1, \tilde{\mathbf{Q}}_3) \tilde{f}_{R,\text{subtr}}(\mathbf{Q}_1 - \tilde{\mathbf{Q}}_1, \mathbf{Q}_3 - \tilde{\mathbf{Q}}_3), \quad (107b)$$

where we inserted the Fourier representation of the regulator and the interaction (Eq. (105)) in the second step. The key point of this result is the fact that the regularized interaction is given by a sum of two terms. While the first term is just the unregularized interaction, the second term is a well-defined integral, which in general needs to be computed numerically. This step involves some intricate numerical problems that are most obvious in the regime of large momenta. Since the regulator cuts off high-energy physics at small distances the regularized interaction in momentum space should be suppressed at large momentum transfers. However, note that in general the unregularized interaction  $V_{3N}(\mathbf{Q}_1, \mathbf{Q}_3)$  is not suppressed at large momenta, which means that also the second term in Eq. (107b) cannot be suppressed in this kinematical region. Eventually, a very delicate cancellation between these two terms is required in order to obtain a regularized interaction that has no contributions at large momenta. In fact, the direct implementation of Eq. (107b) can lead to significant numerical noise contaminations, in particular at large momenta.

However, there is a more clever way to apply coordinate-space local regulators. The basic idea of this

method is to insert an identity in the definition Eq. (103) of the following form<sup>6</sup>

$$V_{3N}^{(i),\text{reg}} = V_{3N}^{(i)}(\mathbf{r}_{12}, \mathbf{r}_{23}) \frac{Q(\mathbf{r}_{12}^2)Q(\mathbf{r}_{23}^2)}{Q(\mathbf{r}_{12}^2)Q(\mathbf{r}_{23}^2)} f_R(\mathbf{r}_{12}, \mathbf{r}_{23}), \quad (108)$$

where  $Q(r^2)$  is at this point an arbitrary function that depends on the square of the interparticle distance, which we will specify further below. We then define a pre-regularized interaction in momentum space by inserting the functions  $Q$  in the *numerator* (compare Eq. (104)):

$$V_{3N}^{(i),\text{prereg}}(\mathbf{Q}_1, \mathbf{Q}_3) = \int d\mathbf{r}_{12} d\mathbf{r}_{23} e^{-i\mathbf{Q}_1 \cdot \mathbf{r}_{12}} e^{-i\mathbf{Q}_3 \cdot \mathbf{r}_{23}} Q(\mathbf{r}_{12}^2) Q(\mathbf{r}_{23}^2) V_{3N}^{(i)}(\mathbf{r}_{12}, \mathbf{r}_{23}) = Q(-\Delta_{\mathbf{Q}_1}) Q(-\Delta_{\mathbf{Q}_3}) V_{3N}^{(i)}(\mathbf{Q}_1, \mathbf{Q}_3), \quad (109)$$

where  $\Delta_{\mathbf{Q}}$  denotes the Laplacian with respect to vector  $\mathbf{Q}$ . Accordingly, we define a pre-regularized regulator in momentum space by incorporating here the functions  $Q$  in the *denominator*:

$$\tilde{f}_R^{\text{prereg}}(\mathbf{Q}_1, \mathbf{Q}_3) = \int d\mathbf{r}_{12} d\mathbf{r}_{23} e^{-i\mathbf{Q}_1 \cdot \mathbf{r}_{12}} e^{-i\mathbf{Q}_3 \cdot \mathbf{r}_{23}} \frac{f_R(\mathbf{r}_{12}, \mathbf{r}_{23})}{Q(\mathbf{r}_{12}^2)Q(\mathbf{r}_{23}^2)}. \quad (110)$$

Choosing the function  $Q(\mathbf{r}^2)$  in a suitable way allows to render the integral Eq. (110) finite and well defined, without the need to subtract the identity like in the original integral in Eq. (104). For example, the choices  $Q(\mathbf{r}^2) = r^2$  or  $Q(\mathbf{r}^2) = r^4$  have the desired properties. In addition, in cases where the original regulator function factorizes and only depends on the absolute values of the interparticle distances, i.e.,  $f_R(\mathbf{r}_{12}, \mathbf{r}_{23}) = f_R(|\mathbf{r}_{12}|)f_R(|\mathbf{r}_{23}|)$ , then also the pre-regularized regulator factorizes and can be calculated in a particularly simple way. For example, for  $Q(r^2) = r^4$  we obtain:

$$\tilde{f}_R^{\text{prereg}}(\mathbf{Q}) = \int d\mathbf{r} e^{-i\mathbf{Q} \cdot \mathbf{r}} \frac{1}{r^4} f_R(r) = 4\pi \int_0^\infty \frac{dr}{r^2} f_R(r) j_0(Qr), \quad (111)$$

where  $j_l$  are the spherical Bessel functions. However, also for non-factorizable regulator functions the computation of the Fourier transform poses no serious problems. Finally, the regularized interaction can then be obtained by

$$V_{3N}^{(i),\text{reg}}(\mathbf{Q}_1, \mathbf{Q}_3) = \int \frac{d\bar{\mathbf{Q}}_1}{(2\pi)^6} \frac{d\bar{\mathbf{Q}}_3}{(2\pi)^6} V_{3N}^{(i),\text{prereg}}(\bar{\mathbf{Q}}_1, \bar{\mathbf{Q}}_3) \tilde{f}_R^{\text{prereg}}(\mathbf{Q}_1 - \bar{\mathbf{Q}}_1, \mathbf{Q}_3 - \bar{\mathbf{Q}}_3). \quad (112)$$

In contrast to Eq. (107a) this integral can be directly evaluated and no subtractions with delicate cancellations are required for the regularization of the interaction. By choosing a basis representation  $\{ab\}$  it is now straightforward to express Eq. (112) in terms of Jacobi momenta:

$${}_{\{ab\}} \langle \mathbf{p}' \mathbf{q}' | V_{3N}^{(i),\text{reg}} | \mathbf{p} \mathbf{q} \rangle_{\{ab\}} = \int \frac{d\mathbf{p}''}{(2\pi)^6} \frac{d\mathbf{q}''}{(2\pi)^6} {}_{\{ab\}} \langle \mathbf{p}' \mathbf{q}' | V_{3N}^{(i),\text{prereg}} | \mathbf{p}'' \mathbf{q}'' \rangle_{\{ab\}} {}_{\{ab\}} \langle \mathbf{p}'' \mathbf{q}'' | \tilde{f}_R^{\text{prereg}} | \mathbf{p} \mathbf{q} \rangle_{\{ab\}}, \quad (113)$$

and after including spin and isospin degrees of freedom we obtain the following results in the momentum partial-wave representation:

$${}_{\{ab\}} \langle p' q' \alpha' | V_{3N}^{(i),\text{reg}} | p q \alpha \rangle_{\{ab\}} = \int dp'' p''^2 dq'' q''^2 \sum_{\alpha''} {}_{\{ab\}} \langle p' q' \alpha' | V_{3N}^{(i),\text{prereg}} | p'' q'' \alpha'' \rangle_{\{ab\}} {}_{\{ab\}} \langle p'' q'' \alpha'' | \tilde{f}_R^{\text{prereg}} | p q \alpha \rangle_{\{ab\}}. \quad (114)$$

The key steps for the application of Eq. (114) consist in the computation of the pre-regularized interaction as defined in Eq. (109) and the momentum-space partial-wave decomposition of the interaction  $V_{3N}^{\text{prereg}}$  and the regulator  $\tilde{f}_R^{\text{prereg}}$ . We will discuss these steps in more detail in the next section, where we apply the

<sup>6</sup>This method was originally developed by Hermann Krebs.



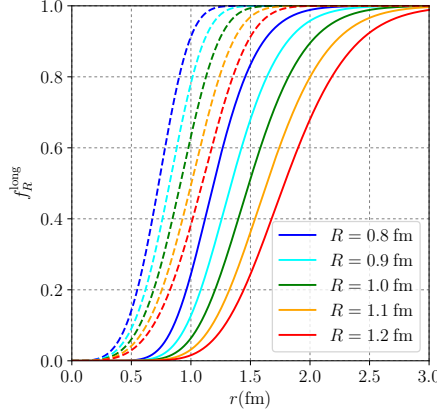


Figure 26: Coordinate-space regulator functions of the “semilocal CS” regularization [189, 204] (solid lines, see Eq. (115)) compared to those of the “local CS” regularization [50, 51] (dashed lines) for the coordinate-space regularization scales  $R = 0.8 - 1.2$  fm. Note the different effective form and effective cutoff scales of these two sets of regulators even when using formally the same regularization scale  $R$ .

framework presented here to semilocally regularized 3N interactions, corresponding to the NN interactions presented in Refs. [189, 204] and later extended by contributions from 3N interactions [33].

### 3.7.5. Semilocal coordinate-space regularization

The underlying idea of the semilocal coordinate-space regularization is the same as for the semilocal momentum-space regularization (see Section 3.7.3), with the only difference being that the local regulator functions for the long-range parts of the interactions are now given in coordinate space. Specifically, in Ref. [33] the following form was chosen:

$$f_R^{\text{long}}(r) = (1 - \exp[-r^2/R^2])^6. \quad (115)$$

Here  $R$  is a coordinate cutoff scale which is typically chosen to be in the range  $R = 0.8 - 1.2$  fm. As shown in Figure 26, this regulator function is virtually vanishing at  $r = 0$ , which implies that all short-range coupling contributions are projected out by the local regulator and only long range contributions from the pion exchange terms remain. However, the figure also demonstrates that this regulator function differs quite significantly from the regulators chosen in Refs. [50, 51] for the same values of coordinate-space cutoff scales  $R$  (see also Ref. [264]). This emphasizes that some care has to be taken when comparing interactions with the same regularization cutoff scales but different forms of the regulators.

For interaction contributions with multiple pion-exchange interactions each contribution is regularized via the regulator  $f_R^{\text{long}}(\mathbf{r})$ . The short-range parts of the interaction are regularized in the same way as for the semilocal momentum-space regularization by nonlocal regulators in momentum space. In Ref. [33] a Gaussian form was chosen:

$$f_\Lambda^{\text{short}}(\mathbf{p}) = \exp[-p^2/\Lambda^2]. \quad (116)$$

We again illustrate the regularization scheme explicitly using the 3N interaction contributions at N<sup>2</sup>LO (see Figure 27) as discussed in Section 2.1. We start with the long-range  $2\pi$  exchange topologies, given in Eqs. (1) and (2). For the diagram shown in panel (a) of Figure 27 we need to apply two long-range regulators:

$$V_{3N}^{c_i, \text{reg}}(\mathbf{r}_{12}, \mathbf{r}_{32}) = V_{3N}^{c_i}(\mathbf{r}_{12}, \mathbf{r}_{32}) f_R^{\text{long}}(\mathbf{r}_{12}) f_R^{\text{long}}(\mathbf{r}_{32}). \quad (117)$$

For the practical calculation of the momentum-space elements of the regularized interaction  $\langle p'q'\alpha' | V_{3N}^{2\pi, \text{reg}} | pq\alpha \rangle$  we follow the strategy discussed in Section 3.7.4. As a first step we need to calculate the pre-regularized interactions:

$$V_{3N}^{c_i, \text{prereg}}(\mathbf{Q}_1, \mathbf{Q}_3) = \mathcal{Q}(-\Delta_{\mathbf{Q}_1}) \mathcal{Q}(-\Delta_{\mathbf{Q}_3}) V_{3N}^{c_i}(\mathbf{Q}_1, \mathbf{Q}_3). \quad (118)$$

Starting from the unregularized expressions Eqs. (1) and (2) these can be calculated in a straightforward way. To be explicit we give the results for the 3N contributions at N<sup>2</sup>LO for  $Q(-\Delta_{\mathbf{Q}}) = -\Delta_{\mathbf{Q}}$ .

$$\begin{aligned}
V_{3N}^{c1,\text{prereg}}(\mathbf{Q}_1, \mathbf{Q}_3) &= -\frac{2c_1 g_A^2 m_\pi^2}{f_\pi^4} \boldsymbol{\tau}_1 \cdot \boldsymbol{\tau}_3 \frac{(5m_\pi^2 + \mathbf{Q}_1^2)(5m_\pi^2 + \mathbf{Q}_3^2) \boldsymbol{\sigma}_1 \cdot \mathbf{Q}_1 \boldsymbol{\sigma}_3 \cdot \mathbf{Q}_3}{(\mathbf{Q}_1^2 + m_\pi^2)^3 (\mathbf{Q}_3^2 + m_\pi^2)^3}, \\
V_{3N}^{c3,\text{prereg}}(\mathbf{Q}_1, \mathbf{Q}_3) &= \frac{c_3 g_A^2}{f_\pi^4} \boldsymbol{\tau}_1 \cdot \boldsymbol{\tau}_3 \left[ \frac{\boldsymbol{\sigma}_1 \cdot \boldsymbol{\sigma}_3}{(\mathbf{Q}_1^2 + m_\pi^2)(\mathbf{Q}_3^2 + m_\pi^2)} - \frac{(3\mathbf{Q}_1^2 + 7m_\pi^2)\boldsymbol{\sigma}_1 \cdot \mathbf{Q}_1 \boldsymbol{\sigma}_3 \cdot \mathbf{Q}_1}{(\mathbf{Q}_1^2 + m_\pi^2)^3 (\mathbf{Q}_3^2 + m_\pi^2)} \right. \\
&\quad \left. - \frac{(3\mathbf{Q}_3^2 + 7m_\pi^2)\boldsymbol{\sigma}_1 \cdot \mathbf{Q}_3 \boldsymbol{\sigma}_3 \cdot \mathbf{Q}_3}{(\mathbf{Q}_1^2 + m_\pi^2)(\mathbf{Q}_3^2 + m_\pi^2)^3} + \frac{(3\mathbf{Q}_1^2 + 7m_\pi^2)(3\mathbf{Q}_3^2 + 7m_\pi^2)\boldsymbol{\sigma}_1 \cdot \mathbf{Q}_1 \boldsymbol{\sigma}_3 \cdot \mathbf{Q}_3}{(\mathbf{Q}_1^2 + m_\pi^2)^3 (\mathbf{Q}_3^2 + m_\pi^2)^3} \right], \\
V_{3N}^{c4,\text{prereg}}(\mathbf{Q}_1, \mathbf{Q}_3) &= \frac{c_4 g_A^2}{2f_\pi^4} \boldsymbol{\tau}_1 \cdot \boldsymbol{\tau}_2 \times \boldsymbol{\tau}_3 \left[ -\frac{\boldsymbol{\sigma}_1 \cdot \boldsymbol{\sigma}_2 \times \boldsymbol{\sigma}_3}{(\mathbf{Q}_1^2 + m_\pi^2)(\mathbf{Q}_3^2 + m_\pi^2)} - \frac{(3\mathbf{Q}_1^2 + 7m_\pi^2)\boldsymbol{\sigma}_1 \cdot \mathbf{Q}_1 \boldsymbol{\sigma}_3 \cdot \boldsymbol{\sigma}_2 \times \mathbf{Q}_1}{(\mathbf{Q}_1^2 + m_\pi^2)^3 (\mathbf{Q}_3^2 + m_\pi^2)} \right. \\
&\quad \left. + \frac{(3\mathbf{Q}_3^2 + 7m_\pi^2)\boldsymbol{\sigma}_3 \cdot \mathbf{Q}_3 \boldsymbol{\sigma}_1 \cdot \boldsymbol{\sigma}_2 \times \mathbf{Q}_3}{(\mathbf{Q}_1^2 + m_\pi^2)(\mathbf{Q}_3^2 + m_\pi^2)^3} + \frac{(3\mathbf{Q}_1^2 + 7m_\pi^2)(3\mathbf{Q}_3^2 + 7m_\pi^2)\boldsymbol{\sigma}_1 \cdot \mathbf{Q}_1 \boldsymbol{\sigma}_3 \cdot \mathbf{Q}_3 \boldsymbol{\sigma}_2 \cdot \mathbf{Q}_1 \times \mathbf{Q}_3}{(\mathbf{Q}_1^2 + m_\pi^2)^3 (\mathbf{Q}_3^2 + m_\pi^2)^3} \right], \tag{119}
\end{aligned}$$

and the corresponding pre-regularized regulator term (cf. Eq. (111)):

$$\tilde{f}_R^{\text{prereg}}(Q) = 4\pi \int_0^\infty dr (1 - e^{-r^2/R^2})^6 j_0(Qr). \tag{120}$$

These pre-regularized quantities can be straightforwardly decomposed in a partial-wave representation using the framework discussed in Section 3.3. The decomposition of the regulator

$$\tilde{f}_R^{\text{prereg}}(\mathbf{Q}_1, \mathbf{Q}_3) = \tilde{f}_R^{\text{prereg}}(|\mathbf{Q}_1|) \tilde{f}_R^{\text{prereg}}(|\mathbf{Q}_3|) \tag{121}$$

is particularly simple as it does not depend on any spin and isospin quantum numbers. However, note that the regulator does not factorize anymore if the long-range regulator is applied to pion-exchange contributions that involve all three interparticle distances (like, e.g. for the ring contributions at N<sup>3</sup>LO) due to the relation  $\mathbf{r}_{12} + \mathbf{r}_{23} + \mathbf{r}_{31} = 0$ . After the decomposition the matrix elements of the regularized interaction can be computed via Eq. (114).

The regularization of the intermediate-range diagram (b) in Figure 27 is somewhat more intricate as it involves long-range and short-range pieces. Since this interaction contains only one pion-exchange interaction the long-range regularization takes the following form:

$$V_{3N}^{1\pi,\text{reg}}(\mathbf{r}_{12}) = V_{3N}^{1\pi}(\mathbf{r}_{12}) f_R^{\text{long}}(\mathbf{r}_{12}). \tag{122}$$

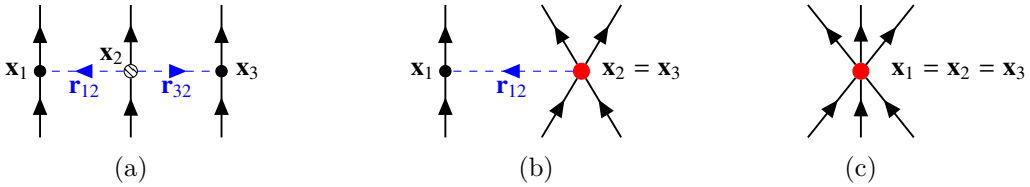


Figure 27: Semilocal coordinate-space regularization of the 3N interactions at N<sup>2</sup>LO. The pion exchange contributions (blue) to all interactions are regularized locally via the long-range regulator  $f_R^{\text{long}}(\mathbf{r}_{ij})$ , whereas the short-range parts (red) are regularized nonlocally in momentum space via the regulator  $f_\Lambda^{\text{short}}(\mathbf{p}_0^2)$  (see caption of Figure 25). Since all interactions terms are local, the relation  $\mathbf{x}_i = \mathbf{x}_i'$  holds.

Accordingly, the pre-regularized interaction reads

$$V_{3N}^{cD,\text{prereg}}(\mathbf{Q}_1) = -\Delta_{\mathbf{Q}_1} V_{3N}^{cD}(\mathbf{Q}_1) = -\frac{g_{ACD}}{4f_\pi^4 \Lambda_\chi} \boldsymbol{\tau}_1 \cdot \boldsymbol{\tau}_3 \left[ -\frac{\boldsymbol{\sigma}_1 \cdot \boldsymbol{\sigma}_3}{\mathbf{Q}_1^2 + m_\pi^2} + \frac{(7m_\pi^2 + 3\mathbf{Q}_1^2)\boldsymbol{\sigma}_1 \cdot \mathbf{Q}_1 \boldsymbol{\sigma}_3 \cdot \mathbf{Q}_1}{(\mathbf{Q}_1^2 + m_\pi^2)^3} \right], \quad (123)$$

and the pre-regularized regulator

$$\tilde{f}_R^{\text{prereg}}(\mathbf{Q}_1, \mathbf{Q}_3) = \int d\mathbf{r}_{12} d\mathbf{r}_{23} e^{-i\mathbf{Q}_1 \cdot \mathbf{r}_{12}} e^{-i\mathbf{Q}_3 \cdot \mathbf{r}_{23}} \frac{f_R^{\text{long}}(r_{12})}{Q(r_{12}^2)} = (2\pi)^3 \delta(\mathbf{Q}_3) \tilde{f}_R^{\text{prereg}}(\mathbf{Q}_1). \quad (124)$$

The partial-wave decomposition of the regulator in Eq. (124) can be simplified significantly by a clever choice of coordinates. If we choose the basis representation {12} the momentum transfer  $\mathbf{Q}_3$  is given by  $\mathbf{Q}_3 = \mathbf{q}'_{\{12\}} - \mathbf{q}_{\{12\}}$ , and the argument of the delta function does not depend on any angles. As a result, it is straightforward to show that the partial-wave matrix elements of the regulator take the following form:

$${}_{\{12\}}\langle p'q'\alpha' | \tilde{f}_R^{\text{prereg}} | pq\alpha \rangle_{\{12\}} = \frac{\delta_{\alpha\alpha'}}{(2\pi)^6} 2\pi \delta(q' - q) \int_{-1}^1 dx P_L(x) \tilde{f}_R^{\text{prereg}}(y) \quad \text{with} \quad y^2 = p^2 + p'^2 - 2pp'x, \quad (125)$$

and  $L$  denotes the relative orbital angular momentum quantum number (see Eq. (41)). Any other basis choice, {13} or {23}, leads to nontrivial angular dependencies of the delta function and significantly complicates the partial wave decomposition. Using the representation Eq. (125) makes the application of the long-range regulator straightforward, but complicates significantly the application of the nonlocal regulator to the short-range coupling. To see this, note that the nonlocal regulator takes the form  $f_\Lambda^{\text{short}}(\mathbf{p}_\delta) f_\Lambda^{\text{short}}(\mathbf{p}'_\delta)$  with  $\mathbf{p}_\delta = (\mathbf{k}_2 - \mathbf{k}_3)/2$  (see Section 3.7.3). In Ref. [33] the values of the local coordinate-space scale  $R$  and nonlocal scale  $\Lambda$  are chosen to be connected via the relation  $R = \Lambda/2$ . However, in the basis representation {12} the momentum  $\mathbf{p}_\delta$  depends on angles between Jacobi momenta:

$$\mathbf{p}_\delta = \frac{1}{2}(\mathbf{k}_2 - \mathbf{k}_3) = -\frac{1}{2}\mathbf{p}_{\{12\}} - \frac{3}{4}\mathbf{q}_{\{12\}} = \mathbf{p}_{\{23\}}, \quad (126)$$

which makes the application of the nonlocal regulator nontrivial. On the other hand, using basis {23} reduces the nonlocal regularization to a simple factor after the partial-wave decomposition.

One way out of this dilemma is to perform the regularization in the basis {23} and compute the corresponding matrix elements of the long-range regulator by applying permutation operators to the expression Eq. (125) (see also Section 3.1):

$${}_{\{23\}}\langle p'q'\alpha' | \tilde{f}_R^{\text{prereg}} | pq\alpha \rangle_{\{23\}} = {}_{\{12\}}\langle p'q'\alpha' | P_{123}^{-1} \tilde{f}_R^{\text{prereg}} P_{123} | pq\alpha \rangle_{\{12\}}. \quad (127)$$

It is important to note that the practical calculation of the matrix products in Eq. (127) requires the calculation of the permutation operator as well as the regulator for both the physical partial waves with  $(-1)^{L+S+T} = -1$ , as well as unphysical partial waves with  $(-1)^{L+S+T} = +1$  (see also discussion in Section 3.5). The unphysical partial waves eventually decouple when the regulator is applied to the interaction via Eq. (114). However, for the calculation of products of auxiliary quantities as in Eq. (127) it is crucial to retain them. Finally, the regularized interaction can be computed via

$$\begin{aligned} & {}_{\{23\}}\langle p'q'\alpha' | V_{3N}^{(i),\text{prereg}} | pq\alpha \rangle_{\{23\}} \\ &= f_\Lambda^{\text{short}}(p') f_\Lambda^{\text{short}}(p) \int dp'' p''^2 dq'' q''^2 \sum_{\alpha''} {}_{\{23\}}\langle p'q'\alpha' | V_{3N}^{(i),\text{prereg}} | p''q''\alpha'' \rangle_{\{23\}} {}_{\{23\}}\langle p''q''\alpha'' | \tilde{f}_R^{\text{prereg}} | pq\alpha \rangle_{\{23\}}. \end{aligned} \quad (128)$$

Obviously, the preferred basis  $\{ab\}$  is determined by the particular choice of the interaction decomposition (see discussion in Section 3.5).

Finally, the regularization of the purely short-range diagram (c) in Figure 27 again reduces to a purely

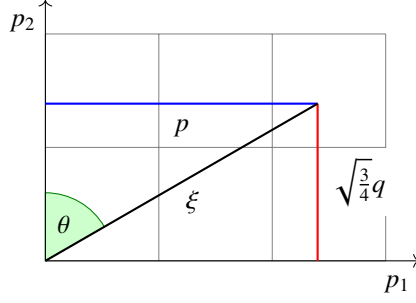


Figure 28: Definition of the hypermomentum  $\xi^2 = p^2 + \frac{3}{4}q^2 = p_1^2 + p_2^2$  and the hyperangle  $\tan \theta = \frac{p}{\sqrt{3/4}q} = \frac{p_1}{p_2}$  for a three-body state with Jacobi momenta  $\{p^2 = p_1^2, q^2 = \frac{4}{3}p_2^2\}$ .

nonlocal momentum regularization, i.e., a simple multiplicative factor of the partial-wave matrix elements:

$${}_{(ab)}\langle p' q' \alpha' | V_{3N}^{cE, \text{reg}} | p q \alpha \rangle_{(ab)} = f_R^{\text{short}}(p', q') {}_{(ab)}\langle p' q' \alpha' | V_{3N}^{cE} | p q \alpha \rangle_{(ab)} f_R^{\text{short}}(p, q), \quad (129)$$

as discussed in Section 3.7.3.

### 3.8. Visualization and comparison of matrix elements

In this section we illustrate and visualize the form of the partial-wave matrix elements of different topologies within chiral EFT using the different regularization schemes discussed in Section 3.7. Since the matrix elements effectively depend on six variables,  $p, q, \alpha, p', q'$  and  $\alpha'$ , it is necessary to reduce the dimensionality of the parameter space. First, we will focus here only on the most important partial-wave channels. Specifically, we select the channel with  $\bar{\alpha} = 0$  for the three-body channel with  $\mathcal{J} = \frac{1}{2}, \mathcal{T} = \frac{1}{2}$  and  $\mathcal{P} = +1$ , i.e.,  $L = 0, S = 0, J = 0, T = 1, l = 0$  and  $j = \frac{1}{2}$  for both initial and final states (see Appendix E). In this channel all orbital angular momenta are zero, which means that it is possible to study the effect of pure  $S$ -wave short-range couplings. Second, we re-parametrize the momentum dependence by introducing the hypermomentum  $\xi$  and the hyperangle  $\theta$  via the following definition (see also Figure 28):

$$\{p, q\} \rightarrow \left\{ \xi^2 = p^2 + \frac{3}{4}q^2, \tan \theta = \frac{p}{\sqrt{3/4}q} \right\}. \quad (130)$$

This transformation of variables is useful since the hypermomentum is directly related to the relative three-body kinetic energy and hence serves as a measure for the energy of the initial and final states. Since the role of the regulators is to separate the low-energy from the high-energy part of the Hilbert space the new variable set  $\{\xi, \theta\}$  is particularly suited to study the nature and properties of different regulators. In the following we visualize the matrix elements as a function of the initial and final state momenta  $\xi$  and  $\xi'$  for a fixed value of the hyperangle. In the following we arbitrarily choose  $\theta = \frac{\pi}{4}$ , i.e.,  $\tan \theta = 1$  for the initial and final states. The global features of the results presented in the following are insensitive to this particular choice.

Here we illustrate the matrix elements of individual 3N topologies in chiral EFT using the following four different regularization schemes (see also Table 4):

- *Nonlocal MS*: Nonlocal momentum-space regularization (see Section 3.7.1).
- *Local MS*: Local momentum-space regularization (see Section 3.7.2).
- *Semilocal MS*: Semilocal momentum-space regularization (see Section 3.7.3).
- *Semilocal CS*: Semilocal coordinate-space regularization (see Section 3.7.5).

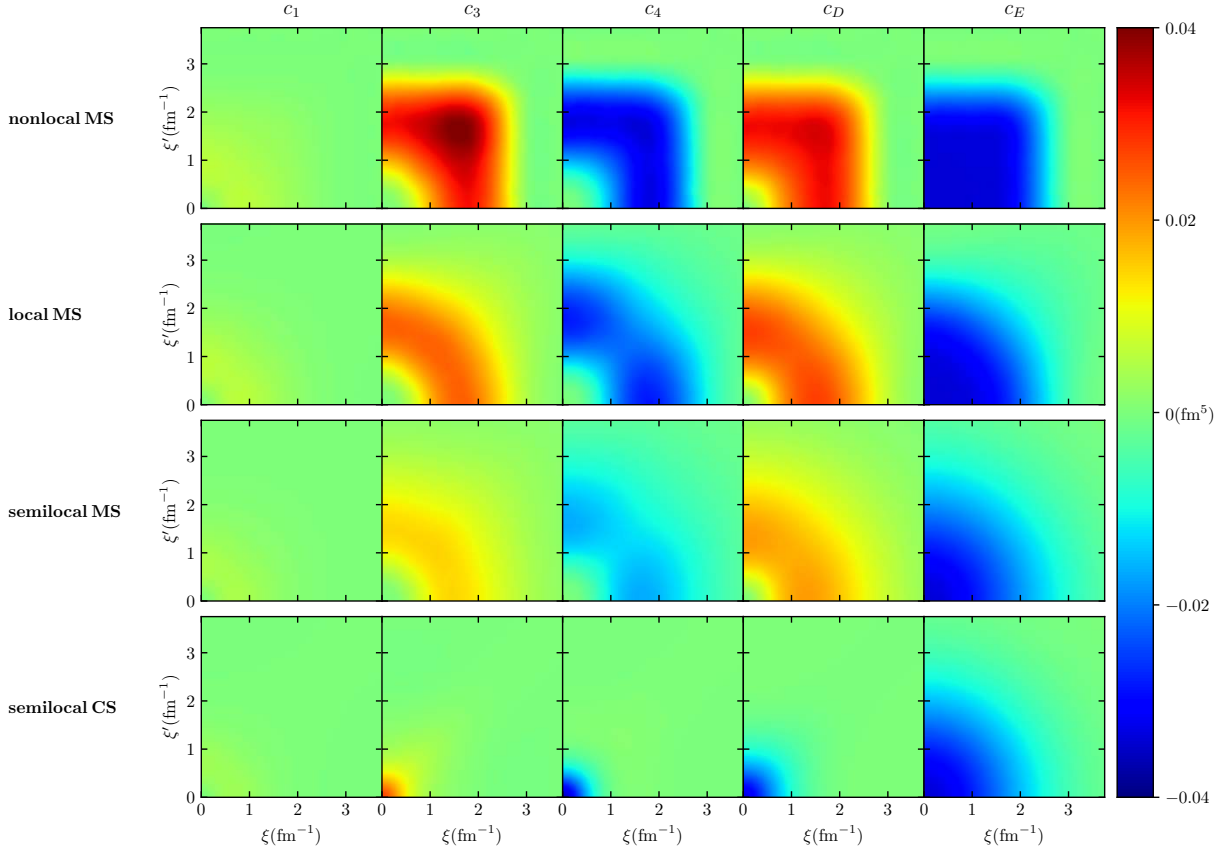


Figure 29: Matrix elements of the antisymmetrized interaction  $\langle p'q'\bar{\alpha}|V_{3N}^{\text{as}}|pq\bar{\alpha}\rangle$  for the individual topologies at N<sup>2</sup>LO (columns, indicated by the corresponding LEC) and different regularization schemes (rows, see main text and Table 4) as a function of the hypermomentum  $\xi^2 = p^2 + \frac{3}{4}q^2$  at the hyperangle  $\tan\theta = p/(\sqrt{3}/2q) = \frac{\pi}{4}$  and in the partial wave with  $\bar{\alpha} = \{L=0, S=0, J=0, T=1, l=0, j=\frac{1}{2}\}$ . For the long-range LECs, we choose the values of the Roy-Steiner analysis of Refs. [174, 175]:  $c_1 = -0.74 \text{ GeV}^{-1}$ ,  $c_3 = -3.61 \text{ GeV}^{-1}$  and  $c_4 = 2.44 \text{ GeV}^{-1}$ . The short-range couplings are chosen for optimized visibility:  $c_D = 2.0$  and  $c_E = 0.5$ . For the momentum-space regularization scales we set  $\Lambda = 500 \text{ MeV}$  and  $R = 0.9 \text{ fm}$  for the semilocal coordinate-space regularization (corresponding to  $\Lambda = 2R \approx 355 \text{ MeV}$  for the nonlocal regulators).

Based on the power counting of chiral EFT, the sum of all contributions to observables at a given order in the chiral expansion should be suppressed compared to contributions at lower order. However, we stress that studying the matrix elements of individual topologies separately may be misleading due to possible cancellation effects when computing observables. In particular, we stress that the definition of individual topologies is in general scheme-dependent and not unique (compare discussion in Ref. [191]).

Figure 29 shows the matrix elements for the five leading-order (N<sup>2</sup>LO) 3N interaction topologies for typical cutoff values:  $\Lambda = 500 \text{ MeV}$  for momentum-space regulators and  $R = 0.9 \text{ fm}$  for coordinate-space regulators. Clearly, the values and structure of the matrix elements are quite sensitive to the employed regularization scheme. In general, the values are largest for the “nonlocal MS” (first row) regularization, while the elements for the “local MS” and “semilocal MS” schemes look qualitatively similar, but tend to be more strongly suppressed. In particular, the long-range topologies (first three columns) of the “local MS” and “semilocal MS” regularized matrix elements are equal up to an additional suppression factor  $\exp[-2m_\pi^2/\Lambda^2]$  (see Table 4). The “semilocal CS” matrix elements (bottom row) on the other hand show a very different qualitative form compared to all momentum-space regularization schemes. Here the coordinate-space regulator  $f_R^{\text{long}}(\mathbf{r})$  completely suppresses all short-range contributions of the pion exchange interactions (see discussion in Section 3.7.5) as the regulator function virtually vanishes at  $r = 0$ . The remaining

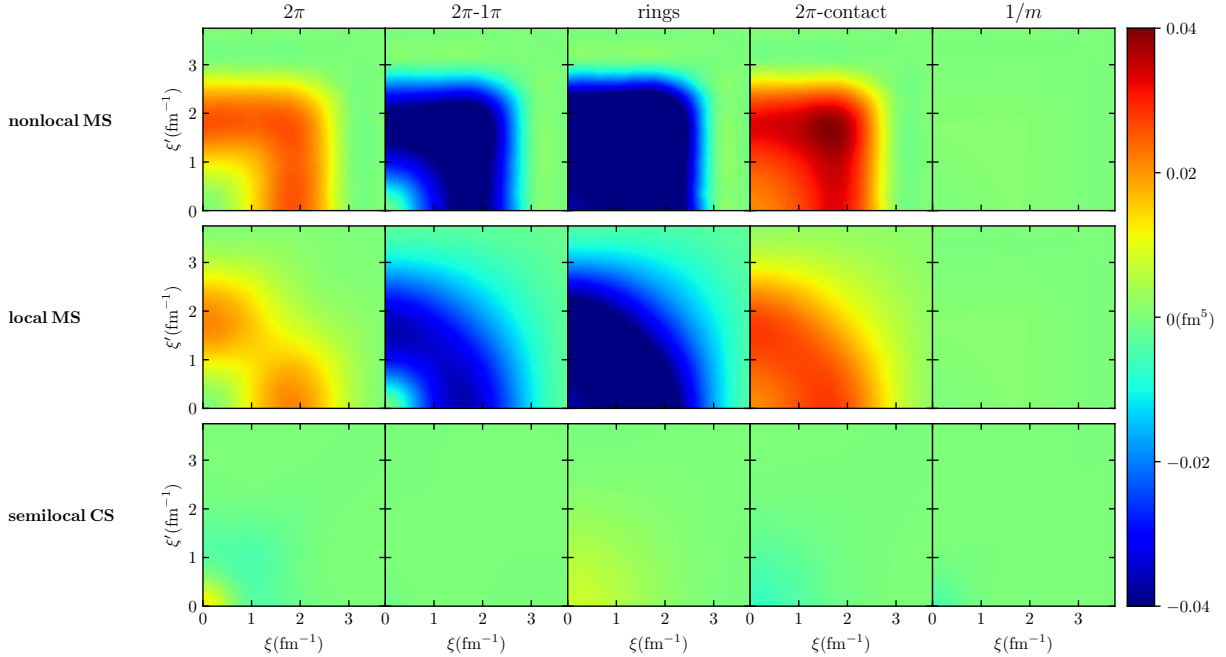


Figure 30: The matrix elements for the individual  $N^3\text{LO}$  topologies for the same parameters and plot ranges as in Figure 29. For optimized visibility of the  $2\pi$ -contact matrix elements we set  $C_T = 0.2$ . In the right column we show the relativistic corrections to the two-pion exchange contributions. The relativistic corrections to the one-pion exchange interactions are of the same order of magnitude and vanishingly small on the shown plot scale. The  $N^3\text{LO}$  contributions in the “semilocal MC” regularization scheme are not yet fully developed.

contributions shown in the bottom row of Figure 29 only contain long-range contributions to the  $2\pi$ -exchange topologies. For the momentum-space regulators on the other hand the pion exchange interactions still contain the short-range contact terms. This qualitative difference in the matrix elements is also reflected in observables as we demonstrate in Section 4.1 based on nuclear matter properties.

In Figure 30 we show the corresponding matrix elements for the subleading topologies at  $N^3\text{LO}$  for the same parameters and regularization schemes as in Figure 29. We can observe some striking differences between the different regularization schemes. First, the matrix elements of the individual topologies at  $N^2\text{LO}$  and  $N^3\text{LO}$  for the shown partial-wave channel are of the same order of magnitude for both the “nonlocal MS” and “local MS” regularization scheme. This is per se not a problem for power counting as the contributions can still add up to a relatively small total contribution. However, the cancellation becomes more and more fine-tuned as the size of the matrix elements for the individual topologies increase, which might eventually lead to serious practical problems. Second, there is a significant difference between the semilocal regularization schemes and the nonlocal and purely local regularization schemes. This indicates that the chosen regularization scheme could have some significant impact on the convergence of the chiral expansion.

Finally, in Figure 31 we show the matrix elements of the pure contact interaction topology proportional to the LEC  $c_E$  for different configuration channels in the three-body channel with  $\mathcal{J} = \frac{1}{2}$ ,  $\mathcal{T} = \frac{1}{2}$  and  $\mathcal{P} = +1$ . Note that for the regularization schemes “nonlocal MS”, “semilocal MS” and “semilocal CS” the matrix elements always vanish for all channels with  $L > 0$  or  $l > 0$  due to the nonlocal regularization of this topology in these schemes. In contrast, for the “local MS” scheme a finite range is induced, which leads to finite contributions in channels with nonvanishing angular momenta.

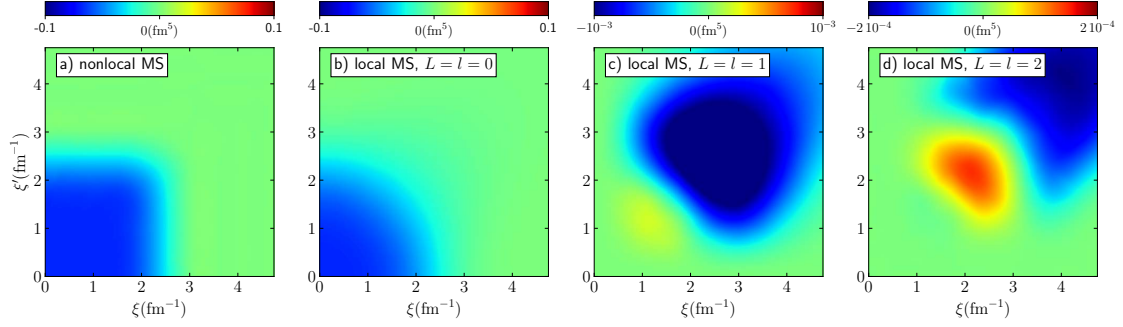


Figure 31: Matrix elements of the antisymmetrized interaction  $\langle p'q'\bar{\alpha}|V_{3N}^{\text{as}}|pq\bar{\alpha}\rangle$  for the short-range interaction proportional to  $c_E$  using the nonlocal regularization (a) and the “local MS” regularization (b, c and d) using  $\Lambda = 500\text{MeV}$  at the hyperangle  $\tan\theta = \frac{\pi}{4}$ . In the different panels we show the partial waves with  $\bar{\alpha}_a = \bar{\alpha}_b = \{L=0, S=0, J=0, T=1, l=0, j=\frac{1}{2}\}$ ,  $\bar{\alpha}_c = \{L=1, S=0, J=1, T=0, l=1, j=\frac{3}{2}\}$  and  $\bar{\alpha}_d = \{L=2, S=0, J=2, T=1, l=2, j=\frac{5}{2}\}$  (see Appendix B). The matrix elements for  $L > 0$  or  $l > 0$  vanish for the nonlocal regularization for this interaction topology. Note the different plot scales in panels c and d.

### 3.9. Transformation of matrix elements to harmonic oscillator basis

Most many-body frameworks based on partial-wave expansion methods are developed in harmonic oscillator (HO) bases. It is straightforward to transform momentum-space matrix elements of the form  $\langle p'q'\alpha'|V_{3N}|pq\alpha\rangle$  to the corresponding Jacobi HO basis. Since the partial-wave expansion of the angular dependence is identical in both bases, the transformation can be performed individually for the different partial-wave channels:

$$\langle N'n'\alpha'|V_{3N}|Nn\alpha\rangle = \int dp p^2 dp' p'^2 \int dq q^2 dq' q'^2 R_{N'L}(p', b) R_{n'l}(q', b) \langle p'q'\alpha'|V_{3N}|pq\alpha\rangle R_{NL}(p, b) R_{nl}(q, b), \quad (131)$$

with the radial harmonic oscillator wave functions<sup>7</sup>

$$R_{nl}(p, b) = \sqrt{\frac{2n!b^3}{\Gamma(n+l+\frac{3}{2})}} (pb)^l e^{-p^2b^2/2} L_n^{l+\frac{1}{2}}(p^2b^2). \quad (132)$$

Here  $b$  denotes the oscillator parameter  $b^{-1} = \sqrt{m\Omega}$  with the nucleon mass  $m$  and the oscillator frequency  $\Omega$  and  $L_n^k$  are the generalized Laguerre polynomials.

In the limit of infinite basis size many-body results become independent of  $\Omega$ . For practical calculations the frequency  $\Omega$  is usually chosen such that the ground-state energy results are minimized for a given basis size (see Figure 41).

We note that some care has to be taken regarding the value of the oscillator parameter due to different conventions of Jacobi coordinates. In the coordinate system introduced in Section 3.1 the isotropic oscillator Hamiltonian for three particles of mass  $m$  takes the following form:

$$H = \frac{\mathbf{k}_1^2 + \mathbf{k}_2^2 + \mathbf{k}_3^2}{2m} + \frac{1}{2}m\Omega^2(\mathbf{x}_1^2 + \mathbf{x}_2^2 + \mathbf{x}_3^2) = \frac{\mathbf{P}_{3N}^2}{2M} + \frac{\mathbf{P}_{\{12\}}^2}{2\mu_1} + \frac{\mathbf{q}_{\{12\}}^2}{2\mu_2} + \frac{1}{2}M\Omega^2\mathbf{R}_{3N}^2 + \frac{1}{2}\mu_1\Omega^2\mathbf{r}_{\{12\}}^2 + \frac{1}{2}\mu_2\Omega^2\mathbf{s}_{\{12\}}^2, \quad (133)$$

with  $M = 3m, \mu_1 = \frac{m}{2}, \mu_2 = \frac{2}{3}m$ . An alternative common choice of Jacobi coordinates is a more symmetric

<sup>7</sup>There exist different phase conventions for the harmonic oscillator wave functions. In some conventions an additional phase  $(-1)^n$  is added. This phase is either present in the coordinate-space wave function or in the momentum space representation.



choice of factors in momentum and coordinate space:

$$\begin{aligned}
\tilde{\mathbf{p}}_{\{12\}} &= \frac{\mathbf{k}_1 - \mathbf{k}_2}{\sqrt{2}}, & \tilde{\mathbf{q}}_{\{12\}} &= \sqrt{\frac{2}{3}} \left( \mathbf{k}_3 - \frac{1}{2}(\mathbf{k}_1 + \mathbf{k}_2) \right), & \tilde{\mathbf{P}}_{3N} &= \frac{\mathbf{k}_1 + \mathbf{k}_2 + \mathbf{k}_3}{\sqrt{3}} \\
\tilde{\mathbf{r}}_{\{12\}} &= \frac{\mathbf{x}_1 - \mathbf{x}_2}{\sqrt{2}}, & \tilde{\mathbf{s}}_{\{12\}} &= \sqrt{\frac{2}{3}} \left( \mathbf{x}_3 - \frac{1}{2}(\mathbf{x}_1 + \mathbf{x}_2) \right), & \tilde{\mathbf{R}}_{3N} &= \frac{\mathbf{x}_1 + \mathbf{x}_2 + \mathbf{x}_3}{\sqrt{3}}.
\end{aligned} \tag{134}$$

In this representation the harmonic oscillator Hamiltonian takes the following form, as can be easily verified:

$$H = \frac{\tilde{\mathbf{P}}_{3N}^2}{2m} + \frac{\tilde{\mathbf{p}}_{\{12\}}^2}{2m} + \frac{\tilde{\mathbf{q}}_{\{12\}}^2}{2m} + \frac{1}{2}m\Omega^2(\tilde{\mathbf{R}}_{3N}^2 + \tilde{\mathbf{r}}_{\{12\}}^2 + \tilde{\mathbf{s}}_{\{12\}}^2). \tag{135}$$

By comparing of Eqs. (133) and (135) we can identify the relations between the oscillator frequencies and oscillator parameters in both Jacobi coordinate representations for the transformation Eq. (131) for the three Jacobi variables:

$$\tilde{b}_{cm} = \frac{1}{\sqrt{3}}b, \quad \tilde{b}_p = \sqrt{2}b, \quad \tilde{b}_q = \sqrt{\frac{3}{2}}b, \tag{136}$$

where  $b$  is the value of the oscillator parameter in representation (133), and  $\tilde{b}_p$  and  $\tilde{b}_q$  are the oscillator parameters in the momentum  $p$  and  $q$ , respectively.

#### 4. Incorporation of 3N interactions in many-body frameworks

In Section 3 we discussed the representation and practical calculation of 3N interaction matrix elements in a partial-wave momentum basis. These matrix elements represent the microscopic input of most *ab initio* many-body frameworks for finite nuclei as well as dense matter. However, the step from interaction matrix elements to the extraction of many-body observables involves several challenges, in particular since the required many-body basis sizes grow with the particle number of the studied nuclei. In this section we discuss different novel and established techniques that facilitate the incorporation of 3N interactions in many-body frameworks and help to push the reach of *ab initio* methods toward heavier nuclei. Specifically, in Section 4.1 we illustrate the partial-wave convergence of results for nuclear-matter energies. In addition we demonstrate that the choice of the regularization scheme has a significant impact on the size of contributions from 3N interactions. In Section 4.2 we discuss the Similarity Renormalization Group (SRG) evolution of NN and 3N interactions to a lower resolution scale in the partial-wave momentum basis, which helps to significantly accelerate the convergence of many-body calculations of matter and atomic nuclei. In Section 4.3 we review recent and ongoing developments for the normal ordering of 3N interactions. This method allows to incorporate the main contributions from 3N interactions in many-body calculations at the cost of NN interactions. This technique is now used in basically all basis-expansion many-body methods that aim at studying properties of medium-mass and heavy nuclei. Typically, SRG evolution and normal ordering are combined in most many-body frameworks. Finally, we discuss in Section 4.4 a novel method to apply 3N interactions in many-body perturbation theory without partial-wave expansion. This method is particularly suited for calculations of nuclear matter, as it drastically simplifies the calculation of individual diagrams in MBPT compared to conventional approaches based on partial-wave decomposed 3N interactions. In addition, the developed framework can also be combined with a recently developed coupled cluster framework for nuclear matter [139].

For all these applications we will consider a general Hamiltonian in the center-of-mass reference frame, including contributions from the kinetic energy, NN and 3N interactions. For all the applications discussed in the following, it is most convenient to represent all quantities in second quantized form (see, e.g. Ref. [121]):

$$\hat{H} = \hat{T}_{\text{rel}} + \hat{V}_{\text{NN}} + \hat{V}_{\text{3N}}, \quad (137)$$

with

$$\begin{aligned} \hat{T}_{\text{rel}} &= \sum_{ij} \langle i|T|j\rangle \hat{a}_i^\dagger \hat{a}_j, \\ \hat{V}_{\text{NN}} &= \frac{1}{(2!)^2} \sum_{ijkl} \langle ij|V_{\text{NN}}^{\text{as}}|kl\rangle \hat{a}_i^\dagger \hat{a}_j^\dagger \hat{a}_l \hat{a}_k, \\ \hat{V}_{\text{3N}} &= \frac{1}{(3!)^2} \sum_{ijklmn} \langle ijk|V_{\text{3N}}^{\text{as}}|lmn\rangle \hat{a}_i^\dagger \hat{a}_j^\dagger \hat{a}_k^\dagger \hat{a}_n \hat{a}_m \hat{a}_l. \end{aligned} \quad (138)$$

Here all interactions are represented in terms of antisymmetrized matrix elements:

$$\begin{aligned} \langle ij|V_{\text{NN}}^{\text{as}}|kl\rangle &= \langle ij|\mathcal{A}_{12}V_{\text{NN}}|kl\rangle = \langle ij|V_{\text{NN}}|kl\rangle - \langle ji|V_{\text{NN}}|kl\rangle \\ \langle ijk|V_{\text{3N}}^{\text{as}}|lmn\rangle &= \langle ijk|\mathcal{A}_{123}V_{\text{3N}}|lmn\rangle \\ &= \langle ijk|V_{\text{3N}}|lmn\rangle - \langle jik|V_{\text{3N}}|lmn\rangle - \langle ikj|V_{\text{3N}}|lmn\rangle - \langle kji|V_{\text{3N}}|lmn\rangle + \langle jki|V_{\text{3N}}|lmn\rangle + \langle kji|V_{\text{3N}}|lmn\rangle, \end{aligned} \quad (139)$$

with the two- and three-body antisymmetrizers (see Section 3.5):

$$\mathcal{A}_{12} = 1 - P_{12}, \quad \mathcal{A}_{123} = 1 - P_{12} - P_{13} - P_{23} + P_{123} + P_{132}. \quad (140)$$

The matrix elements are assumed to fulfill the general symmetries under simultaneous interchange of particles

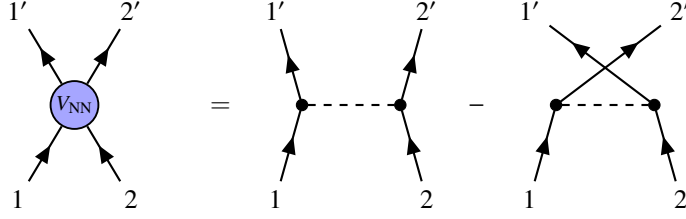


Figure 32: The two contributions to the antisymmetrized NN interaction  $V_{\text{NN}}^{\text{as}}$ . On the right hand side we show for illustration a long-range  $1\pi$ -exchange contribution.

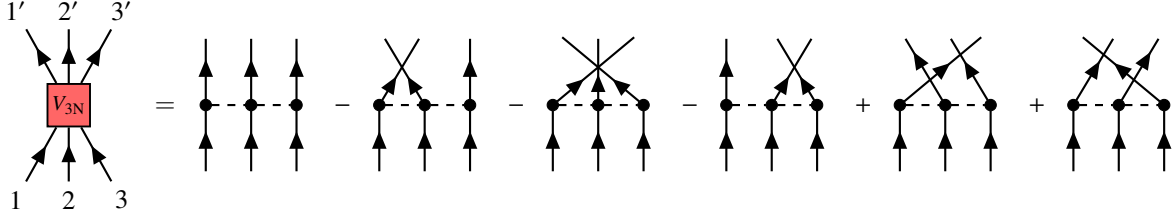


Figure 33: The six contributions to the antisymmetrized 3N interaction  $V_{3\text{N}}^{\text{as}}$ . On the right hand side we choose for illustration a  $2\pi$ -exchange contribution.

in the initial and final states:

$$\begin{aligned} \langle ij|V_{\text{NN}}|kl\rangle &= \langle ji|V_{\text{NN}}|lk\rangle \\ \langle ijk|V_{3\text{N}}|lmn\rangle &= \langle jik|V_{3\text{N}}|mln\rangle = \langle kji|V_{3\text{N}}|nml\rangle \quad \text{etc.} \end{aligned} \quad (141)$$

These relations are obviously fulfilled for 3N interactions of the form Eq. (53). The individual contributions to the antisymmetrized interactions  $V_{\text{NN}}^{\text{as}}$  and  $V_{3\text{N}}^{\text{as}}$  are illustrated in Figures 32 and 33.

#### 4.1. Partial-wave convergence of 3N interaction in dense matter

As a first illustration we apply the 3N interactions computed in Section 3 to calculate the energy of nuclear matter in the Hartree-Fock approximation at zero temperature. Even though this many-body approximation is usually not sufficient to obtain converged results, such calculations are instructive for several reasons:

- 1.) In this approximation the contributions from NN and 3N interactions decouple completely. In addition, the contributions of the individual 3N topologies do not mix. This allows to study the typical scale of the different 3N contributions to the energy of dense matter, independent of a particular chosen NN interaction.
- 2.) Even though higher order terms in the many-body expansion provide non-negligible contributions (depending on the regularization scheme and properties of the NN interactions), for several recently developed chiral NN interactions like, e.g., those of Refs. [140, 141, 188, 205, 266], the interactions behave perturbatively, at least for neutron-rich matter and smaller regularization cutoff scales. For such interactions, calculations in the Hartree-Fock approximation provide a reasonable estimate of the fully converged results.
- 3.) In the Hartree-Fock approximation it is also possible to calculate the 3N contributions exactly without employing a partial-wave decomposition of the interactions [124, 265]. These results represent an independent benchmark of the partial-wave matrix elements and also provide insight into the nature of the partial-wave convergence and the required partial-wave basis sizes (see Table 3) at the mean-field level. Typically these convergence patterns extend reasonably well to calculations at higher orders in the many-body expansion or also for calculations of finite nuclei such as those discussed in Section 5.

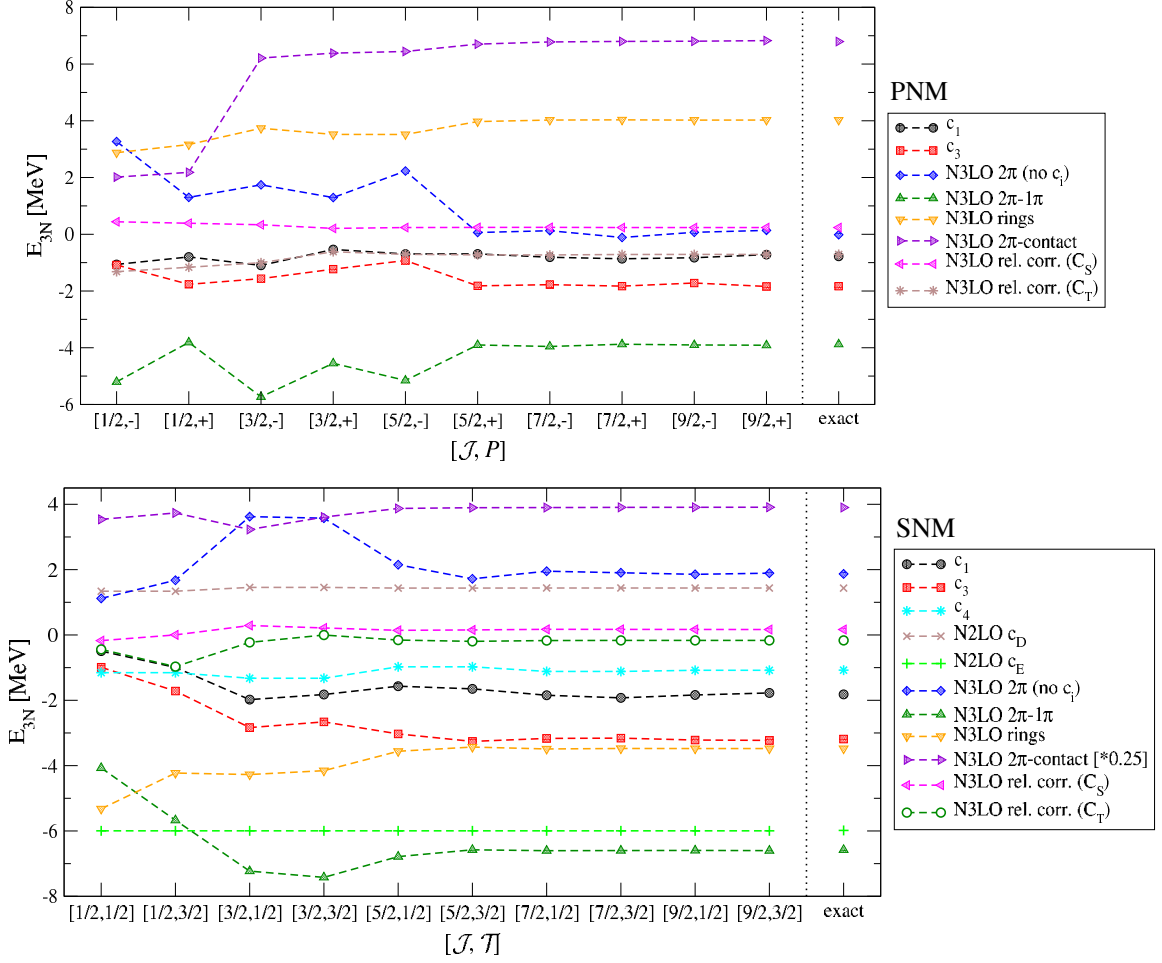


Figure 34: Partial-wave contributions to the energy per particle to pure neutron matter (top panel) and symmetric nuclear matter (lower panel) in the Hartree-Fock approximation at nuclear saturation density for the individual unregularized 3N interaction contributions and all topologies up to  $N^3\text{LO}$ . For the shown results we use the Fermi momenta  $k_F^n = 1.7 \text{ fm}^{-1}$  for PNM and  $k_F^n = k_F^p = 1.35 \text{ fm}^{-1}$  for SNM. For the LECs we use the values  $c_D = c_E = 1$ ,  $C_S = C_T = 1 \text{ fm}^2$  and  $c_i = 1 \text{ GeV}^{-1}$ . All results show the accumulated energies including contributions up to the given partial-wave channel using  $J_{\text{max}} = 5$  for each three-body partial wave. The exact benchmark results are calculated based on Refs. [124, 265].  
*Source:* Figures adapted from Ref. [177].

In the Hartree-Fock approximation, the 3N interaction contributions to the energy per volume of nuclear matter is given by [121, 122]:

$$\frac{E_{\text{HF}}}{V} = \frac{1}{6} \prod_{i=1}^3 \text{Tr}_{\sigma_i} \text{Tr}_{\tau_i} \int \frac{d\mathbf{k}_i}{(2\pi)^3} \langle 123 | V_{3N}^{\text{as}} | 123 \rangle n_{\mathbf{k}_1}^{\sigma_1 \tau_1} n_{\mathbf{k}_2}^{\sigma_2 \tau_2} n_{\mathbf{k}_3}^{\sigma_3 \tau_3}, \quad (142)$$

where  $n_{\mathbf{k}}^{\sigma\tau}$  are the zero-temperature occupation numbers for particles with spin  $\sigma$  and isospin  $\tau$ :  $n_{\mathbf{k}}^{\sigma\tau} = \Theta(k_F^{\sigma\tau} - |\mathbf{k}|)$ , with the Fermi momenta  $k_F^{\sigma\tau}$ . For the matrix elements we introduced the short-hand notation  $|123\rangle = |\mathbf{k}_1 \sigma_1 \tau_1 \mathbf{k}_2 \sigma_2 \tau_2 \mathbf{k}_3 \sigma_3 \tau_3\rangle$ . In the following we consider only spin-saturated systems, i.e.,  $n_{\mathbf{k}}^{\sigma\tau} = n_{\mathbf{k}}^{\tau}$ . In particular, in this section we will focus on pure neutron matter (PNM,  $n_{\mathbf{k}}^p = 0$ ) and symmetric nuclear matter (SNM,  $n_{\mathbf{k}}^p = n_{\mathbf{k}}^n$ ).

The sums and integrals in Eq. (142) can be either performed directly based on the operator form of the interactions by performing all momentum integrals analytically in a three-dimensional vector representation

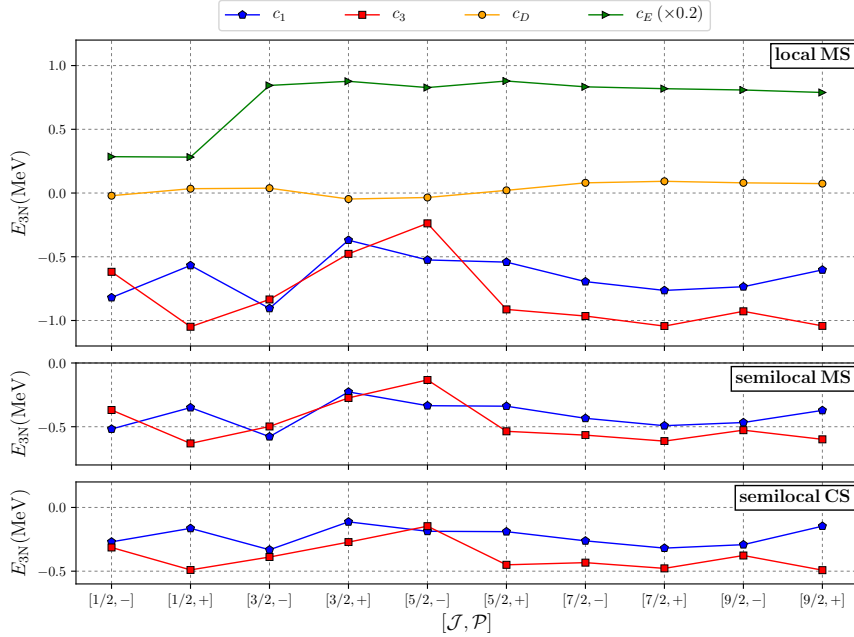


Figure 35: Partial-pave contributions to the energy per particle of PNM in the Hartree-Fock approximation at nuclear saturation density,  $k_F^s = 1.7 \text{ fm}^{-1}$ , for the individual 3N interaction contributions of all topologies at N<sup>2</sup>LO for the different regularization schemes (compare to top panel of Figure 34). As in Figure 34 we use the LEC values  $c_i = 1 \text{ GeV}^{-1}$  and  $c_D = c_E = 1$ . Note that the contributions from  $c_E$  in the top panel have been scaled by a factor  $\frac{1}{5}$  for optimized visibility. For both semilocal regularization schemes all contributions from the  $c_4$ ,  $c_D$  and  $c_E$  topology vanish. The cutoff values  $\Lambda = 500 \text{ MeV}$  and  $R = 0.9 \text{ fm}$  were chosen for the momentum-space and coordinate-space regulators, respectively, and the truncation  $J_{\text{max}} = 5$  has been employed for each three-body partial wave.

(see Refs. [124, 265]) or numerically [130] (see also Section 4.4). The analytical approach is in principle straightforward, but requires some work for antisymmetrizing the interactions. The final results can be expressed in a rather compact way for the individual 3N topologies up to N<sup>3</sup>LO (see Ref. [265] for details). Another alternative for evaluating Eq. (142) is to make use of the partial-wave representation of the 3N interactions. Here we need to represent the spin- and isospin sums as well as the momentum integrals in Eq. (142) in the partial-wave momentum basis discussed in Section 3.4. For example, for PNM the expression for the HF energy per volume takes the following form [267]:

$$\begin{aligned}
\frac{E_{\text{HF}}^{\text{PNM}}(k_F)}{V} &= \frac{1}{3\pi} \frac{1}{(4\pi)^2} \int dp p^2 dq q^2 \int d \cos \theta_{\mathbf{p}\mathbf{q}} \int dP_{3\text{N}} P_{3\text{N}}^2 \int d \cos \theta_{\mathbf{p}_{3\text{N}}} \int d\phi_{\mathbf{p}_{3\text{N}}} \\
&\times \sum_{\alpha, \alpha'} \delta_{S S'} \sum_{\bar{L}, S, \mathcal{L}, \mathcal{J}} \hat{S} \hat{L} \hat{\mathcal{J}} \sqrt{\hat{j} \hat{j}' \hat{l} \hat{l}' \hat{\mathcal{L}} \hat{\mathcal{L}}'} (-1)^{l+l'+\mathcal{L}} C_{r0l0}^{\bar{L}0} C_{L'0L0}^{\bar{L}0} P_{\bar{L}}(\hat{\mathbf{p}} \cdot \hat{\mathbf{q}}) \\
&\times n_{\mathbf{p}-\mathbf{q}/2+\mathbf{P}_{3\text{N}}/3} n_{\mathbf{p}+\mathbf{q}/2-\mathbf{P}_{3\text{N}}/3} n_{\mathbf{q}+\mathbf{P}_{3\text{N}}/3} \\
&\times \left\{ \begin{matrix} L' & L & \bar{L} \\ l & l' & \mathcal{L} \end{matrix} \right\} \left\{ \begin{matrix} L & S & J \\ l & \frac{1}{2} & j \\ \mathcal{L} & S & \mathcal{J} \end{matrix} \right\} \left\{ \begin{matrix} L' & S & J' \\ l' & \frac{1}{2} & j' \\ \mathcal{L} & S & \mathcal{J} \end{matrix} \right\} \langle pq\alpha' | V_{3\text{N}}^{\text{as,reg}} | pq\alpha \rangle, \quad (143)
\end{aligned}$$

with  $\hat{x} \equiv 2x + 1$ . The corresponding relation for SNM is identical up to an isospin factor  $2\mathcal{T} + 1$  plus an additional sum over the three-body isospin quantum number  $\mathcal{T}$ .

Figure 34 illustrates the partial-wave convergence of 3N contributions to the energy per particle in PNM and SNM based on unregularized 3N interactions compared to exact results calculated in Refs. [124, 265]. Since the Fermi momenta serve as natural ultraviolet cutoffs (see Eq. (143)), we do not need to regularize the

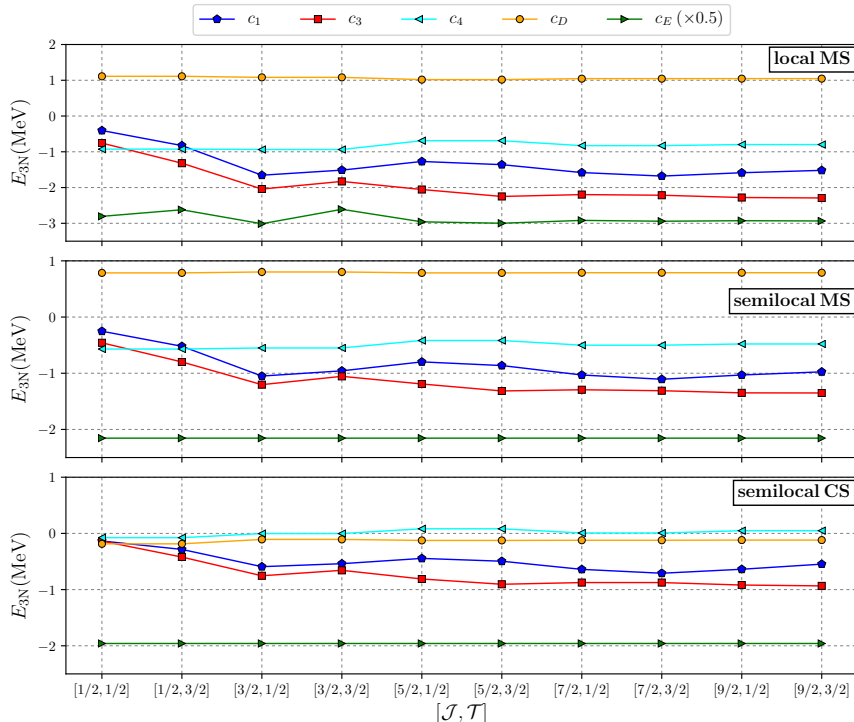


Figure 36: Partial-wave contributions to the energy per particle of SNM in the Hartree-Fock approximation at nuclear saturation density ( $k_F^n = k_F^p = 1.35 \text{ fm}^{-1}$ ) for the individual 3N interaction contributions of all topologies at N<sup>2</sup>LO for the different regularization schemes (compare with lower panel of Figure 34). The same LEC and cutoff values as in Figure 35 have been used. Note that the contributions from  $c_E$  have been scaled by a factor  $\frac{1}{2}$  for optimized visibility.

interactions for these benchmark calculations. The plots show the accumulated 3N interaction contributions to the energy per particle of PNM (upper panel) and SNM (lower panel) as a function of the three-body quantum number  $\mathcal{J}$  for the individual 3N interaction topologies up to N<sup>3</sup>LO in chiral EFT. Specifically, for the PNM results shown in the upper panel of Figure 34 we use  $k_F = 1.7 \text{ fm}^{-1}$  for the neutron Fermi momentum, which corresponds to a neutron number density of  $n \simeq 0.166 \text{ fm}^{-3}$ . In neutron matter only matrix elements in the three-body isospin channel  $\mathcal{T} = \frac{3}{2}$  contribute, while the N<sup>2</sup>LO topologies that include the low-energy coupling constants  $c_4$ ,  $c_D$  and  $c_E$  vanish exactly for unregularized 3N interactions [122]. The results of Figure 34 show that matrix elements up to the partial-wave channel with  $\mathcal{J} = \frac{5}{2}$  and both three-body parities  $\mathcal{P} = (-1)^{L+I}$  can provide significant contributions to the energy, whereas higher partial waves give only small corrections. Overall, we find that the results including all contributions up to  $\mathcal{J} = \frac{9}{2}$  are well converged and show excellent agreement with the exact results.

For symmetric nuclear matter we find a very similar convergence pattern. In contrast to neutron matter, here all 3N interaction topologies and also both three-body isospin channels,  $\mathcal{T} = \frac{1}{2}$  and  $\mathcal{T} = \frac{3}{2}$ , contribute to the energy. For the results shown in the lower panel of Figure 34 we fix the neutron and proton Fermi momenta to  $k_F^n = k_F^p = 1.35 \text{ fm}^{-1}$ , which again corresponds to a total number density of  $n \simeq 0.166 \text{ fm}^{-3}$ . We show the accumulated contributions to the energy for the individual partial-wave channels, where each  $[\mathcal{J}, \mathcal{T}]$  channel includes contributions from both three-body parity channels  $\mathcal{P} = \pm 1$ . Again, we observe excellent partial-wave convergence and essentially perfect agreement with the exact Hartree-Fock results.

In Figures 35 and 36 we show for comparison the corresponding partial-wave contributions from the 3NF topologies at N<sup>2</sup>LO to PNM and SNM for the regularization schemes “local MS”, “semilocal MS” and “semilocal CS” (see Section 3.7). Overall, we find that in these schemes the overall size of the contributions in PNM tend to be suppressed compared to the “nonlocal MS” or unregularized scheme. For SNM the size

of the contributions are of similar size for the “local MS” scheme and the unregularized case. Moreover, for the “local MS” scheme we find nonzero contributions for PNM for the short-range topologies proportional to the LECs  $c_D$  and  $c_E$ . This is due to the local nature of the regulator, which induces a finite range for the short-range couplings in these interaction topologies (see also Figure 31 and related discussion). In particular, we find significant contributions from the pure short-range interaction  $c_E$ . The qualitative trends of the contributions from the long-range topologies are remarkably similar in all shown regularization schemes, except for the  $c_4$  topology, which gives very small contributions in the “semilocal CS” scheme.

In summary, the results of this section demonstrate that the partial-wave contributions to the Hartree-Fock energy contributions to nuclear matter show an excellent agreement with exact mean-field results for unregularized 3N interactions by summing up all contributions up to the total three-body angular momentum  $\mathcal{J} = \frac{9}{2}$ . In addition, for the other studied regularization schemes the results are reasonably well converged in this model space. Even though certain qualitative trends appear universal, the specific size of the individual contributions can depend quite significantly on the employed regularization scheme.

## 4.2. SRG evolution in momentum basis

### 4.2.1. Flow equations

One of the key challenges of all basis-expansion *ab initio* many-body frameworks is achieving convergence of observables as a function of the basis size. The total number of required basis states is mainly determined by two factors:

- 1.) The total number of particles in the system, plus possible additional challenges like, e.g., the need to include scattering states in the basis if the system is only loosely bound as one approaches the drip lines of the nuclear chart (see, e.g. Refs. [98, 268]).
- 2.) The coupling strength of the nuclear interactions between low-energy states to high-energy intermediate virtual states.

The first factor is predetermined by the system under investigation and there is *a priori* no freedom for optimization within a given many-body framework, except for possibly switching to more suitable single-particle bases (see, e.g. Ref. [269]). Since different methods exhibit different scaling behaviors as a function of particles (see Section 1), frameworks like IM-SRG, MBPT, CC are more suited for studying medium-mass and heavier nuclei than conceptually exact methods like, e.g. NCSM. The second factor, on the other hand, is determined by properties of the employed nuclear interactions. If the NN or 3N interactions have sizable coupling strength of low- and high-energy states, the many-body basis needs to be large enough such that these virtual excitations induced by these couplings can be captured. This is the case even if we are eventually only interested in low-energy properties of nuclei, like ground-state energies, radii, quadrupole moments or low-lying excited states [20]. The Similarity Renormalization Group (SRG) provides a framework to systematically decouple low- and high-energy states via a unitary transformations that consistently renormalize all operators, including many-body forces, while preserving low-energy observables [21, 270, 271].

The basic underlying idea of the SRG consists of the construction of a unitary operator  $U(s)$  that transforms the Hamiltonian  $\hat{H}$  (as well as other operators, see Refs. [272–275]):

$$\hat{H}(s) = \hat{U}(s)\hat{H}\hat{U}^\dagger(s) \equiv \hat{T}_{\text{rel}} + \hat{V}_{\text{NN}}(s) + \hat{V}_{\text{3N}}(s). \quad (144)$$

At this point  $s$  is an arbitrary parameter and will be specified further below. Since the relative kinetic energy is effectively a two-body operator (see Eq. (86)), the separation of contributions from the kinetic energy and NN interactions of the transformed Hamiltonian is in general ambiguous. The transformed NN and 3N interactions  $\hat{V}_{\text{NN}}(s)$  and  $\hat{V}_{\text{3N}}(s)$  can be defined uniquely as done in Eq. (144) by choosing the relative kinetic energy to be independent of  $s$ . Taking the derivative of Eq. (144) with respect to the parameter  $s$  we obtain the following flow equation

$$\frac{d\hat{H}(s)}{ds} = \frac{d\hat{V}_{\text{NN}}(s)}{ds} + \frac{d\hat{V}_{\text{3N}}(s)}{ds} = [\hat{\eta}(s), \hat{H}(s)], \quad (145)$$



with the anti-unitary generator

$$\hat{\eta}(s) = \frac{d\hat{U}(s)}{ds} \hat{U}^\dagger(s) = -\hat{\eta}^\dagger(s). \quad (146)$$

Here  $\hat{\eta}(s)$  specifies the unitary transformation and can be chosen in a suitable way in order to achieve particular decoupling patterns. By far the most common choice for practical applications of the SRG in the context of nuclear structure has been the choice

$$\hat{\eta}(s) = [\hat{T}_{\text{rel}}, \hat{H}(s)], \quad (147)$$

which leads to the flow equation

$$\frac{d\hat{H}(s)}{ds} = \frac{d\hat{V}_{\text{NN}}(s)}{ds} + \frac{d\hat{V}_{\text{3N}}(s)}{ds} = [[\hat{T}_{\text{rel}}, \hat{H}(s)], \hat{H}(s)]. \quad (148)$$

In this flow equation the parameter  $s$  plays the role of a resolution scale [20]. It is also customary to introduce an alternative parameter  $\lambda$ , which has units of momenta:

$$\lambda = s^{-1/4}. \quad (149)$$

This parameter serves as a measure of the degree of decoupling in NN interactions as  $\lambda^2$  is directly related to the width of the band-diagonal structure in NN matrix elements as a function of the square of the relative momenta [21]. This implies that the evolution of NN interactions via Eq. (148) leads to a decoupling of low and high momenta as they are evolved to lower resolution scales  $\lambda$  and to significantly less correlated wave functions, which means that the nuclear many-body problem becomes more perturbative [20, 115, 276]. The SRG flow for a given initial NN and 3N interaction is completely determined by the generator  $\hat{\eta}_s$  defined in Eq. (146). We emphasize that SRG transformations generally reshuffle strength within a given many-body sector in Fock space like NN or 3N interactions, but also couple to other sectors like four- and higher-body forces, even when such forces are initially absent (see discussion below). Since SRG transformations need to be truncated in practice at a given order in many-body operators, the chosen generator should ideally not induce strong contributions in a regime beyond a given truncation scheme. The study of alternative efficient generators rather than the canonical choice Eq. (147) is presently an active field of research. Several choices have been explored (see, e.g., Refs. [277–279]), but so far no more powerful generator has been found, and the generator shown in Eq. (147) still represents the preferred choice for many state-of-the-art calculations. Hence, in the following we will stick for illustration to the particular flow equation Eq. (148), but stress that the framework discussed below can be straightforwardly extended to alternative generators.

We also emphasize that Eqs. (145) and (148) are operator identities and can hence be represented in arbitrary bases. In recent years two different strategies have been employed to evolve NN and 3N interactions via these flow equations:

- (a) Starting from realistic nuclear NN and 3N interactions it is possible to systematically evolve the full Hamiltonian  $\hat{H}(s)$  as defined in Eq. (138). This has been achieved by representing Eq. (145) in a discrete three-body harmonic oscillator basis [22, 43, 44, 280–282] or hyperspherical momentum basis [283]. The sum of all contributions of the initial Hamiltonian at  $s = 0$  are represented in the chosen three-body basis and then evolved via the flow equation (148). After the evolution the matrix elements of the evolved NN and 3N interactions can be extracted by suitable subtractions from the full Hamiltonian.
- (b) The approach (a) involves fundamental problems for continuous bases like the momentum basis in Eq. (41) due to the presence of delta functions for two-body operators, related to spectator particles (see Ref. [21] and discussion below). Instead, for continuous bases the evolution of NN and 3N forces needs to be separated explicitly, which allows to avoid the need for subtractions of NN interactions from the total Hamiltonian in a three-body basis completely. In practice that means Eq. (148) is being reformulated in terms of two explicit flow equations for  $\hat{V}_{\text{NN}}(s)$  and  $\hat{V}_{\text{3N}}(s)$  (see Refs. [284, 285]). Since SRG transformations are usually characterized by the coupling patterns of momentum eigenstates, the momentum basis is a well-suited basis in which to construct the SRG generator  $\eta(s)$ .

In the following we discuss in detail the implementation of approach (b) using the partial-wave momentum representation discussed in detail in Section 3. The approach (a) is well established by now and details can be found, e.g., in Ref. [282]. However, evolution in a momentum basis has several advantages compared to a discrete oscillator basis. First, the oscillator basis has intrinsic infrared and ultraviolet cutoffs that depend on the basis size and oscillator parameter  $\Omega$  [282], which could lead to convergence issues for 3N forces. This problem can be avoided by first evolving in momentum space and then using a straightforward transformation to an oscillator basis with *any*  $\Omega$  (see Section 3.9). Second, the momentum-space interactions can be used directly in calculations of infinite matter (see Section 5.2 for first results). This allows tests of whether consistently-evolved NN plus 3N forces, initially fit only to few-body properties, predict empirical nuclear saturation properties within theoretical errors, as found previously for evolved NN forces combined with fitted 3N forces [123] (see Section 2.3.1). Finally, since SRG transformations are usually characterized by the decoupling of momentum eigenstates, the momentum basis is a natural basis in which to construct the SRG generator  $\hat{\eta}_s$ . In particular, momentum-diagonal generators such as  $T_{\text{rel}}$  (as chosen here) can be implemented very efficiently in a momentum basis and it is straightforward to generalize to the Hamiltonian-diagonal form advocated by Wegner [271]. The possibility of using the generator to suppress the growth of many-body forces is also under active investigation.

For the derivation of the flow equation in momentum space we make, as a first step, the representation of Eq. (148) more explicit by adapting the notation of Ref. [21] and representing all quantities as matrix elements in a generic three-body basis  $|123\rangle = \hat{a}_1^\dagger \hat{a}_2^\dagger \hat{a}_3^\dagger |0\rangle$ ,  $\langle 1'2'3'| = \langle 0|\hat{a}_3 \hat{a}_2 \hat{a}_1$  and  $\langle 1'2'3'|123\rangle = \delta_{11'} \delta_{22'} \delta_{33'}$ . Evaluating the matrix elements of the second-quantized operators in this basis by employing Wick's theorem [286] results in:

$$\begin{aligned} \langle 1'2'3'|\hat{V}_{\text{NN}}|123\rangle &= \sum_{ijkl} \langle ij|V_{\text{NN}}^{\text{as}}|kl\rangle \left[ \langle 1'2'3'|\hat{a}_i^\dagger \hat{a}_j^\dagger \hat{a}_l \hat{a}_k|123\rangle + \langle 1'2'3'|\hat{a}_i^\dagger \hat{a}_j^\dagger \hat{a}_l \hat{a}_k|123\rangle + \langle 1'2'3'|\hat{a}_i^\dagger \hat{a}_j^\dagger \hat{a}_l \hat{a}_k|123\rangle \right] \\ &= \langle 2'3'|V_{\text{NN}}^{\text{as}}|23\rangle \delta_{11'} + \langle 1'3'|V_{\text{NN}}^{\text{as}}|13\rangle \delta_{22'} + \langle 1'2'|V_{\text{NN}}^{\text{as}}|12\rangle \delta_{33'} \\ &\equiv V_{23} + V_{13} + V_{12}, \end{aligned} \quad (150)$$

where we used the fact that there are four contractions for each of the three terms. Each of these four contractions provide identical contributions due to the antisymmetry of the matrix elements. This combinatorial factor cancels the factor  $\frac{1}{4}$  in Eq. (138). Note that the two-body interactions  $V_{ij}$  between particles  $i$  and  $j$  include an implicit delta function  $\delta_{kk'}$  with  $k \neq i, j$ , corresponding to the spectator particle  $k$  (see Figure 37). For the antisymmetrized 3N interaction we obtain 36 possible contractions<sup>8</sup>, each providing the same contribution:

$$\langle 1'2'3'|\hat{V}_{3\text{N}}|123\rangle = \sum_{ijklmn} \langle ijk|V_{3\text{N}}^{\text{as}}|lmn\rangle \langle 1'2'3'|\hat{a}_i^\dagger \hat{a}_j^\dagger \hat{a}_k^\dagger \hat{a}_n \hat{a}_m \hat{a}_l|123\rangle = \langle 1'2'3'|V_{3\text{N}}^{\text{as}}|123\rangle \equiv V_{123}. \quad (151)$$

The kinetic energy can be decomposed in the following way [21] (see also discussion in Section 3.1):

$$\langle 1'2'3'|\hat{T}_{\text{rel}}|123\rangle = T_{23} + T_1 = T_{31} + T_2 = T_{12} + T_3 = T_{\text{rel}}, \quad (152)$$

where the kinetic energy terms  $T_{ij}$  and  $T_k$  correspond to the relative kinetic energy between particles  $i$  and  $j$  and the contribution of particle  $k$ , respectively.

Note that there exist natural basis representations for each of the kinetic energy contributions and the NN interaction terms when using the Jacobi momentum basis defined in Eq. (41). For example, the NN

<sup>8</sup>As a first step pick one creation operator. There are three possible single-particle final states to contract it with. For the second creation operator there are two states left, whereas for the last one there is just a single contraction left, giving a total factor of 6. The same factor is obtained for the annihilation operators, giving a total factor of 36.

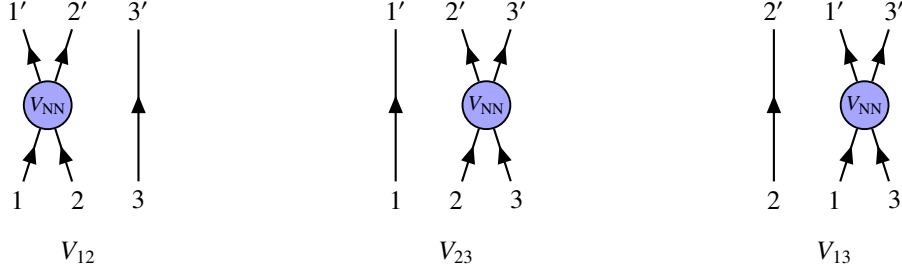


Figure 37: The three contributions of two-body interactions  $V_{ij}$  in a three-body basis. The vertices denote antisymmetrized interactions, where we also included the spectator particle in each diagram. The different diagrams are related by permutation of states, specifically  $V_{23} = P_{123}V_{12}P_{123}^{-1}$  and  $V_{13} = P_{132}^{-1}V_{12}P_{132}$  (see main text).

interaction term  $V_{12}$  takes the following form in basis representation  $\{12\}$  (see Appendix A):

$${}_{\{12\}}\langle p'q'\alpha'|V_{12}|pq\alpha\rangle_{\{12\}} = \langle p'\alpha'_{12}|V_{\text{NN}}|p\alpha_{12}\rangle \frac{\delta(q-q')}{qq'} \delta_{\alpha_3\alpha'_3}, \quad (153)$$

where  $\alpha_{12} = \{L, S, J, T\}$  represents all quantum numbers of the subsystem consisting of particles 1 and 2 and accordingly  $\alpha_3 = \{l, j\}$  those of particle 3 (see Section 3.4). According representations can be obtained for the interaction contributions  $V_{23}$  and  $V_{31}$  in the representations  $\{23\}$  and  $\{31\}$ , respectively. Using other basis representations makes the embedding of NN interactions into the three-body basis more complicated. However, eventually we need to represent all the terms of the flow equation (148) in a single chosen three-body basis. This step will be discussed further below.

Similarly we obtain for the kinetic energy:

$${}_{\{12\}}\langle p'q'\alpha'|T_{12}|pq\alpha\rangle_{\{12\}} = \frac{p^2}{m} \frac{\delta(p-p')}{pp'} \frac{\delta(q-q')}{qq'} \delta_{\alpha\alpha'}, \quad {}_{\{12\}}\langle p'q'\alpha'|T_3|pq\alpha\rangle_{\{12\}} = \frac{3}{4} \frac{q^2}{m} \frac{\delta(p-p')}{pp'} \frac{\delta(q-q')}{qq'} \delta_{\alpha\alpha'}, \quad (154)$$

and accordingly for the other terms in their natural basis representations. Note that from the relations above the following commutator relations follow:

$$[V_{12}, T_3] = [V_{23}, T_1] = [V_{13}, T_2] = 0. \quad (155)$$

The representations in Eqs. (150) and (152) allow to recast Eq. (148) as separate SRG flow equations for the two- and three-body interactions [21]:

$$\begin{aligned} \frac{dV_{ij}}{ds} &= [[T_{ij}, V_{ij}], T_{ij} + V_{ij}], \\ \frac{dV_{123}}{ds} &= [[T_{12}, V_{12}], V_{31} + V_{23} + V_{123}] \\ &\quad + [[T_{31}, V_{31}], V_{12} + V_{23} + V_{123}] \\ &\quad + [[T_{23}, V_{23}], V_{12} + V_{31} + V_{123}] \\ &\quad + [[T_{\text{rel}}, V_{123}], H_s]. \end{aligned} \quad (157)$$

Equation (156) follows directly from representing Eq. (148) in a two-body basis for the subsystem consisting of particles  $i$  and  $j$ . In this case the kinetic energy only consists of the term  $T_{ij}$  and three-body interactions do not contribute. Eq. (157) can then be derived by representing Eq. (148) including all terms of the Hamiltonian in the three-body basis, making use of the commutator relations (155) and the flow equation (156) for the two-body interactions.

Equation (157) demonstrates explicitly that 3N forces are being induced even if they are initially absent

at  $s = 0$  or  $\lambda = \infty$ , respectively. The same is true for all higher-body forces. That means, for maintaining unitarity for a  $N$ -body system, in general  $N - 1$  flow equations for the two-body to  $N$ -body forces need to be solved. In practice this hierarchy of equations is typically truncated at the three-body level. Some attempts to extend it to four-body forces have been pursued [287], but reaching sufficiently large model spaces is currently still out of reach. A more promising and feasible approach for dealing with higher-body forces seems to be a more suitable choice of generators which only induce weak higher-body interactions. This is work in progress.

Compared to Eq. (148), the system of differential equations (156) and (157) has the important advantage that terms resulting from spectator particles in two-body interaction processes have been eliminated explicitly. That means the flow equation for  $V_{ij}$  only involves particles  $i$  and  $j$ , whereas in the evolution equation for  $V_{123}$  every term on the right hand side involves interaction processes involving all three particles. The flow equation (156) can be easily represented in two-body partial-wave bases by inserting complete sets of states. For example, for  $V_{ij} = V_{12}$  (see Eq. (153)):

$$\begin{aligned} \frac{d}{ds} \langle p' \alpha'_{12} | V_{\text{NN}} | p \alpha_{12} \rangle &= - \left( \frac{p^2 - p'^2}{m} \right)^2 \langle p' \alpha'_{12} | V_{\text{NN}} | p \alpha_{12} \rangle \\ &+ \sum_{\alpha''_{12}} \int_0^\infty dp'' p''^2 \frac{p^2 + p'^2 - 2p''^2}{m} \langle p' \alpha'_{12} | V_{\text{NN}} | p'' \alpha''_{12} \rangle \langle p'' \alpha''_{12} | V_{\text{NN}} | p \alpha_{12} \rangle, \end{aligned} \quad (158)$$

where we used the normalization<sup>9</sup> (see Appendix A)

$$\langle p' \alpha'_{12} | p \alpha_{12} \rangle = \frac{\delta(p - p')}{pp'} \delta_{\alpha_{12} \alpha'_{12}}, \quad \sum_{\alpha_{12}} \int dp p^2 |p \alpha_{12} \rangle \langle p \alpha_{12}| = 1. \quad (159)$$

For the representation of Eq. (157) we choose a three-body basis representation  $\{ab\}$ . Let us choose without loss of generality representation  $\{12\}$ . One key step represents the embedding of the NN interactions  $V_{23}$  and  $V_{13}$  in this three-body basis. For this step, note that all three NN interaction terms are related by cyclic (or anticyclic) permutations of the initial and final states, i.e. (see Section 3.1):

$$\begin{aligned} {}_{\{23\}} \langle p' q' \alpha' | V_{23} | p q \alpha \rangle_{\{23\}} &= {}_{\{12\}} \langle p' q' \alpha' | V_{12} | p q \alpha \rangle_{\{12\}} \\ &= {}_{\{12\}} \langle p' q' \alpha' | P_{123}^{-1} P_{123} V_{12} P_{123}^{-1} P_{123} | p q \alpha \rangle_{\{12\}} \\ &= {}_{\{23\}} \langle p' q' \alpha' | P_{123} V_{12} P_{123}^{-1} | p q \alpha \rangle_{\{23\}}, \end{aligned} \quad (160)$$

which implies

$$V_{23} = P_{123} V_{12} P_{123}^{-1}, \quad \text{and accordingly} \quad V_{31} = P_{132} V_{12} P_{132}^{-1} = P_{123}^{-1} V_{12} P_{123}. \quad (161)$$

Corresponding relations hold for the kinetic energy. Hence we can rewrite Eq. (157) in the following form:

$$\begin{aligned} \frac{dV_{123}}{ds} &= \left[ [T_{12}, V_{12}], P_{123}^{-1} V_{12} P_{123} + P_{123} V_{12} P_{123}^{-1} + V_{123} \right] \\ &+ \left[ P_{123}^{-1} [T_{12}, V_{12}] P_{123}, V_{12} + P_{123} V_{12} P_{123}^{-1} + V_{123} \right] \\ &+ \left[ P_{123} [T_{12}, V_{12}] P_{123}^{-1}, V_{12} + P_{123}^{-1} V_{12} P_{123} + V_{123} \right] \\ &+ \left[ [T_{\text{rel}}, V_{123}], T_{\text{rel}} + V_{12} + P_{123} V_{12} P_{123}^{-1} + P_{123}^{-1} V_{12} P_{123} + V_{123} \right]. \end{aligned} \quad (162)$$

Equation (162) can be further simplified by noting that the kinetic energy  $T_{\text{rel}}$ , as well as the sum of all three

<sup>9</sup>Note that the normalization  $\frac{2}{\pi} \sum_{\alpha_{12}} \int dp p^2 |p \alpha_{12} \rangle \langle p \alpha_{12}| = 1$  is more common in the literature (see, e.g., Ref. [20]). The normalization of Eq. (159) leads to more compact expressions and represents a natural reduction of the three-body state normalization in Eq. (42), see Appendix A.

NN interactions,  $V_{12} + V_{23} + V_{31}$ , and also the 3N interaction  $V_{123}$  are each invariant under the multiplication with the sum of permutation operators  $(1 + P_{123} + P_{123}^{-1})/3$  from the left or from the right. This follows directly from the relations (161) and the representation Eq. (61) for the antisymmetrized 3N interaction. After evaluating the products of permutation operators we finally obtain the following flow equation in the partial-wave momentum representation:

$$\begin{aligned}
\frac{d}{ds} \langle p'q'\alpha' | V_{123} | pq\alpha \rangle = & \\
& \frac{2}{3} \langle p'q'\alpha' | (1 + 2P_{123}) ([T_{12}, V_{12}] P_{123} V_{12} - V_{12} P_{123} [T_{12}, V_{12}]) (1 + 2P_{123}) | pq\alpha \rangle \\
& + \langle p'q'\alpha' | (1 + 2P_{123}) [T_{12}, V_{12}] V_{123} - V_{123} [T_{12}, V_{12}] (1 + 2P_{123}) | pq\alpha \rangle \\
& + \langle p'q'\alpha' | [T_{\text{rel}}, V_{123}] V_{12} (1 + 2P_{123}) - (1 + 2P_{123}) V_{12} [T_{\text{rel}}, V_{123}] | pq\alpha \rangle \\
& + \langle p'q'\alpha' | [[T_{\text{rel}}, V_{123}], T_{\text{rel}} + V_{123}] | pq\alpha \rangle .
\end{aligned} \tag{163}$$

For the derivation of Eq. (163) we used that the permutation operators  $P_{123}$  and  $P_{132} = P_{123}^{-1}$  have the same momentum-space representation (see Section 3.5). Note, again, that this property can only be used after all products of permutation operators have been evaluated due to the coupling to unphysical intermediate states (see discussion in Section 3.7.5). Once all products are evaluated and each permutation operator is acting on interactions or kinetic energy terms, contributions from these unphysical states decouple and both operators have identical representations within the physical subset of states. Finally, we also suppressed the basis index  $\{ab\}$  in Eq. (163) since the matrix elements of antisymmetrized 3N matrix elements are invariant under this choice (see Eq. (61)). However, for our particular choice here it is most convenient to choose basis  $\{12\}$ , the natural basis for the two-body interaction  $V_{12}$ . Of course, we could have equally well represented all NN interactions in terms of  $V_{23}$  or  $V_{31}$ . It is now straightforward to represent the different terms in Eq. (163) by inserting complete sets of states, for example:

$$\begin{aligned}
\langle p'q'\alpha' | [[T_{\text{rel}}, V_{123}], V_{123}] | pq\alpha \rangle = & \int dp'' p''^2 dq'' q''^2 \sum_{\alpha''} \left[ \frac{p^2 + p'^2 - 2p''^2}{m} + \frac{3}{4} \frac{q^2 + q'^2 - 2q''^2}{m} \right] \\
& \times \langle p'q'\alpha' | V_{123} | p''q''\alpha'' \rangle \langle p''q''\alpha'' | V_{123} | pq\alpha \rangle .
\end{aligned} \tag{164}$$

For a consistent evolution of NN and 3N interactions Eqs. (158) and (163) need to be solved simultaneously. This task is in principle straightforward, but it involves some practical challenges [285]. First, it is necessary to define a model space for the calculations. This step consists of a choice for the maximal value of the three-body total angular momentum  $\mathcal{J}$  and a truncation for each three-body channel, e.g., by choosing a maximal value for the relative angular momentum  $J$  (see Section 3.4). Since three-body interactions are diagonal in the quantum numbers  $\mathcal{J}, \mathcal{T}$  and  $\mathcal{P}$ , all three-body channels can be treated separately. The basis size choices determine the dimension of the matrices as shown in Table 3, which in turn define the runtime and memory requirements. Both can become quite substantial. In order to provide a sense of scales, we consider as an example a typical truncation:  $J_{\text{max}} = 5, N_p = N_q = 25$  and all three-body channels up to  $\mathcal{J} = \frac{9}{2}$ . This basis is usually sufficient for well-converged many-body calculations of heavier nuclei as well as matter (see Section 4.1). For  $\mathcal{J} = \frac{9}{2}$  the matrix dimension is about  $7 \times 10^9$  in this case (see Table 3), which amounts to about 50 gigabytes of memory for the storage of a single 3N interaction matrix in double precision (64 bit). Since a typical differential equation solver requires several (up to about 10) copies of the kernel, the total memory requirement can reach about 0.5 terabyte. In addition, the calculation of matrix products of this dimension can become quite time consuming even when using highly optimized BLAS routines as done for the code implementation used in Ref. [285] and used for the results shown in the following section.

#### 4.2.2. Application to state-of-the-art chiral NN and 3N interactions

Apart from the many-body convergence, the model space choice also controls the degree of unitarity of the SRG transformation when solving Eq. (163). This is because a finite basis of the form shown in Eq. (41) is not complete under cyclic and anticyclic permutations of particles, as the permutation operator

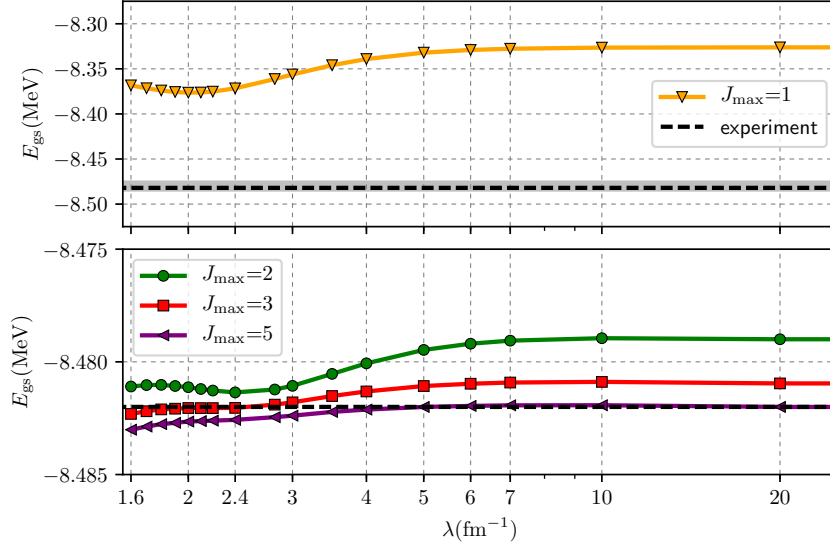


Figure 38: Ground-state energy of  ${}^3\text{H}$  as a function of resolution scale  $\lambda = s^{-1/4}$  based on consistently-evolved NN and 3N interactions for different model spaces defined by  $J_{\text{max}}$  (for both NN and 3N interactions), obtained from solutions of the Faddeev equations [255]. We employed the NN interaction of Ref. [188] at N<sup>2</sup>LO with  $\Lambda = 500$  MeV plus 3N interactions at N<sup>2</sup>LO fitted to the experimental ground-state energy  $E_{\text{gs}} = -8.482$  MeV (black dashed lines). The precise values of the LECs and the regulator form are given in the main text. The upper panel shows the results for  $J_{\text{max}}=1$ , whereas the lower panel shows the results for higher values of  $J_{\text{max}}$ . Note the different scales of the y axis in both panels. The lower panel shows the very narrow energy range around the experimental value, indicated by the gray band in the upper panel.

$P_{123}$  couples in general all partial waves (see Eq. (64)). As a consequence, non-vanishing matrix elements in all three-body partial waves are induced when two-body operators are embedded in a three-body momentum basis via Eq. (161). This problem is absent in one dimension [284] or in a discrete oscillator basis [22], where the permutation operator is block-diagonal in a given model space of size  $N_{\text{max}}$ . However, in practice this violation of unitarity can be reduced to a negligible degree as we demonstrate now.

We illustrate the degree of unitarity using the ground-state energy of  ${}^3\text{H}$ , i.e., we set  $\mathcal{J} = \frac{1}{2}$ ,  $\mathcal{T} = \frac{1}{2}$  and  $\mathcal{P} = +1$ . Such studies of three-body systems are particularly instructive since four- and higher-body forces cannot contribute and it is possible to cleanly disentangle effects from neglected higher-body forces and model space truncations for NN and 3N interactions. In Figure 38 we show the ground-state energy of  ${}^3\text{H}$  for different values of  $J_{\text{max}}$  as a function of the resolution scale. The calculations are based on the nonlocal NN interaction of Ref. [188] at N<sup>2</sup>LO for the cutoff value of  $\Lambda = 500$  MeV and the ground-state energies have been obtained from the T-matrix solutions of the momentum-space Faddeev equations. The three-body force has been fitted to reproduce the experimental binding energy of  ${}^3\text{H}$  with  $E_{\text{gs}} = -8.482$  MeV. Specifically, we used the values  $c_1 = -0.74$  GeV<sup>-1</sup>,  $c_3 = -3.61$  GeV<sup>-1</sup>,  $c_4 = 2.44$  GeV<sup>-1</sup>,  $c_D = 1.0$ ,  $c_E = -0.384$  and a regulator of the form shown in Eq. (87) with  $n = 4$ . However, we stress that these particular values are rather arbitrary and the general features shown in this figure are independent of these specific choices. The figure demonstrates that the results converge rapidly as a function of  $J_{\text{max}}$  for the present Hamiltonian. We find that the variation of the energy for model spaces  $J_{\text{max}} \geq 2$  is smaller than 4 keV over the shown range of resolution scales, while the variation decreases systematically with increasing model space. When reaching a level of less than 1 keV (like for  $J_{\text{max}} = 5$ ), results start to become sensitive to numerical truncation effects due to the finite discretization of the momentum basis when representing the flow equation Eq. (163) using  $N_p = N_q = 25$ .

In Figure 39 we demonstrate the decoupling of low- and high-energy components of 3N interactions as a function of resolution scale  $\lambda$  (columns) for different regularization schemes. The panels show the matrix elements as a function of the hypermomentum  $\xi^2 = p^2 + \frac{3}{4}q^2$  for a fixed hyperangle  $\tan \theta = p/(\sqrt{3}/2q) = \frac{\pi}{4}$

(see Section 3.8) for the partial wave with  $\bar{\alpha} = 0$ , i.e.,  $L = 0, S = 0, J = 0, T = 1, l = 0$  and  $j = \frac{1}{2}$  (see Appendix E). The values of the LECs of the 3N interactions are chosen such that the experimental binding energy of  ${}^3\text{H}$  is reproduced. The precise values are given in Table 5. The figure shows that the initial matrix elements at  $\lambda = \infty$  differ quite substantially in the different regularization schemes. However, as the resolution scale  $\lambda$  is lowered, attractive components at small momenta are generated for all interactions, while the off-diagonal contributions get systematically suppressed. Here, the width of the diagonal band is also approximately given by the scale  $\lambda^2$ , similarly to NN interactions [21]. These features are general and hold for matrix elements at different hyperangles and partial waves. In addition, the overall effects of the SRG evolution are stronger for initial potentials with stronger off-diagonal couplings. In addition, it is quite remarkable that at the lowest shown resolution scale  $\lambda = 1.7 \text{ fm}^{-1}$ , all interactions are very similar for the shown hyperangle and partial-wave channel, at least qualitatively. This property has already been observed for NN Interactions and is usually referred to as “universality” [20, 21]. This universality of NN interactions can be attributed to common long-range pion physics and phase-shift equivalence of all realistic potentials, which is reflected in the matrix elements at low resolution. It is an interesting question to what extent the same is true for 3N forces since there are important differences: First, 3N forces up to  $\text{N}^3\text{LO}$  are fixed by fitting only two low-energy constants  $c_D$  and  $c_E$ , in contrast to numerous couplings in NN interactions. Second, 3N forces give only subleading contributions to observables. Since universality is only approximate in NN interactions, it is not obvious to what extent 3N forces are constrained by long-range physics at low resolution. The results shown in Figure 39 indicate that universality also holds for 3N interactions at low resolution scales, even though not to such a quantitative degree as for NN interactions (see also Ref. [285]). However, more detailed investigations are needed to draw more robust conclusions.

In Figure 40 we demonstrate the improved perturbativeness and the accelerated convergence of many-body calculations based on interactions at lower resolution scales. The different panels show the binding energy of  ${}^3\text{H}$  for different resolution scales  $\lambda$  as a function of the model space indicated by  $N_{\text{max}}$ , obtained by a diagonalization of the Hamiltonian in a Jacobi harmonic oscillator three-body basis [40]<sup>10</sup>. It is obvious that the convergence properties of the initial interactions at  $\lambda = \infty$  differ quite significantly for the different regularization schemes and the shown oscillator parameter  $\Omega = 20 \text{ MeV}$ . However, note that the optimal frequency is not the same for all interactions and also depends on the resolution scale. In particular, for the “semilocal MS” and “semilocal CS” interactions in the bottom row the calculations converge much faster for an oscillator parameter of about  $\Omega = 40 \text{ MeV}$  at  $\lambda = \infty$ , while the optimal frequency gets shifted systematically to lower values as we evolve to lower resolution scales (see Figure 41). This shift represents a challenge when performing the SRG evolution in an oscillator basis at a given frequency. In order to ensure a converged SRG evolution, a frequency conversion method was employed [44]. In contrast, at low scales the many-body convergence is quite similar for all shown interactions and we are able to obtain converged results using only moderate model space sizes of about  $N_{\text{max}} = 16$ .

Note that such three-body calculations can be performed without any fundamental constraints on the resolution scale  $\lambda$  since it is possible to solve the SRG flow equations exactly up to numerical effects. For systems with  $A > 3$ , however, the evolution will not be unitary anymore since contributions from four- and

<sup>10</sup>Credits to Andreas Ekström for providing the diagonalization code.

regularization	$c_1 [\text{GeV}^{-1}]$	$c_3 [\text{GeV}^{-1}]$	$c_4 [\text{GeV}^{-1}]$	$c_D$	$c_E$	Ref.
<b>nonlocal MS</b>	-0.74	-3.61	2.44	-1.5	-0.61	[130]
<b>local MS</b>	-0.81	-3.2	5.4	0.83	-0.052	[148]
<b>semilocal MS</b>	-0.74	-3.61	2.44	2.0	0.23	
<b>semilocal CS</b>	-0.81	-4.69	3.4	1.0	-0.25	[33]

Table 5: LEC values of 3N interactions at  $\text{N}^2\text{LO}$  in the different regularization schemes discussed in Section 3.7. The couplings  $c_D$  and  $c_E$  have been fitted to the  ${}^3\text{H}$  binding energy plus another observable (details can be found in the given references). Except for the “local MS” scheme, according NN interactions at  $\text{N}^2\text{LO}$  with the same cutoff scale as for the 3N interactions have been employed. For the momentum-space and coordinate-space cutoff scales  $\Lambda = 500 \text{ MeV}$  and  $R = 0.9 \text{ fm}$  have been chosen, respectively.



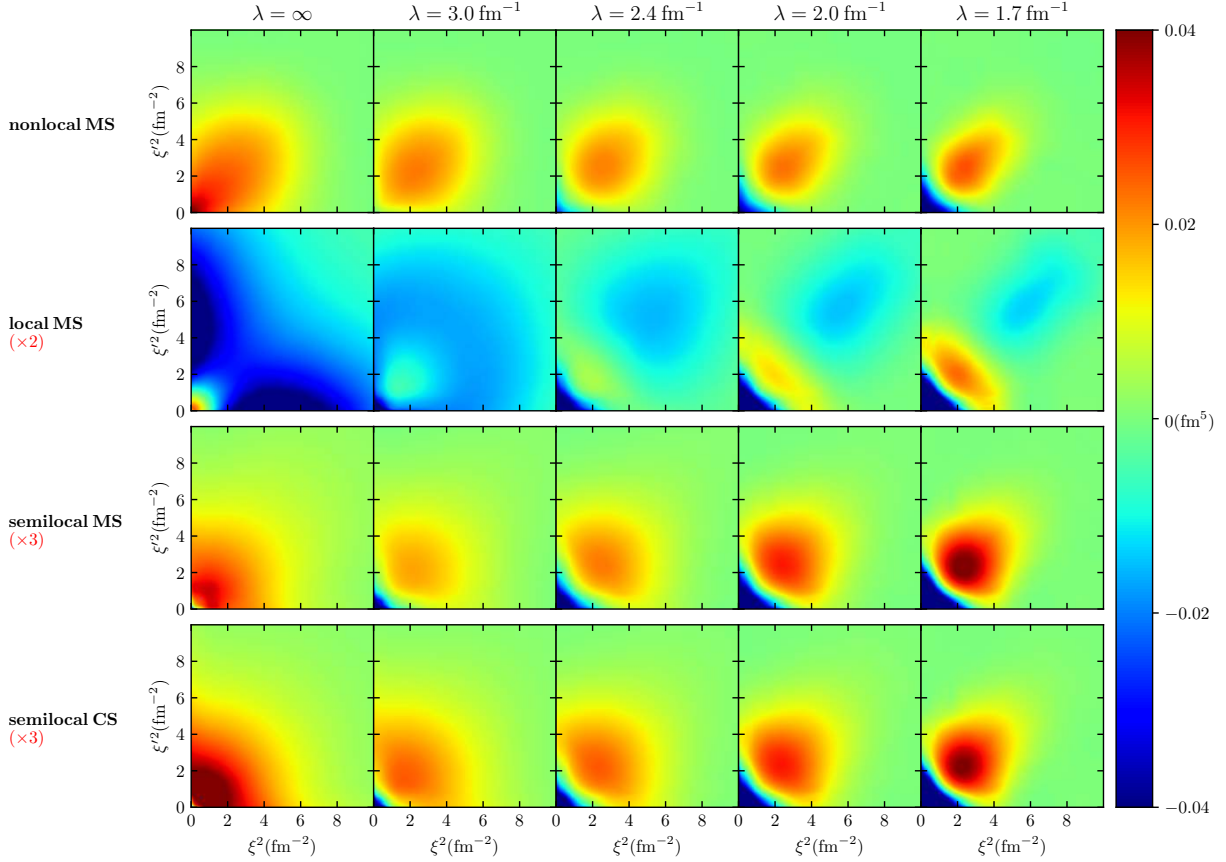


Figure 39: Matrix elements of the antisymmetrized interaction  $\langle p'q'\bar{\alpha}|V_{3N}^{\text{as}}|pq\bar{\alpha}\rangle$  at different resolution scales  $\lambda$  (columns) for the different regularization schemes (rows, see Section 3.7). In contrast to the figures of Section 3.8 we show the matrix elements as a function of the square of the hypermomentum  $\xi^2 = p^2 + \frac{3}{4}q^2$ . As in Figure 29, we choose the hyperangle  $\tan\theta = p/(\sqrt{3}/2q) = \frac{\pi}{4}$  and the partial wave with the quantum numbers  $\bar{\alpha} = 0 \equiv \{L=0, S=0, J=0, T=1, l=0, j=\frac{1}{2}\}$  (see Appendix E). The values of the LECs for the interactions within the different regularization schemes are shown in Table 5. For optimized visibility we multiplied the matrix elements for the “local MS” interactions by 2 and those of the “semilocal MS” and “semilocal CS” regularization scheme by 3.

higher-body interactions tend to become stronger with decreasing resolution scale. This puts some implicit constraints on the range of the resolution scales:

- First, the resolution scale  $\lambda$  needs to be *sufficiently small*, such that the low- and high-momentum components are sufficiently decoupled and it is possible to converge the many-body calculations.
- Second, the resolution scale should be *sufficiently large*, such that contributions from induced four- and higher-body interactions remain small.

These two conditions define a range of resolution scales that are particularly useful for practical calculations, given the currents basis size constraints and the typical strength of induced four- and higher-body interactions for presently used generators and interactions. This region typically comprises the range  $\lambda \approx 1.6\text{--}2.4\text{fm}^{-1}$  or, equivalently,  $s \approx 0.03\text{--}0.15\text{fm}^4$  for modern interactions derived within chiral EFT (see, e.g., Refs. [20, 43]). A practical way to check if both conditions are met is to perform calculations at different resolution scales and investigate the dependence of the results on this scale and on the many-body basis size. We will present an overview of recent state-of-the-art calculations in Section 5.

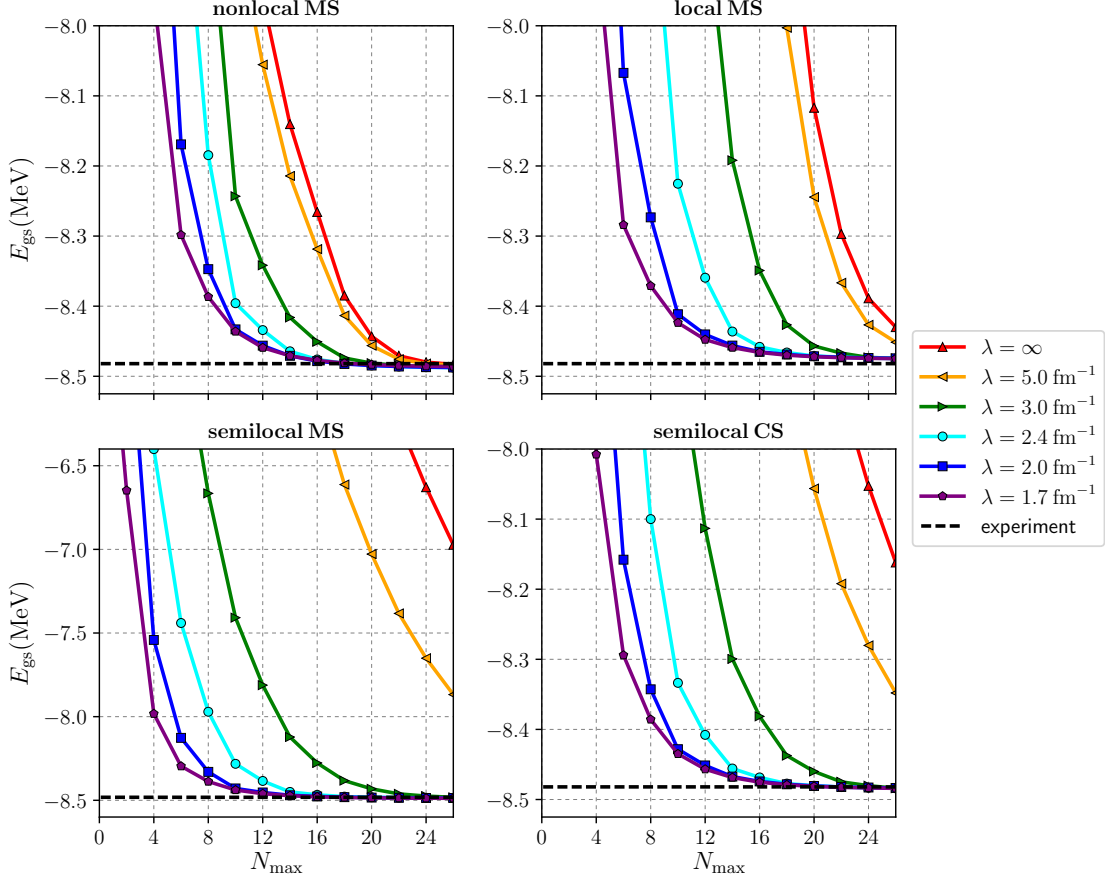


Figure 40: Ground-state energies of  ${}^3\text{H}$  based on the Hamiltonians specified in Table 5 as a function of SRG resolution scale  $\lambda$  and the harmonic oscillator basis size  $N_{\text{max}}$ . For all calculations the oscillator parameter  $\Omega = 20$  MeV and  $J_{\text{max}} = 5$  was used. Note the different energy scale in the panel for the “semilocal MS” interaction.

#### 4.3. Normal ordering of $3N$ interactions

Normal ordering is a powerful and well-established method that allows to transform the representation of a given Hamiltonian in an exact way, such that contributions from  $3N$  interactions can approximately be incorporated in many-body calculations at the computational cost of two-nucleon interactions. The underlying idea of normal ordering is to rewrite the Hamiltonian given in Eq. (138) by using Wick’s theorem [286, 288]:

$$\begin{aligned}
 \hat{A}\hat{B}\hat{C}\hat{D}\hat{E}\hat{F}\dots &= N(\hat{A}\hat{B}\hat{C}\hat{D}\hat{E}\hat{F}\dots) \\
 &+ \sum_{\text{singles}} N(\overline{\hat{A}\hat{B}\hat{C}\hat{D}\hat{E}\hat{F}\dots}) + \sum_{\text{doubles}} N(\overline{\hat{A}\hat{B}\hat{C}\hat{D}\hat{E}\hat{F}\dots}) + \dots + N(\overline{\hat{A}\hat{B}\hat{C}\hat{D}\hat{E}\hat{F}\dots}). \quad (165)
 \end{aligned}$$

Here the operators  $\hat{A}$ ,  $\hat{B}$ , etc. represent some generic creation or annihilation operators,  $N(\dots)$  denotes the normal-ordering of these operators with respect to a chosen reference state  $|\psi_{\text{ref}}\rangle$ , such that

$$\langle \psi_{\text{ref}} | N(\overline{\hat{A}\hat{B}\hat{C}\hat{D}\hat{E}\hat{F}\dots}) | \psi_{\text{ref}} \rangle = \langle \psi_{\text{ref}} | N(\hat{A}\hat{B}\hat{C}\hat{D}\hat{E}\hat{F}\dots) | \psi_{\text{ref}} \rangle = 0 \quad (166)$$

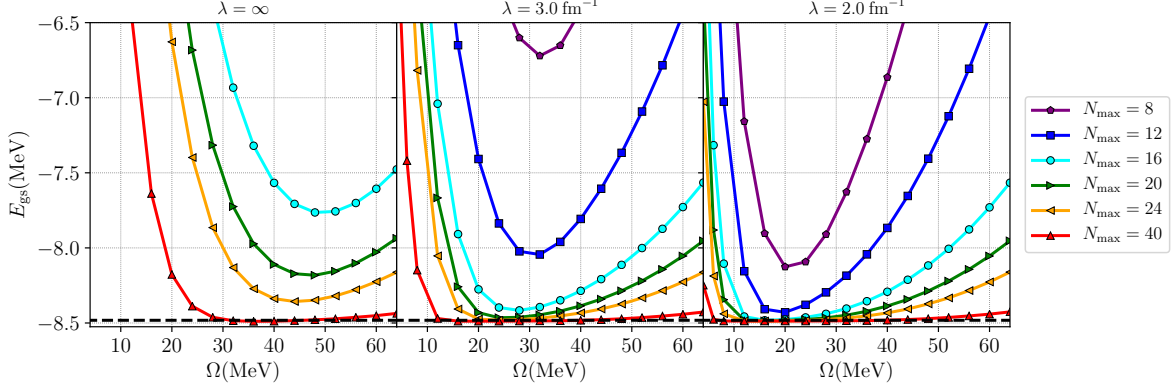


Figure 41: Ground-state energies of  ${}^3\text{H}$  based on the “semilocal MS” NN plus 3N interactions specified in Table 5 at three different resolutions scales  $\lambda$  as a function of the oscillator frequency  $\Omega$  and the basis size  $N_{\text{max}}$ .

for all non-fully-contracted strings of operators, where the contraction is defined by

$$\overline{\hat{A}\hat{B}} = \hat{A}\hat{B} - N(\hat{A}\hat{B}). \quad (167)$$

We emphasize that normal ordering generally depends on the definition of the reference state  $|\psi_{\text{ref}}\rangle$  since creation and annihilation operators are only defined with respect to a particular state. If we consider, e.g., a Hartree-Fock reference state  $|\psi_{\text{HF}}\rangle$  in which all the lowest  $A$  single-particle orbitals are occupied, normal ordering involves the anticommutation of all creation operators  $\hat{a}_i^\dagger$  with  $i \leq A$  to the left, and all annihilation operators  $\hat{a}_i$  with  $i > A$  to the right. As a result, only one type of contraction is nonvanishing and takes the simple form:

$$\overline{\hat{a}_i^\dagger \hat{a}_j} = \delta_{ij} - \overline{\hat{a}_j \hat{a}_i^\dagger} = n_i \delta_{ij} \quad \text{with} \quad n_i = \begin{cases} 1 & \text{for } i \leq A \\ 0 & \text{for } i > A \end{cases}. \quad (168)$$

Evaluating the contractions in Eq. (165), we obtain:

$$\hat{H} = \Gamma_{\text{HF}}^{(0)} + \hat{\Gamma}_{\text{HF}}^{(1)} + \hat{\Gamma}_{\text{HF}}^{(2)} + \hat{\Gamma}_{\text{HF}}^{(3)}, \quad (169)$$

with

$$\begin{aligned} \Gamma_{\text{HF}}^{(0)} &= \sum_i n_i \langle i|T|i\rangle + \frac{1}{2} \sum_{ij} n_i n_j \langle ij|V_{\text{NN}}^{\text{as}}|ij\rangle + \frac{1}{6} \sum_{ijk} n_i n_j n_k \langle ijk|V_{\text{3N}}^{\text{as}}|ijk\rangle, \\ \hat{\Gamma}_{\text{HF}}^{(1)} &= \sum_{ij} \left[ \langle i|T|j\rangle + \sum_k n_k \langle ik|V_{\text{NN}}^{\text{as}}|jk\rangle + \frac{1}{2} \sum_{kl} n_k n_l \langle ik|V_{\text{3N}}^{\text{as}}|jkl\rangle \right] N(\hat{a}_i^\dagger \hat{a}_j), \\ \hat{\Gamma}_{\text{HF}}^{(2)} &= \sum_{ijkl} \left[ \langle ij|V_{\text{NN}}^{\text{as}}|kl\rangle + \sum_m n_m \langle ijm|V_{\text{3N}}^{\text{as}}|klm\rangle \right] N(\hat{a}_i^\dagger \hat{a}_j^\dagger \hat{a}_l \hat{a}_k), \\ \hat{\Gamma}_{\text{HF}}^{(3)} &= \sum_{ijklmn} \langle ijk|V_{\text{3N}}^{\text{as}}|lmn\rangle N(\hat{a}_i^\dagger \hat{a}_j^\dagger \hat{a}_k^\dagger \hat{a}_n \hat{a}_m \hat{a}_l). \end{aligned} \quad (170)$$

The non-trivial prefactors in Eq. (170) result from the combinatorial factors associated with number of possible contractions  $n_{\text{NN}}$  and  $n_{\text{3N}}$  for the zero-body term  $\Gamma^{(0)}$ , the one-body term  $\hat{\Gamma}^{(1)}$  and the two-body term  $\hat{\Gamma}^{(2)}$ . The factors are shown in detail in Table 6. From Eq. (170) it follows that normal ordering allows to combine contributions from free-space two-body interactions with normal-ordered three-body contributions

$n_a$	$n_{a^\dagger}$	NN	$n_{\text{NN}}$	3N	$n_{\text{3N}}$	$\zeta$
0	0	$N(\frac{1}{4}V_{\text{NN}}\overline{\hat{a}^\dagger\hat{a}^\dagger\hat{a}\hat{a}})$	2	$N(\frac{1}{36}V_{\text{3N}}\overline{\hat{a}^\dagger\hat{a}^\dagger\hat{a}^\dagger\hat{a}\hat{a}\hat{a}})$	6	$\frac{1}{3}$
1	1	$N(\frac{1}{4}V_{\text{NN}}\overline{\hat{a}^\dagger\hat{a}^\dagger\hat{a}\hat{a}})$	4	$N(\frac{1}{36}V_{\text{3N}}\overline{\hat{a}^\dagger\hat{a}^\dagger\hat{a}^\dagger\hat{a}\hat{a}\hat{a}})$	18	$\frac{1}{2}$
2	2	$N(\frac{1}{4}V_{\text{NN}}\overline{\hat{a}^\dagger\hat{a}^\dagger\hat{a}\hat{a}})$	1	$N(\frac{1}{36}V_{\text{3N}}\overline{\hat{a}^\dagger\hat{a}^\dagger\hat{a}^\dagger\hat{a}\hat{a}\hat{a}})$	9	1
0	0	$N(\frac{1}{4}V_{\text{NN}}\overline{\hat{a}^\dagger\hat{a}^\dagger\hat{a}\hat{a}})$	1	$N(\frac{1}{36}V_{\text{3N}}\overline{\hat{a}^\dagger\hat{a}^\dagger\hat{a}^\dagger\hat{a}\hat{a}\hat{a}})$	9	1
2	0	$N(\frac{1}{4}V_{\text{NN}}\overline{\hat{a}^\dagger\hat{a}^\dagger\hat{a}\hat{a}})$	1	$N(\frac{1}{36}V_{\text{3N}}\overline{\hat{a}^\dagger\hat{a}^\dagger\hat{a}^\dagger\hat{a}\hat{a}\hat{a}})$	9	1
0	2	$N(\frac{1}{4}V_{\text{NN}}\overline{\hat{a}^\dagger\hat{a}^\dagger\hat{a}\hat{a}})$	1	$N(\frac{1}{36}V_{\text{3N}}\overline{\hat{a}^\dagger\hat{a}^\dagger\hat{a}^\dagger\hat{a}\hat{a}\hat{a}})$	9	1

Table 6: Combinatorial factors of the Wick contractions including normal contractions (upper half) and anomalous contractions (lower half). For the three-body terms only contributions including at least one normal contraction are shown.  $n_a$  denotes the number of uncontracted annihilation operators,  $n_{a^\dagger}$  the according number of creation operators,  $n_{\text{NN}}$  the number of possible contractions for NN interactions (or number of terms if there are no contractions) and  $n_{\text{3N}}$  the corresponding number of contractions for 3N interactions.

in the form of an effective two-body vertex function  $V_{\text{eff}}$  (see Figure 42):

$$\langle ij|V_{\text{eff}}^{\text{as}}|kl\rangle = \langle ij|V_{\text{NN}}^{\text{as}}|kl\rangle + \zeta\langle ij|\bar{V}_{\text{3N}}|kl\rangle, \quad (171)$$

with

$$\langle ij|\bar{V}_{\text{3N}}|kl\rangle \equiv \sum_m n_m \langle ij|V_{\text{3N}}^{\text{as}}|klm\rangle. \quad (172)$$

It is important to stress two crucial properties of the vertex function  $V_{\text{eff}}$ , defined in Eq. (171):

- The value of the combinatorial factor  $\zeta$  depends on the quantity of interest, as can be seen explicitly in Eq. (170). For example, for the calculation of Hartree-Fock energies the factor takes the value  $\zeta = \frac{1}{3}$  (as in  $\Gamma_{\text{HF}}^{(0)}$ ), whereas for the calculations of self energies  $\Sigma$  in the Hartree-Fock approximation we obtain  $\zeta = \frac{1}{2}$  (see  $\Gamma_{\text{HF}}^{(1)}$ ).
- In contrast to the free-space NN interaction  $V_{\text{NN}}^{\text{as}}$ , the effective interaction  $V_{\text{eff}}^{\text{as}}$  is in general not Galilean invariant, i.e., it depends on the two-body center-of-mass momenta (see also discussion in Section 3.2). This property is a consequence of the fact that the reference state defines a specific reference frame for the single-particle states  $m$  in Eq. (172) and hence violates translational symmetry.

The type and number of nonvanishing contractions depends on the type of reference state. For example, for superfluid and open-shell systems it is convenient to choose the BCS ground state [286, 289]:

$$|\psi_{\text{BCS}}\rangle = \prod_i (u_i + v_i \hat{a}_i^\dagger \hat{a}_{-i}^\dagger) |0\rangle, \quad (173)$$

with  $u_i^2 + v_i^2 = 1$ ,  $u_{-i} = u_i$  and  $v_{-i} = -v_i$ . The BCS state is a vacuum state with respect to the Bogoliubov-transformed operators:

$$\hat{\alpha}_i |\psi_{\text{BCS}}\rangle = 0 \quad \text{with} \quad \hat{\alpha}_i = u_i \hat{a}_i - v_i \hat{a}_{-i}^\dagger. \quad (174)$$

Hence, in the present case normal ordering involves the anticommutation of all  $\hat{a}^\dagger$  operators to the left and all  $\hat{a}$  to the right. By using Eq. (174) it follows  $\hat{\alpha}_i = u_i \hat{a}_i + v_i \hat{a}_{-i}^\dagger$  and it is straightforward to verify that the

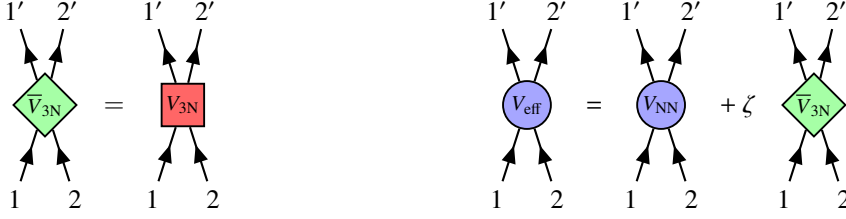


Figure 42: Diagrammatic representation of the integration over single-particle states as defined in Eq. (172) as part of the normal ordering operation (left panel) and the definition of the resulting effective two-nucleon interaction (see Eq. (171). Note the presence of the nontrivial combinatorial factor  $\zeta$  (see discussion in Section 4.3).

contractions take the following form:

$$\begin{aligned}
\hat{a}_i^\dagger \hat{a}_j &= v_i v_j \hat{\alpha}_{-i} \hat{\alpha}_{-j}^\dagger = v_i^2 \delta_{ij}, \\
\hat{\alpha}_i \hat{a}_j^\dagger &= u_i u_j \hat{\alpha}_i \hat{\alpha}_j^\dagger = u_i^2 \delta_{ij} = (1 - v_i^2) \delta_{ij}, \\
\hat{\alpha}_i \hat{a}_j &= u_i v_j \hat{\alpha}_i \hat{\alpha}_{-j}^\dagger = u_i v_j \delta_{-ij} = -u_i v_i \delta_{-ij}, \\
\hat{a}_i^\dagger \hat{a}_j^\dagger &= v_i u_j \hat{\alpha}_{-i} \hat{\alpha}_j^\dagger = v_i u_j \delta_{-ij} = u_i v_i \delta_{-ij}.
\end{aligned} \tag{175}$$

Clearly, in the present case the number of nonvanishing contractions is larger than for a Hartree-Fock reference state (see Eq. (168)). In particular, we find nonvanishing contributions from anomalous contractions, i.e., contractions of two creation or two annihilation operators. This is a consequence of the fact that the BCS state is not a state with a fixed particle number. Hence the normal-ordered Hamiltonian takes a more complicated form than for a Hartree-Fock reference state [103, 290]:

$$\hat{H} = \Gamma_{\text{BCS}}^{(0)} + \hat{\Gamma}_{1,\text{BCS}}^{(1)} + \hat{\Gamma}_{2,\text{BCS}}^{(1)} + \hat{\Gamma}_{3,\text{BCS}}^{(1)} + \hat{\Gamma}_{\text{BCS}}^{(2)} + \hat{\Gamma}_{\text{BCS}}^{(3)} + \dots, \tag{176}$$

with

$$\begin{aligned}
\Gamma_{\text{BCS}}^{(0)} &= \sum_i v_i^2 \langle i|T|i \rangle + \frac{1}{2} \sum_{ij} v_i^2 v_j^2 \langle ij|V_{\text{NN}}|ij \rangle + \frac{1}{6} \sum_{ijk} v_i^2 v_j^2 v_k^2 \langle ijk|V_{3\text{N}}|ijk \rangle \\
&\quad - \frac{1}{4} \sum_{ij} u_i v_i u_j v_j \langle i-i|V_{\text{NN}}|j-j \rangle - \frac{1}{4} \sum_{ijk} u_i v_i u_j v_j v_k^2 \langle i-ik|V_{3\text{N}}|j-jk \rangle + \dots, \\
\hat{\Gamma}_{1,\text{BCS}}^{(1)} &= \sum_{ij} \left[ \langle i|T|j \rangle + \sum_k v_k^2 \langle ik|V_{\text{NN}}|jk \rangle + \frac{1}{2} \sum_{kl} v_k^2 v_l^2 \langle ikl|V_{3\text{N}}|jkl \rangle + \dots \right] N(\hat{a}_i^\dagger \hat{a}_j), \\
\hat{\Gamma}_{2,\text{BCS}}^{(1)} &= \frac{1}{4} \sum_{ij} \left[ \sum_k u_k v_k \langle k-k|V_{\text{NN}}|ij \rangle + \sum_{kl} u_k v_k v_l^2 \langle k-kl|V_{3\text{N}}|ijl \rangle + \dots \right] N(\hat{a}_i \hat{a}_j), \\
\hat{\Gamma}_{3,\text{BCS}}^{(1)} &= \frac{1}{4} \sum_{ij} \left[ \sum_k u_k v_k \langle ij|V_{\text{NN}}|k-k \rangle - \sum_{kl} u_k v_k v_l^2 \langle ij|V_{3\text{N}}|k-kl \rangle + \dots \right] N(\hat{a}_i^\dagger \hat{a}_j^\dagger), \\
\hat{\Gamma}_{\text{BCS}}^{(2)} &= \sum_{ijkl} \left[ \langle ij|V_{\text{NN}}|kl \rangle + \sum_m v_m^2 \langle ijm|V_{3\text{N}}|klm \rangle \right] N(\hat{a}_i^\dagger \hat{a}_j^\dagger \hat{a}_l \hat{a}_k), \\
\hat{\Gamma}_{\text{BCS}}^{(3)} &= \sum_{ijklmn} \langle ijk|V_{3\text{N}}|lmn \rangle N(\hat{a}_i^\dagger \hat{a}_j^\dagger \hat{a}_k^\dagger \hat{a}_n \hat{a}_m \hat{a}_l),
\end{aligned} \tag{177}$$

where we have neglected terms involving only anomalous contractions in the 3N interactions in Eqs.(176)

and (177). Generally, anomalous contractions include only contributions around the Fermi surface in nuclear matter and consequently provide typically only small contributions to bulk properties of matter compared to normal contractions. In finite nuclei such contributions might be more relevant. In addition to Hartree-Fock and BCS reference states it is also possible to use reference states including additional many-body correlations (see, e.g., Ref. [132]).

The effectiveness of normal ordering relies on the assumption that the reference state is sufficiently close to the exact ground state of the system, such that the contributions from the vertex functions  $\hat{\Gamma}^{(1)}$ ,  $\hat{\Gamma}^{(2)}$  and  $\hat{\Gamma}^{(3)}$  only give small contributions when evaluating expectation values with respect to the real ground state  $|\psi_0\rangle$ :

$$\langle\psi_0|\hat{H}|\psi_0\rangle. \quad (178)$$

Obviously, if the normal-ordering reference state agrees with the exact ground state, all contributions from the vertex functions  $\hat{\Gamma}^{(1,2,3)}$  vanish, while the zero-body term  $\Gamma^{(0)}$  takes the value of the exact ground-state energy for a given Hamiltonian. In particular, for the practical usefulness of normal ordering it is key to choose a reference state such that contributions from the three-body vertex function  $\hat{\Gamma}^{(3)}$  (also called *residual* 3N contributions) are small compared to the lower-body operators and can be neglected to good approximation. In this case the total Hamiltonian  $\hat{H}$  can be written only in terms of operators up to the two-body level, which obviously simplifies calculations tremendously. In fact, the smallness of the contributions from  $\hat{\Gamma}^{(3)}$  has been demonstrated explicitly for calculations of ground-state energies of atomic nuclei for specific NN and 3N interactions derived within chiral EFT in Refs. [96, 291] using a Hartree-Fock reference state and recently also for multi-reference calculations of ground and excited states [59]. However, we stress that the choice of a useful reference state generally depends on the employed Hamiltonian and the system. For example, interactions that are highly non-perturbative, such as, e.g., the Argonne  $v_{18}$  potential [223], induce stronger high-energy virtual excitations, and the Hartree-Fock wave function will most likely not be a suitable reference state for normal ordering. Instead a state with more many-body correlations most likely needs to be chosen for such interactions.

#### 4.3.1. Normal ordering in nuclear matter

In this section we discuss normal ordering for nuclear matter, i.e., for a reference state defined in terms of momentum eigenstates. If we denote the single-particle states by momentum  $\mathbf{k}_i$ , spin  $\sigma_i$  and isospin  $\tau_i$ ,  $|i\rangle = |\mathbf{k}_i\sigma_i\tau_i\rangle$ , Eq. (172) takes the following form:

$$\langle 1'2'|\bar{V}_{3N}|12\rangle = \sum_{\sigma_3} \sum_{\tau_3} \int \frac{d\mathbf{k}_3}{(2\pi)^3} n_{\mathbf{k}_3}^{\tau_3} \langle 1'2'3|V_{3N}^{\text{as}}|123\rangle, \quad (179)$$

which involves sums over spin and isospin projection quantum numbers  $\sigma_3$  and  $\tau_3$ , as well as an integration over all momentum states, weighted by the momentum distribution functions  $n_{\mathbf{k}}^{\tau_3}$  for a given neutron and proton density. Here we choose, without loss of generality, to integrate over particle state 3. Due to the antisymmetry of  $V_{3N}^{\text{as}}$  we have the freedom to choose any other single-particle state. In addition, we assumed for the sake of simplicity that the distribution function does not depend on spin, i.e., we consider spin-unpolarized matter. However, the generalization to spin-polarized systems is straightforward [292]. The simplest and most common choice for the reference state is a Hartree-Fock wave function, for which all single-particle levels up to a Fermi momentum  $k_F$  are occupied. For the following examples, we consider for the sake of simplicity matter at zero temperature, i.e., the distribution function takes the following form:  $n_{\mathbf{k}}^{\tau} = \theta(k_F^{\tau} - |\mathbf{k}|)$ . We stress, however, that the treatment can be extended to more general distribution functions (see e.g. Refs. [132, 293]) or finite temperatures in a straightforward way.

Normal ordering takes the simplest form when expressed in single-particle coordinates, like Eq. (179). However, since the 3N interaction matrix elements are most efficiently expressed in a relative coordinate basis (see Section 3.2) it is desirable to perform the normal ordering in a Jacobi momentum representation. Since we chose to integrate over particle 3 in Eq. (179), it is most convenient to choose basis representation  $\{12\}$  (see Section 3.1). By expressing all single-particle momenta in terms of the Jacobi momenta and the

two-body center-of-mass momentum  $\mathbf{P} = \mathbf{P}_{\{12\}} = \mathbf{k}_1 + \mathbf{k}_2 = \mathbf{k}'_1 + \mathbf{k}'_2$  we obtain [128]:

$$\langle \mathbf{p}' | \bar{V}_{3N}(\mathbf{P}) | \mathbf{p} \rangle = \left( \frac{3}{2} \right)^3 \sum_{\sigma_3} \sum_{\tau_3} \int \frac{d\mathbf{q}}{(2\pi)^3} n_{(3\mathbf{q}+\mathbf{P})/2}^{\tau_3} \langle \mathbf{p}' \mathbf{q} | V_{3N}^{\text{as}} | \mathbf{p} \mathbf{q} \rangle_{\{12\}}. \quad (180)$$

Here we suppressed the spin and isospin quantum numbers in the matrix elements in order to keep the notation simple and transparent. It is important to note that, in contrast to the 3N interaction, the distribution function  $n_{\mathbf{p}}^{\tau}$  is not Galilean invariant as it depends on the two-body center-of-mass momentum  $\mathbf{P}$ . This in turn leads to a center-of-mass dependence of the effective interaction  $\bar{V}_{3N}$  (see discussion in Section 4.3), which makes the calculation of normal ordering technically quite challenging.

An exact calculation of partial-wave matrix elements for the effective NN interaction  $\bar{V}_{3N}$  in nuclear matter for general values and angles of the center-of-mass momentum  $\mathbf{P}$  has not been achieved so far.<sup>11</sup> Note that even if such an exact calculation would be available, the application of the resulting effective interaction in many-body frameworks becomes significantly more involved than free-space NN interactions in Eq. (171) due to the dependence on the vector  $\mathbf{P}$ . In most many-body frameworks for nuclear matter the interaction matrix elements are expressed in a Jacobi partial-wave momentum basis, consisting of the Jacobi momenta  $\mathbf{p}$  and  $\mathbf{p}'$ . This representation needs to be extended for general normal-ordered 3N interactions by the center-of-mass momentum  $\mathbf{P}$  plus corresponding additional angular quantum numbers, which usually requires significant modifications of existing frameworks that have been designed only for free-space NN interactions.

Due to these complications the dependence on the momentum  $\mathbf{P}$  is usually approximated for nuclear matter calculations. So far, the following two strategies have been employed:

- The simplest approximation consists of working in the center-of-mass reference frame, i.e., setting  $\mathbf{P} = 0$ . This approximation has been first employed in the Refs. [122, 123, 294] using a Hartree-Fock reference state. It was shown that this approximation leads to remarkable agreement with exact energy results at the Hartree-Fock level up to nuclear saturation density (see Figure 43), which indicates that even this rather crude approximation captures the most important contributions from 3N interactions rather well, at least at this order in the many-body expansion. In addition, in this approximation scheme the normal ordered 3N interaction takes exactly the same form as free-space NN interactions, which makes the application to many-body frameworks straightforward. However, some care has to be taken for the correct treatment of the combinatorial factor  $\zeta$  in Eq. (172).
- In Ref. [128] the normal ordering procedure was extended to finite values of  $\mathbf{P}$  by averaging this vector over all directions:

$$n_{(3\mathbf{q}+\mathbf{P})/2}^{\tau} \longrightarrow \Gamma^{\tau}(q, P) = \frac{1}{4\pi} \int d\hat{\mathbf{P}} n_{(3\mathbf{q}+\mathbf{P})/2}^{\tau}. \quad (181)$$

Within this approximation the effective interaction  $\bar{V}_{3N}$  acquires an additional dependence on the absolute value of  $\mathbf{P}$ , while its partial-wave structure is still sufficiently simple so that it can be combined in a straightforward way with contributions from free-space NN interactions in many-body calculations. In addition, this approximation reduces to the  $\mathbf{P} = 0$  approximation for  $P = |\mathbf{P}| \rightarrow 0$  in Eq. (181).

We now discuss and compare both approximations above in more detail. For  $\mathbf{P} = 0$  the analytical structure of the effective NN interaction is sufficiently simple so that normal ordering can be performed in a semi-analytical way, at least for simple 3N interactions like those at N<sup>2</sup>LO in chiral EFT. In Refs. [122, 123]  $\bar{V}_{3N}$  was derived via an automated implementation of the momentum- and spin-exchange operations by representing all spin and isospin operators in matrix form. The antisymmetrized 3N force was then represented in this three-particle basis for general single-particle momenta  $\mathbf{k}_i$ . The traces over spin and isospin degrees of freedom can then be performed in a straightforward way. In the last step the resulting interaction was projected

<sup>11</sup>In Section 4.4 we present a novel method that allows to perform the normal order operation in Eq. (179) exactly, using a framework that does not rely on a partial-wave basis.



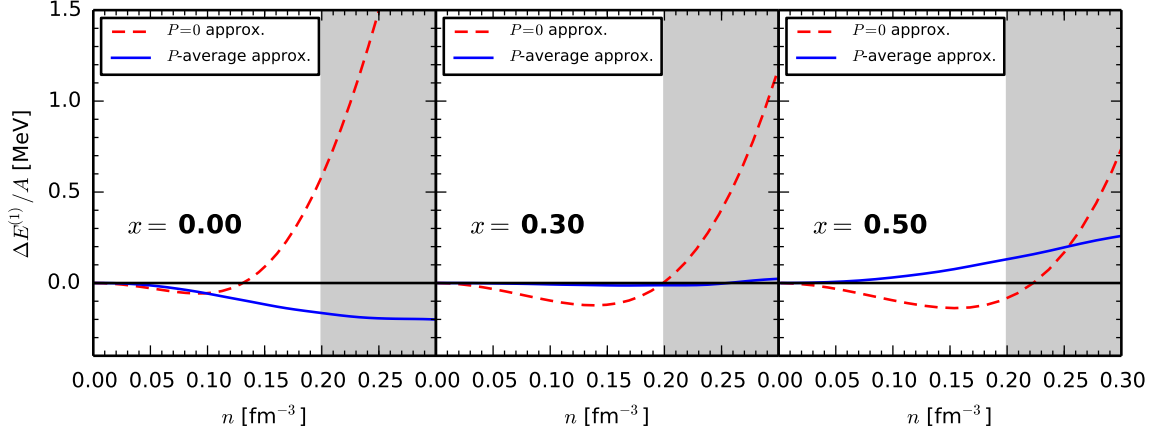


Figure 43: Comparison of 3N Hartree-Fock energies for the  $P=0$  (red dashed) and  $P$ -average approximation (blue solid line) for the effective interaction  $\bar{V}_{3N}$ . Results are shown as difference to the exact Hartree-Fock energy for three proton fractions  $x = n_p/(n_p + n_n)$ , with the proton and neutron densities  $n_p$  and  $n_n$  respectively. The three panels show the results for  $x = 0$  (left),  $x = 0.3$  (center), and  $x = 0.5$  (right panel). The  $P = 0$  values give larger deviations above saturation density, whereas the  $P$ -average approximation behaves more systematic over the entire density range. *Source:* Figure taken from Ref. [128].

on a complete set of two-body spin and isospin operators. For completeness, we provide in Appendix D the complete expressions for the effective interaction  $\bar{V}_{3N}$  in neutron matter ( $n_p^{\text{proton}} = 0$ ) and symmetric nuclear matter ( $n_p^{\text{proton}} = n_p^{\text{neutron}}$ ) in operator form for the N<sup>2</sup>LO 3N interactions in chiral EFT for angularly independent regulators. The interaction includes all spin structures that are invariant under combined rotations in spin and space in a spin-saturated system. In addition to the central spin-independent and spin-spin  $\sigma_1 \cdot \sigma_2$  interactions, it also includes tensor forces  $S_{12}$ , spin-orbit interactions and additional tensor structures, which can be expressed in terms of  $S_{12}$  and quadratic spin-orbit interactions. The resulting expression can be decomposed into partial-wave states in a straightforward way. Obviously, for finite values of  $\mathbf{P}$  the number of possible operators increases significantly, such that this analytical treatment becomes very tedious and impractical.

In Ref. [294] an alternative but related approach for the derivation of the partial-wave matrix elements was followed. Here semi-analytical expressions for the partial-wave momentum matrix elements for  $|\mathbf{p}| = |\mathbf{p}'|$  were derived for the N<sup>2</sup>LO 3N topologies using a Hartree-Fock reference state. These analytical approaches have the advantage that they do not require any large input files of 3N matrix elements, but quickly become tedious when trying to generalize them to more complicated 3N interactions [295–297], angularly-dependent regulators [231], more general reference states or more sophisticated treatments of the center-of-mass momentum dependence.

A more general and flexible approach is to make use of partial-wave representations of 3N interactions. In this case it is possible to derive general relations in different approximations for any 3N interaction that is available in a partial-wave decomposed form. In Ref. [128] normal ordering was first presented for general isospin-asymmetric matter using the angular averaging prescription Eq. (181) for the  $\mathbf{P}$ -dependence. For a Hartree-Fock reference state at zero temperature we can immediately simplify the angular integrals:

$$\Gamma^\tau(q, P) = \frac{1}{4\pi} \int d\hat{\mathbf{P}} n_{(3\mathbf{q}+\mathbf{P})/2}^\tau = \begin{cases} 1 & (3q + P) \leq 2k_{F,\tau}, \\ 0 & |3q - P| \geq 2k_{F,\tau}, \\ \frac{1}{2} \int_{-1}^{\gamma} d \cos \theta n_{(3\mathbf{q}+\mathbf{P})/2}^\tau & \text{otherwise,} \end{cases} \quad (182)$$

with  $\gamma = (4k_{F,\tau}^2 - 9q^2 - P^2)/(6Pq)$  and  $\cos \theta = \hat{\mathbf{q}} \cdot \hat{\mathbf{P}}$ . Explicitly, we obtain for the partial-wave matrix

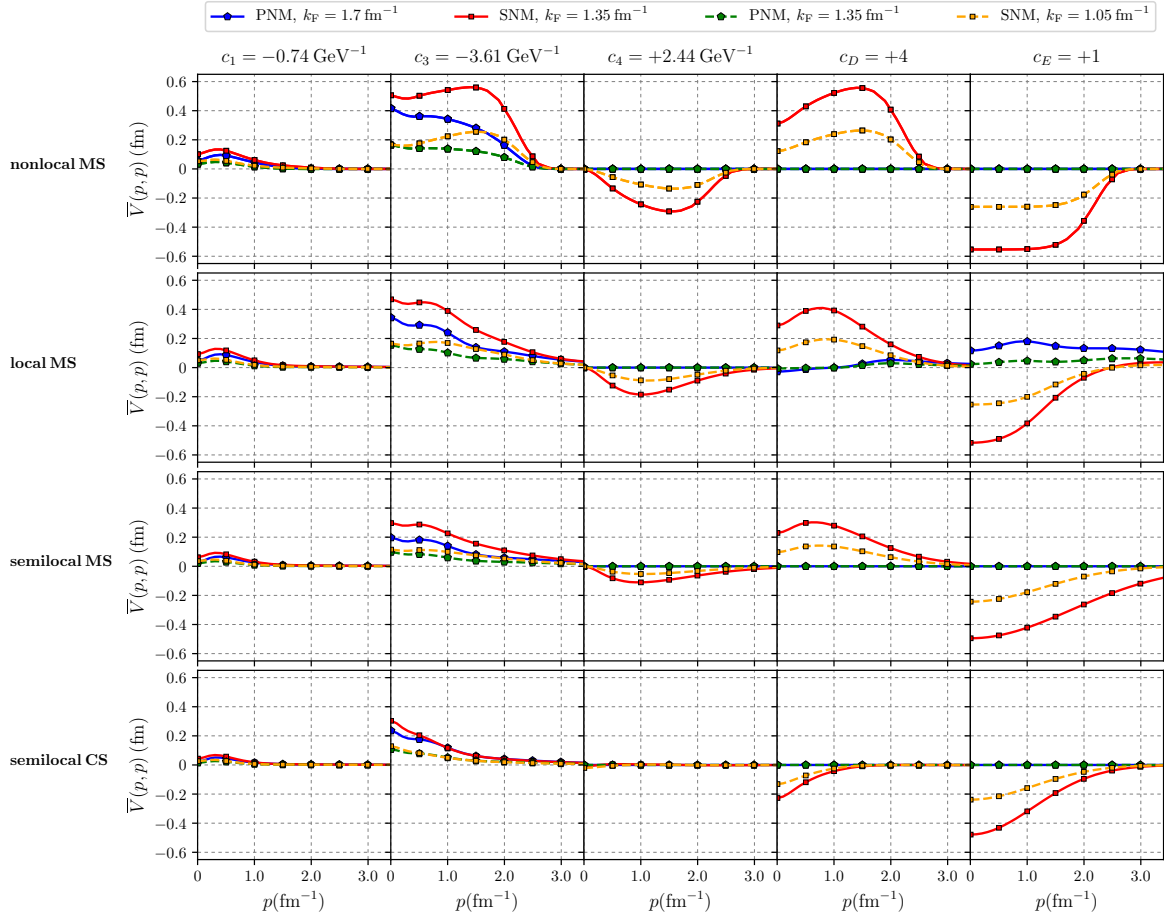


Figure 44: Diagonal momentum-space matrix elements of the effective interaction  $\bar{V}_{3N}(p,p)$  in the channel  $^1S_0$  resulting from normal ordering of the leading-order chiral 3N interactions at  $N^2$ LO in pure neutron matter (PNM) and symmetric nuclear matter (SNM) for two different particle densities. We present the results for the individual contributions at  $N^2$ LO for the 4 different regularization schemes discussed in Section 3.7. The used Fermi momenta correspond approximately to saturation density and half saturation density for neutron matter ( $n_{\text{PNM}}(k_F) = k_F^3/(3\pi^2)$ ) and symmetric matter ( $n_{\text{SNM}}(k_F) = 2k_F^3/(3\pi^2)$ ). For the regulator cutoff scales we used  $\Lambda = 500$  MeV for the momentum-space regulators and  $R = 0.9$  fm for the coordinate-space regularization “semilocal CS”. For the shown results all partial waves up to  $\mathcal{J} = \frac{9}{2}$  have been included.

elements [128]:

$$\begin{aligned}
& \langle p'(L'S')J'T'm_T | \bar{V}_{3N}(P) | p(LS)JTm_T \rangle \\
&= \frac{3}{(4\pi)^2} \left( \frac{3}{4\pi} \right)^3 \int dq q^2 \sum_{\tau, \mathcal{J}} C_{Tm_T \frac{1}{2}\tau}^{\mathcal{J} m_T + \tau} C_{T'm_T \frac{1}{2}\tau}^{\mathcal{J} m_T + \tau} \Gamma^\tau(q, P) \sum_{l,j,\mathcal{J}} \frac{2\mathcal{J}+1}{2J+1} \delta_{ll'} \delta_{jj'} \delta_{JJ'} \langle p'q\alpha' | V_{3N}^{\text{as,reg}} | pq\alpha \rangle, \quad (183)
\end{aligned}$$

where  $V_{3N}^{\text{as,reg}}$  denote the regularized antisymmetrized matrix elements as defined in Eqs. (61) and (90) for nonlocal regulators. However, we stress that the relation in Eq. (183) holds for any type of regulator, since the regulators and their angular dependence are already included in the matrix elements of  $V_{3N}^{\text{as,reg}}$ . Note that, except for neutron and symmetric matter, off-diagonal matrix elements in spin and isospin quantum numbers  $S$  and  $T$  in general contribute to the effective potential. In addition, it also depends on the isospin projection  $m_T$ , as a consequence of the isospin dependence of the occupation function  $n_k^\tau$ . For pure neutron matter and symmetric nuclear matter the sum over the quantum number  $\tau$  can be performed immediately

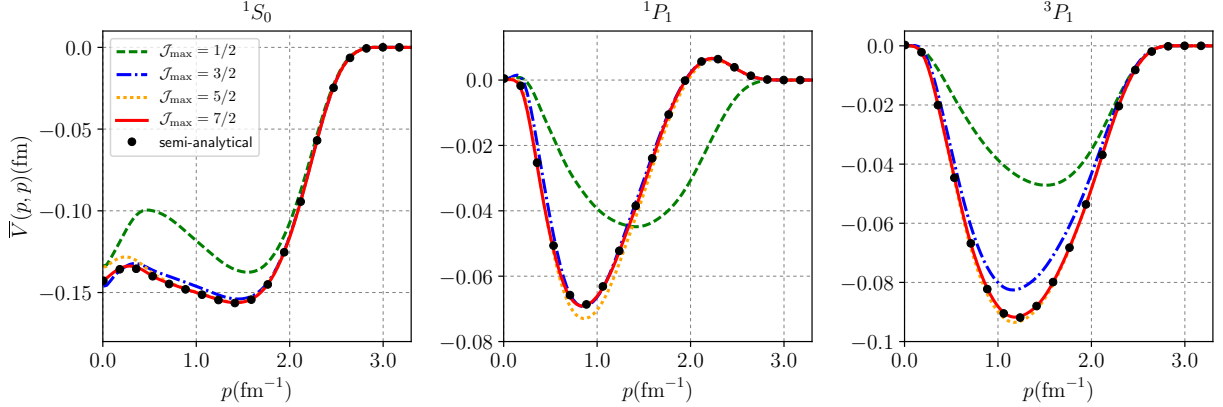


Figure 45: Partial-wave convergence of the effective interaction  $\bar{V}_{3N}(p, p)$  resulting from normal ordering of the leading order chiral 3N interaction proportional to the LEC  $c_3$  at N<sup>2</sup>LO ( $c_3 = 1 \text{ GeV}^{-1}$ ) in symmetric nuclear matter (SNM) at nuclear saturation density  $k_F = 1.35 \text{ fm}^{-1}$  using a Hartree-Fock reference state at zero temperature and using a “nonlocal MS” regularization with  $n = 4$  and  $\Lambda = 500 \text{ MeV}$  (see Eq. (87)). In the different panels we show the diagonal momentum-space matrix elements for the partial-wave channels  $^1S_0$  (left),  $^1P_1$  (center) and  $^3P_1$  (right). For comparison we also show the results obtained from the semi-analytical approach of Ref. [122, 123], i.e., by partial-wave decomposing the effective interaction  $\bar{V}_{3N}^{\text{SNM}}$  given in Eq. (D.6) in Appendix B.

and the isospin factor simplifies to

$$\sum_{\tau} C_{T m_T \frac{1}{2} \tau}^{\mathcal{J} m_{\mathcal{J}} + \tau} C_{T' m_{T'} \frac{1}{2} \tau}^{\mathcal{J} m_{\mathcal{J}} + \tau} = \begin{cases} \delta_{\mathcal{J}, \frac{3}{2}} \delta_{T, 1} \delta_{m_T, -1} & \text{for PNM} \\ \frac{2\mathcal{J}+1}{2T+1} & \text{for SNM} \end{cases} . \quad (184)$$

In Figure 43 we compare results for the 3N Hartree-Fock energies based on the different approximations for the effective NN interaction. The three panels show the energy difference to the exact Hartree-Fock result for proton fraction  $x = 0$  (left),  $x = 0.3$  (center), and  $x = 0.5$  (right). The effective NN interaction based on the  $P = 0$  approximation reproduces the exact results well up to  $n \simeq (0.13 - 0.23) \text{ fm}^{-3}$ , depending on the proton fraction. For higher densities the deviation systematically increases, indicating a breakdown of the  $P = 0$  approximation. In contrast, the results based on the  $P$ -average approximation agree reasonably well with the exact results over the entire density range.

In Figure 44 we present the results of some representative matrix elements of  $\bar{V}_{3N}$  in the  $^1S_0$  channel, computed via Eq. (183). The normalization of the matrix elements is chosen such that they can be combined with those of the free-space NN interaction matrix elements for calculations in the Hartree-Fock approximation using a combinatorial factor of  $\zeta = \frac{1}{3}$  (see Eq. (171))<sup>12</sup>. Like in Figure 29, we show the matrix elements for the individual 3N topologies at N<sup>2</sup>LO for the four different regularization schemes discussed in Section 3.7 for a Hartree-Fock reference state at zero temperature for pure neutron matter and symmetric nuclear matter at two different densities each. The values of the long-range LECs  $c_1$ ,  $c_3$  and  $c_4$  are taken from the Roy-Steiner analysis of Refs. [175, 298], and the short-range LECs  $c_D$  and  $c_E$  are chosen for optimized visibility. The figure shows that the regularization scheme has a significant impact on the values of the matrix elements. While the overall form is quite similar for the different regularizations, the precise values are quite sensitive to the regulator. In particular, for pure neutron matter the effective potential is always vanishing for nonlocal regularizations due to the Pauli principle [122]. Local regulators, in contrast,

<sup>12</sup>In the used normalization and unit convention the NN partial-wave matrix elements the half on-shell Lippmann-Schwinger equation takes the form (compare also Appendix A)

$$\langle p' L' | T_{\text{NN}} | p L \rangle = \langle p' L' | V_{\text{NN}} | p L \rangle + \frac{2}{\pi} \mathcal{P} \sum_{L''} \int dq q^2 \frac{\langle p' L' | V_{\text{NN}} | p'' L'' \rangle \langle p'' L'' | T_{\text{NN}} | p L \rangle}{p^2 - q^2}, \quad (185)$$

with the units  $[V_{\text{NN}}] = [T_{\text{NN}}] = \text{fm}$ . This convention is commonly used in the literature [20] (see also footnote 9).

generally induce a finite range for this interaction and hence leads to finite contributions in pure neutron matter (see also Figure 31 and Refs. [52, 146, 231, 299]).

Finally, in Figure 45 we illustrate the partial-wave convergence of the results for the effective potential for the “nonlocal MS” scheme. For this scheme the normal ordering has been also worked out in a semi-analytical approach (see Appendix D) and hence it provides some independent benchmark results. We show some representative results for the diagonal matrix elements for the partial-wave channels  $^1S_0$ ,  $^1P_1$  and  $^3P_1$  and the N<sup>2</sup>LO topology proportional to the LEC  $c_3 = 1 \text{ GeV}^{-1}$ . It is manifest that the results obtained in a partial wave representation via Eq. (183) show excellent agreement with the semi-analytical results for  $\mathcal{J}_{\text{max}} = \frac{7}{2}$ .

#### 4.3.2. Normal ordering in finite nuclei

Most many-body frameworks for finite nuclei based on basis expansion representations, like, e.g., IM-SRG or CC, are formulated in a harmonic oscillator (HO) basis. That means for these frameworks normal ordering of 3N interactions involves summations over single-particle HO orbitals of the form

$$|a\rangle = |n_a(l_a s_a) j_a m_{j_a} t_a m_{t_a}\rangle, \quad (186)$$

where  $n_a$  is the radial quantum number,  $l_a$  the single-particle orbital angular momentum quantum number coupled with the spin  $s_a = \frac{1}{2}$  to the total angular momentum  $j_a$ . The isospin projection quantum number  $m_{t_a}$  denotes the proton ( $m_{t_a} = +\frac{1}{2}$ ) and neutron orbitals ( $m_{t_a} = -\frac{1}{2}$ ). In order to distinguish the HO Orbital quantum number from the occupation numbers  $n_i$  in Eq. (179), we denote the occupation number in the following by  $\tilde{n}_i$ .

The traditional approach to normal ordering of 3N interactions for applications to finite nuclei consists of the following steps (see Ref. [44] for more details):

- 1.) Transformation of 3N interaction matrix elements, calculated as shown in Section 3 from a Jacobi momentum-space representation to a HO Jacobi representation (see Section 3.9):

$$\langle p' q' \alpha' | V_{3N}^{(i), \text{reg}} | p q \alpha \rangle \rightarrow \langle N' n' \alpha' | V_{3N}^{(i), \text{reg}} | N n \alpha \rangle. \quad (187)$$

Of course, if the interaction matrix elements are calculated directly in HO basis (like, e.g., in Ref. [224]) this step is not necessary.

- 2.) Antisymmetrization of matrix elements. This step can either already be performed in the momentum basis (see Section 3.5) or in the HO basis [40]. Both choices eventually result formally in 3N matrix elements of the form

$$\langle N' n' \alpha' | V_{3N}^{\text{as}, \text{reg}} | N n \alpha \rangle. \quad (188)$$

- 3.) Transformation of the Jacobi HO matrix elements to a single-particle HO basis representation via a three-body Talmi-Moshinski transformation [44, 300]

$$\langle N' n' \alpha' | V_{3N}^{\text{as}, \text{reg}} | N n \alpha \rangle \rightarrow \langle 1' 2' 3' | V_{3N}^{\text{as}, \text{reg}} | 1 2 3 \rangle, \quad (189)$$

where the single-particle states are given by Eq. (186). We note that Eq. (189) is only a formal representation. In practice this  $m$ -scheme representation of the 3N interaction can be optimized by angular-momentum recoupling (see Ref. [44] and Figure 46).

- 4.) Normal ordering of the single-particle 3N interaction matrix elements by summing over a reference state expanded in the HO basis. As for infinite matter, a common choice is a Hartree-Fock reference state. Then Eq. (171) takes the form

$$\langle 1' 2' | \bar{V}_{3N} | 1 2 \rangle = \sum_3 \tilde{n}_3 \langle 1' 2' 3 | V_{3N}^{\text{as}} | 1 2 3 \rangle, \quad (190)$$

where  $\tilde{n}_3$  denote the HO orbital occupation numbers of the Hartree-Fock state.

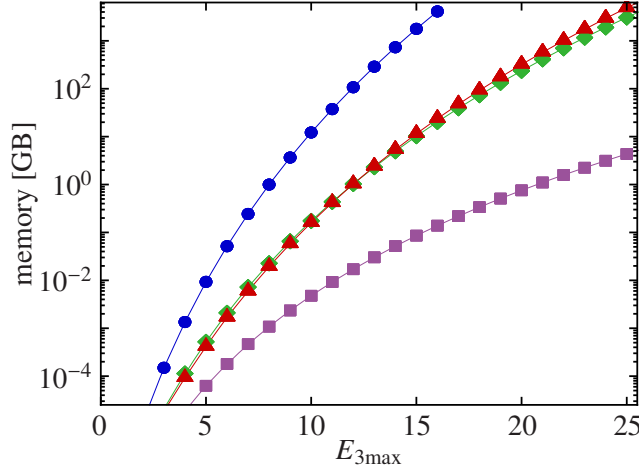


Figure 46: Memory required to store the  $T$ -coefficients ( $\blacklozenge$ ), as well as the three-body matrix elements in the antisymmetrized-Jacobi ( $\blacksquare$ ),  $JT$ -coupled ( $\blacktriangle$ ) and  $m$ -scheme ( $\bullet$ ) representation as function of the maximum three-body energy quantum number  $E_{3\max}$ . All quantities are assumed to be single-precision floating point numbers.

*Source:* Figure taken from Ref. [44].

The corresponding normal-ordered one- and zero-body contributions can then be easily obtained by additional summations over the remaining single-particle states in  $\bar{V}_{3N}$ , as shown in Eq. (170) and (177). Since many-body calculations for nuclei beyond the light sector are performed in a single-particle representation, all these contributions can then be incorporated in a straightforward way in many-body frameworks, under consideration of the correct combinatorial factors  $\zeta$  (see discussion after Eq. (171)).

Although all steps above are straightforward conceptually, the practical implementation involves some technical challenges and limitations. In particular the transformation of 3N interactions to single-particle coordinates (step 3) poses some severe challenges, in particular when studying heavier nuclei. In this regime of the nuclear chart the required basis sizes for storing and computing the required 3N matrix elements become substantial (see Figure 46) and pose serious limitations.

These problems can be avoided by performing normal ordering in a Jacobi coordinate representation of the underlying 3N interaction rather than a single-particle representation. We now illustrate a framework that allows to calculate the effective interaction  $\bar{V}_{3N}$  in a Jacobi momentum representation using a HO reference state. To this end, we will neglect spin and isospin degrees of freedom for the sake of simple and transparent notation. For details and the treatment of general 3N interactions we refer the reader to Ref. [301, 302].

As a first step we introduce a short hand notation for the HO quantum numbers:  $|\gamma_a\rangle = |n_a l_a m_a\rangle$ , and start from the definition of normal ordering in a single-particle HO representation:

$$\langle \gamma_1 \gamma_2 | \bar{V}_{3N} | \gamma_1 \gamma_2 \rangle = \sum_{n_3 l_3 m_3} \tilde{n}_3 \langle \gamma_1 \gamma_2 \gamma_3 | V_{3N}^{\text{as}} | \gamma_1 \gamma_2 \gamma_3 \rangle. \quad (191)$$

By inserting a complete set of two-body single-particle momentum states and projecting on these states this can be rewritten in the form

$$\begin{aligned} \langle \mathbf{k}'_1 \mathbf{k}'_2 | \bar{V}_{3N} | \mathbf{k}_1 \mathbf{k}_2 \rangle &= \sum_{n_3 l_3 m_3} \tilde{n}_3 \langle \mathbf{k}'_1 \mathbf{k}'_2 \gamma_3 | V_{3N}^{\text{as}} | \mathbf{k}_1 \mathbf{k}_2 \gamma_3 \rangle \\ &= \int \frac{d\mathbf{k}_3}{(2\pi)^3} \frac{d\mathbf{k}'_3}{(2\pi)^3} \langle \mathbf{k}'_1 \mathbf{k}'_2 \mathbf{k}'_3 | V_{3N}^{\text{as}} | \mathbf{k}_1 \mathbf{k}_2 \mathbf{k}_3 \rangle \sum_{n_3 l_3 m_3} \tilde{n}_3 \langle \gamma_3 | \mathbf{k}'_3 \rangle \langle \mathbf{k}_3 | \gamma_3 \rangle, \end{aligned} \quad (192)$$

with  $\langle \mathbf{k} | n l m \rangle = R_{nl}(k) Y_{lm}(\hat{\mathbf{k}})$ . Here we used the completeness of the single-particle momentum states  $\int \frac{d\mathbf{k}_i}{(2\pi)^3} |\mathbf{k}_i\rangle \langle \mathbf{k}_i| =$

1 and projected on the momentum states of particles 1, 2, 1' and 2' on both sides by using the orthogonality of the HO wave functions. As a next step we rewrite the single-particle momentum representation of  $\bar{V}_{3N}$  and  $V_{3N}^{\text{as}}$  in a Jacobi representation by using Eq. (26):

$$\langle \mathbf{p}'\mathbf{P}'|\bar{V}_{3N}|\mathbf{p}\mathbf{P}\rangle = \int \frac{d\mathbf{k}_3}{(2\pi)^3} \frac{d\mathbf{k}'_3}{(2\pi)^3} \langle \mathbf{p}'\mathbf{q}'|V_{3N}^{\text{as}}|\mathbf{p}\mathbf{q}\rangle \delta(\mathbf{P} + \mathbf{k}_3 - \mathbf{P}' - \mathbf{k}'_3) \sum_{n_3 l_3 m_3} \tilde{n}_3 \langle \gamma_3|\mathbf{k}'_3\rangle \langle \mathbf{k}_3|\gamma_3\rangle. \quad (193)$$

We expressed the effective potential in terms of the Jacobi momentum  $\mathbf{p}$  and the two-body center-of-mass momentum  $\mathbf{P}$ , i.e.,  $\mathbf{P} = \mathbf{k}_1 + \mathbf{k}_2$  and  $\mathbf{P}' = \mathbf{k}'_1 + \mathbf{k}'_2$ . The single-particle momentum of particle 3 can be easily expressed in terms of these momenta (see Table 2):  $\mathbf{k}_3 = \frac{3}{2}\mathbf{q} + \frac{\mathbf{P}}{2}$ . Note that the two-body center-of-mass momentum  $\mathbf{P}$  is in general not conserved since  $\mathbf{k}_3 \neq \mathbf{k}'_3$ , in contrast to normal ordering with respect to a momentum eigenstate like for nuclear matter (see Section 4.3.1). If the orbital occupation numbers  $\tilde{n}_3$  do not depend on  $m_3$  the sum can be performed immediately:

$$\langle \mathbf{p}'\mathbf{P}'|\bar{V}_{3N}|\mathbf{p}\mathbf{P}\rangle = \int \frac{d\mathbf{k}_3}{(2\pi)^3} \frac{d\mathbf{k}'_3}{(2\pi)^3} \langle \mathbf{p}'\mathbf{q}'|V_{3N}^{\text{as}}|\mathbf{p}\mathbf{q}\rangle \delta(\mathbf{P} + \mathbf{k}_3 - \mathbf{P}' - \mathbf{k}'_3) \sum_{n_3 l_3} \tilde{n}_3 R_{n_3 l_3}(k_3) R_{n_3 l_3}(k'_3) \frac{2l_3 + 1}{4\pi} P_{l_3}(\hat{\mathbf{k}}_3 \cdot \hat{\mathbf{k}}'_3). \quad (194)$$

In the following we stick to this simplified case for illustration. However, the generalization poses no fundamental problems. Eventually, we are interested in the partial-wave matrix elements of the effective potential  $\bar{V}_{3N}$ . Due to the non-Galilean invariance the partial-wave structure becomes more complex compared to a free-space NN interaction (see discussion in Section 4.3). We extend the partial-wave basis by the center-of-mass quantum numbers and project the interaction in Eq. (194) onto these states (compare Eq. (30)):

$$\langle p'\mathbf{P}'(L'L'_{cm})\mathcal{L}|\bar{V}_{3N}|p\mathbf{P}(LL_{cm})\mathcal{L}\rangle = \frac{1}{(2\pi)^6} \sum_{M_L} \int d\hat{\mathbf{p}}d\hat{\mathbf{P}}d\hat{\mathbf{p}}'d\hat{\mathbf{P}}' \mathcal{Y}_{L'L'_{cm}}^{*LM_L}(\hat{\mathbf{P}}', \hat{\mathbf{p}}') \langle \mathbf{p}'\mathbf{P}'|\bar{V}_{3N}|\mathbf{p}\mathbf{P}\rangle \mathcal{Y}_{LL_{cm}}^{LM_L}(\hat{\mathbf{P}}, \hat{\mathbf{p}}). \quad (195)$$

In Eq. (194) we can finally make use of the partial-wave representation of the 3N interaction such that in total the relations (194) together with (195) give a relation for the effective interaction. These relations can be generalized to spin- and isospin-dependent 3N interactions [301, 302] and result in partial wave matrix elements of the form

$$\langle p'\mathbf{P}'[(L'S')J'L'_{cm}]J_{\text{tot}}T|\bar{V}_{3N}|p\mathbf{P}[(LS)JL_{cm}]J_{\text{tot}}T\rangle. \quad (196)$$

The two final steps consist of a transformation of these relative-coordinate momentum matrix elements of  $\bar{V}_{3N}$  to a relative-coordinate HO basis and a successive transformation to a single-particle coordinate representation for applications to many-body frameworks. While the first step is straightforward the latter one requires a generalization of the well-established two-body Talmi-Moshinsky transformation, which usually assumes a Galilean-invariant interaction, i.e., a trivial dependence on the center-of-mass quantum numbers. The model space in the Jacobi representation is characterized by the total energy quantum number  $E$ , which involves relative and center-of-mass quantum numbers:

$$E = 2N_{\text{cm}} + L_{\text{cm}} + 2N + L = e_1 + e_2. \quad (197)$$

Here  $N_{\text{cm}}$  denotes the radial center-of-mass HO quantum number,  $N$  the corresponding quantum number of relative excitations and  $e_i$  the according single-particle energy quantum numbers:  $e_i = 2n_i + l_i$  (see Ref. [44]). In order to take into account all possible recoupling contributions from the Jacobi representation to a single-particle representation, matrix elements for sufficiently large values of  $L_{\text{cm}}$  and  $L$  have to be computed for a given truncation scheme for  $e_i$ . In practice, however, the matrix elements of  $\bar{V}_{3N}$  get suppressed as the values of  $L$  and  $L_{\text{cm}}$  increase. A systematic study of these convergence patterns is work in progress and is key for applications of this framework to realistic many-body calculations [302].

The framework above relates the partial-wave matrix elements of the effective potential directly to the Jacobi momentum-space matrix elements of the underlying 3N interactions. Consequently, it is not necessary

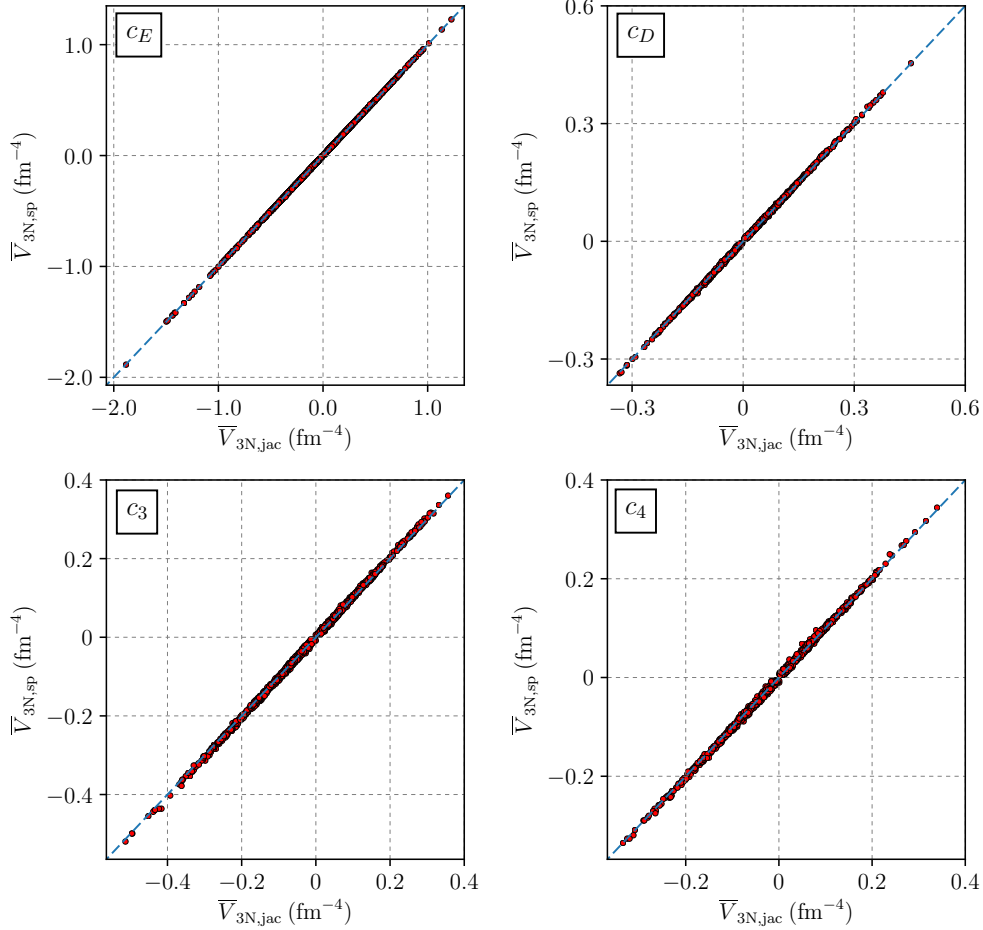


Figure 47: Comparison of normal-ordered 3N matrix elements in the model space  $e_{\max} = 4$  using the established framework formulated in single-particle representation ( $\bar{V}_{3N,\text{sp}}$ ) and the new framework in Jacobi momentum representation ( $\bar{V}_{3N,\text{jac}}$ ) for different 3N topologies at  $N^2\text{LO}$  using  $c_3 = c_4 = 1 \text{ GeV}^{-1}$ ,  $c_D = c_E = 1$ ,  $\Lambda_{3N} = \infty$  and  $\Omega = 13.53 \text{ MeV}$ . For the calculations a harmonic oscillator  $^{16}\text{O}$  reference state was used and the partial-wave truncations  $L, L_{\text{cm}} \leq 4$ . Credits to Johannes Simonis for providing the reference results for  $\bar{V}_{3N,\text{sp}}$ . For details see Refs. [301, 302].

to represent the matrix elements in a single-particle basis at any point and we can hence avoid the basis dimension problems illustrated in Figure 46. In Figure 47 we compare results for  $\bar{V}_{3N}$  obtained in the traditional normal-ordering implementation in a single-particle basis ( $\bar{V}_{3N,\text{sp}}$ ) and those obtained in the novel framework formulated in a Jacobi basis ( $\bar{V}_{3N,\text{jac}}$ ). For all the shown results we use the model space truncations  $L, L_{\text{cm}}, e_i \leq 4$  and  $J_{\text{tot}} \leq 2$ . Furthermore we include all three-body channels up to  $\mathcal{J} = \frac{5}{2}$ . For simplicity we use a harmonic oscillator  $^{16}\text{O}$  reference state and  $\Lambda_{3N} = \infty$  for these first proof-of-principle calculations. For the pure contact 3N interaction proportional to  $c_E$  (top left panel) the results of both approaches show perfect agreement. Here the possible angular momentum couplings are severely restricted by the constraints  $L = l = L' = l' = 0$  for the three-body states  $|\alpha\rangle$ . For 3N interactions containing long-range pion exchange contributions the incorporation of all relevant partial-wave channels becomes more challenging. For the one-pion exchange interaction proportional to  $c_D$  the agreement is still excellent. For the long-range topologies proportional to  $c_3$  and  $c_4$  (lower panels) the coupling of channels with different



angular momenta is stronger than for the one-pion-exchange interaction. We still find good agreement for results with  $J_{\text{tot}} \leq 1$ , while the agreement is not as good as for the interactions proportional to  $c_D$ , indicating that contributions from channels of larger  $L$  and  $L_{\text{cm}}$  are more significant. One big advantage of the new framework is the fact that the values for the radial HO quantum numbers  $N_{\text{cm}}$  and  $N$  can be increased in a simple and straightforward way since these quantum numbers are only introduced in the transformation to HO basis after normal ordering in momentum space, which is computationally very cheap. The main remaining challenges consist in optimizing the normal ordering algorithm such that the accessible partial-wave model space can be increased and in generalizing the framework to more general reference states such that the resulting normal-ordered interactions can be applied to state-of-the-art many-body calculations. Both these improvements are currently work in progress [302].

#### 4.4. Application of 3N interactions without partial-wave decomposition

In Ref. [130] a novel many-body framework was presented for computing the equation of state of dense matter based on NN and 3N interactions within many-body perturbation theory (MBPT) without employing a partial-wave decomposition. This approach has some practical advantages compared to traditional approaches based on partial-wave representation as we illustrate now.

The new framework is formulated in a single-particle basis of the form  $|\mathbf{k}_i \sigma_i \tau_i\rangle$ , where  $\mathbf{k}_i$  are the single-particle momenta of particle  $i$  (see Section 3) and  $\sigma_i$  ( $\tau_i$ ) are the corresponding spin and isospin projections. That means NN and 3N interaction matrix elements take the following form:

$$\begin{aligned} \langle 1'2'|V_{\text{NN}}|12\rangle &= \langle \mathbf{k}'_1 \sigma'_1 \tau'_1 \mathbf{k}'_2 \sigma'_2 \tau'_2 | V_{\text{NN}} | \mathbf{k}_1 \sigma_1 \tau_1 \mathbf{k}_2 \sigma_2 \tau_2 \rangle, \\ \langle 1'2'3'|V_{\text{3N}}|123\rangle &= \langle \mathbf{k}'_1 \sigma'_1 \tau'_1 \mathbf{k}'_2 \sigma'_2 \tau'_2 \mathbf{k}'_3 \sigma'_3 \tau'_3 | V_{\text{3N}} | \mathbf{k}_1 \sigma_1 \tau_1 \mathbf{k}_2 \sigma_2 \tau_2 \mathbf{k}_3 \sigma_3 \tau_3 \rangle. \end{aligned} \quad (198)$$

Instead of prestoring these interaction matrix elements on a discrete grid of mesh points, they can also be represented exactly as matrices in spin-isospin space, where the matrix elements are analytic functions of the single-particle momenta  $\mathbf{k}_i$ . This allows to evaluate matrix elements efficiently on the fly for arbitrary values of momenta, spin and isospin. This is particularly important when using Monte-Carlo integration routines, because it is impossible to know *a priori* which mesh points are being sampled during the many-body calculation.

For the calculations presented in Ref. [130] all NN and 3N interactions up to N<sup>3</sup>LO (for nonlocal regulators) were implemented in this vector representation, where the antisymmetrization was performed in an automated way. For the inclusion of NN and 3N interactions whose operatorial structure is not directly accessible, like RG-evolved potentials (see Section 4.2), it is also possible to resum the contributions of all partial-wave channels in order to obtain the interaction matrix elements in momentum vector representation, e.g. for 3N interactions (see Section 3.4):

$$\begin{aligned} \langle 1'2'3'|V_{\text{3N}}|123\rangle &= \sum_{\mathcal{J}, \mathcal{P}} \frac{1}{2\mathcal{J}+1} \sum_{\alpha, \alpha'} \sum_{M_{\mathcal{J}}} \sum_{\substack{M_L, m_L, M'_L, m'_L \\ M_S, m_S, M'_S, m'_S}} \sum_{M_J, m_J, M'_J, m'_J} C_{\frac{1}{2}\sigma_1 \frac{1}{2}\sigma_2}^{S M_S} C_{\frac{1}{2}\sigma'_1 \frac{1}{2}\sigma'_2}^{S' M'_S} \langle p' q' \alpha' | V_{\text{3N}} | p q \alpha \rangle_{\{ab\}} \\ &\times C_{JM_J m_J}^{\mathcal{J} M_{\mathcal{J}}} C_{J'M'_J m'_J}^{\mathcal{J} M_{\mathcal{J}}} C_{LM_L m_L}^{JM_J} C_{L'M'_L m'_L}^{J'M'_J} C_{lm_l \frac{1}{2}\sigma_3}^{j m_j} C_{l'm'_l \frac{1}{2}\sigma'_3}^{j' m'_j} Y_{L'M'_L}^*(\hat{\mathbf{p}}'_{\{ab\}}) Y_{l'm'_l}^*(\hat{\mathbf{q}}'_{\{ab\}}) Y_{LM_L}(\hat{\mathbf{p}}_{\{ab\}}) Y_{lm_l}(\hat{\mathbf{q}}_{\{ab\}}), \end{aligned} \quad (199)$$

where we have suppressed the isospin quantum numbers in these relations for the sake of a more compact notation. The Jacobi momenta  $\mathbf{p}$ ,  $\mathbf{q}$ ,  $\mathbf{p}'$  and  $\mathbf{q}'$  in the chosen representation  $\{ab\}$  are given in terms of the single particle momenta  $\mathbf{k}_i$  and  $\mathbf{k}'_i$  by the relations summarized in Table 2. In practice all calculations are usually performed based on antisymmetrized interactions, i.e. in terms of Hugenholtz diagrams, so that the matrix elements become independent of the chosen basis representation  $\{ab\}$  (see discussion in Section 3.5).

This representation allows to express and implement individual diagrams in MBPT in a very compact form and opens the way to efficient calculations in MBPT up to much higher orders than was possible in a partial-wave representation. We illustrate the advantage of the new method by considering as an example

the second-order NN contribution in MBPT to the energy of neutron matter (see Figure 48). In order to keep the notation simple we assume without loss of generality spin-independent occupation numbers  $n_{\mathbf{k}}$  and single-particle energies  $\varepsilon_{\mathbf{k}}$ . In a partial-wave representation this contribution takes the following form (using the same normalization convention for the NN matrix elements as for Figure 44, see also footnote on page 81) [122]:

$$\begin{aligned}
\frac{E_{\text{NN}}^{(2)}}{V} &= \frac{1}{4\pi^5} \int dp p^2 dp' p'^2 d \cos \theta_{\mathbf{p}\mathbf{p}'} \int dP_{\text{NN}} P_{\text{NN}}^2 \int d \cos \theta_{\mathbf{P}_{\text{NN}}} \int d\phi_{\mathbf{P}_{\text{NN}}} \sum_{\tilde{L}} P_{\tilde{L}}(\hat{\mathbf{p}} \cdot \hat{\mathbf{p}}') \\
&\times \frac{n_{\mathbf{p}-\mathbf{P}_{\text{NN}}/2} n_{\mathbf{p}+\mathbf{P}_{\text{NN}}/2} (1 - n_{\mathbf{p}'-\mathbf{P}_{\text{NN}}/2}) (1 - n_{\mathbf{p}'+\mathbf{P}_{\text{NN}}/2})}{\varepsilon_{\mathbf{p}-\mathbf{P}_{\text{NN}}/2} - \varepsilon_{\mathbf{p}+\mathbf{P}_{\text{NN}}/2} - \varepsilon_{\mathbf{p}'-\mathbf{P}_{\text{NN}}/2} - \varepsilon_{\mathbf{p}'+\mathbf{P}_{\text{NN}}/2}} \\
&\times \sum_S \sum_{J, L, L'} \sum_{\tilde{J}, \tilde{L}, \tilde{L}'} (-1)^{L+L'+L} C_{L0L0}^{L0} C_{L'0L'0}^{L0} (1 - (-1)^{L+S+1}) (1 - (-1)^{\tilde{L}+S+1}) \sqrt{\hat{L}\hat{L}'\hat{\tilde{L}}\hat{\tilde{L}}'} \hat{J}\hat{J}' \\
&\times \left\{ \begin{matrix} L & S & J \\ \tilde{J} & \tilde{L} & \tilde{L}' \end{matrix} \right\} \left\{ \begin{matrix} J & S & L' \\ \tilde{L} & \tilde{L} & \tilde{J}' \end{matrix} \right\} \langle p'(\tilde{L}'S)\tilde{J} | V_{\text{NN}}^{\text{as}} | p(S\tilde{L})\tilde{J} \rangle \langle p(LS)J | V_{\text{NN}}^{\text{as}} | p'(\tilde{L}'S)J \rangle, \quad (200)
\end{aligned}$$

where  $\mathbf{P}_{\text{NN}}$  is the two-body center-of-mass momentum  $\mathbf{P}_{\text{NN}} = \mathbf{k}_1 + \mathbf{k}_2 = \mathbf{k}'_1 + \mathbf{k}'_2$ . Although this expression can be implemented in a straightforward way on a computer, it is quite involved already at this low order in MBPT, and the analytical derivation requires some effort. Furthermore, the implementation and benchmarking of the corresponding expressions at third order in MBPT becomes quite challenging and tedious [126, 129, 303]. In addition, pushing this approach to even higher orders becomes eventually impractical.

In contrast, in the single-particle vector representation given in Eq. (198) the same diagram can be expressed in a much more compact form:

$$\begin{aligned}
\frac{E_{\text{NN}}^{(2)}}{V} &= \frac{1}{4} \prod_{i=1}^2 \text{Tr}_{\sigma_i} \int \frac{d\mathbf{k}_i}{(2\pi)^3} \frac{d\mathbf{k}'_i}{(2\pi)^3} (2\pi)^3 \delta(\mathbf{k}_1 + \mathbf{k}_2 - \mathbf{k}'_1 - \mathbf{k}'_2) \left| \langle \mathbf{k}'_1 \sigma'_1 \mathbf{k}'_2 \sigma'_2 | \hat{V}_{\text{NN}} | \mathbf{k}_1 \sigma_1 \mathbf{k}_2 \sigma_2 \rangle \right|^2 \frac{n_{\mathbf{k}_1} n_{\mathbf{k}_2} (1 - n_{\mathbf{k}'_1}) (1 - n_{\mathbf{k}'_2})}{\varepsilon_{\mathbf{k}_1} + \varepsilon_{\mathbf{k}_2} - \varepsilon_{\mathbf{k}'_1} - \varepsilon_{\mathbf{k}'_2}} \\
&= \frac{1}{4} \sum_{1,2} \sum_{1',2'} \langle 1'2' | V_{\text{NN}} | 12 \rangle \langle 12 | V_{\text{NN}} | 1'2' \rangle \delta_{1+2,1'+2'} \frac{n_1 n_2 (1 - n_{1'}) (1 - n_{2'})}{\varepsilon_1 + \varepsilon_2 - \varepsilon_{1'} - \varepsilon_{2'}} \\
&= \frac{1}{4} \sum_{\substack{i,j \\ \alpha\beta}} \frac{\langle \alpha\beta | V_{\text{NN}} | ij \rangle \langle ij | V_{\text{NN}} | \alpha\beta \rangle}{D_{ij\alpha\beta}}, \quad (201)
\end{aligned}$$

where we suppressed the isospin projection quantum numbers  $\tau_i = -\frac{1}{2}$ . In the last steps we introduced a compact notation via the definition

$$D_{ijk\dots\alpha\beta\gamma\dots} = \varepsilon_i + \varepsilon_j + \varepsilon_k + \dots - \varepsilon_\alpha - \varepsilon_\beta - \varepsilon_\gamma - \dots \quad (202)$$

Here, greek indices  $\alpha, \beta, \gamma, \dots$  denote particle states and latin indices  $i, j, k, \dots$  holes, e.g.:

$$\sum_{\beta} = \text{Tr}_{\sigma_{\beta}} \int \frac{d\mathbf{k}_{\beta}}{(2\pi)^3} (1 - n_{\mathbf{k}_{\beta}}), \quad \sum_i = \text{Tr}_{\sigma_i} \int \frac{d\mathbf{k}_i}{(2\pi)^3} n_{\mathbf{k}_i}, \quad (203)$$

with implicit delta functions that enforce the conservation of the center-of-mass momentum in each interaction process. For systems with a finite proton fraction these relations can be generalized in a straightforward way by appropriate traces over isospin quantum numbers.

Equation (201) shows that the computation of diagrams effectively amounts to the evaluation of high-dimensional phase-space integrals over the single-particle momenta, restricted by the occupation numbers  $n_{\mathbf{k}}$  and the cutoff regularization scales of the NN and 3N interactions, plus the computation of discrete sums over spin quantum numbers. Tracing over spin and isospin states of each particle is straightforward

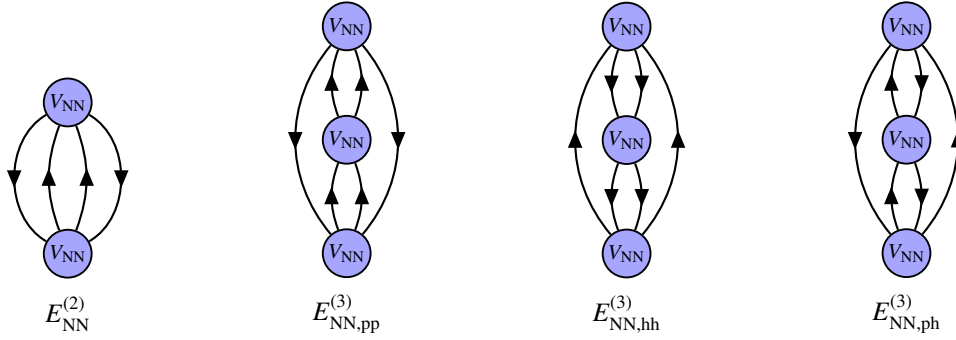


Figure 48: Diagrammatic representation of the second-order (left) and third-order contributions (three right diagrams) to the energy density from NN interactions. Arrows pointing up in the propagators indicate particle states and arrows pointing down hole states.

and can be fully automated in the representation Eq. (198). The integrals over the momenta can be computed efficiently using adaptive Monte-Carlo algorithms [304–306], which are especially suitable for high-dimensional integrals.

The compact form of the expressions for each diagram makes the implementation of arbitrary energy diagrams straightforward, even up to high orders in MBPT. Since the number of diagrams at a given order increases rapidly, with 3, 39 and 840 at third, fourth and fifth order for NN-only interactions [307–309], we developed a general framework that allows to generate the analytic expressions for each diagram in a fully automated way [130]. This framework can also be combined with other sophisticated automated many-body diagram generation frameworks [310] that allow to push MBPT calculations to even higher orders.

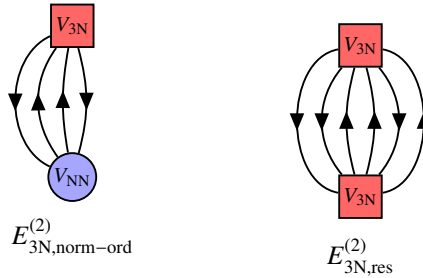


Figure 49: Diagrammatic representation of second-order contributions to the energy density from NN interactions and 3N interactions. Arrows pointing up in the propagators indicate particle states and arrows pointing down hole states. The left diagram shows a contribution that involves one normal-ordered 3N interaction (see Figure 42), whereas the right diagram shows the contributions from residual 3N interactions at this order (see Section 4.3).

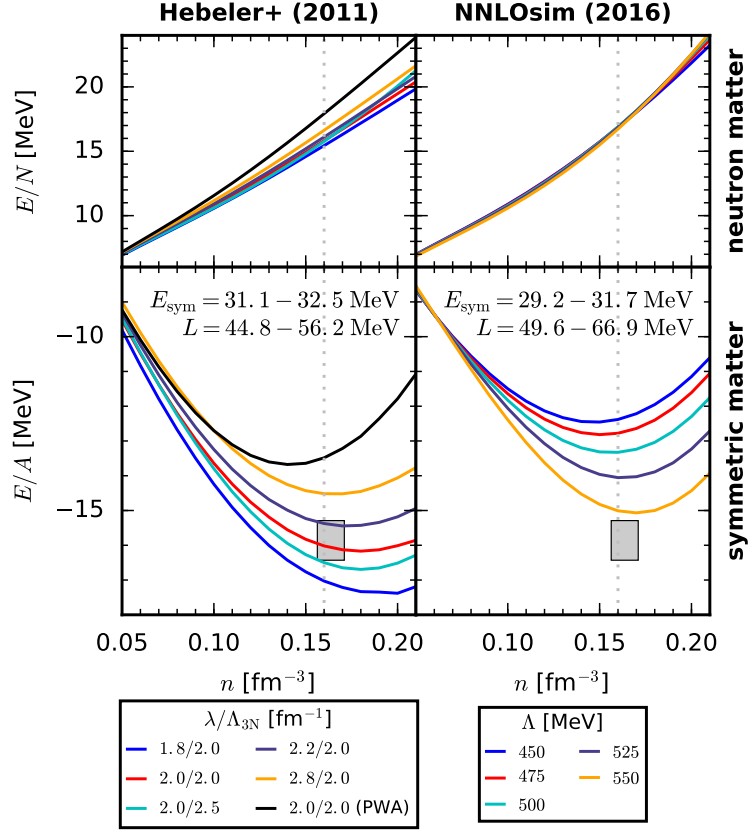


Figure 50: Energy per particle of neutron matter (top row) and symmetric nuclear matter (bottom row) based on the “Hebeler+” [123] and “N<sup>2</sup>LO<sub>sim</sub>” [206] NN and 3N interactions (columns), computed in MBPT including contributions up to 4th order in the many-body expansion. Results are shown for  $\lambda/\Lambda_{3N}$  for the interactions of Ref. [123] (see also Section 5.1) and  $\Lambda = \Lambda_{NN, 3N}$  for those of Ref. [206].  
*Source:* Figure taken from Ref. [130].

For example, the expressions for the third order diagrams (see Figure 48) are given by [309]

$$\begin{aligned}
\frac{E_{NN,pp}^{(3)}}{V} &= \frac{1}{8} \sum_{\substack{ij \\ \alpha\beta\gamma\delta}} \frac{\langle ij|V_{NN}|\alpha\beta\rangle \langle \alpha\beta|V_{NN}|\gamma\delta\rangle \langle \gamma\delta|V_{NN}|ij\rangle}{D_{i\alpha\beta}D_{i\gamma\delta}}, \\
\frac{E_{NN,hh}^{(3)}}{V} &= \frac{1}{8} \sum_{\substack{ijkl \\ \alpha\beta}} \frac{\langle \alpha\beta|V_{NN}|kl\rangle \langle kl|V_{NN}|ij\rangle \langle ij|V_{NN}|\alpha\beta\rangle}{D_{i\alpha\beta}D_{kl\alpha\beta}}, \\
\frac{E_{NN,ph}^{(3)}}{V} &= \sum_{\substack{ijk \\ \alpha\beta\gamma}} \frac{\langle ij|V_{NN}|\alpha\beta\rangle \langle \alpha k|V_{NN}|i\gamma\rangle \langle \beta\gamma|V_{NN}|jk\rangle}{D_{i\alpha\beta}D_{jk\beta\gamma}},
\end{aligned} \tag{204}$$

where the individual contributions are usually referred to particle-particle (“pp”), hole-hole (“hh”), and particle-hole (“ph”) excitations, respectively, according to the type of intermediate states connecting the three interaction vertices.

The contribution at second order in the MBPT expansion including one three-body interaction (Fig-

ure 49) takes the following form:

$$\frac{E_{3\text{N},\text{norm-ord}}^{(2)}}{V} = \frac{1}{2} \sum_{\substack{ijk \\ \alpha\beta}} \frac{\langle ij|V_{\text{NN}}|\alpha\beta\rangle \langle \alpha\beta k|V_{3\text{N}}|ijk\rangle}{D_{ij\alpha\beta}}. \quad (205)$$

Note that this contribution corresponds to a contribution that includes a normal-ordered 3N interaction (see Section 4.3). Figure 49 also shows an example of contributions from residual 3N contributions,  $E_{3\text{N},\text{res}}^{(2)}$ . This diagram is given by the following expression:

$$\frac{E_{3\text{N},\text{res}}^{(2)}}{V} = \frac{1}{36} \sum_{\substack{ijk \\ \alpha\beta\gamma}} \frac{\langle ijk|V_{3\text{N}}|\alpha\beta\gamma\rangle \langle \alpha\beta\gamma|V_{3\text{N}}|ijk\rangle}{D_{ij\alpha\beta\gamma}}. \quad (206)$$

In Ref. [130] all the contributions discussed above, plus all NN diagrams up to fourth order have been included. This new framework offers new paths to check the normal-ordering approximation for 3N interactions in nuclear matter and allows to push MBPT for nuclear matter to much higher orders and hence allows to estimate uncertainties due to the many-body expansion in a more systematic way (see also Figure 14). Of course, the Monte-Carlo evaluation contains inherent statistical uncertainties, which need to be checked for each diagram.

In Figure 50 we show the results for the energy per particle in symmetric nuclear matter and neutron matter based on the interactions of Ref. [123] (“Hebeler+”) and the “N<sup>2</sup>LO<sub>sim</sub>” [206] NN and 3N interactions (see also discussion in Section 2.3.1) up to fourth order in MBPT. For symmetric matter we show the empirical saturation region by a gray box. We also give results for the symmetry energy  $E_{\text{sym}} = E/N - E/A$  as well as its slope parameter  $L = 3n_0\partial_n E_{\text{sym}}$  at nuclear saturation density,  $n_0 = 0.16 \text{ fm}^{-3}$  (dashed vertical line).

Note that the “Hebeler+” potentials include NN (N<sup>3</sup>LO) and 3N forces (N<sup>2</sup>LO) up to different orders in the chiral expansion. Despite being fitted to only few-body data, these interactions are able to reproduce empirical saturation in Figure 50 within uncertainties given by the spread of the individual “Hebeler+” interactions [123]. In addition, recent calculations of medium to heavy nuclei based on some of these interactions show remarkable agreement with experiment [93, 104–106, 228, 311] and thus offer new ab initio possibilities to investigate the nuclear chart. The second column of Figure 50 shows results for the “N<sup>2</sup>LO<sub>sim</sub>” potentials [206] for different cutoff values (see legend). These interactions were obtained by a simultaneous fit of all low-energy couplings to two-body and few-body data for  $\Lambda_{\text{NN}} = \Lambda_{3\text{N}}$ . We observe a weak cutoff dependence for these potentials in neutron matter over the entire density range and in symmetric matter up to  $n \lesssim 0.08 \text{ fm}^{-3}$ . At higher densities, the variation of the energy per particle increases up to  $\approx 3 \text{ MeV}$  at  $n_0 = 0.16 \text{ fm}^{-3}$  with a very similar density dependence. Overall, all the “N<sup>2</sup>LO<sub>sim</sub>” interactions turn out to be too repulsive compared to the empirical saturation region.

## 5. Applications to nuclei and matter

In this chapter we present recent results of ab initio calculations of light nuclei, medium-mass nuclei as well as dense matter based on state-of-the-art chiral NN and 3N interactions. The selection is not intended to be exhaustive, but is rather supposed to illustrate the current status and open issues in nuclear structure theory. The discussed results cover various observables of nuclei in different regimes of the nuclear chart and highlight the capabilities as well as limitations of presently used interactions and many-body frameworks. The employed interactions include different regularization schemes (see Section 3.7) and fitting strategies for the LECs of the NN and 3N interactions (see Section 2.3).

### 5.1. SRG evolution of 3N interactions versus low-resolution fits

Many of the studies discussed in the following sections are based on the NN plus 3N interactions derived in Ref. [123]. As already discussed in Section 2.3.1, these interactions consist of NN interactions evolved to different SRG resolution scales  $\lambda_{\text{SRG}}$  plus 3N interactions fitted to the binding energy of  ${}^3\text{H}$  and the point-proton radius of  ${}^4\text{He}$  at each scale (see also Table 7). Even though the interactions are only fitted to NN and few-body observables, the interactions exhibit realistic saturation properties of symmetric matter (see Figure 50). Furthermore, calculations based on the interaction with  $\lambda_{\text{SRG}}/\Lambda_{3\text{N}} = 1.8/2.0$  (“1.8/2.0 (EM)”) show a remarkable agreement with experimental binding energies for medium-mass nuclei (see also Figure 13). In Table 7 we give the specific values of the 3N couplings  $c_D$  and  $c_E$  for the different values of the SRG resolution scale  $\lambda_{\text{SRG}}$  and the 3N cutoff scale  $\Lambda_{3\text{N}}$ . The listed values include the results published in Ref. [123] as well as results for additional resolution scales. The fits at different scales map out a continuous trajectory for the couplings  $c_D$  and  $c_E$ . We also provide results for the point charge radius of  ${}^3\text{H}$  and the binding energy of  ${}^4\text{He}$  at the different scales. Given that there exists a correlation between the ground-state energies of three- and four-body systems (“Tjon line”) [208, 209] we expect that the ground state energies for

$\lambda_{\text{SRG}}$ (fm $^{-1}$ )	NN SRG evolution + 3N fits					NN+3N SRG evolution		
	$\Lambda_{3\text{NF}}$ (fm $^{-1}$ )	$c_D$	$c_E$	$r_{3\text{H}}$ (fm)	$E_{4\text{He}}$ (MeV)	$E_{3\text{H}}$ (MeV)	$r_{3\text{H}}$ (fm)	$E_{4\text{He}}$ (MeV)
$\infty$	2.0	+1.5	0.114	1.601	-28.64(4)	-8.482	1.601	-28.64(4)
2.8	2.0 [123]	+1.278	-0.078	1.604	-28.75(2)	-8.482	1.605	-28.72(2)
2.6	2.0	+1.26	-0.099	1.605	-28.77(2)	-8.481	1.606	-28.73(2)
2.4	2.0	+1.265	-0.115	1.606	-28.80(2)	-8.481	1.608	-28.73(2)
2.2	2.0 [123]	+1.214	-0.137	1.608	-28.86(2)	-8.480	1.611	-28.74(2)
2.0	2.0 [123]	+1.271	-0.131	1.612	-28.95(2)	-8.479	1.615	-28.75(2)
1.8	2.0 [123]	+1.264	-0.120	1.617	-29.11(2)	-8.478	1.622	-28.76(2)
1.6	2.0	+1.25	-0.075	1.626	-29.42(2)	-8.476	1.635	-28.79(2)
$\infty$	2.5	-1.45	-0.633	1.604	-28.65(4)	-8.482	1.604	-28.65(4)
2.8	2.5	-1.35	-0.735	1.606	-28.84(2)	-8.482	1.608	-28.75(2)
2.6	2.5	-1.2	-0.75	1.606	-28.85(2)	-8.482	1.609	-28.76(2)
2.4	2.5	-1.0	-0.725	1.607	-28.89(2)	-8.482	1.610	-28.77(2)
2.2	2.5	-0.7	-0.675	1.609	-28.95(2)	-8.481	1.613	-28.77(2)
2.0	2.5 [123]	-0.292	-0.592	1.612	-29.05(2)	-8.481	1.617	-28.77(2)
1.8	2.5	0.05	-0.503	1.617	-29.21(2)	-8.480	1.625	-28.77(2)
1.6	2.5	0.55	-0.353	1.626	-29.48(2)	-8.478	1.638	-28.77(2)

Table 7: Results for the  $c_D$  and  $c_E$  couplings, fit to  $E_{3\text{H}} = -8.482\text{MeV}$  and to the point charge radius  $r_{4\text{He}} = 1.464\text{fm}$  (based on Ref. [312]) for the NN/3N cutoffs and the EM  $c_i$  values ( $c_1 = -0.81\text{GeV}^{-1}$ ,  $c_3 = -3.2\text{GeV}^{-1}$ ,  $c_4 = +5.4\text{GeV}^{-1}$ ) used, see Ref. [123] for details. The  ${}^3\text{H}$  point charge radius  $r_{3\text{H}}$  is calculated from the charge form factor solutions of the Faddeev equations and the energies  $E_{4\text{He}}$  are computed via a Jacobi NCSM harmonic oscillator diagonalization code (credits to Andreas Ekström for providing the code). For comparison, the experimental  ${}^3\text{H}$  point charge radius is  $1.5978 \pm 0.040$  [227]. The basis space truncations  $\mathcal{J}_{\text{max}} = \frac{7}{2}$  and  $J_{\text{max}} = 5$  have been used for the four-body calculations (see Section 3.4). The slight violation of unitarity as seen in the  ${}^3\text{H}$  binding energy is mainly due to the treatment of the charge dependence of the NN interaction in the SRG evolution (see main text and also discussion in Section 4.2.2 for details).

${}^4\text{He}$  should not change too much when varying  $\lambda_{\text{SRG}}$ , since the binding energy of  ${}^3\text{H}$  is fixed by construction in the fit. Still, the observed variation is about 800 keV over the full range of scales, while all energies are slightly overbound compared to the experimental ground-state energy  $E_{\text{gs}} = -28.296$  MeV [149]. The point charge radius of  ${}^3\text{He}$  changes only by about 0.025 fm for both values of  $\Lambda_{3\text{N}}$ .

For comparison, we present the corresponding results for consistently-evolved NN+3N interactions, using the SRG framework presented in Section 4.2.1. The SRG evolution is performed using an isospin-averaged NN interaction, i.e., the isospin  $T = 1$  channels are treated as

$$V_{\text{NN}} = \frac{V_{\text{NN}}^{\text{nn}} + V_{\text{NN}}^{\text{np}} + V_{\text{NN}}^{\text{pp}}}{3}, \quad (207)$$

where  $V_{\text{NN}}^{\text{nn}}$ ,  $V_{\text{NN}}^{\text{np}}$  and  $V_{\text{NN}}^{\text{pp}}$  represent the neutron-neutron, neutron-proton and proton-proton interactions,

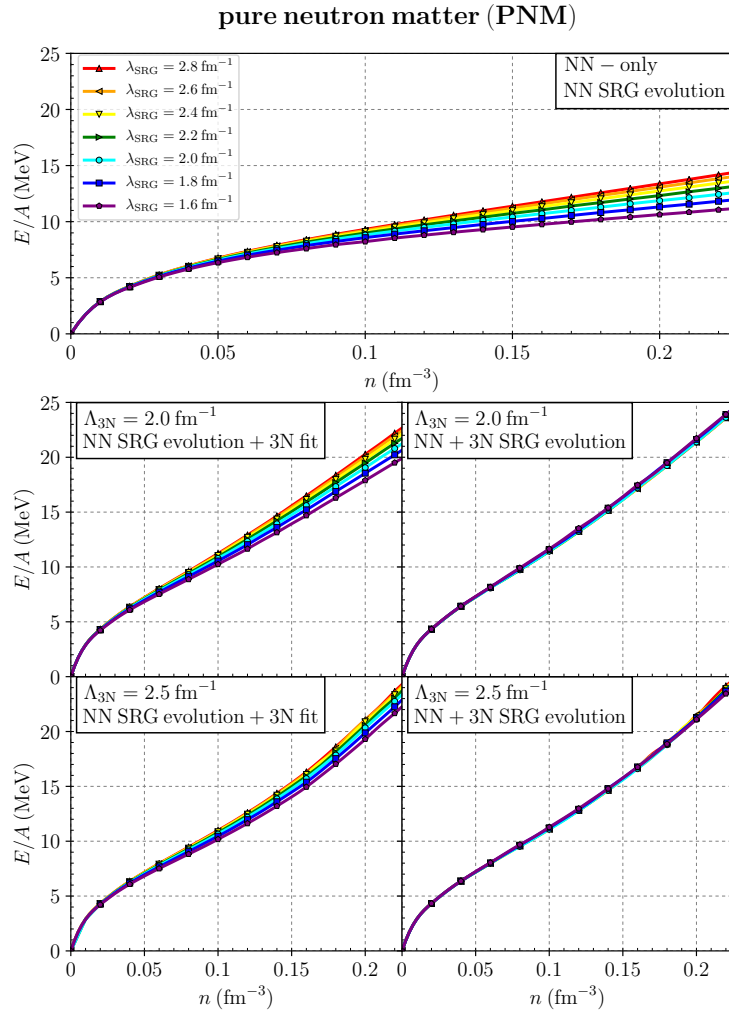


Figure 51: The energy per particle of pure neutron matter for the interactions specified in Table 7. The plots show results of MBPT calculations under consideration of all NN and 3N contributions, including residual terms up to 2nd order. The 3N contributions at 3rd order are treated in normal-ordering approximation (using  $\mathbf{P} = 0$ ). The top panels show the NN-only results at different resolution scales, while the lower two rows show the results based on the interactions defined in the left and right columns of Table 7.



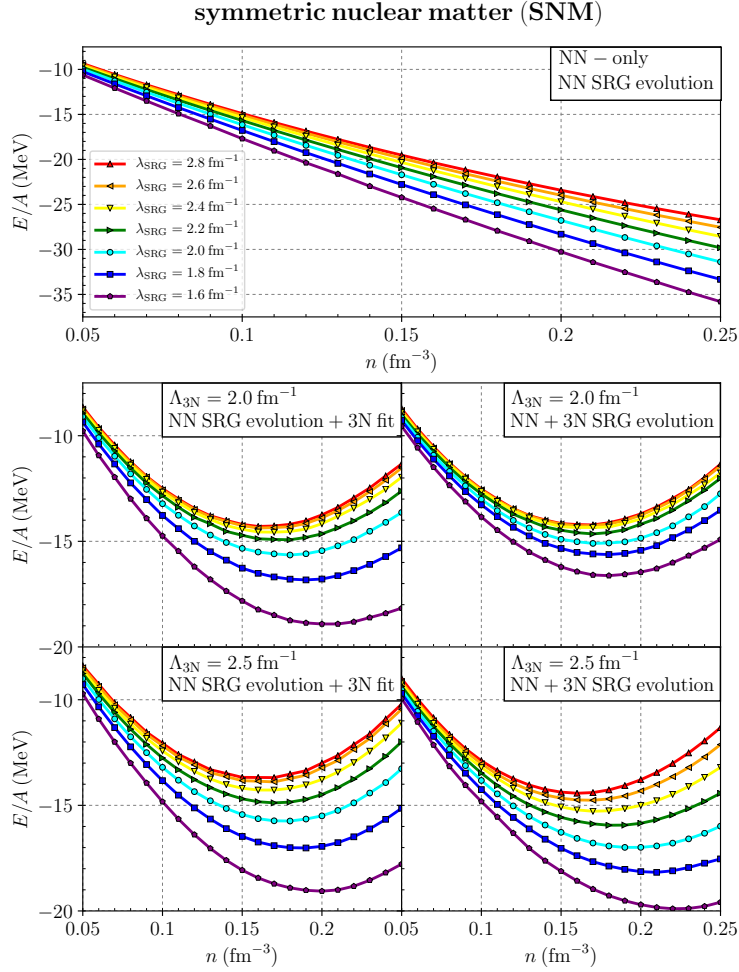


Figure 52: The energy per particle of symmetric nuclear matter for the interactions specified in Table 7. See caption of Figure 51 for details regarding the many-body calculations and the shown results.

respectively. We note that this approximation leads to a violation of unitarity for the  ${}^3\text{H}$  binding energy, which is determined from the solutions of the Faddeev equations including the proper treatment of the charge dependence of NN interactions [313]. For the calculations of nuclear matter (see next section) all Coulomb interactions are switched off in the SRG evolution, while for the few-body results in Table 7 the Coulomb contributions are included in  $V_{\text{NN}}^{\text{PP}}$  and are evolved consistently. We emphasize that for the shown results for  $r_{3\text{H}}$  in Table 7 we did not evolve the radius operator for these calculations. Due to this and due to the isospin treatment, the radius varies by about 0.03 fm over the shown resolution scale range. The energy of  ${}^4\text{He}$  exhibits a significantly smaller variation for the consistently-evolved 3N interactions for both cutoff values  $\Lambda_{3\text{N}}$  compared to the low-resolution fits shown in the left column.

### 5.2. Nuclear matter based on consistently SRG-evolved 3N interactions

The consistent evolution of NN and 3N interactions within the SRG has opened new avenues that allowed to push the scope of various *ab initio* frameworks for nuclei to heavier masses (see Sections 1 and 4.2). On the other hand, SRG-evolved NN and 3N forces have not yet been applied to many-body frameworks for nuclear matter since the SRG evolution of 3N interactions was always performed in a harmonic oscillator representation. Thanks to the new developments discussed in Section 4.2 it is now possible to perform the

SRG evolution in the plane-wave momentum representation so that a given evolved interaction can now be applied to light nuclei, medium-mass nuclei as well as nuclear matter. In this section we present first results for pure neutron matter as well as symmetric nuclear matter based on consistently-evolved NN plus 3N interactions. To this end, we start from the set of interactions derived in Ref. [123] plus the new fits as specified in Table 7. In particular, we perform matter calculations based on the interactions “NN SRG evolution + 3N fits” and “NN+3N SRG evolution” at the SRG scales in the range  $\lambda_{\text{SRG}} = [1.6, 2.8]$ . The many-body calculations are performed within many-body perturbation theory (MBPT), under consideration of all contributions from NN and 3N interactions up to 2nd order, including residual 3N contributions (see Section 4.3). The third-order diagrams are taken into account in the normal-ordering approximation setting  $\mathbf{P} = 0$  for the two-body center-of-mass momentum (see Section 4.3.1). For the evaluation of the diagrams we use the Monte-Carlo approach discussed in Section 4.4, while all NN and 3N partial-wave contributions are resummed for each Monte-Carlo evaluation. The results are shown in Figures 51 and 52. For the discussion of the results it is important to note the following points:

- The many-body convergence is usually more rapid for PNM than for SNM using typical chiral interactions. Specifically, the employed many-body truncation leads to almost perfectly converged results for PNM, in particular at small  $\lambda_{\text{SRG}}$  for the consistently-evolved interactions, whereas for SNM higher order terms in the many-body expansion can still contribute significant contributions.
- The relative size of 3N contributions compared to NN terms is typically smaller in PNM than in SNM by a significant amount. This suggests that effects of induced higher-body forces will typically be more important in SNM than in PNM.

The results for PNM exhibit only a very mild dependence on the SRG resolution scale for consistently-evolved interactions, whereas for the fitted 3N interactions we observe a variation of up to about 2 MeV per particle at saturation density (see left panels of Figure 51). The SNM results, on the other hand, sensitively depend on the chosen regularization scale  $\Lambda_{3\text{N}}$ , as shown in Figure 52. While for  $\Lambda_{3\text{N}} = 2.0 \text{ fm}^{-1}$  we find a significantly smaller dependence on  $\lambda_{\text{SRG}}$  for the consistently-evolved 3N interactions compared to the fitted interactions, for  $\Lambda_{3\text{N}} = 2.5 \text{ fm}^{-1}$  we find a sizable dependence in both cases. This is an indication that the strength of induced higher-body contributions increases as the regularization cutoff scale  $\Lambda_{3\text{N}}$  of the initial 3N interactions gets larger. This trend has also been found in calculations of atomic nuclei (see, e.g., Refs. [43, 88]). On the other hand, the good invariance of the ground state energy results of  ${}^4\text{He}$  for consistently-evolved NN and 3N interactions suggests that the contributions of induced 4N interactions are rather small in light nuclei. Furthermore, it is remarkable that for  $\Lambda_{3\text{N}} = 2.0 \text{ fm}^{-1}$  the rather narrow uncertainty band includes the phenomenological saturation region. These findings suggest that it could be worthwhile to apply these consistently-evolved NN and 3N interactions also to many-body frameworks for finite nuclei.

### 5.3. Ground-state energies of nuclei

In Ref. [314] ground-state energies of nuclei from helium to iron were studied within the VS-IM-SRG framework (see Section 1) using the interaction “1.8/2.0 (EM)” of Ref. [123] (see previous section). Within this framework an effective interaction is computed via the IM-SRG for a given nucleus and is then used as input for a valence-space diagonalization, which gives access to observables of closed- and open-shell systems within a given isotopic chain. A particular focus of this work was put on the location of the drip line, i.e., the point in the nuclear chart beyond which the nucleons no longer form a bound system. One indication for the drip line is a negative one- and two-body nucleon separation energy, which involves the decay of a nucleus via nucleon emission. Predicting the location of the drip line plays a key role for our understanding of  $r$ -processes that govern the synthesis of heavy elements in neutron star mergers [315, 316]. Given the excellent agreement of computed ground-state energies with experimental data in the known regime of the nuclear chart (see Figure 53), these calculations are expected to provide reasonable theoretical predictions beyond the region where data exists, including some uncertainty estimates. While this work does not yet include, e.g., uncertainties from the chiral EFT truncation (see Section 2.4) or many-body uncertainties from

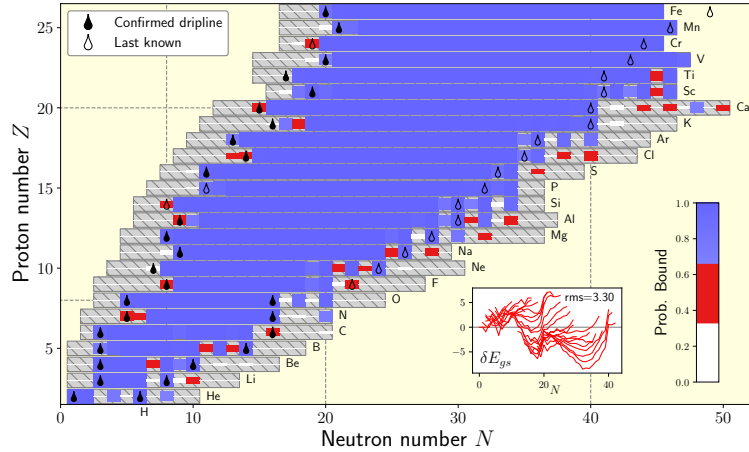


Figure 53: Theoretical probabilities of isotopes to be bound with respect to one- or two-nucleon separation, indicated by the size and color of the boxes (see legend). The gray region marks all calculated nuclei within the VS-IM-SRG framework. The inset shows the global agreement with experimental data.

Source: Figure taken from Ref. [314].

continuum contributions, this work represents a first step toward improved global studies of the nuclear chart including a more rigorous estimate of theoretical uncertainties.

In Ref. [93] the structure of nuclei around  $^{100}\text{Sn}$  was studied based on the same nuclear interactions within CC and VS-IM-SRG (see Section 1). The nucleus  $^{100}\text{Sn}$  is currently the heaviest known doubly-magic nucleus ( $N = Z = 50$ ), shows the largest known allowed  $\beta$  decay strength [317], and is located very close to the proton drip line. However, beyond that not much is known about the structure of nuclei in this regime of the nuclear chart, in particular regarding the spectrum of these nuclei [318]. These properties make the tin isotopes a prime target of current theoretical and experimental investigations and also a natural benchmark system for *ab initio* calculations. The computation of nuclei in this mass regime poses significant computational challenges due to the required model spaces for the employed nuclear interactions as well as the many-body truncation. In fact, for these studies a new method was developed that allows to include perturbatively higher order particle-hole excitations in CC calculations. The left panel of Figure 54 shows the energy per particle of doubly-magic nuclei up to  $^{100}\text{Sn}$  and highlights once again the remarkable agreement with experimental data for the interaction “1.8/2.0 (EM)”. In the right panel first results for the spectrum of  $^{100}\text{Sn}$ , the  $B(E2)$  strength in comparison with experimental data, and the theoretical and experimental energies of the excited  $J^\pi = 2^+$  states for different isotopes are shown.

The results of Figures 53 and 54 show that calculations based on specific nuclear NN and 3N interactions are able to reproduce ground-state energies of nuclei in different regimes of the nuclear chart remarkably well. However, so far it is not clear why the particular interaction “1.8/2.0 (EM)” performs so well for energies, whereas Hamiltonians with slightly different cutoffs of the same interaction set lead to a significant underbinding of heavier nuclei (see left panel of Figures 13 and 54). In addition, other observables like radii turn out to be too small compared to experiment for all these interactions (see, e.g., the right panel of Figure 13). In general, calculations should ideally be performed based on a set of interactions at different orders of the chiral expansion and also for a range of cutoff scales rather than just for a single specific interaction. Such calculations at different orders in the chiral expansion allow to extract systematic uncertainty bands (see Section 2.4) and to rule out accidental agreement of particular interactions for specific observables.

In Ref. [319] a new interaction, “NN+3N (lnl)” was introduced. This interaction includes NN contributions up to  $N^3\text{LO}$  given by the potential of Ref. [199] and 3N contributions up to  $N^2\text{LO}$ . Triggered by the deficiencies of the local 3N interaction derived in Ref. [224] (see e.g. Ref. [102] and Figure 3) an additional nonlocal regulator was introduced, leading to a significantly improved description of medium-mass nuclei beyond the oxygen isotopic chain, while the good agreement with experiment for light systems was main-

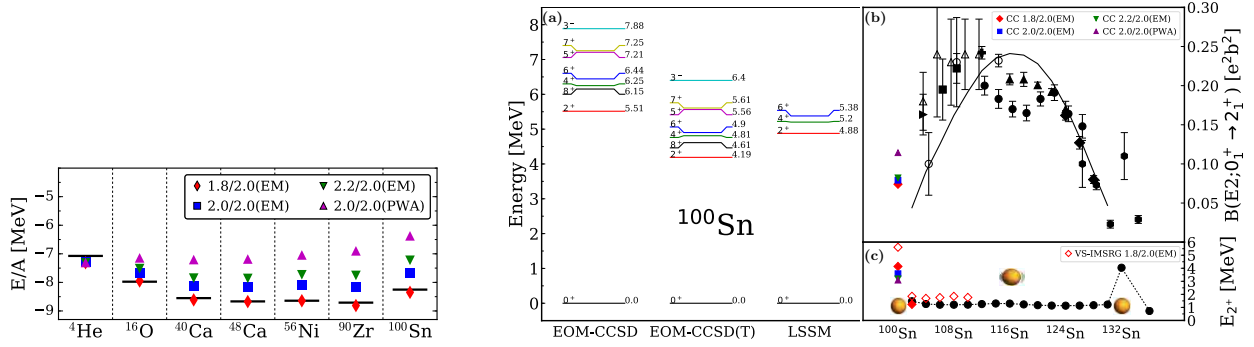


Figure 54: Left: Ground-state energies per nucleon of closed-shell nuclei computed with the IM-SRG based on the interactions of Ref. [123] compared to experiment (black lines), Right: Panel (a) shows the first excited states in  $^{100}\text{Sn}$  based on CC calculations using the interaction “1.8/2.0 (EM)” compared to calculations based on phenomenological interactions (LSSM). Panel (b) shows CC results for the  $B(E2)$  transition strength in  $^{100}\text{Sn}$  compared to the experimental data for all other even tin isotopes, while panel (c) shows the experimental and theoretical result for the energy of the  $J^\pi = 2^+$  states in even tin isotopes. *Source:* Figures taken from Ref. [93].

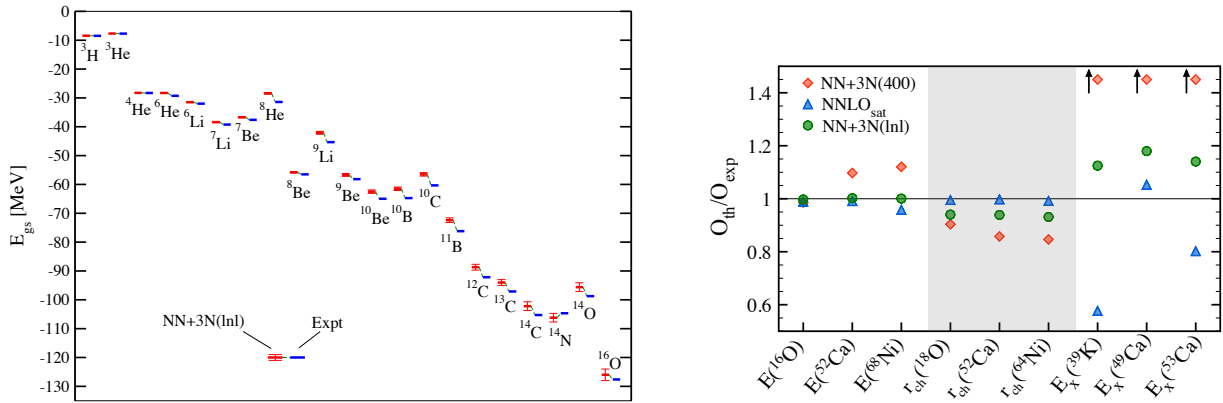


Figure 55: Left: Ground-state energies of nuclei calculated within the NCSM based on the “NN+3N (lnl)” interaction (red lines) compared to experiment (blue lines). The interaction has been SRG-evolved to  $\lambda_{\text{SRG}} = 2.0 \text{ fm}^{-1}$ . The shown error bars indicate many-body uncertainties. Right: The ratio of theoretical and experimental results for the ground-state energies  $E$ , the charge radius  $r_{\text{ch}}$  and one-nucleon separation energies  $E_x$  obtained within the SCGF framework. *Source:* Figures taken from Ref. [319].

tained by increasing the value of the local cutoff scale to  $\Lambda = 600 \text{ MeV}$ . The left panel of Figure 55 illustrates the agreement for ground-state energies of various s-shell and p-shell nuclei. The right panel shows the results of SCGF calculations for different nuclei and observables (see caption). Particularly striking is the improvement of the results based on the novel “NN+3N (lnl)” interaction compared to the purely local 3N interaction “NN+3N (400)” for the description of heavier nuclei.

In Ref. [243] ground-state energies and charge radii of closed-shell medium-mass nuclei were computed in IM-SRG based on a set of chiral NN and 3N interactions at different orders in the chiral expansion, with a particular focus on exploring the connection between properties of finite nuclei and nuclear matter. Specifically, the calculations were performed using chiral interactions at NLO,  $\text{N}^2\text{LO}$  and  $\text{N}^3\text{LO}$  [188], where the 3N interactions at  $\text{N}^2\text{LO}$  and  $\text{N}^3\text{LO}$  were fit to the empirical saturation point of nuclear matter and to the  $^3\text{H}$  binding energy [130] (see Figures 8 and 14). It is found that the results for energies and radii of closed-shell systems at  $\text{N}^2\text{LO}$  and  $\text{N}^3\text{LO}$  overlap within uncertainties (see Figure 56) and the cutoff variation of the interactions is within the EFT uncertainty band, which has been determined following the prescription

of Ref. [204] (see also Section 2.4). Overall, the ground-state energies are found to be underbound compared to experiment, as expected from the comparison to the empirical saturation point (see Figure 14), while the charge radii are systematically too large.

In the left panel of Figure 57 results of NCSM calculations are shown for the ground-state energies of various nuclei up to  $^{16}\text{O}$  using the semilocal NN and 3N interactions of Refs. [33, 246]. Also indicated are the chiral truncation error estimates for these ground-state energies following Refs. [204]. For most of the 15 nuclei the complete results at  $\text{N}^2\text{LO}$  agree with the experimental values. It is interesting to note that the effect of the 3N interactions is noticeably larger for  $^8\text{He}$  and  $^9\text{Li}$  than for  $^8\text{Be}$  and  $^9\text{Be}$ . On the other hand,  $^{16}\text{O}$  is noticeably overbound at  $\text{N}^2\text{LO}$ , with or without 3NFs, see also Ref. [70] for a related discussion in the context of nuclear lattice simulations. This overbinding starts at  $A = 12$ , where, with 3N interactions, both  $^{12}\text{B}$  and  $^{12}\text{C}$  are overbound, with the experimental value only slightly outside the chiral truncation error estimate, and seems to be systematic for the heavier nuclei. In the right panel of Figure 57 results for ground-state energies of AFDMC calculations are shown for nuclei up to  $^{16}\text{O}$  at different orders in the chiral expansion and different parametrizations for 3N interactions, see Refs. [52, 55]. The shown error bars include both the Monte Carlo many-body uncertainties and the uncertainties from the truncation of the chiral expansion. For the shown interactions at the regulator scale  $R_0 = 1.0$  fm, the computed binding energies at  $\text{N}^2\text{LO}$  are in good agreement with experiment. For softer interactions ( $R_0 = 1.2$ , not shown) the agreement is also reasonable, while the size of the uncertainties become sizable for  $^{16}\text{O}$  (see Ref. [55]).

In summary, the results discussed above illustrate that there are now various different interactions available which provide ground-state energies consistent with experimental data within theoretical uncertainties for nuclei in a restricted sector of the nuclear chart based on order-by-order calculations. For calculations based on specific interactions at a given order, like, e.g., the “1.8/2.0 (EM)” interaction [123] or the “ $\text{N}^2\text{LO}_{\text{sat}}$ ” interaction [141] (see Figure 17) it is even possible to reproduce known ground-state energies over a significant part of the nuclear chart from light systems to medium-mass nuclei up to  $A \approx 100$ .

#### 5.4. Charge radii of nuclei

The goal of *ab initio* calculations is to obtain a comprehensive understanding of the structure of nuclei. This includes ground-state energies, as discussed in the previous section, as well as various additional

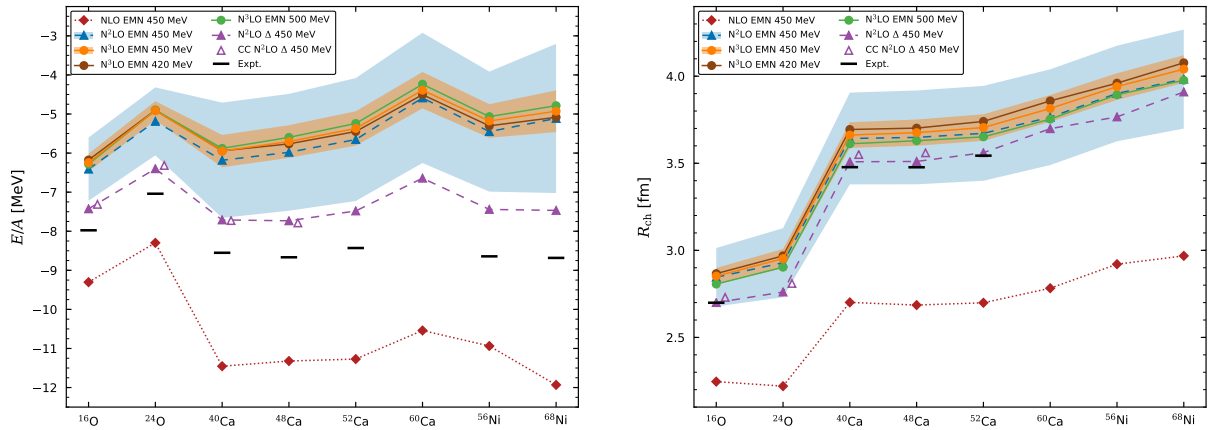


Figure 56: Ground-state energies per nucleon (left) and charge radii (right) of selected closed-shell nuclei. Results are shown at  $\text{N}^3\text{LO}$  for the EMN potential of Ref. [188] with cutoffs  $\Lambda = 420, 450$ , and  $500$  MeV depicted by the brown, orange, and green solid lines and circles, respectively. The  $\text{N}^2\text{LO}$  results are given by the dashed lines for the EMN 450 MeV potential (blue line and solid up triangles) and the  $\Delta$ -full interaction of Ref. [142] (purple line and solid up triangles), while NLO results are displayed by the red-dotted line and diamonds. The open triangles give the CC results for the  $\Delta$ -full interaction from Ref. [142] for comparison. The blue and orange bands give the  $\text{N}^2\text{LO}$  and  $\text{N}^3\text{LO}$  uncertainty estimate, respectively, for the EMN 450 MeV interaction.

Source: Figures taken from Ref. [243].

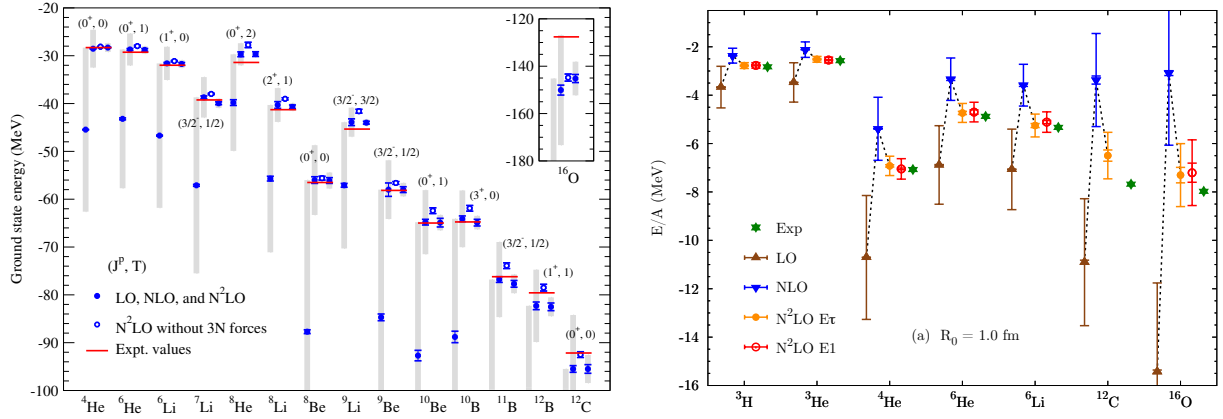


Figure 57: Left: Ground-state energies of nuclei using semilocal chiral LO, NLO, and  $\text{N}^2\text{LO}$  interactions of Refs. [33, 204, 246] at  $R = 1.0$  fm (blue symbols) in comparison with experimental values (red lines). For each nucleus the LO, NLO and  $\text{N}^2\text{LO}$  results are the left, middle and right symbols and bars, respectively. The open blue symbols correspond to incomplete calculations at  $\text{N}^2\text{LO}$  using NN-only interactions. Blue error bars indicate the many-body extrapolation. The shaded bars indicate the estimated truncation error at each chiral order following Ref. [204]. Right: Ground-state energies of nuclei obtained from auxiliary-diffusion Monte-Carlo (AFDMC) results using the local chiral interaction of Ref. [52]. Results at different orders of the chiral expansion and for different 3N parametrizations are shown. Smaller error bars (barely visible up to  $A = 6$ ) indicate the statistical Monte Carlo uncertainties, whereas the larger error bars represent the uncertainties from the chiral EFT truncation following Ref. [204].

Source: Left figure taken from Ref. [33] and right figure taken from Ref. [55].

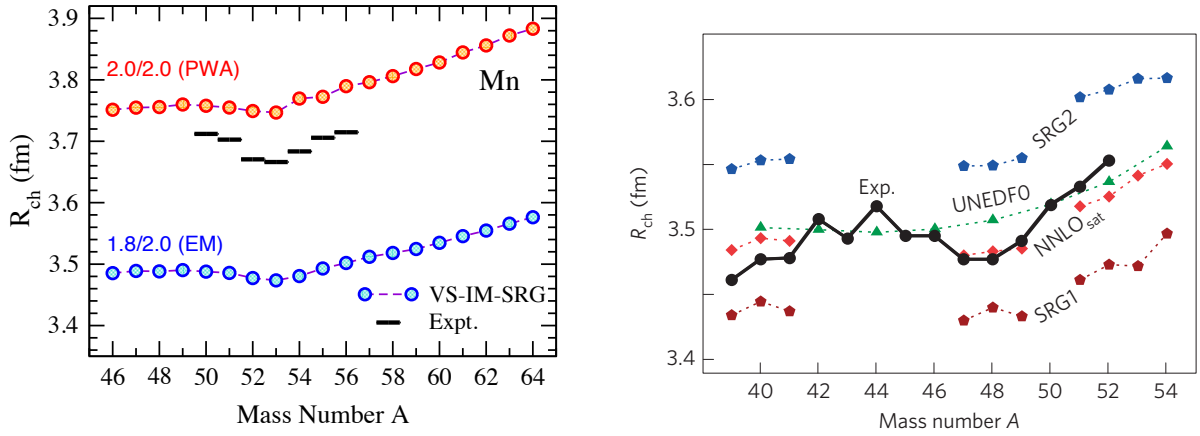


Figure 58: Left: Charge radii of manganese isotopes for the “1.8/2.0 (EM)” (blue circles) and “2.0/2.0 (PWA)” (red circles) interactions of Ref. [123] computed within the VS-IM-SRG. Right: Experimental charge radii of calcium isotopes compared to *ab initio* CC calculations with chiral EFT interactions “ $\text{N}^2\text{LO}_{\text{sat}}$ ” [141] and “SRG1/SRG2” [123], as well as DFT calculations with the UNEDF0 functional. Experimental error bars are smaller than the symbols. Note that the interaction labeled “SRG1” in the right panel corresponds to the interaction usually labeled as “2.8/2.0 (EM)” and “SRG2” to “2.0/2.0 (PWA)”.

Source: Left figure taken from Ref. [228] and right figure taken from Ref. [104].

observables, like charge and matter radii, quadrupole moments or electromagnetic response functions. A simultaneous and realistic prediction of several or ideally all of these quantities is a very challenging task (see, e.g., Ref. [320]). As shown in Figures 15, 17 and 56 the interactions “ $\text{N}^2\text{LO}_{\text{sat}}$ ” [141] and “ $\text{N}^2\text{LO}-\Delta$ ” [142] are able to provide ground state energies and charge radii in good agreement with experiment (see also Ref. [321] for a recent study), while most interactions of Ref. [123] give too small radii, in particular the interaction



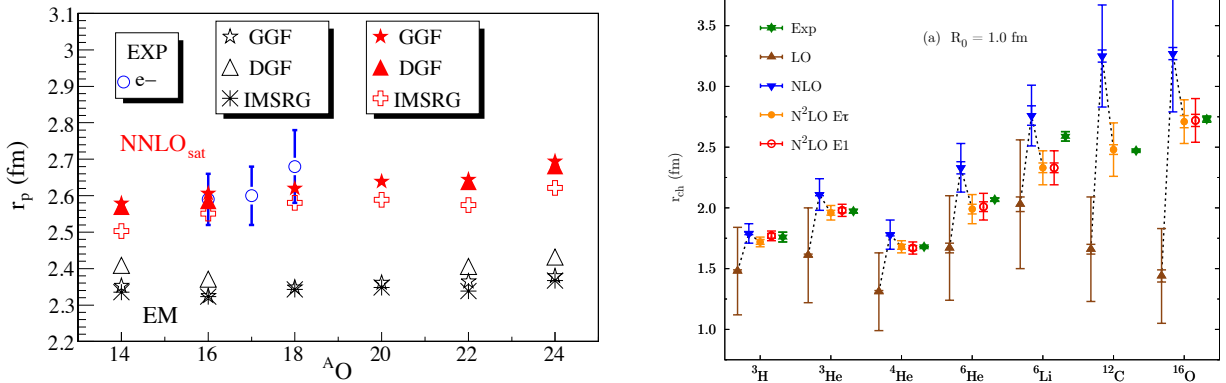


Figure 59: Left: Proton radius of oxygen isotopes calculated with the IM-SRG and SCGF based on the EM interaction [199] and “ $N^2LO_{\text{sat}}$ ” [141]. Right: Charge radii of nuclei obtained from auxiliary-field diffusion Monte-Carlo (AFDMC) using the local chiral interaction of Ref. [52]. Results at different orders of the chiral expansion and for different 3N parametrizations are shown (compare Figure 57).

Source: Left figure taken from Ref. [320] and right figure taken from Ref. [55].

“1.8/2.0 (EM)” (see right panel of Figure 13 and left panel of Figure 58), which on the other hand provides an excellent description of ground-state energies (see Section 5.3). In Figure 58 we show some representative results for charge radii based on the interactions of Ref. [123] for manganese isotopes computed within the VS-IM-SRG (left) and calcium isotopes computed within the coupled-cluster framework (right). Apart from the observed overall shifts compared to experiment, the reproduction of the trends within an isotopic chain like the steep increase in the radius toward neutron rich systems remains a challenge for *ab initio* nuclear theory [104]. Also shown in the right panel are nuclear DFT results obtained with the Skyrme energy density functional UNEDF0 [322], which fails to describe the details of the experimental trend within the shown isotopic chain.

In the left panel of Figure 59 we show charge radius results for oxygen isotopes computed within IM-SRG, the Dyson-SCGF framework (DGF) [107] and the Gorkov-SCGF (GGF) [109] using the “ $N^2LO_{\text{sat}}$ ” [141] and the NN interaction of Ref. [199] plus 3N interactions [320]. Again, a remarkable agreement between results obtained within different many-body frameworks is observed (see discussion in Section 1). For a given interaction, the uncertainties due to the many-body calculations is smaller than the experimental uncertainties and the uncertainty coming from the use of different interactions. On the other hand, the interaction EM significantly underestimates the experimental radii, whereas the absolute radii are well reproduced by “ $N^2LO_{\text{sat}}$ ”. However, we note that the charge radius of  $^{16}\text{O}$  has been included in the fit of the interaction (see Section 2.3). In the right panel we present the charge radii at different orders of the chiral expansion and parametrizations of the 3N force for different nuclei up to  $^{16}\text{O}$  based on AFDMC calculations [55]. We emphasize that the employed local interactions in these calculations differ quite significantly from the interactions shown in Figure 58 in terms of the softness and the nature of the regulator. Overall, a good agreement with experiment is found for the interaction at  $R_0 = 1.0$  fm with a natural order-by-order convergence. For a softer interaction at  $R_0 = 1.2$  fm (not shown, see Ref. [55]), the results resemble those of the hard potential up to  $A = 6$ , while the agreement slightly deteriorates for heavier system and shows a stronger sensitivity to the 3N parametrization.

In Figure 60 we show ground-state energies and charge radii, obtained from IM-SRG calculations performed in Ref. [323], based on the NN interactions of Ref. [188] plus 3N interactions up to  $N^3LO$ . For these calculations the 3N interactions have been regularized nonlocally (see Section 3.7.1) and the value of the coupling  $c_E$  as a function of  $c_D$  is fixed by a fit to the  $^3\text{H}$  ground state energy, i.e. following the same strategy like in Ref. [243] (see also Figure 56 and related discussion). The left figure illustrates the dependence of the results on  $c_D$  (see also Figure 75). Remarkably, while the ground-state energies depend quite



sensitively on the value of the coupling, the charge radius results remain almost invariant and are in very good agreement with experimental data. This offers the opportunity to fit  $c_D$  to the ground state energies without sacrificing the agreement for the radii. In this work, the fit was performed using  $^{16}\text{O}$ , which results in  $c_D = +4$  for the shown cutoff scale. The same trends were found for the other studied cutoff scales  $\Lambda = 400$  and  $550$  MeV. Note that the LEC values differ quite significantly from those obtained from fits to empirical nuclear matter properties based on the same interactions [130, 243], which in turn lead to a significant underbinding of nuclei. The right figure shows the resulting uncertainty bands for the energies and radii of selected medium-mass nuclei. Obviously, the calculations can simultaneously reproduce both observables from p-shell nuclei up to the nickel isotopic chain and resolves several deficiencies of previous interactions. While this new family of interactions certainly offers new perspectives for *ab initio* studies of medium-mass and heavier nuclei including estimates of theoretical uncertainties and also demonstrates that it is possible to derive NN and 3N interactions that can correctly describe NN scattering phase shifts as well as different many-body observables over a wide range of the nuclear chart, it still exhibits deficiencies for few-body systems and hence re-emphasizes an open question (see also Section 6.2): How can the incompatibility of the extracted LEC values, determined based on few-nucleon observables, medium-mass nuclei and nuclear matter saturation properties, be reconciled?

### 5.5. Spectra of nuclei

The correct description of the lowest excited states of nuclei represents another challenge for *ab initio* nuclear structure and a benchmark for nuclear interactions. The spectrum provides important insight into the geometric nature of a nucleus, single-particle and collective excitations, as well as possible cluster structures. In principle, excited states can be accessed in a straightforward way by all wave-function-based many-body methods, like, e.g., NCSM, valence-shell diagonalization or CC (see Section 1). In addition, the IMSRG framework has also been recently extended to excited states [92]. While the valence-shell model approach was historically based on phenomenological interactions, nowadays valence-space Hamiltonians can be computed microscopically in *ab initio* frameworks starting from chiral EFT NN and 3N interactions using MBPT or IMSRG (see, e.g., Refs. [81–83, 91, 314]). The spectrum of light nuclei can be computed, e.g., via large scale (IT)-NCSM or QMC methods (see right panel in Figure 15).

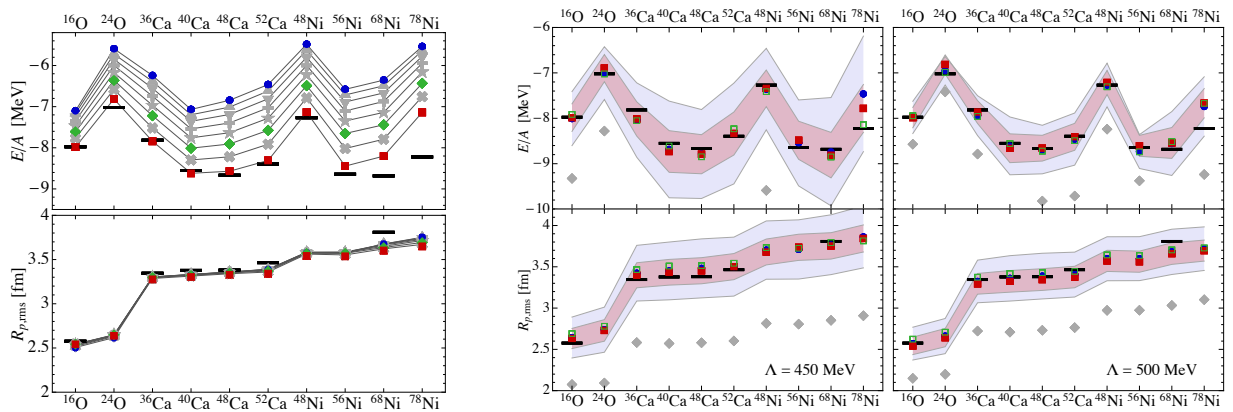


Figure 60: Left: Ground-state energies and point-proton radii for selected medium-mass isotopes obtained in IM-SRG based on NN+3N interaction at  $N^3\text{LO}$  with  $\Lambda = 500$  MeV for a range of  $c_D$  parameters from  $-3$  (blue) to  $+4$  (red) in steps of 1. Right: Ground-state energies (top panels) and point-proton radii (bottom panels) based on interactions at NLO (solid gray diamonds),  $N^2\text{LO}$  (blue circles),  $N^3\text{LO}$  (red boxes), and  $N^3\text{LO}'$  (open green boxes) with  $\Lambda = 450$  MeV (left) and  $500$  MeV (center). Here,  $N^3\text{LO}'$  refers to calculations using NN interactions at  $N^3\text{LO}$  combined with 3N interactions at  $N^2\text{LO}$ . The uncertainty bands at  $N^2\text{LO}$  (blue) and  $N^3\text{LO}$  (red) are obtained from the order-by-order analysis first suggested in Ref. [204] (see also Section 2.4) and also include many-body uncertainties.

Source: Figures taken from Ref. [323], right figure modified.

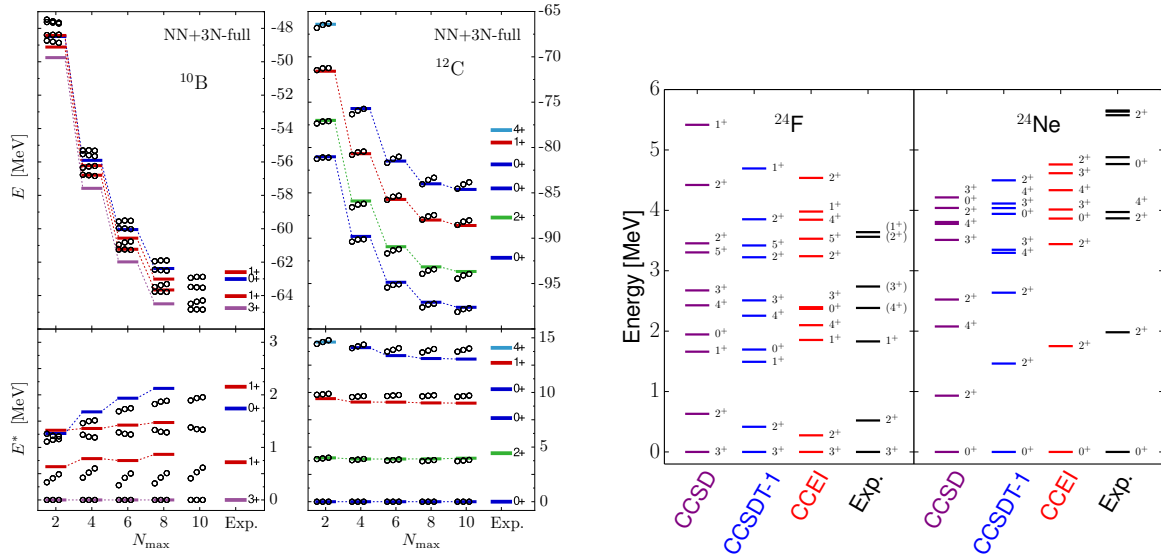


Figure 61: Left: Absolute (top) and relative (bottom) energies of the lowest states of  $^{10}\text{B}$  and  $^{12}\text{C}$  as a function of basis size parameter  $N_{\text{max}}$  calculated in the importance-truncated NCSM based on SRG-evolved NN plus 3N interactions. The solid lines correspond to the complete 3N interaction, the circles to calculations based on normal-ordered 3N interactions. The experimental excitation energies are taken from Ref. [324]. Right: Excited states of  $^{24}\text{F}$  and  $^{24}\text{Ne}$  computed within coupled-cluster plus the valence-shell diagonalization.

Source: Left figure adapted from Ref. [59] and right figure taken from Ref. [81].

In the left panel of Figure 61 we show results of IT-NCSM calculations of the lowest excited state with positive parity of  $^{10}\text{B}$  and  $^{12}\text{C}$  as a representative set of p-shell nuclei based on a chiral NN and 3N interaction [59]. The results show a natural convergence pattern and a reasonable agreement with experiment. We note that excited states in both nuclei have been shown to be sensitive to contributions from 3N interactions [42, 43]. Calculations of odd-odd nuclei like  $^{10}\text{B}$  are particularly challenging since excitation energies are typically smaller and the correct reproduction of the level ordering becomes more tricky. Furthermore, we note that due to the nature of the NCSM configuration basis, the  $0^+$  resonance state in  $^{12}\text{C}$  at about 7.7 MeV excitation energy cannot be properly described in this framework due to its pronounced cluster structure [66, 67]. This “Hoyle-state” plays a key role for the synthesis of carbon, oxygen, nitrogen and other elements, which form the building blocks of complex molecules of living beings [325]. Finally, the shown results also illustrate the accuracy of the normal-ordering approximation for calculations of excited states (see Ref. [59] for details).

In the right panel of Figure 61 we show the lowest excited states of  $^{24}\text{F}$  and  $^{24}\text{Ne}$  computed within CC and the valence-shell model. This plot compares results of CC equation-of-motion calculations (“CCSD”), calculations including linearized contributions from three-particle-three-hole contributions (“CCSDT-1”), and results from a valence space diagonalization based on effective interactions computed within CC (“CCEI”) [81]. The results of all the different approaches are in reasonable agreement. Furthermore, for  $^{24}\text{F}$  both CCEI and full-space coupled-cluster calculations agree well with those calculated with IM-SRG effective interactions and the experimental results from recent measurements [326].

### 5.6. Electromagnetic response of nuclei and neutron distributions

The distribution of protons in nuclei and the resulting charge radii can be accurately measured in electron scattering experiments via the electromagnetic interaction [227]. The determination of the neutron distribution on the other hand is much more challenging. However, an accurate knowledge of neutron distributions in atomic nuclei is key for understanding neutron-rich systems ranging from short-lived isotopes to macroscopically large objects such as neutron stars. The distribution of neutrons in nuclei determines the limits of

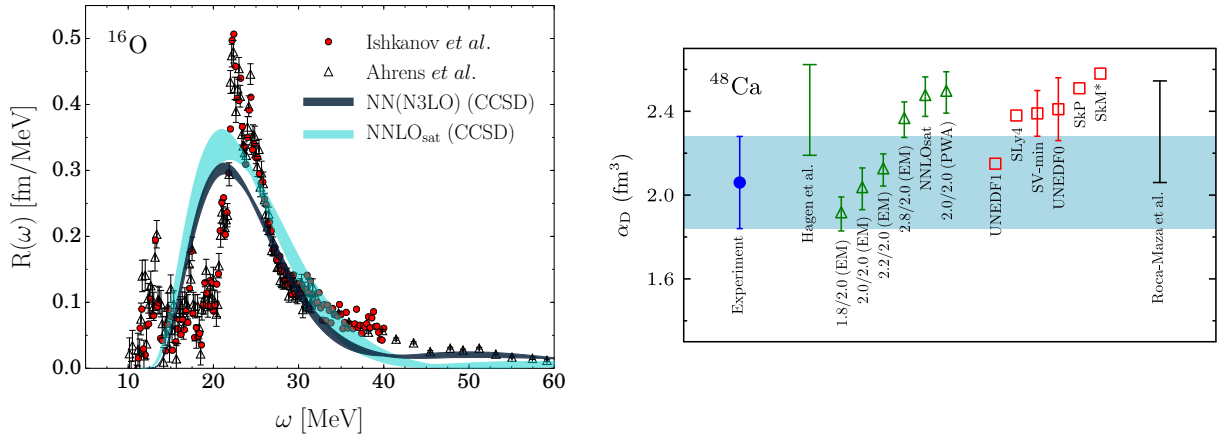


Figure 62: Left: Photo-absorption response function for  $^{16}\text{O}$ . The red circles show the experimental data from Ref. [327], and the white triangles plus error bars are the results by Ahrens et al. [328]. Calculations are performed with coupled cluster based on the interactions of Refs. [141, 199]. Right: Experimental constraints for the electric dipole polarizability of  $^{48}\text{Ca}$  (blue band) and predictions from ab initio calculations based on chiral NN and 3N interactions (green triangles) and energy density functionals (red squares).

Source: Left figure taken from Ref. [329] and right figure taken from Ref. [106].

the nuclear stability [330], gives rise to exotic structures in rare isotopes [331] and governs basic properties of neutron stars [332]. Because of its fundamental importance, experimental efforts worldwide have embarked on a program of measurements of neutron distributions in nuclei using different probes, including hadronic scattering [333], pion photoproduction [334], and parity-violating electron scattering [335]. Since the weak charge of the neutron,  $Q_W^n \approx -1$ , is much larger than that of the proton,  $Q_W^p \approx 0.07$ , a measurement of the parity-violating asymmetry  $A_{\text{pv}}$  offers an opportunity to probe the neutron distribution [336]. In addition, experiments focus on measuring observables that are related to the neutron distribution, such as the dipole polarizability  $\alpha_D$  [337]. The dipole polarizability is directly connected to the electromagnetic response function  $R(\omega)$  and characterizes the low-energy behavior of the dipole strength. Specifically, it is defined by (see, e.g., Ref. [338] for details)

$$R(\omega) = \sum_n |\langle \psi_0 | \hat{\Theta} | \psi_n \rangle|^2 \delta(E_n - E_0 - \omega), \quad (208)$$

where  $\psi_0$  and  $\psi_n$  are the ground- and final-state wave functions of the nucleus with the energies  $E_0$  and  $E_n$ , respectively, and  $\hat{\Theta}$  denotes the corresponding electromagnetic operator. Based on this response function several different moments can be defined via:  $S_n = \int_{\omega_{\text{th}}}^{\infty} d\omega R(\omega) \omega^n$ , with some threshold energy  $\omega_{\text{th}}$ . The dipole polarizability is given by

$$\alpha_D = 2\alpha \int_{\omega_{\text{th}}}^{\infty} d\omega \frac{R(\omega)}{\omega} \sim S_{-1}, \quad (209)$$

where  $\alpha$  is the electromagnetic coupling constant. Recently, this parameter was accurately measured for  $^{208}\text{Pb}$  [339],  $^{120}\text{Sn}$  [340],  $^{68}\text{Ni}$  [341] and  $^{48}\text{Ca}$  [106] (see also right panel of Figure 62). Theoretical calculations of this parameter involve several challenges because most of the dipole strength lies in the scattering continuum, i.e., the according final states  $\psi_n$  in Eq. (208) do not correspond to bound states. There have been significant advances in recent years that allowed to transform this continuum problem into a bound-state problem via the Lorenz integral transform (LIT) method and make these observables accessible by ab initio many-body frameworks (see, e.g., Refs. [38, 106, 329, 338, 342, 343] and references therein). The left panel of Figure 62 shows experimental and theoretical results for the  $^{16}\text{O}$  photo-absorption response function obtained from calculations within CC using a  $\text{N}^3\text{LO}$  NN interaction [199] (dark band) and “ $\text{N}^2\text{LO}_{\text{sat}}$ ” [141] (light blue band). The uncertainty band for the “ $\text{N}^2\text{LO}_{\text{sat}}$ ” interaction is larger since the available model

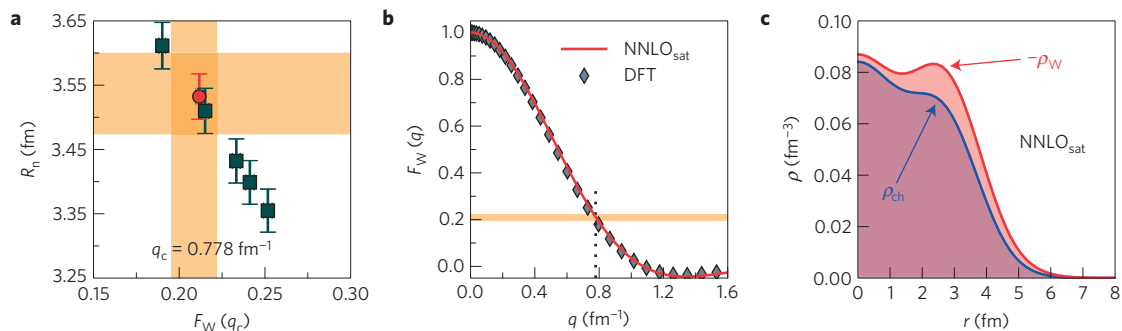


Figure 63: Left: Point-neutron radius  $R_n$  in  $^{48}\text{Ca}$  as a function of the weak-charge form factor  $F_W(q_c)$  at the CREX momentum  $q_c = 0.778 \text{ fm}^{-1}$  computed in *ab initio* calculations with “ $N^2\text{LO}_{\text{sat}}$ ” [141] (red circle) and chiral interactions of Ref. [123] (squares). The width of the horizontal orange band shows the predicted range for  $R_n$ , determined based on a correlation with the proton radius  $R_p$  [105]. Center: weak-charge form factor  $F_W(q)$  as a function of momentum transfer  $q$  with “ $N^2\text{LO}_{\text{sat}}$ ” (red line) and DFT (diamonds). The orange horizontal band shows  $F_W(q_c)$ . Right: Charge density (blue line) and (negative of) weak-charge density (red line). The weak-charge density extends well beyond  $\rho_{\text{ch}}$  as it is tightly connected to the neutron distribution. Source: Figures taken from Ref. [105].

space size for these calculations was smaller than for the NN-only calculations using the  $N^3\text{LO}$  potential. Generally, it is found that the theoretical results are able to capture the bulk features of the experimental data and that the dipole polarizability is more sensitive to the distribution of the dipole strength at low energies rather than to the detailed structure and shape of the response function. The right panel of Figure 62 shows a comparison of recent experimental  $\alpha_D$  values for  $^{48}\text{Ca}$  with predictions from *ab initio* calculations based on chiral NN and 3N interactions of Refs. [123, 141] and state-of-the-art energy-density functionals [106]. These results show that present calculations based on NN plus 3N interactions can provide a realistic description of the dipole polarizability even though it is not yet possible to resolve the detailed structure of the response function (see left panel).

The weak-charge radius  $R_W$  is another quantity that characterizes the size of the nucleus. The CREX experiment will measure the parity-violating asymmetry  $A_{\text{Pv}}$  in electron scattering on  $^{48}\text{Ca}$  at the momentum transfer  $q_c = 0.778 \text{ fm}^{-1}$ . By making some assumptions about the weak-charge form factor, one can deduce  $R_W$  and the neutron radius  $R_n$  from the single CREX data point [336]. Furthermore, Figure 63 shows that there exists a strong correlation between  $R_n$  and  $F_W(q_c)$ , which makes it possible to extract the theoretical constraint  $0.195 \leq F_W(q_c) \leq 0.222$  [105]. This range as well as the momentum dependence of the weak-charge form factor (middle panel) show good agreement with DFT results. As seen in the right panel of Figure 63, the spatial extent of the weak-charge density  $\rho_W(r)$ , being the Fourier transform of the weak-charge form factor  $F_W(q)$ , is significantly greater for  $^{48}\text{Ca}$  than that of the electric charge density  $\rho_{\text{ch}}$ . This is a reflection of the fact that there is an excess of eight neutrons over protons in  $^{48}\text{Ca}$ .

### 5.7. Beta decay transitions

Beta decay ( $\beta$  decay) is the predominant decay process of atomic nuclei, especially up to the medium-mass range. It involves the transformation of a neutron into a proton or vice versa via the weak interaction. Generally,  $\beta$ -decay transitions can be categorized into Fermi transitions and Gamow-Teller transitions. In the case of Gamow-Teller transitions the emitted electron-antineutrino or positron-neutrino pair form a relative  $S = 1$  state, such that the total angular momentum of the nucleus changes by  $\Delta J = -1, 0$  or  $1$ . In contrast, for Fermi transitions, the emitted leptons couple to an  $S = 0$  state and the total angular momentum  $J$  of the nucleus is hence conserved.

Specifically, the half-life  $t$  for the  $\beta$  decay of, e.g.  $^3\text{H}$ , can be expressed in the form [219, 344, 345]

$$(1 + \delta_R)t = \frac{K/G_V^2}{f_V \langle F \rangle^2 + f_A g_A^2 \langle GT \rangle^2}, \quad (210)$$

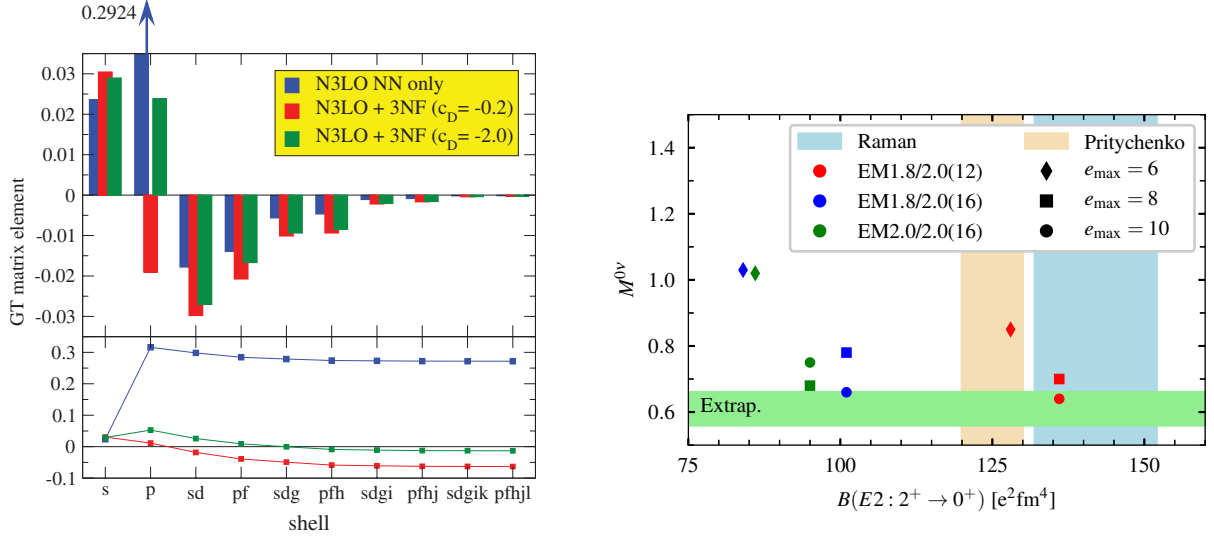


Figure 64: Left: Contributions to the  $^{14}\text{C}$  Gamow-Teller matrix element for individual harmonic oscillator shells determined from NCSM calculations based on chiral NN and 3N interactions. The top panel shows the contributions when only using NN interactions (blue) and including 3N interactions (red and green). The bottom panel displays the accumulated contributions up to the given shell. The results show that the inclusion of 3N interactions lead to a significant suppression of the p-shell contributions to the matrix element for the employed interactions. Right:  $(0\nu\beta\beta)$  beta decay matrix element  $M^{0\nu}$  as a function of the  $B(E2: 2^+ \rightarrow 0^+)$  value for  $^{48}\text{Ti}$  calculated within the IM-SRG+GCM framework using different chiral EFT interactions and basis truncations. The bands show the experimental constraints for the  $B(E2)$  values of Refs. [349, 350]. Source: Left figure taken from Ref. [351] and right figure taken from Ref. [352].

where  $\delta_R$  includes radiative corrections that originate from virtual photon exchange between the charged particles,  $f_V$  and  $f_A$  are Fermi functions, which account for the deformation of the electron wave function due to electromagnetic interactions with the nucleus, and  $G_V = 1$  and  $g_A = 1.27$  denote the vector and axial-vector couplings. The kinematics of the process leads to an additional constant  $K = 2\pi^3 \ln 2/m_e^5$ , where  $m_e$  is the electron mass. The half-life depends on the nuclear matrix elements of the vector and axial-vector currents denoted as Fermi  $\langle F \rangle$  and Gamow-Teller  $\langle GT \rangle$  matrix elements, respectively. The Fermi reduced matrix element is given by  $\langle F \rangle = \langle {}^3\text{He} | \sum_{i=1}^3 \tau_i^+ | {}^3\text{H} \rangle$ , where  $\tau^+ = \frac{1}{2}(\tau^x + i\tau^y)$  is the isospin-raising operator and the wave functions  $| {}^3\text{H} \rangle$  and  $| {}^3\text{He} \rangle$  denote the ground states of the mother and daughter nuclei,  ${}^3\text{H}$  and  ${}^3\text{He}$ . The Gamow-Teller reduced matrix element contains axial-vector one-body (1b) and two-body (2b) current contributions:

$$\langle GT \rangle = \frac{1}{g_A} \langle {}^3\text{He} | \sum_{i=1}^3 \mathbf{J}_{i,1b}^+ + \sum_{i<j} \mathbf{J}_{i,j,2b}^+ | {}^3\text{H} \rangle. \quad (211)$$

The axial-vector current was derived in chiral EFT to third order [346, 347] ( $Q^3$ ), while more recent derivations have been extended to order  $Q^4$  [222, 348]. Since the typical Q-values of  $\beta$  decays are relatively small, all currents can be evaluated to good approximation at vanishing momentum transfer. Therefore to order  $Q^0$  and  $Q^2$ , only the momentum-independent one-body current contributes:  $\mathbf{J}_{i,1b}^+ = g_A \tau_i^+ \boldsymbol{\sigma}_i$ . The first contributions to two-body currents enter at order  $Q^3$ . The corresponding expressions can be found in [219, 346, 347].

Up to now, systematic *ab initio* studies of  $\beta$  decays were limited to light nuclei [148, 218, 219] (see also Figure 11) and a few selected isotopes [93, 353, 354] (see also Figure 54). A particularly prominent nucleus is  $^{14}\text{C}$ , which is characterized by an anomalously large half-life of about 5715 years [355]. This property makes this isotope a very attractive chronometer as it is naturally present in animals and plants and hence allows to reliably date up to about 50000 year-old samples [356]. The left panel of Figure 64 shows results of NCSM calculations for the Gamow-Teller matrix elements based on solutions for the ground-state wave functions

of  $^{14}\text{C}$  and  $^{14}\text{N}$  using chiral EFT NN and 3N interactions and including only one-body current contributions  $\mathbf{J}_{i,1b}$  [351]. The results show that contributions from 3N interactions lead to a significant suppression of the matrix elements and hence to an enhanced life time of  $^{14}\text{C}$  (see Eq. (210)). We emphasize, however, that the shown contributions from the different harmonic oscillator orbitals are not observable. That implies that the conclusion is also scheme-dependent and strictly speaking only valid for the particular employed NN and 3N interactions. Future and current work aim at including also GT transitions to low-lying excited states of the daughter nucleus (see, e.g., Refs. [354, 357]).

On a quantitative level it is remarkable that theoretical results for Gamow-Teller matrix elements agree reasonably well with experimental results if the axial coupling constant  $g_A$  is quenched by a factor of about 0.75 [358–361]. Different possible sources for this deviation have been proposed, like missing correlations in the wave functions [362] or contributions from higher-order nuclear currents [363]. In fact, results from recent *ab initio* calculations indicate that the discrepancies can be resolved when both these factors are treated properly [354] (see also discussion in Section 6.2).

Apart from first-order weak interaction processes like ordinary  $\beta$  decays, also second-order processes have been observed in specific nuclei. These decays involve a simultaneous transformation of two neutrons into protons, or vice versa. Such decays can be observed in nuclei for which a single  $\beta$  decay is energetically forbidden, while the isobar with atomic number two higher or lower has a larger binding energy. Given that second-order processes are strongly suppressed, such nuclei exhibit very long half lives [364]. All observed double-beta ( $\beta\beta$ ) decays correspond to the two-neutrino- $\beta\beta$  ( $2\nu\beta\beta$ ) decay and need to be distinguished from an even more rare type of  $\beta\beta$  decay, which involves no neutrino emission, the neutrinoless- $\beta\beta$  ( $0\nu\beta\beta$ ) decay. This process violates lepton number conservation and can hence only occur if neutrinos are their own antiparticles. The observation of such a decay would have profound implications for our understanding of the nature of neutrinos and the Standard Model [365] and is thus subject of several experimental searches [364, 366–368]. The theoretical calculation of matrix elements for  $\beta\beta$  decays also involves significant challenges [369–371]. As a result, predictions from calculations using different many-body frameworks and nuclear interactions for a given transition can vary significantly. This situation is especially unsatisfactory since precise results are required for the analysis and planning of present and future  $0\nu\beta\beta$  decay experiments. In the right panel of Figure 64 first results for the  $0\nu\beta\beta$  matrix element  $M^{0\nu}$  are shown computed with the IM-SRG+GCM framework [372] including a microscopic treatment of collective correlations based on different NN plus 3N interactions of Ref. [123]. It is found that the matrix element value for the interaction “1.8/2.0 (EM)”, which provides ground-state energies in excellent agreement with experiment (see Section 5.3), turns out to be around 0.6, a value significantly smaller than those of more phenomenological approaches [352]. It will be crucial to benchmark these results against predictions of other many-body approaches and to estimate the theoretical uncertainties due to EFT truncations.

### 5.8. Three-body scattering cross sections

Since their advent, numerically exact 3N continuum Faddeev calculations of the elastic neutron-deuteron (nd) scattering and deuteron breakup reactions have become a powerful tool to test modern nuclear forces [26]. Benchmarking theoretical predictions for scattering cross sections against precise nd elastic scattering and breakup data over a wide range of incoming nucleon energies can help to isolate deficiencies of present nuclear forces in a specific kinematical regime. In particular, for three-body systems effects of four- and higher-body forces in chiral forces can be cleanly disentangled and uncertainties from the few-body calculations are very small since structure and reaction observables can be solved virtually exactly.

In the left subfigure of Figure 65 we show results for the differential cross section of elastic nd scattering (left panels) at three different energies for different LEC values of the 3N interaction with the corresponding  $\chi^2$  values as a function of  $c_D$  (right panels, see also caption). The theoretical results are obtained by solving the Faddeev equations in a partial-wave momentum basis as given in Eq. (41) [25, 26]. The actual calculations have been performed for  $R = 0.9$  fm using the NN interaction of Refs. [189, 204] for five different  $c_D$  values,  $c_D = -2.0, 0.0, 2.0, 4.0$  and  $6.0$  (see also Ref. [376]). In all cases, the  $c_E$ -value is taken from a fit to the  $^3\text{H}$  binding energy. The results show that contributions from 3N interactions have a significant effect on the agreement of the computed cross sections with the experimental data, which is also reflected by the pronounced sensitivity of the  $\chi^2$  values on  $c_D$ . However, a comparison of the results at different energies also



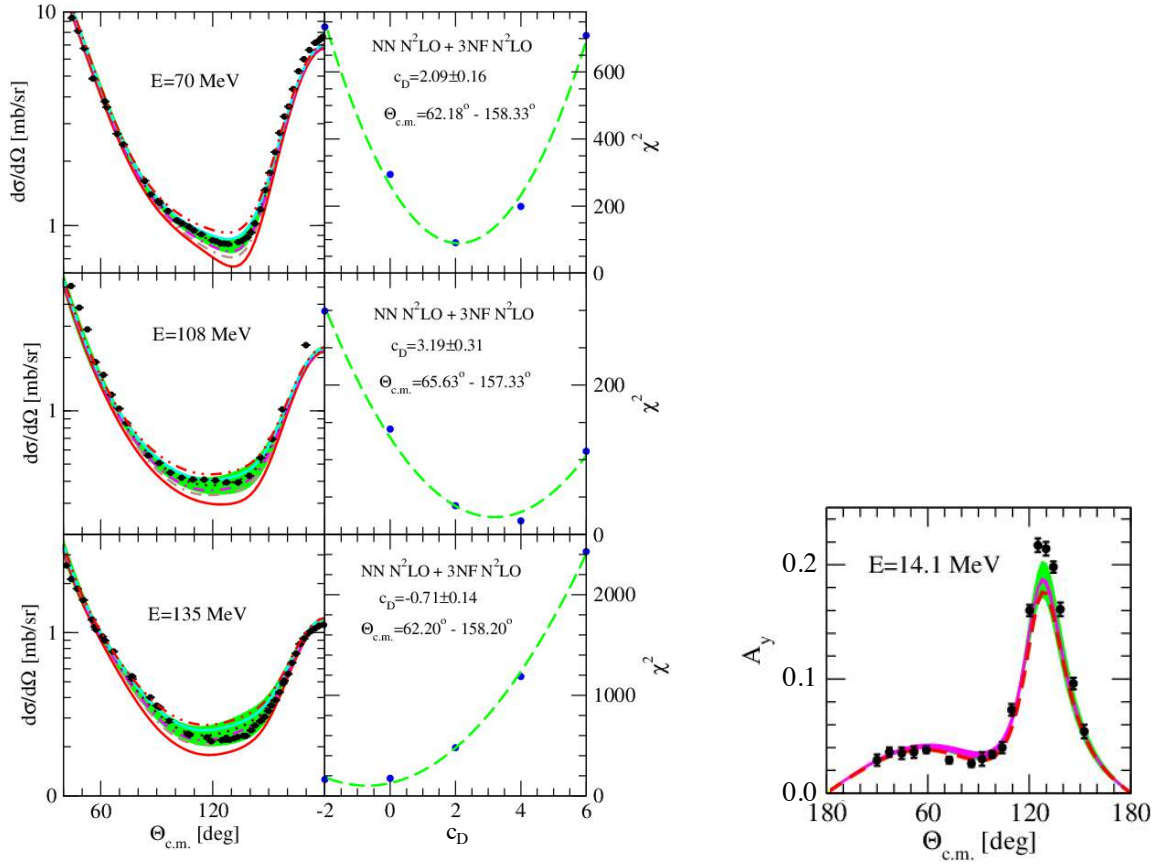


Figure 65: Left: Neutron-deuteron (nd) elastic scattering cross section at different incoming neutron laboratory energies  $E = 70$ ,  $108$  and  $135$  MeV (rows). In the left column, the solid (red) lines are predictions of the  $N^2LO$  NN potential of Refs. [189, 204] with the regulator  $R = 0.9$  fm. This NN interaction is then combined with the  $N^2LO$  3N interactions using five different  $(c_D, c_E)$  combinations. These combinations lead to results shown by the brown double-dashed-dotted, magenta dashed-dotted, maroon dotted, cyan solid and red double-dotted-dashed lines for  $c_D = -2.0, 0.0, 2.0, 4.0$  and  $6.0$ , respectively. The green bands show the estimated theoretical uncertainty of predictions at  $N^2LO$  with  $c_D = 2.0$ . The (black) dots depict experimental proton-deuteron data from Ref. [373] at  $E = 70$  and  $E = 135$  MeV and from Ref. [374] at  $E = 108$  MeV. In the right column, the  $\chi^2$  fits to the experimental data in the indicated angular regions based on these five pairs of  $(c_D, c_E)$  values are shown by dashed (green) lines. The legends in the right column provide the best fit  $c_D$  values to the data at each laboratory energy over the indicated angular range. Right: The neutron analyzing power  $A_y$  in nd elastic scattering at  $E_n = 14.1$  MeV. The dashed (red) line is the prediction of the  $N^2LO$  NN potential of Refs. [189, 204] with the regulator  $R = 0.9$  fm. The (magenta) band covers the predictions obtained with this  $N^2LO$  NN potential combined with the  $N^2LO$  3N interactions using  $c_D = -2.0 \dots 6.0$ . The (green) band gives the estimated theoretical uncertainty at  $N^2LO$  for the value of  $c_D = 2.0$ . The black dots depict the experimental data from Ref. [375].

Source: Figures adapted from Ref. [33].

shows that a  $\chi^2$  minimization leads to different optimal  $c_D$  in different regimes, which makes it necessary to perform a global optimization of the couplings (see also Figure 9 and the discussion in Section 2.3.1).

At low energies, a particularly interesting observable is the analyzing power  $A_y$  for nd elastic scattering with polarized neutrons (see right panel in Figure 65, see also Section 2.3.1). Theoretical predictions of phenomenological high-precision NN potentials tend to underestimate the experimental data for  $A_y$  by up to 30% [33] in the region of the maximum, which corresponds to the center-of-mass angles of  $\Theta_{c.m.} \approx 125^\circ$ . Combining these NN potentials with phenomenological 3N interactions reduces the deviation in some cases by about a factor 2, while for other interactions the addition has practically no effect on  $A_y$  [33] (see right panel in Figure 65). The predictions for  $A_y$  based on the chiral NN potentials appear to be similar to those



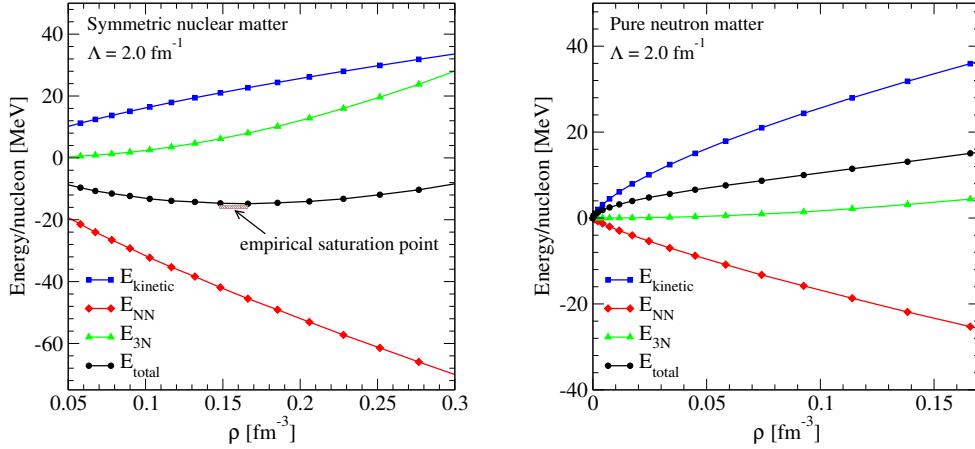


Figure 66: Size of many-body contributions as a function of density for SNM (left) [123] and PNM (right) [122], calculated within MBPT based on SRG-evolved NN interactions plus fitted 3N interactions (“2.0/2.0(EM)”) as defined in Ref. [123].  $E_{\text{kinetic}}$  denotes the kinetic energy,  $E_{\text{NN}}$  the energy contributions from only NN interactions and  $E_{3\text{N}}$  all contributions which include at least one 3N interaction term.

Source: Figures taken from Ref. [276].

of phenomenological models, see Ref. [246] and references therein. Combining the  $N^2\text{LO}$  chiral potential with the  $N^2\text{LO}$  3N interactions only slightly improves the description of  $A_y$ . Interestingly, the theoretical predictions appear to be quite insensitive to the actual value of  $c_D$  as visualized by a rather narrow magenta band, which corresponds to the variation of  $c_D = -2.0\dots 6.0$ . On the other hand, the theoretical uncertainty at  $N^2\text{LO}$  is rather large and, in fact, comparable in magnitude with the observed deviation between the predictions and experimental data. It will be interesting to see whether the  $A_y$  puzzle persists upon inclusion of higher-order corrections to the 3N interactions.

### 5.9. Nuclear equation of state and astrophysical applications

The physics of neutron-rich matter covers a wide range of regimes. At very low densities, the average interparticle distance is sufficiently large so that details of nuclear forces are not resolved and all properties of the system are dominated by the large s-wave scattering length. In this universal regime, neutron matter shares many properties with cold atomic gases close to the unitary limit [377, 378]. At nuclear densities the properties of neutron and symmetric nuclear matter are used to guide the development of energy density functionals and to constrain the physics of neutron-rich systems, which are key for understanding the synthesis of heavy nuclei in the universe (see, e.g., Ref. [379]). At very high densities, far beyond nuclear densities, the composition and properties of nuclear matter are still unknown. Exotic states of matter containing strange particles or quark matter may be present. Furthermore, neutron matter constitutes a unique laboratory for chiral EFT, because only long-range 3N interactions contribute up to  $N^3\text{LO}$ , at least for unregularized interactions (see Sections 2.1 and 3.7). This offers the possibility to derive systematic constraints based on chiral EFT interactions for the equation of state (EOS) of neutron-rich matter in astrophysics, for the symmetry energy and its density dependence, and for the structure of neutron stars, but also makes it possible to test the chiral EFT power counting and the hierarchy of many-body forces at densities relevant for nuclei.

The importance of 3N interactions for the EOS can be clearly seen in Figures 51 and 52. In fact, for calculations based on chiral EFT interactions 3N contributions are the main driving force of nuclear saturation due to the strong density dependence of 3N interactions and their overall repulsive character in SNM (see also discussion in Section 2.3.1). The strong density dependence is a direct consequence of simple phase-space arguments when computing energy contributions for nuclear matter. Naively, since 3N interactions depend on one additional particle state compared to NN interactions, energy contributions at the Hartree-Fock level

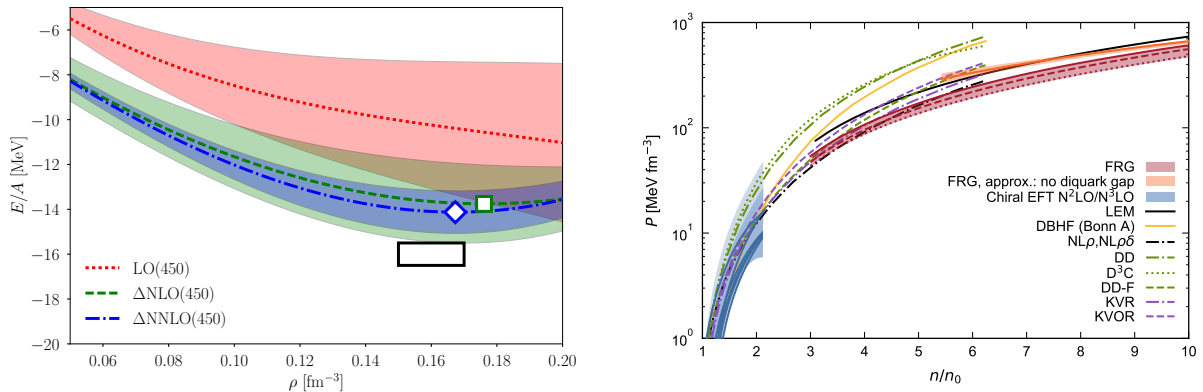


Figure 67: Left: Energy per nucleon of symmetric nuclear matter at different orders in  $\Delta$ -full chiral EFT, computed within CC. The bands show the estimated EFT-truncation errors, and the square/diamond marks the calculated saturation point in symmetric nuclear matter for  $\Delta$ NLO/ $\Delta$ N<sup>2</sup>LO. The black rectangle indicates the region  $E/A = -16 \pm 0.5 \text{ MeV}$  and  $\rho = 0.16 \pm 0.01 \text{ fm}^{-3}$ . Right: Pressure of symmetric nuclear matter as obtained from chiral EFT, functional RG (FRG), and perturbative QCD (pQCD) in comparison with different models (see main text and also Ref. [380]).  
*Source:* Left figure taken from Ref. [142] and right figure taken from Ref. [381].

contain one additional power of density. Of course, for general NN and 3N interactions this argument is only approximately correct due to the rather complicated momentum dependence of the interactions. However, explicit calculations show that this trend is indeed true for realistic interactions as illustrated in Figure 66. Here we show the individual contributions from the kinetic energy, NN interactions and 3N interactions as a function of density, calculated within MBPT. While at small densities the contributions from 3N interactions are very small, as expected, they become sizable around saturation density and continue to grow quicker than NN contributions toward higher densities, at least for SNM.

In Figure 67 we show results for the equation of state of symmetric nuclear matter (see also discussion in Section 2.3.1 and Figures 12 and 50). In the left panel results are shown based on the recently developed NN and 3N interactions within  $\Delta$ -full chiral EFT (see Section 2.3.2) [142]. Even though only observables up to  $A = 4$  were used in the fit (as in Ref. [123]), the interactions provide results in remarkable agreement with the empirical region. Furthermore, the results indicate that the inclusion of the  $\Delta$  degree of freedom might lead to an accelerated convergence consistency of the chiral expansion in the  $\Delta$ -full formulation. In the right panel results are shown for the pressure of symmetric nuclear matter based on the chiral EFT interactions of Ref. [123] (blue bands and lines at low density), results from first nonperturbative functional RG calculations directly based on QCD at higher densities (red band), as well as various relativistic mean-field calculations (see Ref. [381] for details). Interestingly, the chiral EFT results show a remarkable consistency with results obtained from the functional-RG calculations and suggest that a simple interpolation between the two regimes might be possible in order to obtain a comprehensive estimate of EOS uncertainties over the entire density range. In addition, the natural emergence of a maximum in the speed of sound  $c_s$  at supranuclear densities with a value beyond the asymptotic value  $c_s^2 = \frac{1}{3}$  is found. The existence of such a maximum has also been predicted for neutron-rich matter, only based on the observation of heavy neutron stars [383–385].

The left panel of Figure 68 shows the energy per particle of neutron matter up to saturation density. The results are obtained with different many-body methods (see caption). For the results shown with bands, the theoretical uncertainty of the energy is dominated by uncertainties in the low-energy couplings  $c_1$  and  $c_3$ , which specify the long-range two-pion-exchange parts of 3N forces (see Section 2).

These results show that chiral EFT interactions provide strong constraints for the EOS of neutron matter, which are consistent among different many-body methods and considering variations of the Hamiltonian. The significant overlap of the red lines and the blue band indicates that neutron matter is, to a good approximation, perturbative for chiral NN interactions with  $\Lambda = 500 \text{ MeV}$ . These results have also been benchmarked against first QMC calculations with local chiral EFT interactions [50, 51] (see also right

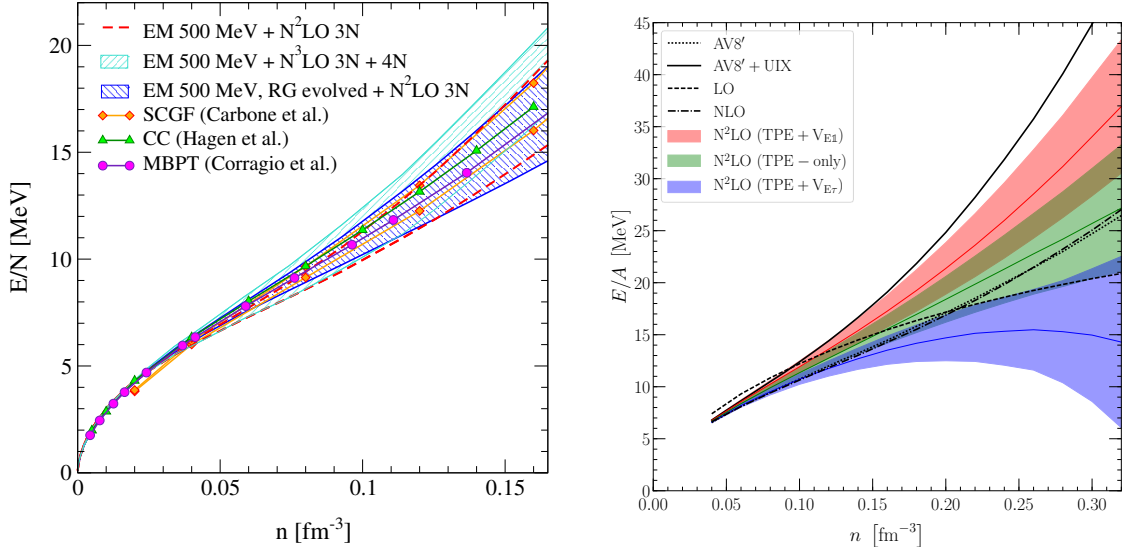


Figure 68: Left: Energy per particle of neutron matter based on different chiral EFT interactions and using different many-body methods. The uncertainty bands in the left panel show the energy range based on the 500 MeV  $N^3\text{LO}$  NN potential of Ref. [199] and including  $N^2\text{LO}$  3N forces in MBPT (red lines) [382] or in the SCGF approach [132], as well as including all 3N and 4N interactions to  $N^3\text{LO}$  (cyan band) [124, 265]. The blue band shows the results after RG-evolution of the NN interaction [122]. In addition, we show results obtained in CC [139] and in MBPT [126]. Right: Auxiliary-field-diffusion Monte-Carlo results for neutron matter based on chiral NN and 3N interactions at  $N^2\text{LO}$ . The bands show the uncertainties from the EFT truncation for different choices of the 3N short-range operator structure. For comparison, shown are also results at LO and NLO as well as results using the phenomenological AV8' NN and UIX 3N forces. *Source:* Left figure taken from Ref. [178] and right figure taken from Ref. [383].

panel). In addition, neutron matter calculations using in-medium chiral perturbation theory approaches results provide similar results [125]. In the right panel we show results for neutron matter using local chiral interactions at LO, NLO, and  $N^2\text{LO}$  with three different parametrizations for the 3N interactions specified in Ref. [52]. The three different choices correspond to equivalent parametrizations in the limit of infinite momentum cutoff scale or, equivalently, in the absence of any coordinate-space regulator functions. However, for finite cutoff scales the different choices clearly have a significant effect on the results due to the loss of Fierz-arrangement symmetries for the employed local regulator functions [383] (see also discussion in Section 3.7.2). Furthermore, the results show that the uncertainty estimates for the energy quickly increase for densities beyond  $n \approx n_0 = 0.16 \text{ fm}^{-3}$ .

In Refs. [386, 387] a new framework for quantifying theoretical uncertainties for infinite matter was presented. Based on the calculations of Ref. [130] a Bayesian framework was employed to extract statistical uncertainties. This approach allows to account for correlations between EOS truncation errors across different observables and different densities [245]. Figure 69 shows the results for the 68% credible intervals at different orders in the chiral EFT expansion as a function of density for PNM (left) [387] and SNM (right) [386]. In agreement with the findings of Ref. [242] the uncertainty bands turn out to be in reasonable agreement with the estimates resulting from the EFT error prescription proposed in Refs. [189, 204] as done in Ref. [130] (see also Ref. [241]). The employed framework also allows to give posterior distributions for the breakdown scale  $\Lambda_b$ , which enters the in-medium EFT expansion parameter in form of the relation  $Q(k_F) = \frac{k_F}{\Lambda_b}$ . The obtained posterior distributions range around  $\Lambda_b = 600 \text{ MeV}$  and are hence consistent with determinations from NN scattering observables.

The systematic increase of the uncertainty bands indicates that the expansion parameter  $Q$  becomes sizable around  $n_0$  such that the chiral EFT expansion gradually becomes inefficient with increasing density. However, for astrophysical applications the equation of state is required over a density regime significantly beyond the range shown in Figures 68 and 69. In order to extend the EOS to densities beyond the regime

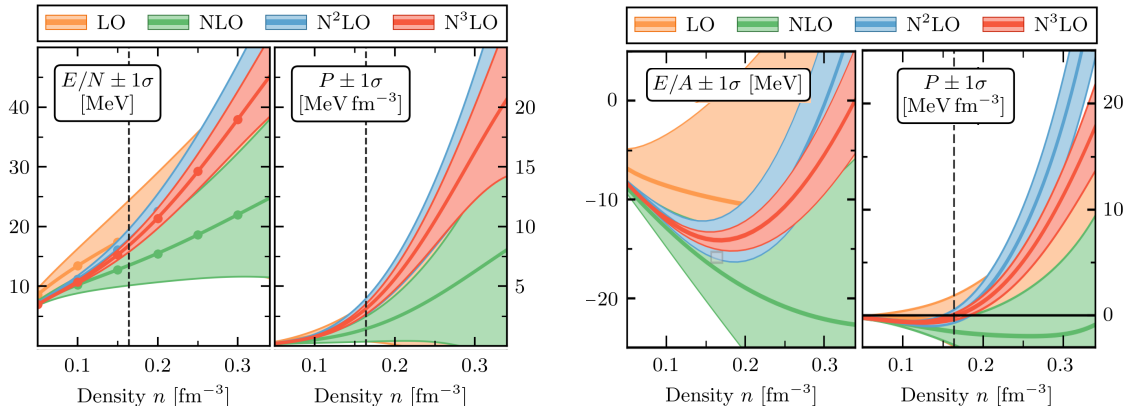


Figure 69: 68% credible intervals for the energy per particle of PNM (left) and SNM (right) at different orders of the chiral EFT expansion. The bands have been determined based on the results of Ref. [130]. The gray box denotes the empirical saturation region  $n_0 = 0.164 \pm 0.007 \text{ fm}^{-3}$  with  $E/A(n_0) = -15.86 \pm 0.57 \text{ MeV}$  obtained from a selection of energy density functionals (see Ref. [386] for details). The vertical lines mark the density  $n_0 = 0.164 \text{ fm}^{-3}$  for guidance.

Source: Left figure taken from Ref. [387] and right figure adapted from Ref. [386].

accessible by chiral EFT interactions, there are two complementary options:

- Performing microscopic calculations at higher densities using frameworks based on degrees of freedom relevant at these density scales. Generally, this approach has the advantage providing direct insight into the composition and properties of matter. On the other hand, the results of such calculations are usually strongly model and scheme dependent.
- Parametrizing the high-density part in some general way and constraining the values of the free parameters using astrophysical observations and general considerations like causality. This strategy assumes that the parametrization is sufficiently complete such that all possible relevant EOSs can be described. Generally, this approach has the advantage that it does not depend on any assumptions regarding the degrees of freedoms and their interactions in matter at high densities. On the downside, it does not provide any direct insight into the microphysics of matter at supranuclear densities.

Some examples of the first approach for symmetric nuclear matter are shown in the right panel of Figure 67, in particular the functional-RG results at supranuclear densities, extracted directly from the quark-gluon dynamics described by QCD. The second approach was applied, e.g., in Refs. [382, 383, 385, 390]. In these works, two different parametrizations were developed. The first is a piecewise polytropic form, which parametrizes the pressure as a function of baryon density  $n$  in the form  $P \sim n^\Gamma$  [382, 391], where  $\Gamma$  is a free parameter that controls the stiffness of the EOS in a given density regime. The second parametrization is based on the speed of sound  $c_s$  [383, 385].

In the left panel of Figure 70 we show the EOS uncertainty bands using these two high-density parametrizations based on chiral EFT results of Refs. [122, 382] up to around saturation density. The key external constraints that determine the uncertainty bands at higher density are the mass  $M = 1.97 M_\odot$  of the most massive neutron star measured to date [392] and causality considerations [382, 385]. Generally, the uncertainty bands are determined by both the low-density results that act as an anchor point as well as the constraints from causality and neutron star observations. We note that the results correspond to the EOS constraints of neutron-star matter. Details on how the finite proton fraction was determined and incorporated in the calculations can be found in Refs. [382]. In neutron stars, matter consists of nuclei embedded in a sea of electrons at low densities in the outer crust, while the nuclei become increasingly neutron-rich structures in the inner crust [388, 389]. The transition to homogeneous neutron-rich matter happens around half nuclear saturation density [382]. In the right panel of Figure 70 the results for the pressure in this den-

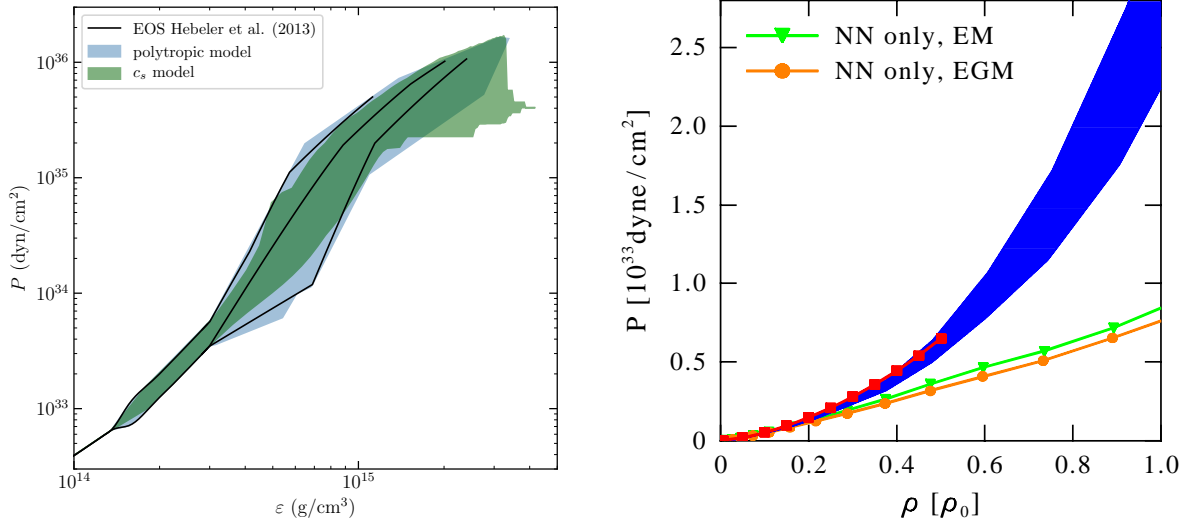


Figure 70: Left: Comparison of the ranges for the EOS based on the piecewise polytropic (PP) and speed-of-sound ( $c_s$ ) high-density parametrizations, after including constraints from causality and neutron star masses (see Ref. [385] for details). The black lines show the three representative equations of state of Ref. [382], the light blue bands show the uncertainty ranges resulting from the PP parametrization and the darker green bands those from the  $c_s$  parametrization. Right: Pressure of neutron star matter based on chiral low-momentum interactions for densities up to nuclear saturation density  $\rho_0$ . The blue band estimates the theoretical uncertainties from many-body forces and from truncations in the many-body calculation. At low densities, the results are compared to a standard BPS crust equation of state [388, 389] (red line), while the green and orange lines show results based on only NN interactions.

Source: Left figure taken from Ref. [385] and right figure taken from Ref. [390].

sity region are shown. Clearly, for the employed low-resolution interactions the inclusion of 3N interactions is crucial for a continuous transition between these two states of matter.

Recent breakthroughs like the first detection of the gravitational wave signal of the binary neutron star

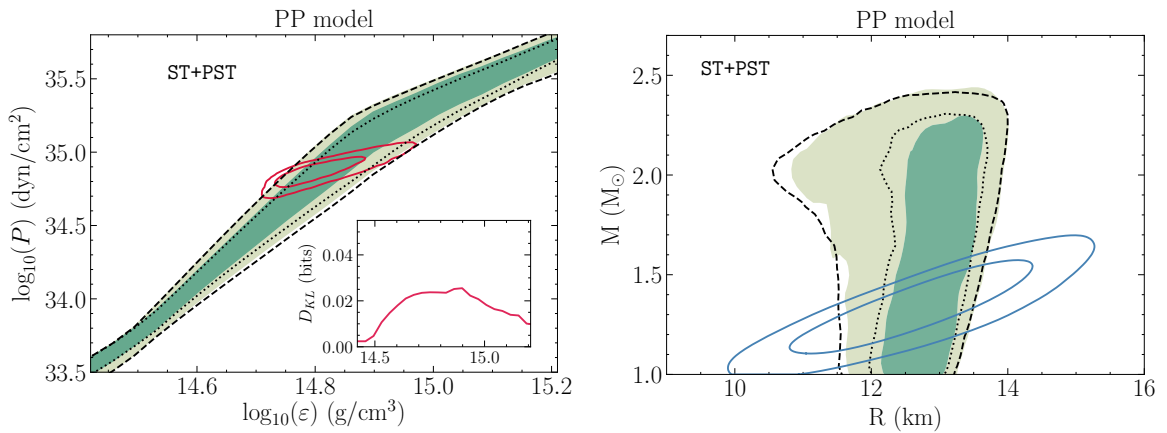


Figure 71: Posterior distributions for the equation of state (left) and the mass-radius relation (right) for the piecewise polytropic parametrization. The dark/light green bands show the 68% and 95% posterior credible intervals, while the black dotted and dashed lines respectively indicate the joined 68% and 95% prior credible intervals. The red contours in the left panel denote the corresponding credible regions of central energy density and central pressure, while the blue contours in the right panel show the likelihood functions of the PSR J0030+0451 measurement. ST+PST refers to the employed hot region model.

Source: Figures taken from Ref. [393].

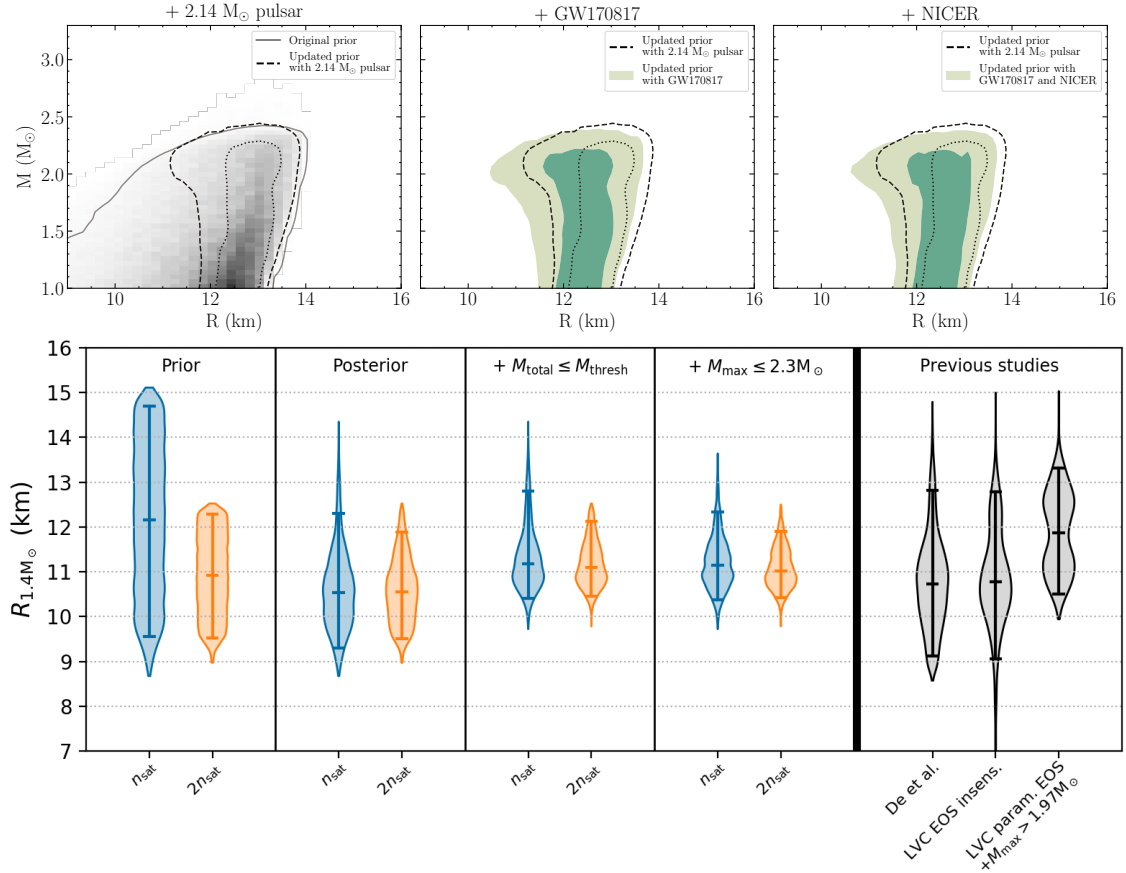


Figure 72: Upper panel: Mass-radius posterior distributions conditional the PP model (compare Figure 71) and given: (i) the  $2.14 M_{\odot}$  pulsar alone (left panel); (ii) inclusion of the GW170817 measurements (middle panel); and (iii) inclusion of the mass and radius of PSR J0030+0451 inferred by the NICER data of Ref. [394] (right panel). The panels show how the posterior distributions update the prior distributions. The contours indicate the 68% and 95% credible intervals as in Figure 71. Lower panel: Posterior distributions for the radius of a  $1.4M_{\odot}$  neutron star based on microscopic calculations (left) and after incorporating information from gravitational-wave analyses and from constraints on the total mass being smaller than the threshold mass  $M_{\text{thresh}}$  for a prompt collapse after merging (see Ref. [395] for details). The blue bands show the results based on microscopic calculation up to nuclear saturation density, while for the the orange bands the calculations are extended to twice nuclear saturation density.

*Source:* Upper figure taken from Ref. [396] and lower figure taken from Ref. [395].

merger GW170817 [316, 397] as well as ongoing missions aiming at first direct neutron star radius measurements using x-ray timing [398–400] are expected to significantly enhance our theoretical understanding of neutron-rich matter under extreme conditions. Combining information from these ongoing efforts with existing observational data like precise mass measurements of heavy neutron stars allows to systematically tighten the EOS uncertainty bands, like those shown in the left panel of Figure 71. Very recently, the mass and radius of the millisecond pulsar PSR J0030+0451 have been inferred via pulse-profile modeling of X-ray data obtained by NASA’s NICER mission [394]. In Ref. [393] the implications of this first measurement on the EOS constraints were investigated using a Bayesian analysis (see also Ref. [401]). Figure 71 shows the posterior probability distributions for the pressure and the mass-radius relation obtained from a combination of constraints from chiral EFT interactions at lower densities and information from the new NICER observations. The posterior distributions show that not much information is gained over the prior from these first measurements. In particular, from the distributions shown in the left panel of Figure 71 we observe



that the changes from the prior to the posterior are not very significant at nuclear densities, so that from this analysis it is not possible to draw robust conclusions about further constraints on dense matter and interactions within chiral EFT. Observations of alternative pulsars, like PSR J0437–4715, which has a tight mass constraint derived via radio-timing, promise to provide tighter constraints on the EOS of dense matter in the near future.

The most promising approach for deriving stringent constraints on the EOS at supranuclear densities consists in combining all available observational constraints from neutron star mass observations, gravitational wave detections and electromagnetic signals. The upper panel of Figure 72 shows the neutron star mass-radius uncertainty bands after incorporating the recent detection of the heaviest known neutron star with mass  $M = 2.14M_{\odot}$  [402] (left), the updated posterior distributions after incorporating the constraints from the GW170817 signal (center) and finally the posterior after inclusion of the NICER signals (right) [396]. The results show that most information is gained from including the  $2.14M_{\odot}$  pulsar. The binary merger GW170817 favors softer EOS than the prior, but the measured radius from PSR J0030+0451 favors stiffer EOS, resulting in a final posterior distribution very similar to the prior (see Ref. [396] for details). The lower panel of Figure 72 shows the radius posterior distributions of a  $1.4M_{\odot}$  neutron star after including constraints from GW170817 and from the constraint that the estimated total mass  $M_{\text{total}}$  to be less than the threshold mass for prompt collapse  $M_{\text{thresh}}$  (see Ref. [395] for details). The shown results in particular highlight the importance of the value for the critical upper density up to which the microscopic calculations based on NN and 3N interactions are being trusted, i.e.  $n_{\text{sat}}$  (blue) versus  $2n_{\text{sat}}$  (orange) (see also discussion in Sect. 6.2).

For the study of individual neutron stars it is sufficient to study the EOS at zero temperature in the very neutron-rich regime (up to about 10% protons). Neutrino emission quickly cools new-born neutron stars to an interior temperature of less than 1 MeV [404], which is much smaller than the Fermi energy of a nucleon at saturation density  $E_{\text{F}} \sim 35$  MeV. However, for neutron-star merger events or supernovae explosions the temperatures can be significantly higher such that EOS data at finite temperature is required as the fundamental input for theoretical simulations of such events. Conceptually, the extension of many-body calculations to finite temperatures is straightforward, at least within MBPT or SCGF. The particle distribution functions in momentum space become Fermi-Dirac functions and the fundamental quantity of interest is now the free energy  $F$ . In the left panel of Figure 73 we show the results of SCGF calculations for the free energy of PNM and SNM at different temperatures as a function of density based on chiral NN and 3N interactions (see Ref. [403] for details). Obviously, as soon as temperatures of about 10–20 MeV are reached, the temperature effects for the EOS become quite significant (see also Refs. [127, 405]). One key challenge for the future will be to systematically extend such finite-temperature results systematically to higher densities like at zero temperature. However, the situation at finite temperature is somewhat more complicated since so far no direct observational data exists that could be used as a constraint at high densities. One promising theoretical approach consists in extending calculations of Ref. [381] to neutron-rich systems and compute the EOS at finite temperature and high densities directly based on QCD using the nonperturbative functional RG framework.

The ultimate challenge consists in deriving systematic uncertainty bands for the EOS over the full range of densities, temperatures and proton fractions relevant for astrophysical application. The bands should be consistent with theoretical calculations at lower densities and with all available astrophysical observations like, e.g., measured neutron star properties. Extending many-body frameworks for infinite matter to general proton fractions is in principle straightforward. However, for general proton and neutron densities the system has fewer symmetries and the calculations hence become somewhat more complicated and more expensive. In the right panel of Figure 73 we show results of MBPT calculations for nuclear matter at zero temperature and general isospin asymmetries based on chiral NN and 3N interactions (see Ref. [128] for details). The system is characterized by the proton fraction defined by  $x = n_p/(n_n + n_p)$ , where  $n_p$  resp.  $n_n$  denote the proton and neutron densities, i.e.  $x = 0$  corresponds to PNM and  $x = 0.5$  to SNM. The results clearly illustrate the increased attraction from nuclear interactions toward larger proton fractions. Typically, this dependence on the proton fraction can be approximated quite accurately by a simple quadratic expansion



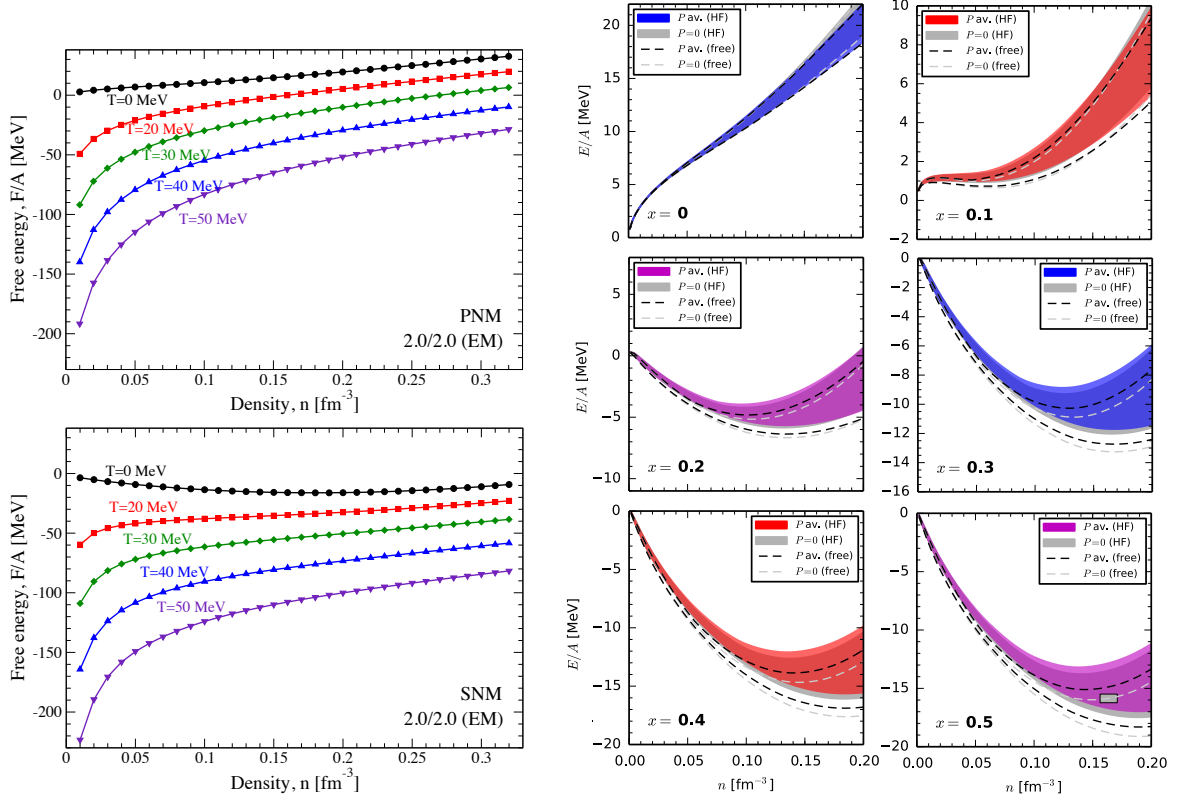


Figure 73: Left: Free energy per nucleon for  $T = 20, 30, 40$  and  $50$  MeV as function of density for PNM (upper panel) and SNM (lower panel). The results are based on SCGF calculations using the “2.0/2.0(EM)” interaction of Ref. [123]. Right: The energy per particle of isospin asymmetric nuclear matter as a function density for different proton fractions  $x = n_p/(n_n + n_p)$  (see main text). The box in the figure for  $x = 0.5$  shows the empirical saturation region. For details see Ref. [128].  
*Source:* Left figure taken from Ref. [403] and right figure adapted from Ref. [128]

in  $x$  around SNM:

$$\frac{E(n, x)}{A} \approx \frac{E(n, 1/2)}{A} + (1 - 2x)^2 S_2(n), \quad (212)$$

where  $S_2(n)$  is the symmetry energy. Terms beyond the quadratic approximation based on chiral EFT interactions have been studied in Refs. [406, 407], which involve quartic, sextic and even logarithmic terms. However, in practice these terms turn out to be rather small compared to the leading quadratic coefficient such that the approximation shown in Eq. (212) is usually very reasonable, at least at small temperatures. For higher temperatures it seems more efficient and reliable to treat the isospin asymmetry of the non-interacting part exactly and approximate only the isospin dependence of the interaction contributions [127].

## 6. Summary and outlook

In this work we discussed in detail fundamental techniques for representing and calculating 3N interactions for *ab initio* studies of nuclei and matter and reviewed a selection of recent calculations. The presented results clearly demonstrate the importance of contributions from 3N interactions for nuclear observables and illustrate the capabilities of state-of-the-art many-body frameworks. In this last section we will make an attempt to summarize the current status of *ab initio* nuclear structure theory and draw some general conclusions based on the discussed results. Finally, we discuss some open questions and give an overview of current and future directions.

### 6.1. Present status and achievements

Most calculations and results discussed in this work have been made possible thanks to major advances in two fundamental areas of *ab initio* nuclear structure theory:

- First, the scope of *ab initio* many-body frameworks with respect to the particle number has significantly increased thanks to the development of novel many-body expansions with a mild polynomial scaling behavior. In addition, several existing methods have been generalized to open-shell nuclei and are being continuously extended such that additional observables can be studied. Presently, the scope of many-body methods formulated in a harmonic oscillator basis representation (see Section 1) are limited to the regime  $A \lesssim 100$  due to the achievable basis sizes for representing 3N interactions.
- Second, in recent years a significant number of novel NN and 3N interactions have been developed, derived within different regularization schemes, using new advanced fitting strategies for the low-energy couplings, as well as in chiral EFT formulations with and without explicit inclusion of  $\Delta$  degrees of freedom. Most of these interactions are made available at different orders of the chiral expansion and at different cutoff scales. This allows to perform order-by-order calculations, which can then be used to estimate theoretical chiral EFT uncertainties. This situation is very different from the time about 15 years ago, when only very few interactions were available for one specific regularization scheme and at one particular chiral order and cutoff scale. Furthermore, the methods discussed in this work allow to compute matrix elements of 3N interactions at higher orders in the chiral expansion and for sufficiently large basis sizes, such that the structure of few-body systems, medium-mass nuclei and matter as well as few-body reactions can be studied based on the same NN and 3N interactions.

The main general lessons learned from *ab initio* studies in recent years can be summarized as follows:

- Overall, a remarkable agreement is found between results based on different many-body frameworks for a given low-resolution nuclear interaction (see Figure 3), which implies that the many-body uncertainties of these calculations are small. Whenever results based on such interactions show a significant discrepancy to experiment, under consideration of the theoretical uncertainties, they can be mainly attributed to deficiencies of the employed nuclear interactions and operators.
- Specific observables can be reproduced remarkably well by particular interactions over a significant range of the nuclear landscape up to  $^{100}\text{Sn}$  (see right panel of Figure 17 and left panel of Figure 54). However, since these results are based on interactions at a specific order of the chiral expansion, it is not possible to assign systematic chiral EFT uncertainty estimates. Furthermore, a deeper understanding why specific interactions perform well for some observables, but relatively poorly for others, is still lacking. However, for all these discussions the inherent theoretical uncertainties due to truncations in the chiral EFT expansion of the nuclear forces need to be taken into account.
- It is challenging to derive nuclear interactions capable of simultaneously predicting different observables of nuclei from the light sector to the medium-mass regime consistent with experiment. Agreement can be achieved when information of heavier nuclei is included in the fit of the interaction. However, in these cases, the accurate reproduction of the nucleon-nucleon phase shifts at higher energies has to be sacrificed, at least at N<sup>2</sup>LO (see, e.g., Figure 17).

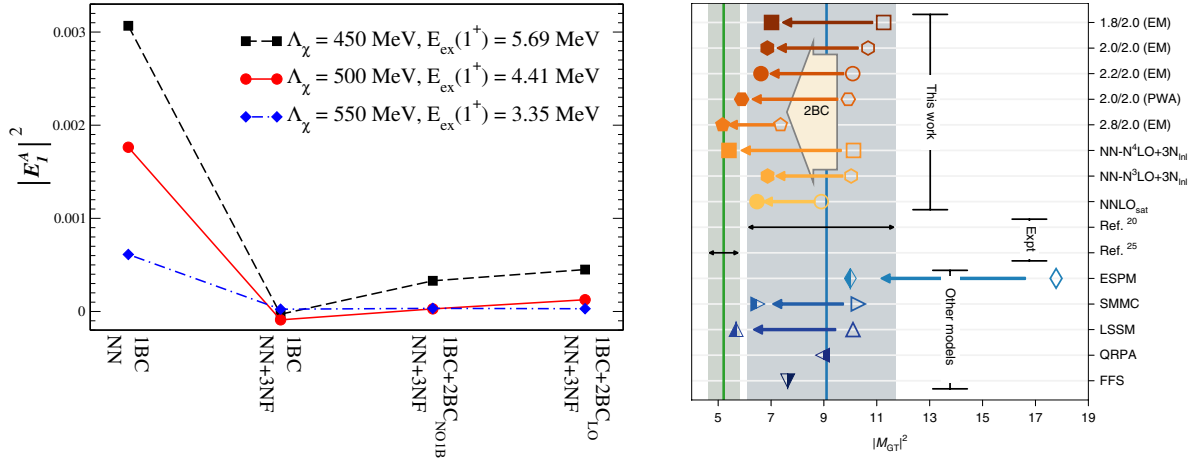


Figure 74: Left: Squared  $\beta$ -decay matrix element of  $^{14}\text{C}$  obtained from increasingly sophisticated calculations, ranging from NN-only calculations including only one-body current contributions (“1BC”, left), to NN+3N interactions including one- and leading-order two-body contributions (“2BC”, right). Here “2BC<sub>NO1B</sub>” refers to the normal ordering approximation of the 2BC contributions, see Ref. [353] for details. Right: Gamow-Teller  $\beta$ -decay matrix elements of  $^{100}\text{Sn}$  calculated within coupled cluster. Unfilled symbols show results obtained with the standard one-body Gamow-Teller operator, while filled symbols correspond to results including two-body currents. Partially filled symbols show the results obtained by multiplying the computed Gamow-Teller strength in the given works (see Ref. [354]) by a phenomenological quenching factor (see discussion in Section 5.7). *Source:* Left figure taken from Ref. [353] and right figure taken from Ref. [354].

- Order-by-order calculations based on specific sets of interactions are able to reproduce simultaneously ground-state energies and charge radii of lighter nuclei (see right panel of Figures 57 and Figures 59 and 60). It will be interesting to further explore such interactions, study additional observables of nuclei and matter and investigate in greater detail the role of regularization schemes and scales for nuclear interactions.
- While theoretical predictions for systems with a significant proton fraction, such as atomic nuclei and isospin-symmetric matter, generally depend more sensitively on properties of the employed interactions, the results for pure neutron systems or very neutron-rich systems exhibit a remarkable insensitivity to such details and are in good agreement with present experimental constraints [408–410]. These findings suggest that, e.g., predictions for the EOS of neutron-rich matter up to about nuclear saturation density are robust and rather well constrained.

## 6.2. Open questions and future directions

Despite all the achievements discussed in the previous section there are still fundamental open questions and challenges. Here we discuss some of them, without any claim to completeness:

- So far, almost all calculations based on chiral EFT interactions have been based on Weinberg’s power counting scheme (see Section 2). There are currently efforts to explore alternative power counting formulations with an improved RG invariance, which allow to vary the cutoff scales over a much wider range [17]. The development of these interactions involve the promotion of counter terms in Weinberg’s scheme to lower orders in the expansion. Furthermore, many-body frameworks based on such interactions need to be modified since contributions beyond leading order have to be treated perturbatively. The availability of such Hamiltonians could be key for gaining a deeper understanding of the deficiencies of presently used interactions.
- In most many-body calculations the contributions to nuclear interactions and currents in the chiral expansion are not treated on equal footing. While there have been recent efforts to include systematically

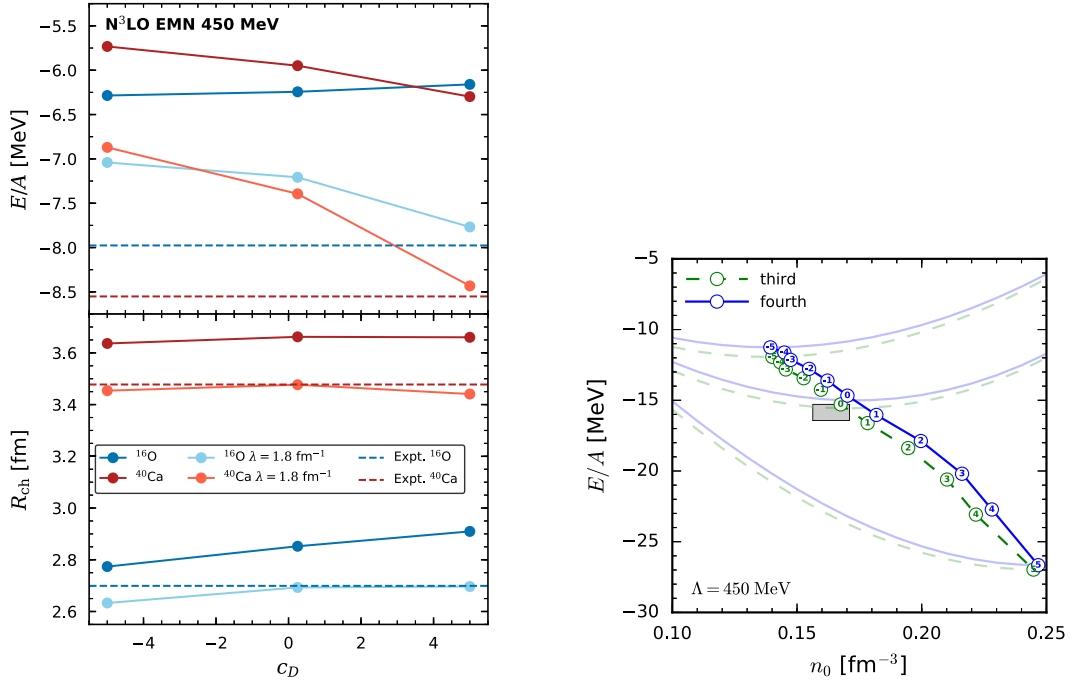


Figure 75: Left: Ground-state energies (top panel) and charge radii (bottom panel) for  $^{16}\text{O}$  and  $^{40}\text{Ca}$  as a function of  $c_D$  (with corresponding  $c_E$  value from the  $^3\text{H}$  binding energy, see Figure 8). Results are shown for unevolved and SRG-evolved potentials with  $\lambda_{\text{SRG}} = 1.8 \text{ fm}^{-1}$  in comparison with experimental values. Right: Theoretical saturation points of symmetric nuclear matter as a function of the coupling  $c_D$ . Also shown is the energy per particle for the three representative values,  $c_D = -5, 0.25$ , and  $5$ , at third and fourth order in MBPT. *Source:* Figures taken from Ref. [243].

higher-order contributions to operators like the Gamow-Teller operator (see also Section 5.7), these calculations are still at their infancy. In addition, higher-order long-range corrections to axial-vector currents have been studied in Refs. [411, 412] in the context of WIMP-nucleus scattering as part of dark matter searches [413]. Figure 74 illustrates that contributions from higher-order two-body currents (2BC) can have significant effects on transition strengths in nuclei. In the left panel the effects of two-body currents on the Gamow-Teller matrix element in  $^{14}\text{C}$  are illustrated, while the right panel shows the effect of 2BC on the Gamow-Teller strength in  $^{100}\text{Sn}$ . The figures show that higher-order contributions can have a significant impact on the results. While for anomalously small matrix elements like for  $^{14}\text{C}$  these contributions can enhance the results by a sizable factor (see also left panel of Figure 64 and related discussion), for  $^{100}\text{Sn}$  they lead to an effective suppression factor, which is in good agreement with phenomenological quenching factors previously introduced in order to improve the agreement with experiment (see discussion in Section 5.7). Finally, in Ref. [414] the effects of two-body contributions to the charge density operator have been investigated for the deuteron using a family of state-of-the-art NN interactions at different orders in the chiral expansion and allowed a very accurate extraction of the charge radius of the neutron. It will be crucial to extend such calculations in a systematic way including estimates of theoretical uncertainties to a larger number of nuclei and observables in the near future.

- The connection between properties of atomic nuclei and nuclear matter based on a given set of interactions is still not well understood on a quantitative level. On a qualitative level, however, some systematic trends between observables of both systems can be found (compare, e.g., right panel of Figure 12 and Figure 13 and related discussion in Section 2.3.1). Since nuclear forces should ideally provide a comprehensive description of nuclei as well as nuclear matter, it will be key to obtain a

better understanding of this link. This is of particular relevance when nuclear matter is being used as an anchor point for fits of future nuclear forces. In Ref. [243] properties of medium-mass nuclei were studied based on 3N interactions fitted to the binding energy of  $^3\text{H}$  and the saturation region of nuclear matter (see Figures 8, 14 and 56). Figure 75 shows results for medium-mass nuclei and the saturation points of symmetric nuclear matter based on the same NN and 3N interactions as a function of the 3N coupling  $c_D$ . While the ground-state energies of  $^{16}\text{O}$  and  $^{40}\text{Ca}$  change by  $< 1$  MeV for SRG-unevolved interactions, the change in saturation energy is 15 MeV over the studied  $c_D$  range [243]. In addition, for  $c_D$  values that lead to a good reproduction of the empirical saturation region, the ground-state energies of nuclei turn out to be significantly underbound (see Figure 56). These findings indicate that nuclear matter at lower densities might be more relevant for atomic nuclei and that the connection between light nuclei, medium-mass nuclei and nuclear matter is generally quite intricate and requires further investigations.

- For calculations of dense matter it will be key to investigate more systematically the density limit up to which chiral EFT interactions can provide reliable predictions. Generally, the size of EOS uncertainties at several times saturation density, determined based on calculations at low densities and neutron star properties, crucially depends on the uncertainty bands around and slightly above nuclear densities (see Refs. [382, 383]). Consequently, being able to push the density limits to slightly larger densities can significantly improve the predictive power of the microscopic calculations for the properties of neutron stars (see lower panel of Figure 72). Even though there are clear indications that the uncertainty bands increase systematically with density (see, e.g., right panel of Figure 68), these studies so far depend on particular choices for the value of the expansion parameter  $Q$  and the chosen prescription for extracting uncertainty bands. Bayesian frameworks might offer a powerful tool to address this question more systematically. Work along these lines is in progress.
- Generally, estimates of theoretical uncertainties should be assigned to all results of *ab initio* calculations. Ideally, these uncertainties should have a well-defined statistical interpretation. In recent years Bayesian frameworks have been developed to estimate EFT truncations errors for two- and three-body calculations (see, e.g., Refs. [240, 241]). It will be crucial to extend these analyses to many-body systems based on NN and 3N interactions formulated in different regularization schemes and for different Bayesian prior choices. Given the availability of various different NN and 3N interactions, it is of central importance to obtain a deeper understanding of the capabilities and limits of particular interactions regarding the correct description of different observables of nuclei. Differences due to possible regulator choices should generally be effects of higher order in the chiral expansion and results should eventually become independent at sufficiently high orders. Strictly, this is true as long as all contributions to interactions and currents are properly taken into account up to a given order. Presently, it has not yet been demonstrated to what extent results based on different interactions are consistent with each other.

Bayesian frameworks offer a promising tool for analyzing the parameter space of existing interactions or for constructing improved nuclear interactions in the future [416]. In Ref. [237] it was demonstrated that such frameworks can be used to study the robustness of the parameter estimation of given NN interactions and to isolate issues connected to redundant and correlated couplings based on phase shift data (see also Section 2.3.4). However, the generalization of these studies to many-body systems and to NN plus 3N interactions for different regularization schemes involves significant computational challenges. Both, parameter fitting and obtaining posterior distributions for calculated observables involve sampling a large number of points in a high-dimensional parameter space, where the required large number of exact calculations would be prohibitively expensive. Recently, in Ref. [417] it was shown that a new method called eigenvector continuation (EC) can be used as a fast and accurate emulator, thereby making uncertainty quantification in multi-nucleon systems practical (see also Refs. [239, 418]). On the basis of calculations for  $^4\text{He}$ , it was demonstrated that EC is superior to established methods like Gaussian processes or polynomial interpolation. For nuclear physics, and statistical analysis of the nuclear many-body problem in particular, the EC method can be the key ingredient that enables

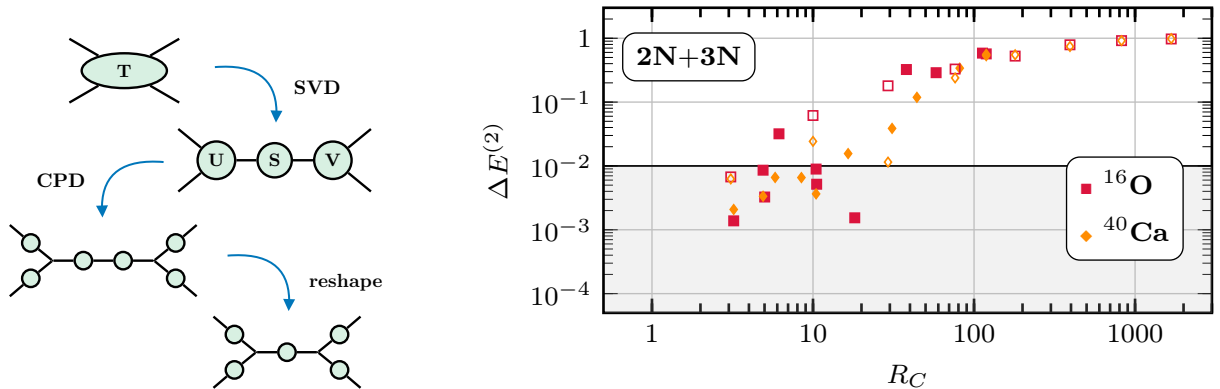


Figure 76: Left: Diagrammatic representation of the tensor hypercontraction (THC) decomposition of a rank-4 tensor. It involves a singular value decomposition (SVD), a canonical polyadic decomposition (CPD) and a final reshaping of the decomposition. Right: Relative energy difference  $\Delta E^{(2)}$  tensor-decomposed ground-state energy correction in second-order many-body perturbation theory as a function of the data compression factor  $R_C$  for  $^{16}\text{O}$  and  $^{40}\text{Ca}$ . Full (empty) symbols correspond to different THC approximations. The gray region denotes the region of sub-percent accuracy. *Source:* Figures taken from Ref. [415], left figure modified.

the large-scale Markov-Chain Monte Carlo evaluation of Bayesian posteriors of parameters in effective field theory models of the nuclear interaction. Applications to this and related studies are already under way.

- Storing and handling three- and higher-body operators represents presently one of the fundamental limitations of many-body frameworks for medium-mass nuclei. Given the complexity of this problem, there is urgent need to develop efficient methods that allow to reduce the computational costs of such calculations and allow to push the scope of these frameworks to larger mass numbers. Inspired by methods used in quantum chemistry and solid-state physics in Ref. [415], a tensor decomposition technique for *ab initio* nuclear structure calculations was presented. The underlying idea of this method is to represent a given tensor approximately in terms of products of lower-rank tensors. If we consider, e.g., a rank-four tensor (i.e., a two-body interaction), which depends on four generic single-particle quantum numbers  $i_a$ , it can be written via a so-called tensor hypercontraction (THC) [415, 419–421]

$$T_{i_1 i_2 i_3 i_4} = \sum_{\alpha, \beta} X_{i_1 \alpha}^1 X_{i_2 \alpha}^2 W_{\alpha \beta} X_{i_3 \alpha}^3 X_{i_4 \alpha}^4. \quad (213)$$

In practice, the THC decomposition can be performed via a multistep process, which involves a singular value decomposition (SVD) and a canonical polyadic decomposition (CPD) (see left panel of Figure 76). For details we refer the reader to Ref. [415]. In this work it was also demonstrated that a significant reduction in the required memory space can be achieved while maintaining a remarkable accuracy for energies compared to the full result for MBPT calculations (see right panel of Figure 76). In Ref. [422] this method was applied to open-shell systems. In the near future this strategy promises to be a powerful tool that allows to significantly scale down the computational complexity of state-of-the-art many-body frameworks and might also be a path toward the inclusion of four- and higher-body interactions in such calculations. Even though four-nucleon (4N) interactions can in principle be treated by a straightforward extension of the methods presented in Section 3, the practical implementation of a partial-wave decomposition is extremely challenging and the required basis sizes for a complete representation are presently beyond the limit of feasibility (see, e.g., Ref. [423]). Even though first studies suggest that effects from 4N interactions in nuclei and matter are small [265, 423–425], chiral EFT dictates the inclusion of these interactions at  $N^3\text{LO}$  and beyond (see Section 2). The utilization of a clever tensor decomposition, possibly in combination with importance truncation methods (see

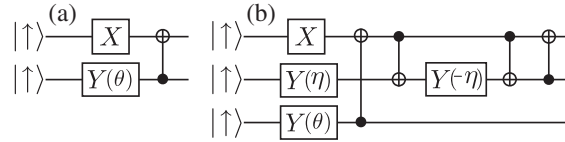


Figure 77: Quantum circuits for generating unitary rotations for one basis state and the corresponding angle  $\theta$  (left) and two states characterized by the angles  $\theta$  and  $\eta$  (right).  $X$  represents a Pauli spin matrix and  $Y(\theta)$  rotation around the  $Y$  axis, see also Ref. [427].

Source: Figure taken from Ref. [433].

Ref. [422]), might allow to include contributions from such many-body interactions approximately at a much lower computational cost.

- The field of quantum computing is rapidly evolving these days with more and more powerful devices becoming available every year. Some inherently hard problems for “classical” computers have been shown to be solvable on quantum computers very efficiently (see, e.g., Refs. [426, 427] for an overview and Ref. [428] for a very recent application). In recent years, it has been demonstrated that problems in quantum chemistry and solid state physics can already be solved via quantum computers [429–432]. The fundamental units of quantum computers are circuits of entangled qubits. Theoretically, the manipulation of qubits can be represented in terms of Pauli matrices [427]. Present quantum devices developed by Google, IonQ and IBM are limited to about 50 to 79 non-error corrected qubits, while full scale many-body problems in nuclear physics would require at least 100 error-corrected bits [433]. One fundamental challenge for the development of algorithms for quantum computers lies in the reduction of the required circuit depths and number of entangling operations, such that all operations can be performed within the device’s decoherence time [434]. In Ref. [433] a first proof-of-principle quantum computation of the deuteron binding energy via two different quantum devices was presented. For the calculations a discrete variable representation was employed to match the connectivity of the available hardware, while the ground-state energy of the system was determined using a variational approach using 2 or 3 basis states. The corresponding qubit gate structures for these deuteron calculations are shown in the left and right panel of Figure 77, respectively. Results of these calculations were in good agreement with exact solutions. However, it was also demonstrated that noise effects connected to measurement errors increase significantly with circuit depth. This highlights the necessity for improved error correction mechanisms for applications of quantum computers to full-scale problems in *ab initio* nuclear physics [435, 436].

## Acknowledgements

A major part of the presented work in this review is the result of very fruitful long-term collaborations I am very happy to be part of. Specifically, I would like to thank Sonia Bacca, Andreas Bauswein, Sven Binder, Scott Bogner, Jens Braun, Angelo Calci, Arianna Carbone, Christian Drischler, Thomas Duguet, Victoria Durant, Alex Dyhdalo, Andreas Ekström, Evgeny Epelbaum, Christian Forssén, Bengt Friman, Dick Furnstahl, Alex Gezerlis, Jacek Golak, Svenja Greif, Gaute Hagen, Hans-Werner Hammer, Heiko Hergert, Javier Hernandez, Matthias Heinz, Martin Hoferichter, Jason Holt, Jan Hoppe, Thomas Hütter, Jonas Keller, Philipp Klos, Sebastian König, Hermann Krebs, Thomas Krüger, Jim Lattimer, Dean Lee, Marc Leonhardt, Joel Lynn, Pieter Maris, Ulf-G. Meißner, Javier Menéndez, Sushant More, Andreas Nogga, Thomas Papenbrock, Chris Pethick, Geert Raaijmakers, Robert Roth, Achim Schwenk, Rodric Seutin, Johannes Simonis, Roman Skibiński, Vittorio Somà, Ragnar Stroberg, Ingo Tews, Alex Tichai, James Vary, and Anna Watts for numerous discussions on various topics discussed in this work over the years. In addition,



I thank Matthias Heinz, Jan Hoppe, Rodric Seutin and Alex Tichai for carefully reading the manuscript and providing most helpful comments. Finally, I thank the entire Theoriezentrum at the TU Darmstadt for the very stimulating and enjoyable atmosphere. The presence of so many bright young researchers makes this truly a special place.

This work was supported by the Deutsche Forschungsgemeinschaft (DFG, German Research Foundation) – Projektnummer 279384907 – SFB 1245 and the BMBF under Contract No. 05P15RDFN1. Computational resources have been provided by the Jülich Supercomputing Center and by the Lichtenberg high performance computer of the TU Darmstadt.

## A. Normalization convention of momentum basis states

A general Galilean-invariant NN interaction takes the following form in vector representation:

$$\langle \mathbf{p}' S M_{S'} T M_T | V_{\text{NN}} | \mathbf{p} S M_S T M_T \rangle. \quad (\text{A.1})$$

Here, the momenta  $\mathbf{p}$  and  $\mathbf{p}'$  denote the Jacobi momenta of the initial and final states (see Section 3.1), the quantum numbers  $S$ ,  $M_S$  and  $M_{S'}$  the two-body spin channel and corresponding spin projections of the initial and final state.  $T$  and  $M_T$  denote the corresponding two-body isospin quantum numbers. Due to the presence of tensor interactions, the interaction has in general finite contributions for different spin projection  $M_S \neq M_{S'}$ , but is diagonal in the quantum numbers  $S$ ,  $T$  and  $M_T$ . In the following we will suppress the isospin quantum numbers for two-body quantities for the sake of compact notation. Since all these quantities are diagonal in both isospin quantum numbers, they can be added in a trivial way at any stage below.

The Lippmann-Schwinger equation for the scattering  $T$ -matrix for the energy  $E$  is given in vector form by [437]

$$\langle \mathbf{p}' S M_{S'} | T_{\text{NN}}(E) | \mathbf{p} S M_S \rangle = \langle \mathbf{p}' S M_{S'} | V_{\text{NN}} | \mathbf{p} S M_S \rangle + \sum_{M_{S''}} \int \frac{d\mathbf{q}}{(2\pi)^3} \frac{\langle \mathbf{p}' S M_{S'} | V_{\text{NN}} | \mathbf{q} S M_{S''} \rangle \langle \mathbf{q} S M_{S''} | T_{\text{NN}}(E) | \mathbf{p} S M_S \rangle}{E - \mathbf{q}^2/(2\mu) \pm i\epsilon}, \quad (\text{A.2})$$

with

$$\langle \mathbf{p}' S' M_{S'} | \mathbf{p} S M_S \rangle = (2\pi)^3 \delta(\mathbf{p} - \mathbf{p}') \delta_{SS'} \delta_{M_S M_{S'}}, \quad (\text{A.3})$$

and the reduced mass  $\mu$  of the interacting particles<sup>13</sup>. We introduce two-body partial-wave states via:

$$| \mathbf{p} S M_S \rangle = A_{\text{NN}} \sum_{L, M_L, J, M_J} C_{LM_L S M_S}^{J M_J} Y_{LM_L}^*(\hat{\mathbf{p}}) | p(LS) J M_J \rangle, \quad (\text{A.4})$$

with  $\langle \hat{\mathbf{p}} | LM \rangle = Y_{LM}(\hat{\mathbf{p}})$ . Here we couple the orbital relative angular momentum quantum number  $L$  with the two-body spin  $S$  to a total relative angular momentum  $J$ . The constant  $A_{\text{NN}}$  defines the normalization convention for the partial-wave states (see below) and can take different values. The definition (A.4) leads to the following decomposition of the two-body quantities, e.g. for NN interactions:

$$\langle \mathbf{p}' S M_{S'} | V_{\text{NN}} | \mathbf{p} S M_S \rangle = A_{\text{NN}}^2 \sum_{L, L', M_L, M_L'} \sum_{J, M_J} C_{L M_L S M_S}^{J M_J} C_{L' M_L' S M_{S'}}^{J M_J} Y_{L' M_L'}^*(\hat{\mathbf{p}}') \langle p'(L'S) J | V_{\text{NN}} | p(LS) J \rangle Y_{L M_L}(\hat{\mathbf{p}}). \quad (\text{A.5})$$

Since the interaction transforms like a scalar under rotations, the partial-wave matrix elements  $\langle p'(L'S) J | V_{\text{NN}} | p(LS) J \rangle$  are diagonal in  $J$  and  $M_J$  and do not depend on the projection quantum number  $M_J$ . Hence we will suppress the  $M_J$  quantum number in the following for the matrix elements. Inverting relation (A.5) gives:

$$\langle p'(L'S) J | V_{\text{NN}} | p(LS) J \rangle = \frac{1}{A_{\text{NN}}^2} \sum_{\substack{M_L, M_S \\ M_L', M_{S'}}} \int d\hat{\mathbf{p}} d\hat{\mathbf{p}}' C_{L M_L S M_S}^{J M_J} C_{L' M_L' S M_{S'}}^{J M_J} Y_{L' M_L'}^*(\hat{\mathbf{p}}') \langle \mathbf{p}' S M_{S'} | V_{\text{NN}} | \mathbf{p} S M_S \rangle Y_{L M_L}(\hat{\mathbf{p}}). \quad (\text{A.6})$$

Inserting the expansion Eq. (A.5) in Eq. (A.2) and projecting onto the individual partial waves leads to

$$\langle p'(L'S) J | T_{\text{NN}} | p(LS) J \rangle = \langle p'(L'S) J | V_{\text{NN}} | p(LS) J \rangle + \frac{A_{\text{NN}}^2}{(2\pi)^3} \sum_{L'} \int dq q^2 \frac{\langle p'(L'S) J | V_{\text{NN}} | q(L'S) J \rangle \langle q(L'S) J | T_{\text{NN}} | p(LS) J \rangle}{E - q^2/(2\mu) \pm i\epsilon}. \quad (\text{A.7})$$

Possible and common choices for the normalization constant  $A_{\text{NN}}$  are  $A_{\text{NN}}^2 = (4\pi)^2$  (see, e.g., Ref. [29]) and  $A_{\text{NN}}^2 = (2\pi)^3$  (see, e.g., Ref. [199]). The convention  $A_{\text{NN}}^2 = (2\pi)^3$  minimizes the number of  $\pi$  factors

<sup>13</sup>It is common to include the mass factor in the definition of the potential.

two-body states

$\langle \mathbf{p}' S' M_{S'} T' M_{T'}   \mathbf{p} S M_S T M_T \rangle = (2\pi)^3 \delta(\mathbf{p} - \mathbf{p}') \delta_{SS'} \delta_{M_S M_{S'}} \delta_{TT'} \delta_{M_T M_{T'}}$ $\sum_{S, M_S, T, M_T} \int \frac{d\mathbf{p}}{(2\pi)^3}   \mathbf{p} S M_S T M_T \rangle \langle \mathbf{p} S M_S T M_T   = 1$
$\langle p' (L' S') J' M_{J'} T' M_{T'}   p (L S) J M_J T M_T \rangle = \frac{\delta(p - p')}{pp'} \delta_{LL'} \delta_{SS'} \delta_{JJ'} \delta_{M_J M_{J'}} \delta_{TT'} \delta_{M_T M_{T'}}$ $\sum_{L, S, J, M_J, T, M_T} \int dp p^2   p (L S) J M_J T M_T \rangle \langle p (L S) J M_J T M_T   = 1$
$\langle \mathbf{p}' S' M_{S'} T' M_{T'}   p (L S) J M_J T M_T \rangle = (2\pi)^{3/2} \frac{\delta(p - p')}{pp'} \delta_{SS'} \delta_{TT'} \delta_{M_T M_{T'}} \sum_{M_L} C_{LM_L S M_{S'}}^{J M_J} Y_{LM_L}(\hat{\mathbf{p}}')$

three-body states

$\langle \mathbf{p}' \mathbf{q}' S' M_{S'} m_{s'} T' M_{T'} m_{t'}   \mathbf{p} \mathbf{q} S M_S m_s T M_T m_t \rangle = (2\pi)^6 \delta(\mathbf{p} - \mathbf{p}') \delta(\mathbf{q} - \mathbf{q}') \delta_{SS'} \delta_{M_S M_{S'}} \delta_{m_s m_{s'}} \delta_{TT'} \delta_{M_T M_{T'}} \delta_{m_t m_{t'}}$ $\sum_{S, M_S, m_s, T, M_T, m_t} \sum_{S', M_{S'}, m_{s'}, T', M_{T'}, m_{t'}} \int \frac{d\mathbf{p}}{(2\pi)^3} \frac{d\mathbf{q}}{(2\pi)^3}   \mathbf{p} \mathbf{q} S M_S m_s T M_T m_t \rangle \langle \mathbf{p} \mathbf{q} S M_S m_s T M_T m_t   = 1$
$\langle \mathbf{p}' \mathbf{q}' [(L' S') J' (l' \frac{1}{2}) j'] \mathcal{J}' M_{\mathcal{J}'} (T' \frac{1}{2}) \mathcal{T}' M_{\mathcal{T}'}   p \mathbf{q} [(L S) J (l \frac{1}{2}) j] \mathcal{J} M_{\mathcal{J}} (T \frac{1}{2}) \mathcal{T} M_{\mathcal{T}} \rangle$ $= \frac{\delta(p - p')}{pp'} \frac{\delta(q - q')}{qq'} \delta_{LL'} \delta_{SS'} \delta_{JJ'} \delta_{TT'} \delta_{ll'} \delta_{jj'} \delta_{m_j m_{j'}} \delta_{\mathcal{J} \mathcal{J}'} \delta_{M_{\mathcal{J}} M_{\mathcal{J}'}} \delta_{\mathcal{T} \mathcal{T}'} \delta_{M_{\mathcal{T}} M_{\mathcal{T}'}}$ $\sum_{L, S, J, T, j, \mathcal{J}, M_{\mathcal{J}}, \mathcal{T}, M_{\mathcal{T}}} \int dp p^2 \int dq q^2   p \mathbf{q} [(L S) J (l \frac{1}{2}) j] \mathcal{J} M_{\mathcal{J}} (T \frac{1}{2}) \mathcal{T} M_{\mathcal{T}} \rangle \langle p \mathbf{q} [(L S) J (l \frac{1}{2}) j] \mathcal{J} M_{\mathcal{J}} (T \frac{1}{2}) \mathcal{T} M_{\mathcal{T}}   = 1$
$\langle \mathbf{p}' \mathbf{q}' S' M_{S'} m_{s'} T' M_{T'} m_{t'}   p \mathbf{q} [(L S) J (l \frac{1}{2}) j] \mathcal{J} M_{\mathcal{J}} (T \frac{1}{2}) \mathcal{T} M_{\mathcal{T}} \rangle$ $= (2\pi)^3 \frac{\delta(p - p')}{pp'} \frac{\delta(q - q')}{qq'} \delta_{SS'} \delta_{TT'} \sum_{\substack{M_L, m_l \\ M_J, m_j}} C_{JM_J m_j}^{\mathcal{J} M_{\mathcal{J}}} C_{LM_L S m_s}^{J M_J} C_{lm_l \frac{1}{2} m_{s'}}^{j m_j} Y_{LM_L}(\hat{\mathbf{p}}') Y_{lm_l}(\hat{\mathbf{q}}') C_{TM_T \frac{1}{2} m_t'}^{\mathcal{T} M_{\mathcal{T}}}$

Table A.8: Normalization convention for two-body and three-body momentum states in vector and partial-wave representation. The spin and isospin quantum numbers  $S, M_S, T$  and  $M_T$  denote the two-body spin and isospin states of the two particles with relative momentum  $\mathbf{p}$ , while  $m_s$  and  $m_t$  denote the spin and isospin projections of the particle with Jacobi momentum  $\mathbf{q}$ .

in equations represented in partial-wave basis. We will adopt this convention in this work as it allows to generalize relations for partial-wave matrix elements in a very simple and natural way to three-body operators (see Table A.8).

Following Eq. (A.1), a general Galilean-invariant 3N interaction can be written in the form (see Section 3)

$$\langle \mathbf{p}' \mathbf{q}' S' M_{S'} m_{s'} T' M_{T'} m_{t'} | V_{3N} | \mathbf{p} \mathbf{q} S M_S m_s T M_T m_t \rangle, \quad (\text{A.8})$$

where  $m_s$  and  $m_t$  are the spin- and isospin projections of the third particle. Note that in contrast to NN interactions, 3N interactions are generally off-diagonal in the isospin quantum numbers  $T$  and  $M_T$ . We adopt the same normalization convention as for NN interactions. The specific relations are given in Table A.8.

We define three-body partial-wave states by generalizing Eq. (A.4):

$$|p\mathbf{q}\mathcal{S}M_S m_s T M_T m_t\rangle = A_{3N} \sum_{\substack{L, M_L, l, m_l \\ J, M_J}} \sum_{\substack{\mathcal{J}, M_{\mathcal{J}} \\ \mathcal{T}, M_{\mathcal{T}}}} \mathcal{C}_{JM_J m_j}^{\mathcal{J} M_{\mathcal{J}}} \mathcal{C}_{LM_L M_S}^{JM_J} \mathcal{C}_{lm_l \frac{1}{2} m_s}^{j m_j} Y_{LM_L}^*(\hat{\mathbf{p}}) Y_{lm_l}^*(\hat{\mathbf{q}}) \mathcal{C}_{TM_T \frac{1}{2} m_t}^{\mathcal{T} M_{\mathcal{T}}} |p[(LS)J(l\frac{1}{2})j]\mathcal{J}M_{\mathcal{J}}(T\frac{1}{2})\mathcal{T}M_{\mathcal{T}}\rangle. \quad (\text{A.9})$$

In this work we choose  $A_{3N} = (2\pi)^3$ , which leads to a particularly compact form of equations in partial-wave representation and allows to generalize relations for two-body operators in a simple way for the choice  $A_{NN} = \sqrt{(2\pi)^3}$ . The specific normalization conventions for two-body and three-body states adopted in this work are summarized in Table A.8.

## B. Integral for partial-wave decomposition of local 3N interactions

In this Appendix we describe the integral transformations that allow for a decoupling of the three non-trivial integrations over spherical harmonics in the partial-wave decomposition of 3N interactions (see Eq. (31)) from the other five, which can be performed analytically. We start with Eq. (31) and add a radial integration over  $\tilde{p}'$  and  $\tilde{q}'$  in order to obtain a translationally-invariant measure. We can achieve this by introducing additional integrations with delta-functions via

$$F_{LL'L'}^{m_L m_l m_{L'} m_{l'}}(p, q, p', q') = \int \frac{d\tilde{p}' d\tilde{q}' d\hat{\mathbf{p}} d\hat{\mathbf{q}}}{(2\pi)^6} \frac{\delta(p' - \tilde{p}')}{p'^2} \frac{\delta(q' - \tilde{q}')}{q'^2} Y_{L'm_{L'}}^*(\hat{\mathbf{p}}') Y_{l'm_{l'}}^*(\hat{\mathbf{q}}') Y_{Lm_L}(\hat{\mathbf{p}}) Y_{lm_l}(\hat{\mathbf{q}}) V_{3N}^{\text{local}}(\tilde{\mathbf{p}}' - \mathbf{p}, \tilde{\mathbf{q}}' - \mathbf{q}), \quad (\text{B.1})$$

where we renamed the angular parts of the vectors,  $\hat{\mathbf{p}}' \rightarrow \hat{\mathbf{p}}'$  and  $\hat{\mathbf{q}}' \rightarrow \hat{\mathbf{q}}'$ , and made the local nature of the 3N interaction explicit (see Section 3.3). Now we can make the substitutions:

$$\tilde{\mathbf{p}}' \rightarrow \tilde{\mathbf{p}} + \mathbf{p} \quad \text{and} \quad \tilde{\mathbf{q}}' \rightarrow \tilde{\mathbf{q}} + \mathbf{q}, \quad (\text{B.2})$$

which leads to:

$$F_{LL'L'}^{m_L m_l m_{L'} m_{l'}}(p, q, p', q') = \frac{1}{(2\pi)^6} \int d\tilde{\mathbf{p}} d\tilde{\mathbf{q}} d\hat{\mathbf{p}} d\hat{\mathbf{q}} \frac{\delta(p' - |\tilde{\mathbf{p}} + \mathbf{p}|)}{p'^2} \frac{\delta(q' - |\tilde{\mathbf{q}} + \mathbf{q}|)}{q'^2} V_{3N}^{\text{local}}(\tilde{\mathbf{p}}, \tilde{\mathbf{q}}) \times Y_{L'm_{L'}}^*(\widehat{\tilde{\mathbf{p}} + \mathbf{p}}) Y_{l'm_{l'}}^*(\widehat{\tilde{\mathbf{q}} + \mathbf{q}}) Y_{Lm_L}(\hat{\mathbf{p}}) Y_{lm_l}(\hat{\mathbf{q}}). \quad (\text{B.3})$$

To evaluate these integrals, we perform as a first step a rotation  $R(\tilde{\mathbf{p}})$  of the vectors  $\tilde{\mathbf{q}}$  and  $\mathbf{p}$ ,

$$\tilde{\mathbf{q}} \rightarrow R(\tilde{\mathbf{p}})\tilde{\mathbf{q}} \quad \text{and} \quad \mathbf{p} \rightarrow R(\tilde{\mathbf{p}})\mathbf{p} \quad \text{with} \quad R^{-1}\tilde{\mathbf{p}} = \tilde{p}\mathbf{e}_z. \quad (\text{B.4})$$

As a second step, we perform a rotation of the vector  $\mathbf{q}$ ,

$$\mathbf{q} \rightarrow R(\tilde{\mathbf{p}})Q(\tilde{\mathbf{q}})\mathbf{q} \quad \text{with} \quad Q^{-1}\tilde{\mathbf{q}} = \tilde{q}\mathbf{e}_z. \quad (\text{B.5})$$

This results in:

$$F_{LL'L'}^{m_L m_l m_{L'} m_{l'}}(p, q, p', q') = \frac{1}{(2\pi)^6} \frac{1}{p'^2 q'^2} \int d\tilde{p} d\tilde{q} d\hat{\mathbf{p}} d\hat{\mathbf{q}} \delta(p' - |\tilde{p}\mathbf{e}_z + \mathbf{p}|) \delta(q' - |\tilde{q}\mathbf{e}_z + \mathbf{q}|) V_{3N}^{\text{local}}(\tilde{p}, \tilde{q}, \hat{\mathbf{q}} \cdot \mathbf{e}_z) \times Y_{L'm_{L'}}^*(R(\tilde{p}\mathbf{e}_z + \mathbf{p})) Y_{l'm_{l'}}^*(RQ(\tilde{q}\mathbf{e}_z + \mathbf{q})) Y_{Lm_L}(\hat{\mathbf{p}}) Y_{lm_l}(RQ\hat{\mathbf{q}}) = \frac{1}{(2\pi)^6} \frac{1}{p'^2 q'^2} \int d\tilde{p} d\tilde{q} d\hat{\mathbf{p}} d\hat{\mathbf{q}} \delta(p' - |\tilde{p}\mathbf{e}_z + \mathbf{p}|) \delta(q' - |\tilde{q}\mathbf{e}_z + \mathbf{q}|) V_{3N}^{\text{local}}(\tilde{p}, \tilde{q}, \hat{\mathbf{q}} \cdot \mathbf{e}_z) \times \sum_{\tilde{m}_L, \tilde{m}_{L'}, \tilde{m}_l, \tilde{m}_{l'}} Y_{L'\tilde{m}_{L'}}^*(\widehat{\tilde{p}\mathbf{e}_z + \mathbf{p}}) Y_{l'\tilde{m}_{l'}}^*(\widehat{\tilde{q}\mathbf{e}_z + \mathbf{q}}) Y_{L\tilde{m}_L}(\hat{\mathbf{p}}) Y_{l\tilde{m}_l}(\hat{\mathbf{q}}) D_{\tilde{m}_{L'} m_{L'}}^{*L'}(R) D_{\tilde{m}_{l'} m_{l'}}^{*l'}(RQ) D_{\tilde{m}_L m_L}^L(R) D_{\tilde{m}_l m_l}^l(RQ), \quad (\text{B.6})$$

where  $D$  denote the Wigner  $D$ -functions. The product of  $D$ -functions can be expanded:

$$D_{\bar{m}_L, m_L}^{*L'}(R) D_{\bar{m}_L, m_L}^{*L'}(RQ) D_{\bar{m}_L, m_L}^L(R) D_{\bar{m}_L, m_L}^L(RQ) = \sum_{\bar{m}_l, \bar{m}_l'} D_{\bar{m}_L, m_L}^{*L'}(R) D_{\bar{m}_l, \bar{m}_l'}^{*L'}(Q) D_{\bar{m}_L, m_L}^{*L'}(R) D_{\bar{m}_L, m_L}^L(R) D_{\bar{m}_l, \bar{m}_l'}^L(Q) D_{\bar{m}_L, m_L}^L(R). \quad (\text{B.7})$$

For the evaluation of Eq. (B.6) it is important to note that the integration over the azimuthal angles  $\phi_p$  and  $\phi_q$  results in the constraints  $\bar{m}_L = \bar{m}_L'$  and  $\bar{m}_l = \bar{m}_l'$  since the addition of a vector in the  $z$ -direction does not affect the azimuthal angles. Furthermore we can make use of the identities

$$D_{\bar{m}_L, m_L}^{*L'}(R) D_{\bar{m}_L, m_L}^L(R) = (-1)^{\bar{m}-m} \sum_{\bar{l}} C_{\bar{l}, \bar{m}-m}^{\bar{l}0} C_{\bar{l}, m-L}^{\bar{l}m-m'} \sqrt{\frac{4\pi}{2\bar{l}+1}} Y_{\bar{l}, m-m'}(\hat{\mathbf{p}}) \quad (\text{B.8})$$

and the according relation for the rotation  $Q$ . The integration of the latter relation over  $\phi_{\bar{q}}$  implies  $\bar{m}_l = \bar{m}_l'$  in Eq. (B.7), specifically:

$$\int_0^{2\pi} d\phi_{\bar{q}} D_{\bar{m}_l, \bar{m}_l'}^{*L'}(Q) D_{\bar{m}_l, \bar{m}_l'}^L(Q) = 2\pi (-1)^{\bar{m}_l - \bar{m}_l'} \delta_{\bar{m}_l, \bar{m}_l'} \sum_{\bar{l}} C_{\bar{l}, \bar{m}_l, \bar{m}_l}^{\bar{l}0} C_{\bar{l}, \bar{m}_l - \bar{m}_l'}^{\bar{l}\bar{m}_l - \bar{m}_l'} P_{\bar{l}}(\hat{\mathbf{q}} \cdot \mathbf{e}_z). \quad (\text{B.9})$$

Using these relations we can perform also the integral over  $\hat{\mathbf{p}}$ :

$$\begin{aligned} & \int d\hat{\mathbf{p}} D_{\bar{m}_L, m_L}^{*L'}(R) D_{\bar{m}_L, m_L}^L(R) D_{\bar{m}_L, m_L}^{*L'}(R) D_{\bar{m}_L, m_L}^L(R) \\ &= (-1)^{\bar{m}_L + \bar{m}_L + m_L + m_L'} \delta_{m_L - m_L', m_L' - m_L} \sum_{\bar{l} = \max(|L' - L|, |l' - l|)}^{\min(|L' + L|, |l' + l|)} \frac{4\pi}{2\bar{l} + 1} C_{\bar{l}, L' - \bar{m}_L, L \bar{m}_L}^{\bar{l}0} C_{\bar{l}, L' - m_L', L m_L}^{\bar{l}m_L - m_L'} C_{\bar{l}, \bar{m}_L - \bar{m}_L', \bar{m}_L}^{\bar{l}0} C_{\bar{l}, \bar{m}_L - m_L', \bar{m}_L}^{\bar{l}m_L - m_L'}. \end{aligned} \quad (\text{B.10})$$

Finally, the integrals with respect to  $\phi_{\mathbf{p}}$  and  $\phi_{\mathbf{q}}$  in Eq. (B.6) are trivial and just provide a factor  $2\pi$  each. The integrals with respect to  $\theta_{\mathbf{p}}$  and  $\theta_{\mathbf{q}}$  are performed via the delta functions, providing the relations

$$\hat{\mathbf{p}} \cdot \mathbf{e}_z = \frac{p'^2 - p^2 - \tilde{p}^2}{2\tilde{p}p} \quad \text{and} \quad \hat{\mathbf{q}} \cdot \mathbf{e}_z = \frac{q'^2 - q^2 - \tilde{q}^2}{2\tilde{q}q}, \quad (\text{B.11})$$

and also specifying the limits of the  $\tilde{p}$  and  $\tilde{q}$  integrations:

$$|p' - p| \leq \tilde{p} \leq p' + p, \quad \text{and} \quad |q' - q| \leq \tilde{q} \leq q' + q. \quad (\text{B.12})$$

In the end only three non-trivial integrations remain in Eq. (B.6), leading finally to Eq. (40):

$$\begin{aligned} F_{L'L'L'}^{m_L, m_L', m_L, m_L'}(p, q, p', q') &= \delta_{m_L - m_L', m_L' - m_L} \frac{(-1)^{m_L + m_L'}}{(2\pi)^6} \frac{2(2\pi)^4}{pp'qq'} \sum_{\bar{l} = \max(|L' - L|, |l' - l|)}^{\min(L' + L, l' + l)} \frac{C_{L' - m_L', L m_L}^{\bar{l} - m_L' + m_L} C_{L' - m_L', L m_L}^{\bar{l} - m_L' + m_L}}{2\bar{l} + 1} \\ &\times \int_{|p' - p|}^{p' + p} d\tilde{p} \tilde{p} \int_{|q' - q|}^{q' + q} d\tilde{q} \tilde{q} \mathcal{Y}_{L'L}^{\bar{l}0}(\widehat{\tilde{p}\mathbf{e}_z + \mathbf{p}}, \hat{\mathbf{p}}) \Big|_{\phi_{\mathbf{p}}=0, \hat{\mathbf{p}} \cdot \mathbf{e}_z = \frac{p'^2 - p^2 - \tilde{p}^2}{2\tilde{p}p}} \mathcal{Y}_{L'L}^{\bar{l}0}(\widehat{\tilde{q}\mathbf{e}_z + \mathbf{q}}, \hat{\mathbf{q}}) \Big|_{\phi_{\mathbf{q}}=0, \hat{\mathbf{q}} \cdot \mathbf{e}_z = \frac{q'^2 - q^2 - \tilde{q}^2}{2\tilde{q}q}} \\ &\times \int_{-1}^1 d \cos \theta_{\hat{\mathbf{p}}\hat{\mathbf{q}}} P_{\bar{l}}(\cos \theta_{\hat{\mathbf{p}}\hat{\mathbf{q}}}) V_{3N}^{\text{local}}(\tilde{p}, \tilde{q}, \cos \theta_{\hat{\mathbf{p}}\hat{\mathbf{q}}}). \end{aligned} \quad (\text{B.13})$$

### C. Partial-wave matrix elements of permutation operator $P_{123}$

Here we derive the partial-wave matrix elements of the three-body cyclic permutation operator  $P_{123}$ . In Section 3.1 the momentum-space structure of the operator was already discussed. For the derivation of the full matrix elements we start from Eq. (19c) and add spin and isospin degrees of freedom to the particle states. To this end, it is most convenient to work in  $LS$ -coupling scheme since then we can immediately

factorize the momentum space part from the spin and isospin part:

$$\begin{aligned}
& {}_{\{12\}}\langle \mathbf{p}' \mathbf{q}' (S' s) \mathcal{S}' \mathcal{M}_{\mathcal{S}'} (T' t) \mathcal{T}' \mathcal{M}_{\mathcal{T}'} | P_{123} | \mathbf{p} \mathbf{q} (S s) \mathcal{S} \mathcal{M}_{\mathcal{S}} (T t) \mathcal{T} \mathcal{M}_{\mathcal{T}} \rangle_{\{12\}} \\
&= {}_{\{12\}}\langle \mathbf{p}' \mathbf{q}' (S' s) \mathcal{S}' \mathcal{M}_{\mathcal{S}'} (T' t) \mathcal{T}' \mathcal{M}_{\mathcal{T}'} | \mathbf{p} \mathbf{q} (S s) \mathcal{S} \mathcal{M}_{\mathcal{S}} (T t) \mathcal{T} \mathcal{M}_{\mathcal{T}} \rangle_{\{23\}} \\
&= {}_{\{12\}}\langle \mathbf{p}' \mathbf{q}' | \mathbf{p} \mathbf{q} \rangle_{\{23\}} {}_{\{12\}}\langle (S' s) \mathcal{S}' \mathcal{M}_{\mathcal{S}'} | (S s) \mathcal{S} \mathcal{M}_{\mathcal{S}} \rangle_{\{23\}} {}_{\{12\}}\langle (T' t) \mathcal{T}' \mathcal{M}_{\mathcal{T}'} | (T t) \mathcal{T} \mathcal{M}_{\mathcal{T}} \rangle_{\{23\}} .
\end{aligned} \tag{C.1}$$

Now we can discuss the individual factors separately. The spin and isospin terms can be easily evaluated by standard recoupling techniques [1], e.g. for the spin:

$${}_{\{12\}}\langle (S' s) \mathcal{S}' \mathcal{M}_{\mathcal{S}'} | (S s) \mathcal{S} \mathcal{M}_{\mathcal{S}} \rangle_{\{23\}} = \delta_{S S'} \delta_{M_{\mathcal{S}} M_{\mathcal{S}'}} (-1)^S \sqrt{\hat{S} \hat{S}'} \begin{Bmatrix} \frac{1}{2} & \frac{1}{2} & S' \\ \frac{1}{2} & S & S \end{Bmatrix}, \tag{C.2}$$

with the 6j symbol  $\{.. \}$ . We obtain identical results for the overlap matrix elements  ${}_{\{23\}}\langle (S' s) \mathcal{S}' \mathcal{M}_{\mathcal{S}'} | (S s) \mathcal{S} \mathcal{M}_{\mathcal{S}} \rangle_{\{31\}}$  and  ${}_{\{31\}}\langle (S' s) \mathcal{S}' \mathcal{M}_{\mathcal{S}'} | (S s) \mathcal{S} \mathcal{M}_{\mathcal{S}} \rangle_{\{12\}}$ . The momentum part can also be evaluated in a straightforward way. Making use of the partial-wave states defined in Appendix A and Eq. (19c) for the momentum exchange operator, we obtain:

$$\begin{aligned}
& {}_{\{12\}}\langle p' q' (L' l') \mathcal{L}' \mathcal{M}_{\mathcal{L}'} | p q (L l) \mathcal{L} \mathcal{M}_{\mathcal{L}} \rangle_{\{23\}} \\
&= \int \frac{d\mathbf{p}''}{(2\pi)^3} \frac{d\mathbf{q}''}{(2\pi)^3} \frac{d\mathbf{p}'''}{(2\pi)^3} \frac{d\mathbf{q}'''}{(2\pi)^3} {}_{\{12\}}\langle p' q' (L' l') \mathcal{L}' \mathcal{M}_{\mathcal{L}'} | \mathbf{p}'' \mathbf{q}'' \rangle_{\{12\}} {}_{\{12\}}\langle \mathbf{p}'' \mathbf{q}'' | \mathbf{p}''' \mathbf{q}''' \rangle_{\{23\}} {}_{\{23\}}\langle \mathbf{p}''' \mathbf{q}''' | p q (L l) \mathcal{L} \mathcal{M}_{\mathcal{L}} \rangle_{\{23\}} \\
&= \int d\hat{\mathbf{p}}' d\hat{\mathbf{q}}' \mathcal{Y}_{L'l'}^{*\mathcal{L}' \mathcal{M}_{\mathcal{L}'}}(\hat{\mathbf{p}}', \hat{\mathbf{q}}') \mathcal{Y}_{Ll}^{\mathcal{L} \mathcal{M}_{\mathcal{L}}}(\hat{\mathbf{p}}, \hat{\mathbf{q}}) \frac{\delta(p - \bar{p})}{p^2} \frac{\delta(q - \bar{q})}{q^2},
\end{aligned} \tag{C.3}$$

where we renamed the angular integration variables in the second step,  $\hat{\mathbf{p}}'' \rightarrow \hat{\mathbf{p}}'$  and  $\hat{\mathbf{q}}'' \rightarrow \hat{\mathbf{q}}'$ , and introduced the momenta

$$\bar{\mathbf{p}} = -\frac{1}{2}\mathbf{p}' - \frac{3}{4}\mathbf{q}', \quad \bar{\mathbf{q}} = \mathbf{p}' - \frac{1}{2}\mathbf{q}'. \tag{C.4}$$

As a next step we can make use of the fact that this term is a scalar under rotations and hence has to be proportional to  $\delta_{\mathcal{L}\mathcal{L}'} \delta_{M_{\mathcal{L}} M_{\mathcal{L}'}}$  and independent of  $M_{\mathcal{L}}$ . By summing over  $M_{\mathcal{L}}$  and dividing by  $2\mathcal{L} + 1$  we can then arbitrarily fix the direction of our coordinate system. For the practical implementation it is most convenient to choose the z-axis along the direction of the  $\mathbf{p}'$  vector and fix the polar angle of  $\mathbf{q}'$  to zero. In this case the expressions for the spherical harmonics simplify considerably since we can use:  $Y_{LM}(\hat{\mathbf{p}}') = \sqrt{\frac{2L+1}{4\pi}} \delta_{M0}$ .

We can immediately perform three of the four angular integrations in Eq. (C.3), leading to a trivial factor  $8\pi^2$ :

$${}_{\{12\}}\langle p' q' (L' l') \mathcal{L}' | p q (L l) \mathcal{L} \rangle_{\{23\}} = 8\pi^2 \int d \cos \theta_{\mathbf{p}' \mathbf{q}'} \frac{\delta_{\mathcal{L}\mathcal{L}'}}{2\mathcal{L} + 1} \sum_{M_{\mathcal{L}}} \mathcal{Y}_{L'l'}^{*\mathcal{L}' M_{\mathcal{L}'}}(\hat{\mathbf{p}}', \hat{\mathbf{q}}') \mathcal{Y}_{Ll}^{\mathcal{L} M_{\mathcal{L}}}(\hat{\mathbf{p}}, \hat{\mathbf{q}}) \frac{\delta(p - \bar{p})}{p^2} \frac{\delta(q - \bar{q})}{q^2}. \tag{C.5}$$

Now we can combine all results and compute the matrix elements  $\langle p' q' \alpha' | P_{123} | p q \alpha \rangle$  to obtain the matrix elements in  $LS$ -coupling scheme:

$$\begin{aligned}
\langle p' q' \beta' | P_{123} | p q \beta \rangle &= \sum_{M_{\mathcal{L}}, M_{\mathcal{S}}} \sum_{M_{\mathcal{L}'}, M_{\mathcal{S}'}} \mathcal{C}_{\mathcal{L} M_{\mathcal{L}} \mathcal{S} M_{\mathcal{S}}}^{\mathcal{J} M_{\mathcal{J}}} \mathcal{C}_{\mathcal{L}' M_{\mathcal{L}'} \mathcal{S}' M_{\mathcal{S}'}}^{\mathcal{J} M_{\mathcal{J}}} \\
&\times {}_{\{12\}}\langle p' q' (L' l') \mathcal{L}' | p q (L l) \mathcal{L} \rangle_{\{23\}} {}_{\{12\}}\langle (S' s) \mathcal{S}' \mathcal{M}_{\mathcal{S}'} | (S s) \mathcal{S} \mathcal{M}_{\mathcal{S}} \rangle_{\{23\}} {}_{\{12\}}\langle (T' t) \mathcal{T}' \mathcal{M}_{\mathcal{T}'} | (T t) \mathcal{T} \mathcal{M}_{\mathcal{T}} \rangle_{\{23\}} \\
&= {}_{\{12\}}\langle p' q' (L' l') \mathcal{L}' | p q (L l) \mathcal{L} \rangle_{\{23\}} {}_{\{12\}}\langle (S' s) \mathcal{S}' | (S s) \mathcal{S} \rangle_{\{23\}} {}_{\{12\}}\langle (T' t) \mathcal{T}' | (T t) \mathcal{T} \rangle_{\{23\}} \delta_{\mathcal{L}\mathcal{L}'} \delta_{S S'} \delta_{\mathcal{T} \mathcal{T}'}.
\end{aligned} \tag{C.6}$$

In the last step we used the independence of all overlap relations on the projection quantum numbers and the diagonal structure in the total orbital angular momentum, total spin and total isospin quantum numbers.

The application of the standard recoupling relation [1]

$$\langle p'q'\alpha'|P_{123}|pq\alpha\rangle = \sum_{\mathcal{L}\mathcal{S}} \sum_{\mathcal{L}'\mathcal{S}'} \sqrt{\hat{j}\hat{j}\hat{\mathcal{L}}\hat{\mathcal{S}}}\sqrt{\hat{j}'\hat{j}'\hat{\mathcal{L}}'\hat{\mathcal{S}}'} \begin{Bmatrix} L & S & J \\ l & \frac{1}{2} & j \\ \mathcal{L} & \mathcal{S} & \mathcal{J} \end{Bmatrix} \begin{Bmatrix} L' & S' & J' \\ l' & \frac{1}{2} & j' \\ \mathcal{L}' & \mathcal{S}' & \mathcal{J}' \end{Bmatrix} \langle p'q'\beta'|P_{123}|pq\beta\rangle \quad (\text{C.7})$$

leads finally to the result shown in Eq. (64).

#### D. Normal-ordered effective interactions for nuclear matter

In this Appendix we provide the explicit results for the effective interaction given by Eqs. (179) and (180) in the approximation  $\mathbf{P} = \mathbf{0}$  for neutron matter and symmetric nuclear matter. For angularly-independent regulators only the long-range contributions proportional to the LECs  $c_1$  and  $c_3$  contribute in neutron matter, and the effective interaction takes the following form [122]:

$$\bar{V}_{3N}^{\text{PNM}}(\mathbf{p}, \mathbf{p}') = \frac{g_A^2}{4f_\pi^4} \left[ -2c_1 m_\pi^2 A_{\text{PNM}}(\mathbf{p}, \mathbf{p}') + c_3 B_{\text{PNM}}(\mathbf{p}, \mathbf{p}') \right], \quad (\text{D.1})$$

where  $\mathbf{p}$  and  $\mathbf{p}'$  are the Jacobi momenta of the initial and final states,  $\mathbf{p} = \frac{1}{2}(\mathbf{k}_1 - \mathbf{k}_2)$ , and the functions  $A_{\text{PNM}}(\mathbf{p}, \mathbf{p}')$  and  $B_{\text{PNM}}(\mathbf{p}, \mathbf{p}')$  include all spin dependences:

$$\begin{aligned} A_{\text{PNM}}(\mathbf{p}, \mathbf{p}') &= 2 \left[ \rho_+^2(\mathbf{p}, \mathbf{p}') + 2a^1(\mathbf{p}, \mathbf{p}') - a^1(\mathbf{p}, -\mathbf{p}') - \bar{b}^1(\mathbf{p}, \mathbf{p}') \right] \\ &\quad - \frac{2}{3} \boldsymbol{\sigma}_1 \cdot \boldsymbol{\sigma}_2 \left[ 2\rho_-^2(\mathbf{p}, \mathbf{p}') + \rho_+^2(\mathbf{p}, \mathbf{p}') + 3a^1(\mathbf{p}, -\mathbf{p}') - \bar{b}^1(\mathbf{p}, \mathbf{p}') - 2\bar{b}^1(\mathbf{p}, -\mathbf{p}') \right] \\ &\quad + 4 \left[ S_{12}(\mathbf{p} + \mathbf{p}') \rho_+^0(\mathbf{p}, \mathbf{p}') - S_{12}(\mathbf{p} - \mathbf{p}') \rho_-^0(\mathbf{p}, \mathbf{p}') \right] \\ &\quad - 4 \boldsymbol{\sigma}_1^a \boldsymbol{\sigma}_2^b \left[ \bar{d}_{ab}^0(\mathbf{p}, \mathbf{p}') - \bar{d}_{ab}^0(\mathbf{p}, -\mathbf{p}') \right] \\ &\quad - 2i (\boldsymbol{\sigma}_1 + \boldsymbol{\sigma}_2)^a \left[ c_a^0(\mathbf{p}, \mathbf{p}') - c_a^0(\mathbf{p}, -\mathbf{p}') \right], \end{aligned} \quad (\text{D.2})$$

$$\begin{aligned} B_{\text{PNM}}(\mathbf{p}, \mathbf{p}') &= -2 \left[ \rho_+^4(\mathbf{p}, \mathbf{p}') + 2a^2(\mathbf{p}, \mathbf{p}') - a^2(\mathbf{p}, -\mathbf{p}') - \bar{b}^2(\mathbf{p}, \mathbf{p}') \right] \\ &\quad + \frac{2}{3} \boldsymbol{\sigma}_1 \cdot \boldsymbol{\sigma}_2 \left[ 2\rho_-^4(\mathbf{p}, \mathbf{p}') + \rho_+^4(\mathbf{p}, \mathbf{p}') + 3a^2(\mathbf{p}, -\mathbf{p}') - \bar{b}^2(\mathbf{p}, \mathbf{p}') - 2\bar{b}^2(\mathbf{p}, -\mathbf{p}') \right] \\ &\quad - 4 \left[ S_{12}(\mathbf{p} + \mathbf{p}') \rho_+^2(\mathbf{p}, \mathbf{p}') - S_{12}(\mathbf{p} - \mathbf{p}') \rho_-^2(\mathbf{p}, \mathbf{p}') \right] \\ &\quad + 4 \boldsymbol{\sigma}_1^a \boldsymbol{\sigma}_2^b \left[ \bar{d}_{ab}^1(\mathbf{p}, \mathbf{p}') - \bar{d}_{ab}^1(\mathbf{p}, -\mathbf{p}') \right] \\ &\quad + 2i (\boldsymbol{\sigma}_1 + \boldsymbol{\sigma}_2)^a \left[ c_a^1(\mathbf{p}, \mathbf{p}') - c_a^1(\mathbf{p}, -\mathbf{p}') \right], \end{aligned} \quad (\text{D.3})$$



and the basic integral functions are defined by

$$\begin{aligned}
\rho_{\pm}^n(\mathbf{p}, \mathbf{p}') &= \frac{(\mathbf{p} \pm \mathbf{p}')^n}{((\mathbf{p} \pm \mathbf{p}')^2 + m_{\pi}^2)^2} \int_{\mathbf{k}_3} 1, \\
a^n(\mathbf{p}, \mathbf{p}') &= \int_{\mathbf{k}_3} \frac{((\mathbf{p} + \mathbf{k}_3) \cdot (\mathbf{p}' + \mathbf{k}_3))^n}{((\mathbf{p} + \mathbf{k}_3)^2 + m_{\pi}^2)((\mathbf{p}' + \mathbf{k}_3)^2 + m_{\pi}^2)}, \\
b^n(\mathbf{p}, \mathbf{p}') &= \int_{\mathbf{k}_3} \frac{((\mathbf{p} + \mathbf{p}') \cdot (\mathbf{p} + \mathbf{k}_3))^n}{((\mathbf{p} + \mathbf{p}')^2 + m_{\pi}^2)((\mathbf{p} + \mathbf{k}_3)^2 + m_{\pi}^2)}, \\
c_a^n(\mathbf{p}, \mathbf{p}') &= \int_{\mathbf{k}_3} \frac{((\mathbf{p} + \mathbf{k}_3) \cdot (\mathbf{p}' + \mathbf{k}_3))^n ((\mathbf{p} + \mathbf{k}_3) \times (\mathbf{p}' + \mathbf{k}_3))_a}{((\mathbf{p} + \mathbf{k}_3)^2 + m_{\pi}^2)((\mathbf{p}' + \mathbf{k}_3)^2 + m_{\pi}^2)}, \\
d_{ab}^n(\mathbf{p}, \mathbf{p}') &= \int_{\mathbf{k}_3} ((\mathbf{p} + \mathbf{p}') \cdot (\mathbf{p} + \mathbf{k}_3))^n \frac{(\mathbf{p} + \mathbf{p}')_a (\mathbf{p} + \mathbf{k}_3)_b + (\mathbf{p} + \mathbf{p}')_b (\mathbf{p} + \mathbf{k}_3)_a - \frac{2}{3} \delta_{ab} (\mathbf{p} + \mathbf{p}') \cdot (\mathbf{p} + \mathbf{k}_3)}{2((\mathbf{p} + \mathbf{p}')^2 + m_{\pi}^2)((\mathbf{p} + \mathbf{k}_3)^2 + m_{\pi}^2)}. \quad (\text{D.4})
\end{aligned}$$

In Eqs. (D.2)–(D.4), the indices  $a, b$  run over the three Cartesian components of the spin operators, the tensor operator is given by  $S_{12}(\mathbf{p}) = (\boldsymbol{\sigma}_1 \cdot \mathbf{p})(\boldsymbol{\sigma}_2 \cdot \mathbf{p}) - \frac{1}{3} p^2 \boldsymbol{\sigma}_1 \cdot \boldsymbol{\sigma}_2$  and the overline denotes a symmetrization in the relative momentum variables,  $\bar{x}(\mathbf{p}, \mathbf{p}') = x(\mathbf{p}, \mathbf{p}') + x(\mathbf{p}', \mathbf{p})$ . In addition, we have introduced the short-hand notation

$$\int_{\mathbf{k}_3} = \int \frac{d\mathbf{k}_3}{(2\pi)^3} n_{\mathbf{k}_3} \tilde{f}_R(k', k_3) \tilde{f}_R(k, k_3). \quad (\text{D.5})$$

For example, for a nonlocal regulator given in Eq. (87), expressed in terms of the relative and third-particle momenta for  $P = 0$ , is given by  $\tilde{f}_R(k, k_3) = \exp[-((k^2 + k_3^2/3)/\Lambda^2)^n]$ .

In symmetric nuclear matter the effective interaction takes the following form:

$$\begin{aligned}
\bar{V}_{3N}^{\text{SNM}}(\mathbf{p}, \mathbf{p}') &= \frac{1}{2} \frac{g_A^2}{4f_{\pi}^2} \left[ -4c_1 m_{\pi}^2 A_{\text{SNM}}(\mathbf{p}, \mathbf{p}') + 2c_3 B_{\text{SNM}}(\mathbf{p}, \mathbf{p}') + c_4 C_{\text{SNM}}(\mathbf{p}, \mathbf{p}') \right] \\
&\quad - \frac{g_A}{8f_{\pi}^4 \Lambda_{\chi}} c_D D_{\text{SNM}}(\mathbf{p}, \mathbf{p}') + \frac{1}{2} \frac{c_E}{f_{\pi}^4 \Lambda_{\chi}} E_{\text{SNM}}(\mathbf{p}, \mathbf{p}'), \quad (\text{D.6})
\end{aligned}$$

where the functions  $A_{\text{SNM}}(\mathbf{p}, \mathbf{p}')$ ,  $B_{\text{SNM}}(\mathbf{p}, \mathbf{p}')$ ,  $C_{\text{SNM}}(\mathbf{p}, \mathbf{p}')$ ,  $D_{\text{SNM}}(\mathbf{p}, \mathbf{p}')$  and  $E_{\text{SNM}}(\mathbf{p}, \mathbf{p}')$  are given by:

$$\begin{aligned}
A_{\text{SNM}}(\mathbf{p}, \mathbf{p}') &= 3 \left[ 2\rho_+^2(\mathbf{p}, \mathbf{p}') + 4a^1(\mathbf{p}, \mathbf{p}') - a^1(\mathbf{p}, -\mathbf{p}') - \bar{b}^1(\mathbf{p}, \mathbf{p}') \right] \\
&\quad - (\boldsymbol{\sigma}_1 \cdot \boldsymbol{\sigma}_2 + \boldsymbol{\tau}_1 \cdot \boldsymbol{\tau}_2) \left[ 2\rho_+^2(\mathbf{p}, \mathbf{p}') + 3a^1(\mathbf{p}, -\mathbf{p}') - \bar{b}^1(\mathbf{p}, \mathbf{p}') \right] \\
&\quad + \frac{1}{3}(\boldsymbol{\sigma}_1 \cdot \boldsymbol{\sigma}_2)(\boldsymbol{\tau}_1 \cdot \boldsymbol{\tau}_2) \left[ 2\rho_+^2(\mathbf{p}, \mathbf{p}') - 8\rho_-^2(\mathbf{p}, \mathbf{p}') - 9a^1(\mathbf{p}, -\mathbf{p}') - \bar{b}^1(\mathbf{p}, \mathbf{p}') + 4\bar{b}^1(\mathbf{p}, -\mathbf{p}') \right] \\
&\quad + 12S_{12}(\mathbf{p} + \mathbf{p}')\rho_+^0(\mathbf{p}, \mathbf{p}') - 6\sigma_1^a\sigma_2^b\bar{d}_{ab}^0(\mathbf{p}, \mathbf{p}') - 3i(\boldsymbol{\sigma}_1 + \boldsymbol{\sigma}_2)^a \left[ 2c_a^0(\mathbf{p}, \mathbf{p}') - (1 + (\boldsymbol{\tau}_1 \cdot \boldsymbol{\tau}_2))c_a^0(\mathbf{p}, -\mathbf{p}') \right] \\
&\quad - 2(\boldsymbol{\tau}_1 \cdot \boldsymbol{\tau}_2) \left[ 4S_{12}(\mathbf{p} - \mathbf{p}')\rho_-^0(\mathbf{p}, \mathbf{p}') + 2S_{12}(\mathbf{p} + \mathbf{p}')\rho_+^0(\mathbf{p}, \mathbf{p}') - \sigma_1^a\sigma_2^b(\bar{d}_{ab}^0(\mathbf{p}, \mathbf{p}') + 2\bar{d}_{ab}^0(\mathbf{p}, -\mathbf{p}')) \right], \tag{D.7}
\end{aligned}$$

$$\begin{aligned}
B_{\text{SNM}}(\mathbf{p}, \mathbf{p}') &= -3 \left[ 2\rho_+^4(\mathbf{p}, \mathbf{p}') + 4a^2(\mathbf{p}, \mathbf{p}') - a^2(\mathbf{p}, -\mathbf{p}') - \bar{b}^2(\mathbf{p}, \mathbf{p}') \right] \\
&\quad + (\boldsymbol{\sigma}_1 \cdot \boldsymbol{\sigma}_2 + \boldsymbol{\tau}_1 \cdot \boldsymbol{\tau}_2) \left[ 2\rho_+^4(\mathbf{p}, \mathbf{p}') + 3a^2(\mathbf{p}, -\mathbf{p}') - \bar{b}^2(\mathbf{p}, \mathbf{p}') \right] \\
&\quad - \frac{1}{3}(\boldsymbol{\sigma}_1 \cdot \boldsymbol{\sigma}_2)(\boldsymbol{\tau}_1 \cdot \boldsymbol{\tau}_2) \left[ 2\rho_+^4(\mathbf{p}, \mathbf{p}') - 8\rho_-^4(\mathbf{p}, \mathbf{p}') - 9a^2(\mathbf{p}, -\mathbf{p}') - \bar{b}^2(\mathbf{p}, \mathbf{p}') + 4\bar{b}^2(\mathbf{p}, -\mathbf{p}') \right] \\
&\quad - 12S_{12}(\mathbf{p} + \mathbf{p}')\rho_+^2(\mathbf{p}, \mathbf{p}') + 6\sigma_1^a\sigma_2^b\bar{d}_{ab}^1(\mathbf{p}, \mathbf{p}') + 3i(\boldsymbol{\sigma}_1 + \boldsymbol{\sigma}_2)^a \left[ 2c_a^1(\mathbf{p}, \mathbf{p}') - (1 + (\boldsymbol{\tau}_1 \cdot \boldsymbol{\tau}_2))c_a^1(\mathbf{p}, -\mathbf{p}') \right] \\
&\quad + 2(\boldsymbol{\tau}_1 \cdot \boldsymbol{\tau}_2) \left[ 4S_{12}(\mathbf{p} - \mathbf{p}')\rho_-^2(\mathbf{p}, \mathbf{p}') + 2S_{12}(\mathbf{p} + \mathbf{p}')\rho_+^2(\mathbf{p}, \mathbf{p}') - \sigma_1^a\sigma_2^b(\bar{d}_{ab}^1(\mathbf{p}, \mathbf{p}') + 2\bar{d}_{ab}^1(\mathbf{p}, -\mathbf{p}')) \right], \tag{D.8}
\end{aligned}$$

$$\begin{aligned}
C_{\text{SNM}}(\mathbf{p}, \mathbf{p}') &= 2 \left[ (\boldsymbol{\sigma}_1 \cdot \boldsymbol{\sigma}_2) + (\boldsymbol{\tau}_1 \cdot \boldsymbol{\tau}_2) - 3 \right] \left[ \bar{a}^2(\mathbf{p}, -\mathbf{p}') + \bar{b}^2(\mathbf{p}, \mathbf{p}') \right] \\
&\quad + \frac{8}{3}(\boldsymbol{\sigma}_1 \cdot \boldsymbol{\sigma}_2)(\boldsymbol{\tau}_1 \cdot \boldsymbol{\tau}_2) \left[ \bar{b}^2(\mathbf{p}, -\mathbf{p}') + \bar{a}^2(\mathbf{p}, \mathbf{p}') - \frac{1}{4}\bar{b}^2(\mathbf{p}, \mathbf{p}') - \frac{1}{4}\bar{a}^2(\mathbf{p}, -\mathbf{p}') \right] \\
&\quad + 6\sigma_1^a\sigma_2^b \left[ \bar{e}_{ab}(\mathbf{p}, \mathbf{p}') - 2f_{ab}(\mathbf{p}, -\mathbf{p}') \right] \\
&\quad - 2(\boldsymbol{\tau}_1 \cdot \boldsymbol{\tau}_2)\sigma_1^a\sigma_2^b \left[ 2\bar{e}_{ab}(\mathbf{p}, -\mathbf{p}') - 2f_{ab}(\mathbf{p}, -\mathbf{p}') + \bar{e}_{ab}(\mathbf{p}, \mathbf{p}') - 4f_{ab}(\mathbf{p}, \mathbf{p}') \right] \\
&\quad - 12\sigma_1^a\sigma_2^b\bar{g}_{ab}(\mathbf{p}, \mathbf{p}') + 4(\boldsymbol{\tau}_1 \cdot \boldsymbol{\tau}_2)\sigma_1^a\sigma_2^b \left[ 2\bar{g}_{ab}(\mathbf{p}, -\mathbf{p}') + \bar{g}_{ab}(\mathbf{p}, \mathbf{p}') \right] \\
&\quad + i(\boldsymbol{\sigma}_1 + \boldsymbol{\sigma}_2)^a \left[ (2(\boldsymbol{\tau}_1 \cdot \boldsymbol{\tau}_2) - 6)c_a^1(\mathbf{p}, -\mathbf{p}') + 4(\boldsymbol{\tau}_1 \cdot \boldsymbol{\tau}_2)c_a^1(\mathbf{p}, \mathbf{p}') \right], \tag{D.9}
\end{aligned}$$

$$\begin{aligned}
D_{\text{SNM}}(\mathbf{p}, \mathbf{p}') &= \left[ (\boldsymbol{\sigma}_1 \cdot \boldsymbol{\sigma}_2) + (\boldsymbol{\tau}_1 \cdot \boldsymbol{\tau}_2) - 3 \right] \left[ \tilde{\rho}_+^2(\mathbf{p}, \mathbf{p}') + i(\mathbf{p}) + i(\mathbf{p}') \right] \\
&\quad + 2(\boldsymbol{\sigma}_1 \cdot \boldsymbol{\sigma}_2)(\boldsymbol{\tau}_1 \cdot \boldsymbol{\tau}_2) \left[ \frac{2}{3}\tilde{\rho}_-^2(\mathbf{p}, \mathbf{p}') - \frac{1}{6}\tilde{\rho}_+^2(\mathbf{p}, \mathbf{p}') + \frac{i(\mathbf{p})}{2} + \frac{i(\mathbf{p}')}{2} \right] \\
&\quad - 6S_{12}(\mathbf{p} + \mathbf{p}')\tilde{\rho}_+^0(\mathbf{p}, \mathbf{p}') + 3\sigma_1^a\sigma_2^b \left[ h_{ab}(\mathbf{p}) + h_{ab}(\mathbf{p}') \right] \\
&\quad + 6(\boldsymbol{\tau}_1 \cdot \boldsymbol{\tau}_2) \left[ \frac{2}{3}S_{12}(\mathbf{p} - \mathbf{p}')\tilde{\rho}_-^0(\mathbf{p}, \mathbf{p}') + \frac{1}{3}S_{12}(\mathbf{p} + \mathbf{p}')\tilde{\rho}_+^0(\mathbf{p}, \mathbf{p}') - \frac{1}{2}\sigma_1^a\sigma_2^b \left( h_{ab}(\mathbf{p}) + h_{ab}(\mathbf{p}') \right) \right], \tag{D.10}
\end{aligned}$$

$$E_{\text{SNM}}(\mathbf{p}, \mathbf{p}') = \left[ 9 - 3(\boldsymbol{\sigma}_1 \cdot \boldsymbol{\sigma}_2) - 3(\boldsymbol{\tau}_1 \cdot \boldsymbol{\tau}_2) + (\boldsymbol{\sigma}_1 \cdot \boldsymbol{\sigma}_2)(\boldsymbol{\tau}_1 \cdot \boldsymbol{\tau}_2) \right] \int_{\mathbf{k}_3} 1, \tag{D.11}$$

and the basic integral functions are defined by

$$\begin{aligned}
\rho_{\pm}^n(\mathbf{p}, \mathbf{p}') &= \frac{(\mathbf{p} \pm \mathbf{p}')^n}{((\mathbf{p} \pm \mathbf{p}')^2 + m_{\pi}^2)^2} \int_{\mathbf{k}_3} 1, \\
\tilde{\rho}_{\pm}^n(\mathbf{p}, \mathbf{p}') &= \frac{(\mathbf{p} \pm \mathbf{p}')^n}{((\mathbf{p} \pm \mathbf{p}')^2 + m_{\pi}^2)} \int_{\mathbf{k}_3} 1, \\
a^n(\mathbf{p}, \mathbf{p}') &= \int_{\mathbf{k}_3} \frac{((\mathbf{p} + \mathbf{k}_3) \cdot (\mathbf{p}' + \mathbf{k}_3))^n}{((\mathbf{p} + \mathbf{k}_3)^2 + m_{\pi}^2)((\mathbf{p}' + \mathbf{k}_3)^2 + m_{\pi}^2)}, \\
\tilde{a}^n(\mathbf{p}, \mathbf{p}') &= \int_{\mathbf{k}_3} \frac{((\mathbf{p} + \mathbf{k}_3) \times (\mathbf{p}' + \mathbf{k}_3))^n}{((\mathbf{p} + \mathbf{k}_3)^2 + m_{\pi}^2)((\mathbf{p}' + \mathbf{k}_3)^2 + m_{\pi}^2)}, \\
b^n(\mathbf{p}, \mathbf{p}') &= \int_{\mathbf{k}_3} \frac{((\mathbf{p} + \mathbf{p}') \cdot (\mathbf{p} + \mathbf{k}_3))^n}{((\mathbf{p} + \mathbf{p}')^2 + m_{\pi}^2)((\mathbf{p} + \mathbf{k}_3)^2 + m_{\pi}^2)}, \\
\tilde{b}^n(\mathbf{p}, \mathbf{p}') &= \int_{\mathbf{k}_3} \frac{((\mathbf{p} + \mathbf{p}') \times (\mathbf{p} + \mathbf{k}_3))^n}{((\mathbf{p} + \mathbf{p}')^2 + m_{\pi}^2)((\mathbf{p} + \mathbf{k}_3)^2 + m_{\pi}^2)}, \\
c_a^n(\mathbf{p}, \mathbf{p}') &= \int_{\mathbf{k}_3} \frac{((\mathbf{p} + \mathbf{k}_3) \cdot (\mathbf{p}' + \mathbf{k}_3))^n ((\mathbf{p} + \mathbf{k}_3) \times (\mathbf{p}' + \mathbf{k}_3))_a}{((\mathbf{p} + \mathbf{k}_3)^2 + m_{\pi}^2)((\mathbf{p}' + \mathbf{k}_3)^2 + m_{\pi}^2)}, \\
d_{ab}^n(\mathbf{p}, \mathbf{p}') &= \int_{\mathbf{k}_3} ((\mathbf{p} + \mathbf{p}') \cdot (\mathbf{p} + \mathbf{k}_3))^n \frac{(\mathbf{p} + \mathbf{p}')_a (\mathbf{p} + \mathbf{k}_3)_b + (\mathbf{p} + \mathbf{p}')_b (\mathbf{p} + \mathbf{k}_3)_a - \frac{2}{3} \delta_{ab} (\mathbf{p} + \mathbf{p}') \cdot (\mathbf{p} + \mathbf{k}_3)}{2((\mathbf{p} + \mathbf{p}')^2 + m_{\pi}^2)((\mathbf{p} + \mathbf{k}_3)^2 + m_{\pi}^2)}, \\
e_{ab}(\mathbf{p}, \mathbf{p}') &= \int_{\mathbf{k}_3} \frac{((\mathbf{p} + \mathbf{p}') \times (\mathbf{p} + \mathbf{k}_3))_a ((\mathbf{p} + \mathbf{p}') \times (\mathbf{p} + \mathbf{k}_3))_b - \frac{1}{3} \delta_{ab} ((\mathbf{p} + \mathbf{p}') \times (\mathbf{p} + \mathbf{k}_3))^2}{((\mathbf{p} + \mathbf{p}')^2 + m_{\pi}^2)((\mathbf{p} + \mathbf{k}_3)^2 + m_{\pi}^2)}, \\
f_{ab}(\mathbf{p}, \mathbf{p}') &= \int_{\mathbf{k}_3} \frac{((\mathbf{p} + \mathbf{k}_3) \times (\mathbf{p}' + \mathbf{k}_3))_a ((\mathbf{p} + \mathbf{k}_3) \times (\mathbf{p}' + \mathbf{k}_3))_b - \frac{1}{3} \delta_{ab} ((\mathbf{p} + \mathbf{k}_3) \times (\mathbf{p}' + \mathbf{k}_3))^2}{((\mathbf{p} + \mathbf{k}_3)^2 + m_{\pi}^2)((\mathbf{p}' + \mathbf{k}_3)^2 + m_{\pi}^2)}, \\
g_{ab}(\mathbf{p}, \mathbf{p}') &= \int_{\mathbf{k}_3} \frac{(\mathbf{p} + \mathbf{p}')^2 (\mathbf{p} + \mathbf{k}_3)_a (\mathbf{p} + \mathbf{k}_3)_b - (\mathbf{p} + \mathbf{k}_3)^2 (\mathbf{p} + \mathbf{p}')_a (\mathbf{p} + \mathbf{p}')_b}{2((\mathbf{p} + \mathbf{p}')^2 + m_{\pi}^2)((\mathbf{p} + \mathbf{k}_3)^2 + m_{\pi}^2)}, \\
h_{ab}(\mathbf{p}) &= \int_{\mathbf{k}_3} \frac{(\mathbf{p} + \mathbf{k}_3)_a (\mathbf{p} + \mathbf{k}_3)_b - \frac{1}{3} (\mathbf{p} + \mathbf{k}_3)^2 \delta_{ab}}{((\mathbf{p} + \mathbf{k}_3)^2 + m_{\pi}^2)}, \\
i(\mathbf{p}) &= \int_{\mathbf{k}_3} \frac{(\mathbf{p} + \mathbf{k}_3)^2}{((\mathbf{p} + \mathbf{k}_3)^2 + m_{\pi}^2)}. \tag{D.12}
\end{aligned}$$

### E. List of three-body configurations

$\alpha$	$L$	$S$	$J$	$T$	$l$	$j$	$\alpha$	$L$	$S$	$J$	$T$	$l$	$j$
0	0	0	0	1	0	$\frac{1}{2}$	29	3	1	4	1	5	$\frac{9}{2}$
1	1	1	0	1	1	$\frac{1}{2}$	30	4	1	4	0	4	$\frac{7}{2}$
2	1	0	1	0	1	$\frac{1}{2}$	31	4	1	4	0	4	$\frac{9}{2}$
3	1	0	1	0	1	$\frac{3}{2}$	32	5	1	4	1	3	$\frac{7}{2}$
4	0	1	1	0	0	$\frac{1}{2}$	33	5	1	4	1	5	$\frac{9}{2}$
5	0	1	1	0	2	$\frac{3}{2}$	34	5	0	5	0	5	$\frac{9}{2}$
6	1	1	1	1	1	$\frac{1}{2}$	35	5	0	5	0	5	$\frac{11}{2}$
7	1	1	1	1	1	$\frac{3}{2}$	36	4	1	5	0	4	$\frac{9}{2}$
8	2	1	1	0	0	$\frac{1}{2}$	37	4	1	5	0	6	$\frac{11}{2}$
9	2	1	1	0	2	$\frac{3}{2}$	38	5	1	5	1	5	$\frac{9}{2}$
10	2	0	2	1	2	$\frac{3}{2}$	39	5	1	5	1	5	$\frac{11}{2}$
11	2	0	2	1	2	$\frac{5}{2}$	40	6	1	5	0	4	$\frac{9}{2}$
12	1	1	2	1	1	$\frac{3}{2}$	41	6	1	5	0	6	$\frac{11}{2}$
13	1	1	2	1	3	$\frac{5}{2}$	42	6	0	6	1	6	$\frac{11}{2}$
14	2	1	2	0	2	$\frac{3}{2}$	43	6	0	6	1	6	$\frac{13}{2}$
15	2	1	2	0	2	$\frac{5}{2}$	44	5	1	6	1	5	$\frac{11}{2}$
16	3	1	2	1	1	$\frac{3}{2}$	45	5	1	6	1	7	$\frac{13}{2}$
17	3	1	2	1	3	$\frac{5}{2}$	46	6	1	6	0	6	$\frac{11}{2}$
18	3	0	3	0	3	$\frac{5}{2}$	47	6	1	6	0	6	$\frac{13}{2}$
19	3	0	3	0	3	$\frac{7}{2}$	48	7	1	6	1	5	$\frac{11}{2}$
20	2	1	3	0	2	$\frac{5}{2}$	49	7	1	6	1	7	$\frac{13}{2}$
21	2	1	3	0	4	$\frac{7}{2}$	50	7	0	7	0	7	$\frac{13}{2}$
22	3	1	3	1	3	$\frac{5}{2}$	51	7	0	7	0	7	$\frac{15}{2}$
23	3	1	3	1	3	$\frac{7}{2}$	52	6	1	7	0	6	$\frac{13}{2}$
24	4	1	3	0	2	$\frac{5}{2}$	53	6	1	7	0	8	$\frac{15}{2}$
25	4	1	3	0	4	$\frac{7}{2}$	54	7	1	7	1	7	$\frac{13}{2}$
26	4	0	4	1	4	$\frac{7}{2}$	55	7	1	7	1	7	$\frac{15}{2}$
27	4	0	4	1	4	$\frac{9}{2}$	56	8	1	7	0	6	$\frac{13}{2}$
28	3	1	4	1	3	$\frac{7}{2}$	57	8	1	7	0	8	$\frac{15}{2}$

Table E.9: List of three-body configurations for the three-body channel with  $\mathcal{J} = \frac{1}{2}$ ,  $\mathcal{T} = \frac{1}{2}$  and  $\mathcal{P} = +1$  using  $J_{\max} = 7$ .

## References

- [1] D. A. Varshalovich, A. N. Moskalev, V. K. Khersonskii, Quantum Theory Of Angular Momentum, World Scientific, Singapore, 1988.
- [2] S. Dürr, Z. Fodor, J. Frison, C. Hoelbling, R. Hoffmann, S. D. Katz, S. Krieg, T. Kurth, L. Lellouch, T. Lippert, K. K. Szabo, G. Vulvert, Ab Initio Determination of Light Hadron Masses, *Science* 322 (2008) 1224. doi:10.1126/science.1163233.
- [3] Z. Fodor, C. Hoelbling, Light Hadron Masses from Lattice QCD, *Rev. Mod. Phys.* 84 (2012) 449. doi:10.1103/RevModPhys.84.449.
- [4] Y.-B. Yang, J. Liang, Y.-J. Bi, Y. Chen, T. Draper, K.-F. Liu, Z. Liu, Proton Mass Decomposition from the QCD Energy Momentum Tensor, *Phys. Rev. Lett.* 121 (2018) 212001. doi:10.1103/PhysRevLett.121.212001.
- [5] S. R. Beane, W. Detmold, K. Orginos, M. J. Savage, Nuclear Physics from Lattice QCD, *Prog. Part. Nucl. Phys.* 66 (2011) 1. doi:10.1016/j.pnpnp.2010.08.002.
- [6] T. Inoue, N. Ishii, S. Aoki, T. Doi, T. Hatsuda, Y. Ikeda, K. Murano, H. Nemura, K. Sasaki, Bound  $H$  Dibaryon in Flavor SU(3) Limit of Lattice QCD, *Phys. Rev. Lett.* 106 (2011) 162002. doi:10.1103/PhysRevLett.106.162002.
- [7] S. Aoki, T. Doi, T. Hatsuda, Y. Ikeda, T. Inoue, N. Ishii, K. Murano, H. Nemura, K. Sasaki, Lattice quantum chromodynamical approach to nuclear physics, *Progress of Theoretical and Experimental Physics* 2012 (09 2012). doi:10.1093/ptep/pts010.
- [8] S. R. Beane, E. Chang, S. D. Cohen, W. Detmold, H. W. Lin, T. C. Luu, K. Orginos, A. Parreno, M. J. Savage, A. Walker-Loud, Light Nuclei and Hypernuclei from Quantum Chromodynamics in the Limit of SU(3) Flavor Symmetry, *Phys. Rev. D* 87 (2013) 034506. doi:10.1103/PhysRevD.87.034506.
- [9] R. A. Briceño, Z. Davoudi, T. C. Luu, Nuclear Reactions from Lattice QCD, *J. Phys. G: Nucl. Part. Phys.* 42 (2015) 023101. doi:10.1088/0954-3899/42/2/023101.
- [10] K. Orginos, A. Parreno, M. J. Savage, S. R. Beane, E. Chang, W. Detmold, Two nucleon systems at  $m_\pi \sim 450$  MeV from lattice QCD, *Phys. Rev. D* 92 (2015) 114512. doi:10.1103/PhysRevD.92.114512.
- [11] E. Berkowitz, T. Kurth, A. Nicholson, B. Joó, E. Rinaldi, M. Strother, P. M. Vranas, A. Walker-Loud, Two-nucleon higher partial-wave scattering from lattice QCD, *Phys. Lett. B* 765 (2017) 285. doi:https://doi.org/10.1016/j.physletb.2016.12.024.
- [12] W. Detmold, R. G. Edwards, J. J. Dudek, M. Engelhardt, H.-W. Lin, S. Meinel, K. Orginos, P. Shanahan, Hadrons and Nuclei, *Eur. Phys. J. A* 55 (2019) 193. doi:10.1140/epja/i2019-12902-4.
- [13] T. Iritani, S. Aoki, T. Doi, F. Etminan, S. Gongyo, T. Hatsuda, Y. Ikeda, T. Inoue, N. Ishii, T. Miyamoto, K. Sasaki,  $N\Omega$  dibaryon from lattice QCD near the physical point, *Phys. Lett. B* 792 (2019) 284. doi:https://doi.org/10.1016/j.physletb.2019.03.050.
- [14] C. Drischler, W. Haxton, K. McElvain, E. Mereghetti, A. Nicholson, P. Vranas, A. Walker-Loud, Towards grounding nuclear physics in QCD (2019). arXiv:1910.07961.
- [15] E. Epelbaum, H.-W. Hammer, U.-G. Meißner, Modern Theory of Nuclear Forces, *Rev. Mod. Phys.* 81 (2009) 1773. doi:10.1103/RevModPhys.81.1773.
- [16] R. Machleidt, D. R. Entem, Chiral effective field theory and nuclear forces, *Phys. Rep.* 503 (2011) 1. doi:10.1016/j.physrep.2011.02.001.
- [17] H.-W. Hammer, S. König, U. van Kolck, Nuclear effective field theory: status and perspectives, *Rev. Mod. Phys.* 92 (2020) 025004. doi:10.1103/RevModPhys.92.025004.
- [18] H. Hergert, S. K. Bogner, T. D. Morris, A. Schwenk, K. Tsukiyama, The In-Medium Similarity Renormalization Group: A Novel Ab Initio Method for Nuclei, *Phys. Rept.* 621 (2016) 165. doi:10.1016/j.physrep.2015.12.007.
- [19] H. Hergert, private communication (2019).
- [20] S. K. Bogner, R. J. Furnstahl, A. Schwenk, From low-momentum interactions to nuclear structure, *Prog. Part. Nucl. Phys.* 65 (2010) 94. doi:10.1016/j.pnpnp.2010.03.001.
- [21] S. K. Bogner, R. J. Furnstahl, R. J. Perry, Similarity Renormalization Group for Nucleon-Nucleon Interactions, *Phys. Rev. C* 75 (2007) 061001(R). doi:10.1103/PhysRevC.75.061001.
- [22] E. D. Jurgenson, R. J. Furnstahl, Similarity Renormalization Group Evolution of Many-Body Forces in a One-Dimensional Model, *Nucl. Phys. A* 818 (2009) 152. doi:10.1016/j.nuclphysa.2008.12.007.
- [23] A. Tichai, E. Gebrerufael, K. Vobig, R. Roth, Open-Shell Nuclei from No-Core Shell Model with Perturbative Improvement, *Phys. Lett. B* 786 (2018) 448. doi:10.1016/j.physletb.2018.10.029.
- [24] E. Gebrerufael, K. Vobig, H. Hergert, R. Roth, Ab Initio Description of Open-Shell Nuclei: Merging No-Core Shell Model and In-Medium Similarity Renormalization Group, *Phys. Rev. Lett.* 118 (2017) 152503. doi:10.1103/PhysRevLett.118.152503.
- [25] W. Glöckle, The Quantum Mechanical Few-Body Problem, Springer Verlag, 1983.
- [26] W. Glöckle, H. Witała, D. Huber, H. Kamada, J. Golak, The Three nucleon continuum: Achievements, challenges and applications, *Phys. Rept.* 274 (1996) 107. doi:10.1016/0370-1573(95)00085-2.
- [27] A. Stadler, W. Glöckle, P. U. Sauer, Faddeev equations with three-nucleon force in momentum space, *Phys. Rev. C* 44 (1991) 2319. doi:10.1103/PhysRevC.44.2319.
- [28] A. Nogga, H. Kamada, W. Glöckle, Modern nuclear force predictions for the alpha particle, *Phys. Rev. Lett.* 85 (2000) 944. doi:10.1103/PhysRevLett.85.944.
- [29] E. Epelbaum, W. Glöckle, U.-G. Meißner, The Two-nucleon system at next-to-next-to-next-to-leading order, *Nucl. Phys. A* 747 (2005) 362. doi:10.1016/j.nuclphysa.2004.09.107.

- [30] A. Deltuva, A. C. Fonseca, Four-nucleon scattering: Ab initio calculations in momentum space, *Phys. Rev. C* 75 (2007) 014005. doi:10.1103/PhysRevC.75.014005.
- [31] M. Viviani, A. Deltuva, R. Lazauskas, A. C. Fonseca, A. Kievsky, L. E. Marcucci, Benchmark calculation of  $p$ - $^3\text{H}$  and  $n$ - $^3\text{He}$  scattering, *Phys. Rev. C* 95 (2017) 034003. doi:10.1103/PhysRevC.95.034003.
- [32] R. Lazauskas, Solution of the  $n$ - $^4\text{He}$  elastic scattering problem using the Faddeev-Yakubovsky equations, *Phys. Rev. C* 97 (2018) 044002. doi:10.1103/PhysRevC.97.044002.
- [33] E. Epelbaum, J. Golak, K. Hebeler, T. Hüther, H. Kamada, H. Krebs, P. Maris, U.-G. Meißner, A. Nogga, R. Roth, R. Skibiński, K. Topolnicki, J. P. Vary, K. Vobig, H. Witala, Few- and many-nucleon systems with semilocal coordinate-space regularized chiral two- and three-body forces, *Phys. Rev. C* 99 (2019) 024313. doi:10.1103/PhysRevC.99.024313.
- [34] A. Kievsky, S. Rosati, M. Viviani, L. E. Marcucci, L. Girlanda, A high-precision variational approach to three- and four-nucleon bound and zero-energy scattering states, *J. Phys. G* 35 (2008) 063101. doi:10.1088/0954-3899/35/6/063101.
- [35] N. Barnea, W. Leidemann, G. Orlandini, State dependent effective interaction for the hyperspherical formalism with noncentral forces, *Nucl. Phys. A* 693 (2001) 565. doi:10.1016/S0375-9474(01)00794-1.
- [36] M. Viviani, L. E. Marcucci, S. Rosati, A. Kievsky, L. Girlanda, Variational calculation on  $A=3$  and 4 nuclei with non-local potentials, *Few Body Syst.* 39 (2006) 159. doi:10.1007/s00601-006-0158-y.
- [37] L. E. Marcucci, A. Kievsky, S. Rosati, R. Schiavilla, M. Viviani, Chiral effective field theory predictions for muon capture on deuteron and  $^3\text{He}$ , *Phys. Rev. Lett.* 108 (2012) 052502, [Erratum: *Phys. Rev. Lett.* 121 (2018) 049901]. doi:10.1103/PhysRevLett.108.052502.
- [38] S. Bacca, N. Barnea, G. Hagen, G. Orlandini, T. Papenbrock, First Principles Description of the Giant Dipole Resonance in  $^{16}\text{O}$ , *Phys. Rev. Lett.* 111 (2013) 122502. doi:10.1103/PhysRevLett.111.122502.
- [39] B. R. Barrett, P. Navrátil, J. P. Vary, Ab initio no core shell model, *Prog. Part. Nucl. Phys.* 69 (2013) 131. doi:10.1016/j.ppnp.2012.10.003.
- [40] P. Navrátil, G. P. Kamuntavicius, B. R. Barrett, Few nucleon systems in translationally invariant harmonic oscillator basis, *Phys. Rev. C* 61 (2000) 044001. doi:10.1103/PhysRevC.61.044001.
- [41] P. Navrátil, S. Quaglioni, I. Stetcu, B. R. Barrett, Recent developments in no-core shell-model calculations, *J. Phys. G* 36 (2009) 083101. doi:10.1088/0954-3899/36/8/083101.
- [42] P. Navrátil, V. G. Guerguiev, J. P. Vary, W. E. Ormand, A. Nogga, Structure of  $A=10$ –13 Nuclei with Two- Plus Three-Nucleon Interactions from Chiral Effective Field Theory, *Phys. Rev. Lett.* 99 (2007) 042501. doi:10.1103/PhysRevLett.99.042501.
- [43] R. Roth, J. Langhammer, A. Calci, S. Binder, P. Navrátil, Similarity-Transformed Chiral NN+3N Interactions for the Ab Initio Description of  $^{12}\text{C}$  and  $^{16}\text{O}$ , *Phys. Rev. Lett.* 107 (2011) 072501. doi:10.1103/PhysRevLett.107.072501.
- [44] R. Roth, A. Calci, J. Langhammer, S. Binder, Evolved Chiral NN+3N Hamiltonians for Ab Initio Nuclear Structure Calculations, *Phys. Rev. C* 90 (2014) 024325. doi:10.1103/PhysRevC.90.024325.
- [45] R. Wirth, D. Gazda, P. Navrátil, A. Calci, J. Langhammer, R. Roth, Ab Initio Description of  $p$ -Shell Hypernuclei, *Phys. Rev. Lett.* 113 (2014) 192502. doi:10.1103/PhysRevLett.113.192502.
- [46] M. Vorabbi, P. Navrátil, S. Quaglioni, G. Hupin,  $^7\text{Be}$  and  $^7\text{Li}$  nuclei within the no-core shell model with continuum, *Phys. Rev. C* 100 (2019) 024304. doi:10.1103/PhysRevC.100.024304.
- [47] J. Carlson, S. Gandolfi, F. Pederiva, S. C. Pieper, R. Schiavilla, K. E. Schmidt, R. B. Wiringa, Quantum Monte Carlo methods for nuclear physics, *Rev. Mod. Phys.* 87 (2015) 1067. doi:10.1103/RevModPhys.87.1067.
- [48] F. Pederiva, A. Roggero, K. E. Schmidt, Variational and Diffusion Monte Carlo Approaches to the Nuclear Few- and Many-Body Problem, *Lect. Notes Phys.* 936 (2017) 401. doi:10.1007/978-3-319-53336-0\_9.
- [49] J. Lynn, I. Tews, S. Gandolfi, A. Lovato, Quantum monte carlo methods in nuclear physics: Recent advances, *Annual Review of Nuclear and Particle Science* 69 (2019) 1. doi:10.1146/annurev-nucl-101918-023600.
- [50] A. Gezerlis, I. Tews, E. Epelbaum, S. Gandolfi, K. Hebeler, A. Nogga, A. Schwenk, Quantum Monte Carlo Calculations with Chiral Effective Field Theory Interactions, *Phys. Rev. Lett.* 111 (2013) 032501. doi:10.1103/PhysRevLett.111.032501.
- [51] A. Gezerlis, I. Tews, E. Epelbaum, M. Freunek, S. Gandolfi, K. Hebeler, A. Nogga, A. Schwenk, Local chiral effective field theory interactions and quantum Monte Carlo applications, *Phys. Rev. C* 90 (2014) 054323. doi:10.1103/PhysRevC.90.054323.
- [52] J. E. Lynn, I. Tews, J. Carlson, S. Gandolfi, A. Gezerlis, K. E. Schmidt, A. Schwenk, Chiral Three-Nucleon Interactions in Light Nuclei, Neutron- $\alpha$  Scattering, and Neutron Matter, *Phys. Rev. Lett.* 116 (2016) 062501. doi:10.1103/PhysRevLett.116.062501.
- [53] D. Lonardoni, J. Carlson, S. Gandolfi, J. E. Lynn, K. E. Schmidt, A. Schwenk, X. Wang, Properties of nuclei up to  $A = 16$  using local chiral interactions, *Phys. Rev. Lett.* 120 (2018) 122502. doi:10.1103/PhysRevLett.120.122502.
- [54] M. Piarulli, A. Baroni, L. Girlanda, A. Kievsky, A. Lovato, E. Lusk, L. Marcucci, S. C. Pieper, R. Schiavilla, M. Viviani, R. Wiringa, Light-nuclei spectra from chiral dynamics, *Phys. Rev. Lett.* 120 (2018) 052503. doi:10.1103/PhysRevLett.120.052503.
- [55] D. Lonardoni, S. Gandolfi, J. E. Lynn, C. Petrie, J. Carlson, K. E. Schmidt, A. Schwenk, Auxiliary field diffusion Monte Carlo calculations of light and medium-mass nuclei with local chiral interactions, *Phys. Rev. C* 97 (2018) 044318. doi:10.1103/PhysRevC.97.044318.
- [56] R. Roth, Importance Truncation for Large-Scale Configuration Interaction Approaches, *Phys. Rev. C* 79 (2009) 064324. doi:10.1103/PhysRevC.79.064324.
- [57] R. Roth, P. Navrátil, Ab initio study of  $^{40}\text{Ca}$  with an importance truncated no-core shell model, *Phys. Rev. Lett.* 99 (2007) 092501. doi:10.1103/PhysRevLett.99.092501.
- [58] R. Roth, S. Binder, K. Vobig, A. Calci, J. Langhammer, P. Navrátil, Medium-Mass Nuclei with Normal-Ordered Chiral

- NN+3N Interactions, Phys. Rev. Lett. 109 (2012) 052501. doi:10.1103/PhysRevLett.109.052501.
- [59] E. Gebrerufael, A. Calci, R. Roth, Open-shell nuclei and excited states from multireference normal-ordered Hamiltonians, Phys. Rev. C 93 (2016) 031301(R). doi:10.1103/PhysRevC.93.031301.
- [60] R. Wirth, R. Roth, Light Neutron-Rich Hypernuclei from the Importance-Truncated No-Core Shell Model, Phys. Lett. B 779 (2018) 336. doi:10.1016/j.physletb.2018.02.021.
- [61] D. Lee, Lattice simulations for few- and many-body systems, Prog. Part. Nucl. Phys. 63 (2009) 117. doi:10.1016/j.ppnp.2008.12.001.
- [62] D. Lee, Lattice methods and the nuclear few- and many-body problem, Lect. Notes Phys. 936 (2017) 237. doi:10.1007/978-3-319-53336-0\_6.
- [63] E. Epelbaum, H. Krebs, D. Lee, U.-G. Meißner, Lattice effective field theory calculations for  $A = 3, 4, 6, 12$  nuclei, Phys. Rev. Lett. 104 (2010) 142501. doi:10.1103/PhysRevLett.104.142501.
- [64] E. Epelbaum, H. Krebs, D. Lee, U.-G. Meißner, Lattice chiral effective field theory with three-body interactions at next-to-next-to-leading order, Eur. Phys. J. A41 (2009) 125. doi:10.1140/epja/i2009-10764-y.
- [65] E. Epelbaum, H. Krebs, D. Lee, U.-G. Meißner, Lattice calculations for  $A=3, 4, 6, 12$  nuclei using chiral effective field theory, Eur. Phys. J. A 45 (2010) 335. doi:10.1140/epja/i2010-11009-x.
- [66] E. Epelbaum, H. Krebs, D. Lee, U.-G. Meißner, Ab initio calculation of the Hoyle state, Phys. Rev. Lett. 106 (2011) 192501. doi:10.1103/PhysRevLett.106.192501.
- [67] E. Epelbaum, H. Krebs, T. A. Lähde, D. Lee, U.-G. Meißner, Structure and Rotations of the Hoyle State, Phys. Rev. Lett. 109 (2012) 252501. doi:10.1103/PhysRevLett.109.252501.
- [68] E. Epelbaum, H. Krebs, T. A. Lähde, D. Lee, U.-G. Meißner, Viability of Carbon-Based Life as a Function of the Light Quark Mass, Phys. Rev. Lett. 110 (2013) 112502. doi:10.1103/PhysRevLett.110.112502.
- [69] G. Rupak, D. Lee, Radiative capture reactions in lattice effective field theory, Phys. Rev. Lett. 111 (2013) 032502. doi:10.1103/PhysRevLett.111.032502.
- [70] T. A. Lähde, E. Epelbaum, H. Krebs, D. Lee, U.-G. Meißner, G. Rupak, Lattice Effective Field Theory for Medium-Mass Nuclei, Phys. Lett. B 732 (2014) 110. doi:10.1016/j.physletb.2014.03.023.
- [71] E. Epelbaum, H. Krebs, T. A. Lähde, D. Lee, U.-G. Meißner, G. Rupak, Ab Initio Calculation of the Spectrum and Structure of  $^{16}\text{O}$ , Phys. Rev. Lett. 112 (2014) 102501. doi:10.1103/PhysRevLett.112.102501.
- [72] S. Elhatisari, D. Lee, G. Rupak, E. Epelbaum, H. Krebs, T. A. Lähde, T. Luu, U.-G. Meißner, Ab initio alpha-alpha scattering, Nature 528 (2015) 111. doi:10.1038/nature16067.
- [73] S. Elhatisari, N. Li, A. Rokash, J. M. Alarcón, D. Du, N. Klein, B. Lu, U.-G. Meißner, E. Epelbaum, H. Krebs, T. A. Lähde, D. Lee, G. Rupak, Nuclear binding near a quantum phase transition, Phys. Rev. Lett. 117 (2016) 132501. doi:10.1103/PhysRevLett.117.132501.
- [74] S. Elhatisari, E. Epelbaum, H. Krebs, T. A. Lähde, D. Lee, N. Li, B. Lu, U.-G. Meißner, G. Rupak, Ab initio Calculations of the Isotopic Dependence of Nuclear Clustering, Phys. Rev. Lett. 119 (2017) 222505. doi:10.1103/PhysRevLett.119.222505.
- [75] A. F. Lisetskiy, B. R. Barrett, M. K. G. Kruse, P. Navrátil, I. Stetcu, J. P. Vary, Ab-initio shell model with a core, Phys. Rev. C 78 (2008) 044302. doi:10.1103/PhysRevC.78.044302.
- [76] S. R. Stroberg, H. Hergert, S. K. Bogner, J. D. Holt, Nonempirical interactions for the nuclear shell model: An update, Annual Review of Nuclear and Particle Science 69 (2019) 307. doi:10.1146/annurev-nucl-101917-021120.
- [77] F. Wienholtz, D. Beck, K. Blaum, C. Borgmann, M. Breitenfeldt, R. Cakirli, S. George, F. Herfurth, J. Holt, M. Kowalska, S. Kreim, D. Lunney, V. Manea, J. Menéndez, D. Neidherr, M. Rosenbusch, L. Schweikhard, A. Schwenk, J. Simonis, J. Stanja, R. Wolf, Z. K., Masses of exotic calcium isotopes pin down nuclear forces, Nature 498 (2013) 346. doi:10.1038/nature12226.
- [78] J. D. Holt, J. Menéndez, J. Simonis, A. Schwenk, Three-nucleon forces and spectroscopy of neutron-rich calcium isotopes, Phys. Rev. C 90 (2014) 024312. doi:10.1103/PhysRevC.90.024312.
- [79] S. K. Bogner, H. Hergert, J. D. Holt, A. Schwenk, S. Binder, A. Calci, J. Langhammer, R. Roth, Nonperturbative shell-model interactions from the in-medium similarity renormalization group, Phys. Rev. Lett. 113 (2014) 142501. doi:10.1103/PhysRevLett.113.142501.
- [80] G. R. Jansen, J. Engel, G. Hagen, P. Navrátil, A. Signoracci, Ab initio coupled-cluster effective interactions for the shell model: Application to neutron-rich oxygen and carbon isotopes, Phys. Rev. Lett. 113 (2014) 142502. doi:10.1103/PhysRevLett.113.142502.
- [81] G. R. Jansen, A. Signoracci, G. Hagen, P. Navrátil, Open sd-shell nuclei from first principles, Phys. Rev. C 94 (2016) 011301(R). doi:10.1103/PhysRevC.94.011301.
- [82] S. R. Stroberg, A. Calci, H. Hergert, J. D. Holt, S. K. Bogner, R. Roth, A. Schwenk, Nucleus-dependent valence-space approach to nuclear structure, Phys. Rev. Lett. 118 (2017) 032502. doi:10.1103/PhysRevLett.118.032502.
- [83] Z. H. Sun, T. D. Morris, G. Hagen, G. R. Jansen, T. Papenbrock, Shell-model coupled-cluster method for open-shell nuclei, Phys. Rev. C 98 (2018) 054320. doi:10.1103/PhysRevC.98.054320.
- [84] H. Hergert, In-Medium Similarity Renormalization Group for Closed and Open-Shell Nuclei, Phys. Scripta 92 (2017) 023002. doi:10.1088/1402-4896/92/2/023002.
- [85] H. Hergert, S. K. Bogner, J. G. Lietz, T. D. Morris, S. Novario, N. M. Parzuchowski, F. Yuan, In-Medium Similarity Renormalization Group Approach to the Nuclear Many-Body Problem, Lect. Notes Phys. 936 (2017) 477. doi:10.1007/978-3-319-53336-0\_10.
- [86] K. Tsukiyama, S. K. Bogner, A. Schwenk, In-medium Similarity Renormalization Group for Nuclei, Phys. Rev. Lett. 106 (2011) 222502. doi:10.1103/PhysRevLett.106.222502.
- [87] K. Tsukiyama, S. K. Bogner, A. Schwenk, In-medium similarity renormalization group for open-shell nuclei, Phys. Rev.



- C 85 (2012) 061304(R). doi:10.1103/PhysRevC.85.061304.
- [88] H. Hergert, S. Binder, A. Calci, J. Langhammer, R. Roth, Ab Initio Calculations of Even Oxygen Isotopes with Chiral Two-Plus-Three-Nucleon Interactions, Phys. Rev. Lett. 110 (2013) 242501. doi:10.1103/PhysRevLett.110.242501.
- [89] H. Hergert, S. K. Bogner, T. D. Morris, S. Binder, A. Calci, J. Langhammer, R. Roth, Ab initio multireference in-medium similarity renormalization group calculations of even calcium and nickel isotopes, Phys. Rev. C 90 (2014) 041302(R). doi:10.1103/PhysRevC.90.041302.
- [90] T. D. Morris, N. Parzuchowski, S. K. Bogner, Magnus expansion and in-medium similarity renormalization group, Phys. Rev. C 92 (2015) 034331. doi:10.1103/PhysRevC.92.034331.
- [91] S. R. Stroberg, H. Hergert, J. D. Holt, S. K. Bogner, A. Schwenk, Ground and excited states of doubly open-shell nuclei from ab initio valence-space Hamiltonians, Phys. Rev. C 93 (2016) 051301(R). doi:10.1103/PhysRevC.93.051301.
- [92] N. M. Parzuchowski, T. D. Morris, S. K. Bogner, Ab Initio Excited States from the In-Medium Similarity Renormalization Group, Phys. Rev. C 95 (2017) 044304. doi:10.1103/PhysRevC.95.044304.
- [93] T. D. Morris, J. Simonis, S. R. Stroberg, C. Stumpf, G. Hagen, J. D. Holt, G. R. Jansen, T. Papenbrock, R. Roth, A. Schwenk, Structure of the lightest tin isotopes, Phys. Rev. Lett. 120 (2018) 152503. doi:10.1103/PhysRevLett.120.152503.
- [94] G. Hagen, T. Papenbrock, M. Hjorth-Jensen, D. J. Dean, Coupled-cluster computations of atomic nuclei, Rep. Prog. Phys. 77 (2014) 096302. doi:10.1088/0034-4885/77/9/096302.
- [95] K. Kowalski, D. J. Dean, M. Hjorth-Jensen, T. Papenbrock, P. Piecuch, Coupled Cluster Calculations of Ground and Excited States of Nuclei, Phys. Rev. Lett. 92 (2004) 132501. doi:10.1103/PhysRevLett.92.132501.
- [96] G. Hagen, T. Papenbrock, D. J. Dean, A. Schwenk, A. Nogga, M. Włoch, P. Piecuch, Coupled-cluster theory for three-body Hamiltonians, Phys. Rev. C 76 (2007) 034302. doi:10.1103/PhysRevC.76.034302.
- [97] G. Hagen, T. Papenbrock, D. J. Dean, M. Hjorth-Jensen, Medium-mass nuclei from chiral nucleon-nucleon interactions, Phys. Rev. Lett. 101 (2008) 092502. doi:10.1103/PhysRevLett.101.092502.
- [98] G. Hagen, M. Hjorth-Jensen, G. R. Jansen, R. Machleidt, T. Papenbrock, Continuum effects and three-nucleon forces in neutron-rich oxygen isotopes, Phys. Rev. Lett. 108 (2012) 242501. doi:10.1103/PhysRevLett.108.242501.
- [99] S. Binder, J. Langhammer, A. Calci, P. Navrátil, R. Roth, Ab Initio calculations of medium-mass nuclei with explicit chiral 3N interactions, Phys. Rev. C 87 (2013) 021303(R). doi:10.1103/PhysRevC.87.021303.
- [100] S. Binder, P. Piecuch, A. Calci, J. Langhammer, P. Navrátil, R. Roth, Extension of coupled-cluster theory with a noniterative treatment of connected triply excited clusters to three-body Hamiltonians, Phys. Rev. C 88 (2013) 054319. doi:10.1103/PhysRevC.88.054319.
- [101] G. Hagen, M. Hjorth-Jensen, G. R. Jansen, R. Machleidt, T. Papenbrock, Evolution of shell structure in neutron-rich calcium isotopes, Phys. Rev. Lett. 109 (2012) 032502. doi:10.1103/PhysRevLett.109.032502.
- [102] S. Binder, J. Langhammer, A. Calci, R. Roth, Ab initio path to heavy nuclei, Phys. Lett. B 736 (2014) 119. doi:10.1016/j.physletb.2014.07.010.
- [103] A. Signoracci, T. Duguet, G. Hagen, G. Jansen, Ab initio Bogoliubov coupled cluster theory for open-shell nuclei, Phys. Rev. C 91 (2015) 064320. doi:10.1103/PhysRevC.91.064320.
- [104] R. F. Garcia Ruiz, M. L. Bissell, K. Blaum, A. Ekström, N. Frömmgen, G. Hagen, M. Hammen, K. Hebel, J. D. Holt, G. R. Jansen, M. Kowalska, K. Kreim, W. Nazarewicz, R. Neugart, G. Neyens, W. Nörtershäuser, T. Papenbrock, J. Papuga, A. Schwenk, J. Simonis, K. A. Wendt, D. T. Yordanov, Unexpectedly large charge radii of neutron-rich calcium isotopes, Nat. Phys. 12 (2016) 594. doi:10.1038/nphys3645.
- [105] G. Hagen, A. Ekström, C. Forssén, G. R. Jansen, W. Nazarewicz, T. Papenbrock, K. A. Wendt, S. Bacca, N. Barnea, B. Carlsson, C. Drischler, K. Hebel, M. Hjorth-Jensen, M. Miorelli, G. Orlandini, A. Schwenk, J. Simonis, Neutron and weak-charge distributions of the  $^{48}\text{Ca}$  nucleus, Nat. Phys. 12 (2016) 186. doi:10.1038/nphys3529.
- [106] J. Birkhan, M. Miorelli, S. Bacca, S. Bassauer, C. A. Bertulani, G. Hagen, H. Matsubara, P. von Neumann-Cosel, T. Papenbrock, N. Pietralla, V. Y. Ponomarev, A. Richter, A. Schwenk, A. Tamii, Electric dipole polarizability of  $^{48}\text{Ca}$  and implications for the neutron skin, Phys. Rev. Lett. 118 (2017) 252501. doi:10.1103/PhysRevLett.118.252501.
- [107] W. H. Dickhoff, C. Barbieri, Selfconsistent Green's function method for nuclei and nuclear matter, Prog. Part. Nucl. Phys. 52 (2004) 377. doi:10.1016/j.pnpnp.2004.02.038.
- [108] C. Barbieri, A. Carbone, Self-consistent Green's function approaches, Lect. Notes Phys. 936 (2017) 571. doi:10.1007/978-3-319-53336-0\_11.
- [109] V. Somà, T. Duguet, C. Barbieri, Ab initio self-consistent Gorkov-Green's function calculations of semi-magic nuclei: Formalism at second order with a two-nucleon interaction, Phys. Rev. C 84 (2011) 064317. doi:10.1103/PhysRevC.84.064317.
- [110] V. Somà, C. Barbieri, T. Duguet, Ab initio Gorkov-Green's function calculations of open-shell nuclei, Phys. Rev. C 87 (2013) 011303. doi:10.1103/PhysRevC.87.011303.
- [111] A. Carbone, A. Cipollone, C. Barbieri, A. Rios, A. Polls, Self-consistent Green's functions formalism with three-body interactions, Phys. Rev. C 88 (2013) 054326. doi:10.1103/PhysRevC.88.054326.
- [112] A. Cipollone, C. Barbieri, P. Navrátil, Isotopic chains around oxygen from evolved chiral two- and three-nucleon interactions, Phys. Rev. Lett. 111 (2013) 062501. doi:10.1103/PhysRevLett.111.062501.
- [113] V. Somà, A. Cipollone, C. Barbieri, P. Navrátil, T. Duguet, Chiral two- and three-nucleon forces along medium-mass isotope chains, Phys. Rev. C 89 (2014) 061301(R). doi:10.1103/PhysRevC.89.061301.
- [114] A. Cipollone, C. Barbieri, P. Navrátil, Chiral three-nucleon forces and the evolution of correlations along the oxygen isotopic chain, Phys. Rev. C 92 (2015) 014306. doi:10.1103/PhysRevC.92.014306.
- [115] A. Tichai, J. Langhammer, S. Binder, R. Roth, Hartree-Fock many-body perturbation theory for nuclear ground-states, Phys. Lett. B 756 (2016) 283. doi:10.1016/j.physletb.2016.03.029.

- [116] B. Hu, F. Xu, Z. Sun, J. P. Vary, T. Li, Ab initio nuclear many-body perturbation calculations in the Hartree-Fock basis, *Phys. Rev. C* 94 (2016) 014303. [doi:10.1103/PhysRevC.94.014303](https://doi.org/10.1103/PhysRevC.94.014303).
- [117] A. Tichai, P. Arthuis, T. Duguet, H. Hergert, V. Somà, R. Roth, Bogoliubov Many-Body Perturbation Theory for Open-Shell Nuclei, *Phys. Lett. B* 786 (2018) 195. [doi:10.1016/j.physletb.2018.09.044](https://doi.org/10.1016/j.physletb.2018.09.044).
- [118] P. Demol, T. Duguet, A. Ekström, M. Frosini, K. Hebeler, S. König, D. Lee, A. Schwenk, V. Somà, A. Tichai, Improved many-body expansions from eigenvector continuation, *Phys. Rev. C* 101 (2020) 041302. [doi:10.1103/PhysRevC.101.041302](https://doi.org/10.1103/PhysRevC.101.041302).
- [119] A. Tichai, R. Roth, T. Duguet, Many-body perturbation theories for finite nuclei, *Front. in Phys.* 8 (2020) 164. [doi:10.3389/fphy.2020.00164](https://doi.org/10.3389/fphy.2020.00164).
- [120] P. Demol, M. Frosini, A. Tichai, V. Somà, T. Duguet, Bogoliubov many-body perturbation theory under constraint. [arXiv:2002.02724](https://arxiv.org/abs/2002.02724).
- [121] J. Negele, H. Orland, *Quantum Many-Particle Systems*, Redwood City, Addison-Wesley Pub. Co., 1988.
- [122] K. Hebeler, A. Schwenk, Chiral three-nucleon forces and neutron matter, *Phys. Rev. C* 82 (2010) 014314. [doi:10.1103/PhysRevC.82.014314](https://doi.org/10.1103/PhysRevC.82.014314).
- [123] K. Hebeler, S. K. Bogner, R. J. Furnstahl, A. Nogga, A. Schwenk, Improved nuclear matter calculations from chiral low-momentum interactions, *Phys. Rev. C* 83 (2011) 031301(R). [doi:10.1103/PhysRevC.83.031301](https://doi.org/10.1103/PhysRevC.83.031301).
- [124] I. Tews, T. Krüger, K. Hebeler, A. Schwenk, Neutron Matter at Next-to-Next-to-Next-to-Leading Order in Chiral Effective Field Theory, *Phys. Rev. Lett.* 110 (2013) 032504. [doi:10.1103/PhysRevLett.110.032504](https://doi.org/10.1103/PhysRevLett.110.032504).
- [125] J. W. Holt, N. Kaiser, W. Weise, Nuclear chiral dynamics and thermodynamics, *Prog. Part. Nucl. Phys.* 73 (2013) 35. [doi:10.1016/j.pnpnp.2013.08.001](https://doi.org/10.1016/j.pnpnp.2013.08.001).
- [126] L. Coraggio, J. W. Holt, N. Itaco, R. Machleidt, L. E. Marcucci, F. Sammarruca, Nuclear-matter equation of state with consistent two- and three-body perturbative chiral interactions, *Phys. Rev. C* 89 (2014) 044321. [doi:10.1103/PhysRevC.89.044321](https://doi.org/10.1103/PhysRevC.89.044321).
- [127] C. Wellenhofer, J. W. Holt, N. Kaiser, Thermodynamics of isospin-asymmetric nuclear matter from chiral effective field theory, *Phys. Rev. C* 92 (2015) 015801. [doi:10.1103/PhysRevC.92.015801](https://doi.org/10.1103/PhysRevC.92.015801).
- [128] C. Drischler, K. Hebeler, A. Schwenk, Asymmetric nuclear matter based on chiral two- and three-nucleon interactions, *Phys. Rev. C* 93 (2016) 054314. [doi:10.1103/PhysRevC.93.054314](https://doi.org/10.1103/PhysRevC.93.054314).
- [129] J. W. Holt, N. Kaiser, Equation of state of nuclear and neutron matter at third-order in perturbation theory from chiral EFT, *Phys. Rev. C* 95 (2017) 034326. [doi:10.1103/PhysRevC.95.034326](https://doi.org/10.1103/PhysRevC.95.034326).
- [130] C. Drischler, K. Hebeler, A. Schwenk, Chiral interactions up to next-to-next-to-next-to-leading order and nuclear saturation, *Phys. Rev. Lett.* 122 (2019) 042501. [doi:10.1103/PhysRevLett.122.042501](https://doi.org/10.1103/PhysRevLett.122.042501).
- [131] A. Carbone, A. Polls, A. Rios, Symmetric nuclear matter with chiral three-nucleon forces in the self-consistent Green's functions approach, *Phys. Rev. C* 88 (2013) 044302. [doi:10.1103/PhysRevC.88.044302](https://doi.org/10.1103/PhysRevC.88.044302).
- [132] A. Carbone, A. Rios, A. Polls, Correlated density-dependent chiral forces for infinite matter calculations within the Green's function approach, *Phys. Rev. C* 90 (2014) 054322. [doi:10.1103/PhysRevC.90.054322](https://doi.org/10.1103/PhysRevC.90.054322).
- [133] B. D. Day, *Elements of the Brueckner-Goldstone Theory of Nuclear Matter*, *Rev. Mod. Phys.* 39 (1967) 719. [doi:10.1103/RevModPhys.39.719](https://doi.org/10.1103/RevModPhys.39.719).
- [134] Z. H. Li, H. J. Schulze, Nuclear matter with chiral forces in Brueckner-Hartree-Fock approximation, *Phys. Rev. C* 85 (2012) 064002. [doi:10.1103/PhysRevC.85.064002](https://doi.org/10.1103/PhysRevC.85.064002).
- [135] F. Sammarruca, L. Coraggio, J. W. Holt, N. Itaco, R. Machleidt, L. E. Marcucci, Toward order-by-order calculations of the nuclear and neutron matter equations of state in chiral effective field theory, *Phys. Rev. C* 91 (2015) 054311. [doi:10.1103/PhysRevC.91.054311](https://doi.org/10.1103/PhysRevC.91.054311).
- [136] J. Hu, Y. Zhang, E. Epelbaum, U.-G. Meißner, J. Meng, Nuclear matter properties with nucleon-nucleon forces up to fifth order in the chiral expansion, *Phys. Rev. C* 96 (2017) 034307. [doi:10.1103/PhysRevC.96.034307](https://doi.org/10.1103/PhysRevC.96.034307).
- [137] D. Logoteta, I. Bombaci, A. Kievsky, Nuclear matter properties from local chiral interactions with  $\Delta$  isobar intermediate states, *Phys. Rev. C* 94 (2016) 064001. [doi:10.1103/PhysRevC.94.064001](https://doi.org/10.1103/PhysRevC.94.064001).
- [138] G. Baardsen, A. Ekström, G. Hagen, M. Hjorth-Jensen, Coupled-cluster studies of infinite nuclear matter, *Phys. Rev. C* 88 (2013) 054312. [doi:10.1103/PhysRevC.88.054312](https://doi.org/10.1103/PhysRevC.88.054312).
- [139] G. Hagen, T. Papenbrock, A. Ekström, K. Wendt, G. Baardsen, S. Gandolfi, M. Hjorth-Jensen, C. J. Horowitz, Coupled-cluster calculations of nucleonic matter, *Phys. Rev. C* 89 (2014) 014319. [doi:10.1103/PhysRevC.89.014319](https://doi.org/10.1103/PhysRevC.89.014319).
- [140] A. Ekström, G. Baardsen, C. Forssén, G. Hagen, M. Hjorth-Jensen, G. R. Jansen, R. Machleidt, W. Nazarewicz, T. Papenbrock, J. Sarich, S. M. Wild, Optimized Chiral Nucleon-Nucleon Interaction at Next-to-Next-to-Leading Order, *Phys. Rev. Lett.* 110 (2013) 192502. [doi:10.1103/PhysRevLett.110.192502](https://doi.org/10.1103/PhysRevLett.110.192502).
- [141] A. Ekström, G. R. Jansen, K. A. Wendt, G. Hagen, T. Papenbrock, B. D. Carlsson, C. Forssén, M. Hjorth-Jensen, P. Navrátil, W. Nazarewicz, Accurate nuclear radii and binding energies from a chiral interaction, *Phys. Rev. C* 91 (2015) 051301(R). [doi:10.1103/PhysRevC.91.051301](https://doi.org/10.1103/PhysRevC.91.051301).
- [142] A. Ekström, G. Hagen, T. D. Morris, T. Papenbrock, P. D. Schwartz,  $\Delta$  isobars and nuclear saturation, *Phys. Rev. C* 97 (2018) 024332. [doi:10.1103/PhysRevC.97.024332](https://doi.org/10.1103/PhysRevC.97.024332).
- [143] S. Gandolfi, F. Pederiva, S. Fantoni, K. E. Schmidt, Quantum monte carlo calculations of symmetric nuclear matter, *Phys. Rev. Lett.* 98 (2007) 102503. [doi:10.1103/PhysRevLett.98.102503](https://doi.org/10.1103/PhysRevLett.98.102503).
- [144] A. Roggero, A. Mukherjee, F. Pederiva, Quantum Monte Carlo calculations of neutron matter with non-local chiral interactions, *Phys. Rev. Lett.* 112 (2014) 221103. [doi:10.1103/PhysRevLett.112.221103](https://doi.org/10.1103/PhysRevLett.112.221103).
- [145] G. Wlazłowski, J. W. Holt, S. Moroz, A. Bulgac, K. J. Roche, Auxiliary-Field Quantum Monte Carlo Simulations of Neutron Matter in Chiral Effective Field Theory, *Phys. Rev. Lett.* 113 (2014) 182503. [doi:10.1103/PhysRevLett.113.182503](https://doi.org/10.1103/PhysRevLett.113.182503).

- [146] I. Tews, S. Gandolfi, A. Gezerlis, A. Schwenk, Quantum monte carlo calculations of neutron matter with chiral three-body forces, *Phys. Rev. C* 93 (2016) 024305. doi:10.1103/PhysRevC.93.024305.
- [147] B.-N. Lu, N. Li, S. Elhatisari, D. Lee, J. E. Drut, T. A. Lähde, E. Epelbaum, U.-G. Meißner, Ab initio nuclear thermodynamics, *Phys. Rev. Lett.* 125 (2020) 192502. doi:10.1103/PhysRevLett.125.192502.
- [148] D. Gazit, S. Quaglioni, P. Navrátil, Three-Nucleon Low-Energy Constants from the Consistency of Interactions and Currents in Chiral Effective Field Theory, *Phys. Rev. Lett.* 103 (2009) 102502, [Erratum: *Phys. Rev. Lett.* 122 (2019) 029901]. doi:10.1103/PhysRevLett.103.102502.
- [149] M. Wang, G. Audi, F. G. Kondev, W. Huang, S. Naimi, X. Xu, The AME2016 atomic mass evaluation (II). tables, graphs and references, *Chinese Physics C* 41 (2017) 030003. doi:10.1088/1674-1137/41/3/030003.
- [150] E. Epelbaum, Nuclear Forces from Chiral Effective Field Theory: A Primer. arXiv:1001.3229.
- [151] S. Weinberg, Nuclear forces from chiral Lagrangians, *Phys. Lett. B* 251 (1990) 288. doi:10.1016/0370-2693(90)90938-3.
- [152] S. Weinberg, Effective chiral Lagrangians for nucleon - pion interactions and nuclear forces, *Nucl. Phys. B* 363 (1991) 3. doi:10.1016/0550-3213(91)90231-L.
- [153] D. B. Kaplan, M. J. Savage, M. B. Wise, Two nucleon systems from effective field theory, *Nucl. Phys. B* 534 (1998) 329. doi:10.1016/S0550-3213(98)00440-4.
- [154] D. B. Kaplan, M. J. Savage, M. B. Wise, A New expansion for nucleon-nucleon interactions, *Phys. Lett. B* 424 (1998) 390. doi:10.1016/S0370-2693(98)00210-X.
- [155] A. Nogga, R. G. E. Timmermans, U. van Kolck, Renormalization of one-pion exchange and power counting, *Phys. Rev. C* 72 (2005) 054006. doi:10.1103/PhysRevC.72.054006.
- [156] M. C. Birse, Power counting with one-pion exchange, *Phys. Rev. C* 74 (2006) 014003. doi:10.1103/PhysRevC.74.014003.
- [157] B. Long, C. J. Yang, Short-range nuclear forces in singlet channels, *Phys. Rev. C* 86 (2012) 024001. doi:10.1103/PhysRevC.86.024001.
- [158] M. Pavon Valderrama, D. R. Phillips, Power Counting of Contact-Range Currents in Effective Field Theory, *Phys. Rev. Lett.* 114 (2015) 082502. doi:10.1103/PhysRevLett.114.082502.
- [159] B. Long, Power counting for nuclear forces in chiral effective field theory, *Int. J. Mod. Phys. E* 25 (2016) 1641006. doi:10.1142/S0218301316410068.
- [160] M. P. Valderrama, M. S. Sánchez, C.-J. Yang, B. Long, J. Carbonell, U. van Kolck, Power Counting in Peripheral Partial Waves: The Singlet Channels, *Phys. Rev. C* 95 (2017) 054001. doi:10.1103/PhysRevC.95.054001.
- [161] M. P. Valderrama, Power Counting and Wilsonian Renormalization in Nuclear Effective Field Theory, *Int. J. Mod. Phys. E* 25 (2016) 1641007. doi:10.1142/S021830131641007X.
- [162] M. Drissi, T. Duguet, V. Somà, Renormalization of pionless effective field theory in the A-body sector, *Eur. Phys. J. A* 56 (2020) 119. doi:10.1140/epja/s10050-020-00097-w.
- [163] H. Yukawa, On the Interaction of Elementary Particles I, *Proc. Phys. Math. Soc. Jap.* 17 (1935) 48. doi:10.1143/PTPS.1.1.
- [164] C. Ordonez, U. van Kolck, Chiral lagrangians and nuclear forces, *Phys. Lett. B* 291 (1992) 459. doi:10.1016/0370-2693(92)91404-w.
- [165] C. Ordonez, L. Ray, U. van Kolck, Nucleon-nucleon potential from an effective chiral Lagrangian, *Phys. Rev. Lett.* 72 (1994) 1982. doi:10.1103/PhysRevLett.72.1982.
- [166] S. Weinberg, Three-body interactions among nucleons and pions, *Phys. Lett. B* 295 (1992) 114. doi:10.1016/0370-2693(92)90099-P.
- [167] U. van Kolck, Few-nucleon forces from chiral Lagrangians, *Phys. Rev. C* 49 (1994) 2932. doi:10.1103/PhysRevC.49.2932.
- [168] S. N. Yang, W. Glöckle, Three-body mesonic retardation effect, *Phys. Rev. C* 33 (1986) 1774. doi:10.1103/PhysRevC.33.1774.
- [169] S. A. Coon, J. L. Friar, Pionic Retardation Effects in Two Pion Exchange Three Nucleon Forces, *Phys. Rev. C* 34 (1986) 1060. doi:10.1103/PhysRevC.34.1060.
- [170] E. Epelbaum, A. Nogga, W. Glöckle, H. Kamada, U.-G. Meißner, H. Witała, Three-nucleon forces from chiral effective field theory, *Phys. Rev. C* 66 (2002) 064001. doi:10.1103/PhysRevC.66.064001.
- [171] J. Fujita, H. Miyazawa, Pion Theory of Three-Body Forces, *Prog. Theor. Phys.* 17 (1957) 360. doi:10.1143/PTP.17.360.
- [172] S. A. Coon, M. D. Scadron, P. C. McNamee, B. R. Barrett, D. W. E. Blatt, B. H. J. McKellar, The Two Pion Exchange, Three Nucleon Potential and Nuclear Matter, *Nucl. Phys. A* 17 (1979) 242. doi:10.1016/0375-9474(79)90462-7.
- [173] H. T. Coelho, T. K. Das, M. R. Robilotta, Two pion exchange three nucleon force and the  $^3\text{H}$  and  $^3\text{He}$  nuclei, *Phys. Rev. C* 28 (1983) 1812. doi:10.1103/PhysRevC.28.1812.
- [174] M. Hoferichter, J. Ruiz de Elvira, B. Kubis, U.-G. Meißner, Matching pion-nucleon Roy-Steiner equations to chiral perturbation theory, *Phys. Rev. Lett.* 115 (2015) 192301. doi:10.1103/PhysRevLett.115.192301.
- [175] M. Hoferichter, J. Ruiz de Elvira, B. Kubis, U.-G. Meißner, Roy-Steiner equation analysis of pion-nucleon scattering, *Phys. Rept.* 625 (2016) 1. doi:10.1016/j.physrep.2016.02.002.
- [176] D. Siemens, J. Ruiz de Elvira, E. Epelbaum, M. Hoferichter, H. Krebs, B. Kubis, U. G. Meißner, Reconciling threshold and subthreshold expansions for pion-nucleon scattering, *Phys. Lett. B* 770 (2017) 27. doi:10.1016/j.physletb.2017.04.039.
- [177] K. Hebel, H. Krebs, E. Epelbaum, J. Golak, R. Skibiński, Efficient calculation of chiral three-nucleon forces up to  $\text{N}^3\text{LO}$  for ab initio studies, *Phys. Rev. C* 91 (2015) 044001. doi:10.1103/PhysRevC.91.044001.
- [178] K. Hebel, J. D. Holt, J. Menéndez, A. Schwenk, Nuclear forces and their impact on neutron-rich nuclei and neutron-rich matter, *Annu. Rev. Nucl. Part. Sci.* 65 (2015) 457. doi:10.1146/annurev-nucl-102313-025446.
- [179] N. Kaiser, Chiral  $3\pi$ -exchange NN potentials: Results for representation invariant classes of diagrams, *Phys. Rev. C* 61 (2000) 014003. doi:10.1103/PhysRevC.61.014003.
- [180] N. Kaiser, Chiral  $3\pi$ -exchange NN potentials: Results for diagrams proportional to  $g_A^4$  and  $g_A^6$ , *Phys. Rev. C* 62 (2000)

024001. doi:10.1103/PhysRevC.62.024001.
- [181] N. Kaiser, Chiral  $2\pi$ -exchange NN potentials: Two-loop contributions, Phys. Rev. C 64 (2001) 057001. doi:10.1103/PhysRevC.64.057001.
- [182] N. Kaiser, Chiral  $2\pi$ -exchange NN potentials: Relativistic  $1/M^2$  corrections, Phys. Rev. C 65 (2001) 017001. doi:10.1103/PhysRevC.65.017001.
- [183] V. Bernard, E. Epelbaum, H. Krebs, U.-G. Meißner, Subleading contributions to the chiral three-nucleon force. I. Long-range terms, Phys. Rev. C 77 (2008) 064004. doi:10.1103/PhysRevC.77.064004.
- [184] V. Bernard, E. Epelbaum, H. Krebs, U.-G. Meißner, Subleading contributions to the chiral three-nucleon force II: Short-range terms and relativistic corrections, Phys. Rev. C 84 (2011) 054001. doi:10.1103/PhysRevC.84.054001.
- [185] S. Ishikawa, M. R. Robilotta, Two-pion exchange three-nucleon potential:  $O(q^4)$  chiral expansion, Phys. Rev. C 76 (2007) 014006. doi:10.1103/PhysRevC.76.014006.
- [186] E. Epelbaum, Four-nucleon force in chiral effective field theory, Phys. Lett. B 639 (2006) 456. doi:10.1016/j.physletb.2006.06.046.
- [187] J. Golak, R. Skibiński, K. Topolnicki, H. Witała, E. Epelbaum, H. Krebs, H. Kamada, U.-G. Meißner, V. Bernard, P. Maris, J. Vary, S. Binder, A. Calci, K. Hebeler, J. Langhammer, R. Roth, A. Nogga, S. Liebig, D. Minossi, Low-energy neutron-deuteron reactions with  $N^3$ LO chiral forces, Eur. Phys. J. A 50 (2014) 177. doi:10.1140/epja/i2014-14177-7.
- [188] D. R. Entem, R. Machleidt, Y. Nosyk, High-quality two-nucleon potentials up to fifth order of the chiral expansion, Phys. Rev. C 96 (2017) 024004. doi:10.1103/PhysRevC.96.024004.
- [189] E. Epelbaum, H. Krebs, U. G. Meißner, Precision nucleon-nucleon potential at fifth order in the chiral expansion, Phys. Lett. 115 (2015) 122301. doi:10.1103/PhysRevLett.115.122301.
- [190] L. Girlanda, A. Kievsky, M. Viviani, Subleading contributions to the three-nucleon contact interaction, Phys. Rev. C 84 (2011) 014001. doi:10.1103/PhysRevC.84.014001.
- [191] H. Krebs, A. Gasparyan, E. Epelbaum, Chiral three-nucleon force at  $N^4$ LO: Longest-range contributions, Phys. Rev. C 85 (2012) 054006. doi:10.1103/PhysRevC.85.054006.
- [192] H. Krebs, A. Gasparyan, E. Epelbaum, Chiral three-nucleon force at  $N^4$ LO: II. Intermediate-range contributions, Phys. Rev. C 87 (2013) 054007. doi:10.1103/PhysRevC.87.054007.
- [193] H. Krebs, E. Epelbaum, U.-G. Meißner, Nuclear forces with  $\Delta$ -excitations up to next-to-next-to-leading order. I. Peripheral nucleon-nucleon waves, Eur. Phys. J. A 32 (2007) 127. doi:10.1140/epja/i2007-10372-y.
- [194] C. Ordóñez, L. Ray, U. van Kolck, The Two nucleon potential from chiral Lagrangians, Phys. Rev. C 53 (1996) 2086. doi:10.1103/PhysRevC.53.2086.
- [195] N. Kaiser, S. Gerstendorfer, W. Weise, Peripheral NN scattering: Role of delta excitation, correlated two pion and vector meson exchange, Nucl. Phys. A 637 (1998) 395. doi:10.1016/S0375-9474(98)00234-6.
- [196] E. Epelbaum, H. Krebs, U.-G. Meißner,  $\Delta$ -excitations and the three-nucleon force, Nucl. Phys. A 806 (2008) 65. doi:https://doi.org/10.1016/j.nuclphysa.2008.02.305.
- [197] H. Krebs, A. M. Gasparyan, E. Epelbaum, Three-nucleon force in chiral EFT with explicit  $\Delta(1232)$  degrees of freedom: Longest-range contributions at fourth order, Phys. Rev. C 98 (2018) 014003. doi:10.1103/PhysRevC.98.014003.
- [198] E. Epelbaum, A. Nogga, W. Glöckle, H. Kamada, U. G. Meißner, H. Witała, Few nucleon systems with two nucleon forces from chiral effective field theory, Eur. Phys. J. A 15 (2002) 543. doi:10.1140/epja/i2002-10048-2.
- [199] D. R. Entem, R. Machleidt, Accurate charge-dependent nucleon-nucleon potential at fourth order of chiral perturbation theory, Phys. Rev. C 68 (2003) 041001(R). doi:10.1103/PhysRevC.68.041001.
- [200] T. Kortelainen, M. Lesinski, J. Moré, W. Nazarewicz, J. Sarich, N. Schunck, M. V. Stoitsov, S. Wild, Nuclear energy density optimization, Phys. Rev. C 82 (2010) 024313. doi:10.1103/PhysRevC.82.024313.
- [201] P. Navrátil, [http://theorie.ikp.physik.tu-darmstadt.de/ect13/Talks\\_files/navratil.pdf](http://theorie.ikp.physik.tu-darmstadt.de/ect13/Talks_files/navratil.pdf) (2013).
- [202] M. Piarulli, L. Girlanda, R. Schiavilla, R. Navarro Pérez, J. E. Amaro, E. Ruiz Arriola, Minimally nonlocal nucleon-nucleon potentials with chiral two-pion exchange including  $\Delta$  resonances, Phys. Rev. C 91 (2015) 024003. doi:10.1103/PhysRevC.91.024003.
- [203] M. Piarulli, L. Girlanda, R. Schiavilla, A. Kievsky, A. Lovato, L. E. Marcucci, S. C. Pieper, M. Viviani, R. B. Wiringa, Local chiral potentials with  $\Delta$ -intermediate states and the structure of light nuclei, Phys. Rev. C 94 (2016) 054007. doi:10.1103/PhysRevC.94.054007.
- [204] E. Epelbaum, H. Krebs, U.-G. Meißner, Improved chiral nucleon-nucleon potential up to next-to-next-to-next-to-leading order, Eur. Phys. J. A 51 (2015) 53. doi:10.1140/epja/i2015-15053-8.
- [205] P. Reinert, H. Krebs, E. Epelbaum, Semilocal momentum-space regularized chiral two-nucleon potentials up to fifth order, Eur. Phys. J. A 54 (2018) 86. doi:10.1140/epja/i2018-12516-4.
- [206] B. D. Carlsson, A. Ekström, C. Forssén, D. F. Strömberg, G. R. Jansen, O. Lilja, M. Lindby, B. A. Mattsson, K. A. Wendt, Uncertainty analysis and order-by-order optimization of chiral nuclear interactions, Phys. Rev. X 6 (2016) 011019. doi:10.1103/PhysRevX.6.011019.
- [207] I. Tews, Z. Davoudi, A. Ekström, J. D. Holt, J. E. Lynn, New Ideas in Constraining Nuclear Forces, J. Phys. G 47 (2020) 103001. doi:10.1088/1361-6471/ab9079.
- [208] J. A. Tjon, Bound states of  $^4\text{He}$  with local interactions, Phys. Lett. B 56 (1975) 217. doi:10.1016/0370-2693(75)90378-0.
- [209] L. Platter, H. Hammer, U.-G. Meißner, The Four boson system with short range interactions, Phys. Rev. A 70 (2004) 052101. doi:10.1103/PhysRevA.70.052101.
- [210] A. C. Phillips, Consistency of the low-energy three-nucleon observables and the separable interaction model, Nucl. Phys. A 107 (1968) 209. doi:10.1016/0375-9474(68)90737-9.
- [211] S. Shimizu, K. Sagara, H. Nakamura, K. Maeda, T. Miwa, N. Nishimori, S. Ueno, T. Nakashima, S. Morinobu, Analyzing powers of p-d scattering below the deuteron breakup threshold, Phys. Rev. C 52 (1995) 1193. doi:10.1103/PhysRevC.



52.1193.

- [212] H. Witała, W. Glöckle, J. Golak, H. Kamada, J. Kuros-Zolnierczuk, A. Nogga, R. Skibiński, Nd elastic scattering as a tool to probe properties of three nucleon forces, *Phys. Rev. C* 63 (2001) 024007. doi:10.1103/PhysRevC.63.024007.
- [213] A. Kievsky, M. Viviani, S. Rosati, Polarization observables in p-d scattering below 30 MeV, *Phys. Rev. C* 64 (2001) 024002. doi:10.1103/PhysRevC.64.024002.
- [214] B. S. Pudliner, V. R. Pandharipande, J. Carlson, R. B. Wiringa, Quantum Monte Carlo calculations of  $A \leq 6$  nuclei, *Phys. Rev. Lett.* 74 (1995) 4396. doi:10.1103/PhysRevLett.74.4396.
- [215] S. C. Pieper, V. R. Pandharipande, R. B. Wiringa, J. Carlson, Realistic models of pion exchange three nucleon interactions, *Phys. Rev. C* 64 (2001) 014001. doi:10.1103/PhysRevC.64.014001.
- [216] A. Lovato, O. Benhar, S. Fantoni, K. E. Schmidt, Comparative study of three-nucleon potentials in nuclear matter, *Phys. Rev. C* 85 (2012) 024003. doi:10.1103/PhysRevC.85.024003.
- [217] A. Gardestig, D. R. Phillips, How low-energy weak reactions can constrain three-nucleon forces and the neutron-neutron scattering length, *Phys. Rev. Lett.* 96 (2006) 232301. doi:10.1103/PhysRevLett.96.232301.
- [218] A. Baroni, L. Girlanda, A. Kievsky, L. E. Marcucci, R. Schiavilla, M. Viviani, Tritium  $\beta$ -decay in chiral effective field theory, *Phys. Rev. C* 94 (2016) 024003, [Erratum: *Phys. Rev. C* 95 (2017) 059902]. doi:10.1103/PhysRevC.94.024003.
- [219] P. Klos, A. Carbone, K. Hebeler, J. Menéndez, A. Schwenk, Uncertainties in constraining low-energy constants from  $^3\text{H}$   $\beta$  decay, *Eur. Phys. J. A* 53 (2017) 168, [Erratum: *Eur. Phys. J. A* 54 (2018) 76]. doi:10.1140/epja/i2017-12357-7.
- [220] R. Schiavilla, private communication (2017).
- [221] Yu. A. Akulov, B. A. Mamyryn, Half-life and  $fT_{1/2}$  value for the bare triton, *Phys. Lett. B* 610 (2005) 45. doi:10.1016/j.physletb.2005.01.094.
- [222] H. Krebs, E. Epelbaum, U.-G. Meißner, Nuclear axial current operators to fourth order in chiral effective field theory, *Ann. Phys.* 378 (2017) 317. doi:https://doi.org/10.1016/j.aop.2017.01.021.
- [223] R. B. Wiringa, V. G. J. Stoks, R. Schiavilla, Accurate nucleon-nucleon potential with charge independence breaking, *Phys. Rev. C* 51 (1995) 38. doi:10.1103/PhysRevC.51.38.
- [224] P. Navrátil, Local three-nucleon interaction from chiral effective field theory, *Few Body Syst.* 41 (2007) 117. doi:10.1007/s00601-007-0193-3.
- [225] A. Akmal, V. R. Pandharipande, D. G. Ravenhall, The Equation of state of nucleon matter and neutron star structure, *Phys. Rev. C* 58 (1998) 1804. doi:10.1103/PhysRevC.58.1804.
- [226] A. Lejeune, U. Lombardo, W. Zuo, Nuclear matter EOS with a three-body force, *Phys. Lett. B* 477 (2000) 45. doi:10.1016/S0370-2693(00)00211-2.
- [227] I. Angeli, K. Marinova, Table of experimental nuclear ground state charge radii: An update, *Atomic Data and Nuclear Data Tables* 99 (2013) 69. doi:10.1016/j.adt.2011.12.006.
- [228] J. Simonis, S. R. Stroberg, K. Hebeler, J. D. Holt, A. Schwenk, Saturation with chiral interactions and consequences for finite nuclei, *Phys. Rev. C* 96 (2017) 014303. doi:10.1103/PhysRevC.96.014303.
- [229] F. Coester, S. Cohen, B. Day, C. M. Vincent, Variation in nuclear-matter binding energies with phase-shift-equivalent two-body potentials, *Phys. Rev. C* 1 (1970) 769. doi:10.1103/PhysRevC.1.769.
- [230] D. Lee, private communication (2019).
- [231] D. Logoteta, Consistent nuclear matter calculations with local three-nucleon interactions, *Phys. Rev. C* 100 (2019) 045803. doi:10.1103/PhysRevC.100.045803.
- [232] G. Audi, A. H. Wapstra, C. Thibault, The Ame2003 atomic mass evaluation (II). Tables, graphs and references, *Nucl. Phys. A* 729 (2003) 337. doi:10.1016/j.nuclphysa.2003.11.003.
- [233] E. Epelbaum, W. Glöckle, U.-G. Meißner, Improving the convergence of the chiral expansion for nuclear forces II: Low phases and the deuteron, *Eur. Phys. J. A* 19 (2004) 401. doi:10.1140/epja/i2003-10129-8.
- [234] S. Michimasa, M. Kobayashi, Y. Kiyokawa, S. Ota, D. S. Ahn, H. Baba, G. P. A. Berg, M. Dozono, N. Fukuda, T. Furuno, E. Ideguchi, N. Inabe, T. Kawabata, S. Kawase, K. Kisamori, K. Kobayashi, T. Kubo, Y. Kubota, C. S. Lee, M. Matsushita, H. Miya, A. Mizukami, H. Nagakura, D. Nishimura, H. Oikawa, H. Sakai, Y. Shimizu, A. Stolz, H. Suzuki, M. Takaki, H. Takeda, S. Takeuchi, H. Tokieda, T. Uesaka, K. Yako, Y. Yamaguchi, Y. Yanagisawa, R. Yokoyama, K. Yoshida, S. Shimoura, Magic nature of neutrons in  $^{54}\text{Ca}$ : First mass measurements of  $^{55-57}\text{Ca}$ , *Phys. Rev. Lett.* 121 (2018) 022506. doi:10.1103/PhysRevLett.121.022506.
- [235] W. Jiang, A. Ekström, C. Forssén, G. Hagen, G. Jansen, T. Papenbrock, Accurate bulk properties of nuclei from  $A = 2$  to  $\infty$  from potentials with  $\Delta$  isobars, *Phys. Rev. C* 102 (2020) 054301. doi:10.1103/PhysRevC.102.054301.
- [236] V. G. J. Stoks, R. A. M. Klomp, M. C. M. Rentmeester, J. J. de Swart, Partial wave analysis of all nucleon-nucleon scattering data below 350 MeV, *Phys. Rev. C* 48 (1993) 792, Nijmegen NN online program, <http://nn-online.org/>. doi:10.1103/PhysRevC.48.792.
- [237] S. Wesolowski, R. J. Furnstahl, J. A. Melendez, D. R. Phillips, Exploring Bayesian parameter estimation for chiral effective field theory using nucleon–nucleon phase shifts, *J. Phys. G* 46 (2019) 045102. doi:10.1088/1361-6471/aaf5fc.
- [238] S. Wesolowski, N. Klco, R. J. Furnstahl, D. R. Phillips, A. Thapaliya, Bayesian parameter estimation for effective field theories, *J. Phys. G* 43 (2016) 074001. doi:10.1088/0954-3899/43/7/074001.
- [239] A. Ekström, C. Forssén, C. Dimitrakakis, D. Dubhashi, H. T. Johansson, A. S. Muhammad, H. Salomonsson, A. Schliep, Bayesian optimization in ab initio nuclear physics, *J. Phys. G* 46 (2019) 095101. doi:10.1088/1361-6471/ab2b14.
- [240] J. A. Melendez, S. Wesolowski, R. J. Furnstahl, Bayesian truncation errors in chiral effective field theory: nucleon-nucleon observables, *Phys. Rev. C* 96 (2017) 024003. doi:10.1103/PhysRevC.96.024003.
- [241] E. Epelbaum, J. Golak, K. Hebeler, H. Kamada, H. Krebs, U.-G. Meißner, A. Nogga, P. Reinert, R. Skibiński, K. Topolnicki, Y. Volkotrub, W. H., Towards high-order calculations of three-nucleon scattering in chiral effective field theory, *Eur. Phys. J. A* 56 (2020) 92. doi:10.1140/epja/s10050-020-00102-2.

- [242] R. J. Furnstahl, N. Klco, D. R. Phillips, S. Wesolowski, Quantifying truncation errors in effective field theory, *Phys. Rev. C* 92 (2015) 024005. doi:10.1103/PhysRevC.92.024005.
- [243] J. Hoppe, C. Drischler, K. Hebeler, A. Schwenk, J. Simonis, Probing chiral interactions up to next-to-next-to-next-to-leading order in medium-mass nuclei, *Phys. Rev. C* 100 (2019) 024318. doi:10.1103/PhysRevC.100.024318.
- [244] R. J. Furnstahl, D. R. Phillips, S. Wesolowski, A recipe for EFT uncertainty quantification in nuclear physics, *J. Phys. G* 42 (2015) 034028. doi:10.1088/0954-3899/42/3/034028.
- [245] J. A. Melendez, R. J. Furnstahl, D. R. Phillips, M. T. Pratola, S. Wesolowski, Quantifying Correlated Truncation Errors in Effective Field Theory, *Phys. Rev. C* 100 (4) (2019) 044001. doi:10.1103/PhysRevC.100.044001.
- [246] S. Binder, A. Calci, E. Epelbaum, R. J. Furnstahl, J. Golak, K. Hebeler, H. Kamada, H. Krebs, J. Langhammer, S. Liebig, P. Maris, U.-G. Meißner, D. Minossi, A. Nogga, H. Potter, R. Roth, R. Skibiński, K. Topolnicki, J. P. Vary, H. Witała, Few-nucleon systems with state-of-the-art chiral nucleon-nucleon forces, *Phys. Rev. C* 93 (2016) 044002. doi:10.1103/PhysRevC.93.044002.
- [247] S. König, S. K. Bogner, R. J. Furnstahl, S. N. More, T. Papenbrock, Ultraviolet extrapolations in finite oscillator bases, *Phys. Rev. C* 90 (2014) 064007. doi:10.1103/PhysRevC.90.064007.
- [248] R. J. Furnstahl, G. Hagen, T. Papenbrock, K. A. Wendt, Infrared extrapolations for atomic nuclei, *J. Phys. G: Nucl. Part. Phys.* 42 (2015) 034032. doi:10.1088/0954-3899/42/3/034032.
- [249] A. Messiah, *Quantum Mechanics*, Dover Publications, 1999.
- [250] J. Golak, D. Rozpedzik, R. Skibiński, K. Topolnicki, H. Witała, W. Glöckle, A. Nogga, E. Epelbaum, H. Kamada, C. Elster, I. Fachruddin, A new way to perform partial-wave decompositions of few-nucleon forces, *Eur. Phys. J. A* 43 (2010) 241. doi:10.1140/epja/i2009-10903-6.
- [251] R. Skibiński, J. Golak, K. Topolnicki, H. Witała, H. Kamada, W. Glöckle, A. Nogga, The Tucson-Melbourne Three-Nucleon Force in the automatized Partial-Wave Decomposition, *Eur. Phys. J. A* 47 (2011) 48. doi:10.1140/epja/i2011-11048-9.
- [252] R. Skibiński, J. Golak, K. Topolnicki, H. Witała, E. Epelbaum, W. Glöckle, H. Krebs, A. Nogga, H. Kamada, Triton with long-range chiral  $N^3LO$  three-nucleon forces, *Phys. Rev. C* 84 (2011) 054005. doi:10.1103/PhysRevC.84.054005.
- [253] R. Skibiński, J. Golak, K. Topolnicki, H. Witała, E. Epelbaum, W. Glöckle, H. Krebs, H. Kamada, A. Nogga,  $^3H$  at Next-to-Next-to-Next-to Leading Order of the Chiral Expansion, *Few Body Syst.* 54 (2013) 1315. doi:10.1007/s00601-013-0604-6.
- [254] H. Witała, J. Golak, R. Skibiński, K. Topolnicki, Calculations of three-nucleon reactions with  $N^3LO$  chiral forces: achievements and challenges, *J. Phys. G* 41 (2014) 094011. doi:10.1088/0954-3899/41/9/094011.
- [255] W. Glöckle, G. Hasberg, A. R. Neghabian, Numerical treatment of few body equations in momentum space by the Spline method, *Z. Phys. A* 305 (1982) 217. doi:10.1007/BF01417437.
- [256] <http://www.netlib.org/blas/>.
- [257] E. Epelbaum, W. Glöckle, U.-G. Meißner, Nuclear forces from chiral Lagrangians using the method of unitary transformation. 2. The two nucleon system, *Nucl. Phys. A* 671 (2000) 295. doi:10.1016/S0375-9474(99)00821-0.
- [258] L. Huth, I. Tews, J. E. Lynn, A. Schwenk, Analyzing the fierz rearrangement freedom for local chiral two-nucleon potentials, *Phys. Rev. C* 96 (2017) 054003. doi:10.1103/PhysRevC.96.054003.
- [259] A. M. Gasparyan, M. F. M. Lutz, E. Epelbaum, Two-nucleon scattering: Merging chiral effective field theory with dispersion relations, *Eur. Phys. J. A* 49 (2013) 115. doi:10.1140/epja/i2013-13115-7.
- [260] J. A. Oller, Nucleon-Nucleon scattering from dispersion relations: next-to-next-to-leading order study, *Phys. Rev. C* 93 (2016) 024002. doi:10.1103/PhysRevC.93.024002.
- [261] E. Epelbaum, H. Krebs, P. Reinert, High-precision nuclear forces from chiral EFT: State-of-the-art, challenges and outlook, *Front. in Phys.* 8 (2020) 98. doi:10.3389/fphy.2020.00098.
- [262] J. E. Lynn, J. Carlson, E. Epelbaum, S. Gandolfi, A. Gezerlis, A. Schwenk, Quantum Monte Carlo Calculations of Light Nuclei Using Chiral Potentials, *Phys. Rev. Lett.* 113 (2014) 192501. doi:10.1103/PhysRevLett.113.192501.
- [263] I. Tews, Quantum Monte Carlo calculations with chiral effective field theory interactions, Doctoral thesis, Technische Universität Darmstadt (2015), <https://tuprints.ulb.tu-darmstadt.de/5011/>.
- [264] J. Hoppe, C. Drischler, R. J. Furnstahl, K. Hebeler, A. Schwenk, Weinberg eigenvalues for chiral nucleon-nucleon interactions, *Phys. Rev. C* 96 (2017) 054002. doi:10.1103/PhysRevC.96.054002.
- [265] T. Krüger, I. Tews, K. Hebeler, A. Schwenk, Neutron matter from chiral effective field theory interactions, *Phys. Rev. C* 88 (2013) 025802. doi:10.1103/PhysRevC.88.025802.
- [266] B. D. Carlsson, Quantifying statistical uncertainties in ab initio nuclear physics using lagrange multipliers, *Phys. Rev. C* 95 (2017) 034002. doi:10.1103/PhysRevC.95.034002.
- [267] K. Hebeler, R. J. Furnstahl, Neutron matter based on consistently evolved chiral three-nucleon interactions, *Phys. Rev. C* 87 (2013) 031302. doi:10.1103/PhysRevC.87.031302.
- [268] J. Langhammer, P. Navrátil, S. Quaglioni, G. Hupin, A. Calci, R. Roth, Continuum and three-nucleon force effects on  $^9Be$  energy levels, *Phys. Rev. C* 91 (2015) 021301. doi:10.1103/PhysRevC.91.021301.
- [269] A. Tichai, J. Müller, K. Vobig, R. Roth, Natural orbitals for ab initio no-core shell model calculations, *Phys. Rev. C* 99 (2019) 034321. doi:10.1103/PhysRevC.99.034321.
- [270] S. D. Glazek, K. G. Wilson, Renormalization of Hamiltonians, *Phys. Rev. D* 48 (1993) 5863. doi:10.1103/PhysRevD.48.5863.
- [271] F. Wegner, Flow-equations for Hamiltonians, *Ann. Phys.* 506 (1994) 77. doi:10.1002/andp.19945060203.
- [272] E. R. Anderson, S. K. Bogner, R. J. Furnstahl, R. J. Perry, Operator Evolution via the Similarity Renormalization Group I: The Deuteron, *Phys. Rev. C* 82 (2010) 054001. doi:10.1103/PhysRevC.82.054001.
- [273] M. D. Schuster, S. Quaglioni, C. W. Johnson, E. D. Jurgenson, P. Navrátil, Operator evolution for ab initio theory of

- light nuclei, Phys. Rev. C 90 (2014) 011301(R). doi:10.1103/PhysRevC.90.011301.
- [274] S. N. More, S. König, R. J. Furnstahl, K. Hebeler, Deuteron electrodisintegration with unitarily evolved potentials, Phys. Rev. C 92 (2015) 064002. doi:10.1103/PhysRevC.92.064002.
- [275] S. N. More, S. K. Bogner, R. J. Furnstahl, Scale dependence of deuteron electrodisintegration, Phys. Rev. C 96 (2017) 054004. doi:10.1103/PhysRevC.96.054004.
- [276] R. J. Furnstahl, K. Hebeler, New applications of renormalization group methods in nuclear physics, Rep. Prog. Phys. 76 (2013) 126301. doi:10.1088/0034-4885/76/12/126301.
- [277] E. Anderson, S. K. Bogner, R. J. Furnstahl, E. D. Jurgenson, R. J. Perry, A. Schwenk, Block Diagonalization using SRG Flow Equations, Phys. Rev. C 77 (2008) 037001. doi:10.1103/PhysRevC.77.037001.
- [278] W. Li, E. R. Anderson, R. J. Furnstahl, Similarity Renormalization Group with Novel Generators, Phys. Rev. C 84 (2011) 054002. doi:10.1103/PhysRevC.84.054002.
- [279] N. M. Dicaire, C. Omand, P. Navrátil, Alternative similarity renormalization group generators in nuclear structure calculations, Phys. Rev. C 90 (2014) 034302. doi:10.1103/PhysRevC.90.034302.
- [280] E. D. Jurgenson, P. Navrátil, R. J. Furnstahl, Evolution of Nuclear Many-Body Forces with the Similarity Renormalization Group, Phys. Rev. Lett. 103 (2009) 082501. doi:10.1103/PhysRevLett.103.082501.
- [281] E. D. Jurgenson, Applications of the similarity renormalization group to the nuclear interaction, Ph.D. thesis, The Ohio State University (2009), <https://ui.adsabs.harvard.edu/abs/2009PhDT.....51J>.
- [282] E. D. Jurgenson, P. Navrátil, R. J. Furnstahl, Evolving Nuclear Many-Body Forces with the Similarity Renormalization Group, Phys. Rev. C 83 (2011) 034301. doi:10.1103/PhysRevC.83.034301.
- [283] K. A. Wendt, Similarity Renormalization Group Evolution of Three-Nucleon Forces in a Hyperspherical Momentum Representation, Phys. Rev. C 87 (2013) 061001(R). doi:10.1103/PhysRevC.87.061001.
- [284] O. Åkerlund, E. J. Lindgren, J. Bergsten, B. Grevholm, P. Lerner, R. Linscott, C. Forssén, L. Platter, The Similarity Renormalization Group for Three-Body Interactions in One Dimension, Eur. Phys. J. A 47 (2011) 122. doi:10.1140/epja/i2011-11122-4.
- [285] K. Hebeler, Momentum-space evolution of chiral three-nucleon forces, Phys. Rev. C 85 (2012) 021002(R). doi:10.1103/PhysRevC.85.021002.
- [286] A. L. Fetter, J. D. Walecka, Quantum Theory of Many-Particle Systems, McGraw-Hill, New York, 1971.
- [287] S. Schulz, SRG-Induced Four-Body Forces in Ab Initio Nuclear Structure, Master's thesis, Technische Universität Darmstadt (2013).
- [288] G. C. Wick, The Evaluation of the Collision Matrix, Phys. Rev. 80 (1950) 268. doi:10.1103/PhysRev.80.268.
- [289] L. Ballentine, Quantum Mechanics: A Modern Development, World Scientific, 1998.
- [290] J. Ripoché, A. Tichai, T. Duguet, Normal-ordered  $k$ -body approximation in particle-number-breaking theories, Eur. Phys. J. A 56 (2020) 40. doi:10.1140/epja/s10050-020-00045-8.
- [291] R. Roth, S. Binder, K. Vobig, A. Calci, J. Langhammer, P. Navrátil, Ab Initio Calculations of Medium-Mass Nuclei with Normal-Ordered Chiral NN+3N Interactions, Phys. Rev. Lett. 109 (2012) 052501. doi:10.1103/PhysRevLett.109.052501.
- [292] T. Krüger, K. Hebeler, A. Schwenk, To which densities is spin-polarized neutron matter a weakly interacting Fermi gas?, Phys. Lett. B 744 (2015) 18. doi:10.1016/j.physletb.2015.03.027.
- [293] A. Lovato, O. Benhar, S. Fantoni, A. Yu. Illarionov, K. E. Schmidt, Density-dependent nucleon-nucleon interaction from three-nucleon forces, Phys. Rev. C 83 (2011) 054003. doi:10.1103/PhysRevC.83.054003.
- [294] J. W. Holt, N. Kaiser, W. Weise, Density-dependent effective nucleon-nucleon interaction from chiral three-nucleon forces, Phys. Rev. C 81 (2010) 024002. doi:10.1103/PhysRevC.81.024002.
- [295] N. Kaiser, V. Niessner, Density-dependent NN-interaction from subleading chiral 3N-forces: short-range terms and relativistic corrections, Phys. Rev. C 98 (2018) 054002. doi:10.1103/PhysRevC.98.054002.
- [296] N. Kaiser, B. Singh, Density-dependent NN-interaction from subleading chiral 3N-forces: Long-range terms, Phys. Rev. C 100 (2019) 014002. doi:10.1103/PhysRevC.100.014002.
- [297] N. Kaiser, Density-dependent NN interaction from subsubleading chiral 3N forces: Intermediate-range contributions, Phys. Rev. C 101 (2020) 014001. doi:10.1103/PhysRevC.101.014001.
- [298] M. Hoferichter, J. Ruiz de Elvira, B. Kubis, U.-G. Meißner, High-Precision Determination of the Pion-Nucleon  $\sigma$  Term from Roy-Steiner Equations, Phys. Rev. Lett. 115 (2015) 192301. doi:10.1103/PhysRevLett.115.092301.
- [299] J. W. Holt, M. Kawaguchi, N. Kaiser, Implementing chiral three-body forces in terms of medium-dependent two-body forces, Front. in Phys. 8 (2020) 100. doi:10.3389/fphy.2020.00100.
- [300] G. P. Kamuntavičius, R. K. Kalinauskas, B. R. Barrett, S. Mickevičius, D. Germanas, The general harmonic-oscillator brackets: compact expression, symmetries, sums and Fortran code, Nucl. Phys. A 695 (2001) 191. doi:10.1016/S0375-9474(01)01101-0.
- [301] V. Durant, Chiral interactions for nuclear reactions and heavy nuclei, Technische Universität Darmstadt (2019), <https://tuprints.ulb-tu-darmstadt.de/8519/>.
- [302] V. Durant, K. Hebeler, J. Hoppe, A. Schwenk, A. Tichai, in preparation (2020).
- [303] N. Kaiser, Third-order particle-hole ring diagrams with contact-interactions and one-pion exchange, Eur. Phys. J. A 53 (2017) 104. doi:10.1140/epja/i2017-12290-9.
- [304] G. P. Lepage, A new algorithm for adaptive multidimensional integration, J. Comput. Phys. 27 (1978) 192. doi:http://dx.doi.org/10.1016/0021-9991(78)90004-9.
- [305] T. Hahn, Cuba—a library for multidimensional numerical integration, Comput. Phys. Commun. 168 (2005) 78. doi:http://doi.org/10.1016/j.cpc.2005.01.010.
- [306] T. Hahn, Concurrent cuba, Comput. Phys. Commun. 207 (2016) 341. doi:http://doi.org/10.1016/j.cpc.2016.05.012.



- [307] N. J. A. Sloane, The encyclopedia of integer sequences: Number of labeled hugenoltz diagrams with  $n$  nodes, <https://oeis.org/A064732>.
- [308] P. D. Stevenson, Automatic generation of vacuum amplitude many-body perturbation series, *Int. J. Mod. Phys. C* 14 (2003) 1135. doi:10.1142/S0129183103005236.
- [309] I. Shavitt, R. J. Bartlett, Many-Body Methods in Chemistry and Physics: MBPT and Coupled-Cluster Theory, Cambridge Molecular Science, Cambridge University Press, 2009. doi:10.1017/CB09780511596834.
- [310] P. Arthuis, T. Duguet, A. Tichai, R. D. Lasserri, J. P. Ebran, ADG: Automated generation and evaluation of many-body diagrams I. Bogoliubov many-body perturbation theory, *Comput. Phys. Commun.* 240 (2019) 202. doi:10.1016/j.cpc.2018.11.023.
- [311] G. Hagen, G. R. Jansen, T. Papenbrock, Structure of  $^{78}\text{Ni}$  from first-principles computations, *Phys. Rev. Lett.* 117 (2016) 172501. doi:10.1103/PhysRevLett.117.172501.
- [312] I. Sick, Precise root-mean-square radius of  $^4\text{He}$ , *Phys. Rev. C* 77 (2008) 041302(R). doi:10.1103/PhysRevC.77.041302.
- [313] H. Witaa, W. Glöckle, T. Cornelius, Nucleon-induced deuteron breakup: Analysis of 14.1 MeV data by rigorous Faddeev calculations with meson-exchange NN interactions, *Phys. Rev. C* 39 (1989) 384. doi:10.1103/PhysRevC.39.384.
- [314] J. D. Holt, S. R. Stroberg, A. Schwenk, J. Simonis, Ab initio limits of atomic nuclei. arXiv:1905.10475.
- [315] M. R. Mumpower, R. Surman, G. C. McLaughlin, A. Aprahamian, The impact of individual nuclear properties on  $r$ -process nucleosynthesis, *Prog. Part. Nucl. Phys.* 86 (2016) 86, [Erratum: *Prog. Part. Nucl. Phys.* 87 (2016) 116]. doi:10.1016/j.ppnp.2015.09.001.
- [316] B. P. Abbott, et al., GW170817: Observation of gravitational waves from a binary neutron star inspiral, *Phys. Rev. Lett.* 119 (2017) 161101. doi:10.1103/PhysRevLett.119.161101.
- [317] C. Hinke, M. Böhmer, P. Boutachkov, T. Faestermann, H. Geissel, J. Gerl, R. Gernhäuser, M. Gorska, A. Gottardo, H. Grawe, J. L. Grebosz, R. Krücken, N. Kurz, Z. Liu, L. Maier, F. Nowacki, S. Piétri, Z. Podolyak, K. Sieja, K. Steiger, K. Straub, H. Weick, P. J. Woods, N. Al-Dahan, N. Alkhamashi, A. Ataç, A. Blazhev, N. F. Braun, I. Celikovic, T. Davinson, I. Dillmann, C. Domingo-Pardo, P. C. Doornenbal, G. De France, G. F. Farrelly, F. Farinon, N. Goel, T. Habermann, R. Hoischen, R. Janik, M. Karny, A. Kaskas, I. Kojouharov, T. Kröll, Y. Litvinov, S. Myalski, F. Nebel, S. Nishimura, C. Nociforo, J. Nyberg, A. R. Parikh, A. Prochazka, P. H. Regan, C. Rigollet, H. Schaffner, C. Scheidenberger, S. Schwertel, P.-A. Söderström, S. Steer, A. Stolz, P. Strmen, Superallowed Gamow-Teller decay of the doubly magic nucleus  $^{100}\text{Sn}$ , *Nature* 486 (2012) 341. doi:10.1038/nature11116.
- [318] T. Faestermann, M. Gorska, H. Grawe, The structure of  $^{100}\text{Sn}$  and neighbouring nuclei, *Prog. Part. Nucl. Phys.* 69 (2013) 85. doi:10.1016/j.ppnp.2012.10.002.
- [319] V. Somà, P. Navrátil, F. Raimondi, C. Barbieri, T. Duguet, Novel chiral hamiltonian and observables in light and medium-mass nuclei, *Phys. Rev. C* 101 (2020) 014318. doi:10.1103/PhysRevC.101.014318.
- [320] V. Lapoux, V. Somà, C. Barbieri, H. Hergert, J. D. Holt, S. Stroberg, Radii and Binding Energies in Oxygen Isotopes: A Challenge for Nuclear Forces, *Phys. Rev. Lett.* 117 (2016) 052501. doi:10.1103/PhysRevLett.117.052501.
- [321] B. Maaß, T. Hüther, K. König, J. Krämer, J. Krause, A. Lovato, P. Müller, K. Pachucki, M. Puchalski, R. Roth, R. Sánchez, F. Sommer, R. B. Wiringa, W. Nörtershäuser, Nuclear Charge Radii of  $^{10,11}\text{B}$ , *Phys. Rev. Lett.* 122 (2019) 182501. doi:10.1103/PhysRevLett.122.182501.
- [322] M. Kortelainen, J. McDonnell, W. Nazarewicz, E. Olsen, P.-G. Reinhard, J. Sarich, N. Schunck, S. M. Wild, D. Davesne, J. Erler, A. Pastore, Nuclear energy density optimization: Shell structure, *Phys. Rev. C* 89 (2014) 054314. doi:10.1103/PhysRevC.89.054314.
- [323] T. Hüther, K. Vobig, K. Hebeler, R. Machleidt, R. Roth, Family of Chiral Two- plus Three-Nucleon Interactions for Accurate Nuclear Structure Studies, *Phys. Lett. B* 808 (2020) 135651. doi:10.1016/j.physletb.2020.135651.
- [324] <http://www.nndc.bnl.gov/ensdf/>.
- [325] F. Hoyle, On Nuclear Reactions Occuring in Very Hot Stars. 1. The Synthesis of Elements from Carbon to Nickel, *Astrophys. J. Suppl.* 1 (1954) 121. doi:10.1086/190005.
- [326] L. Cáceres, A. Lepailleur, O. Sorlin, M. Stanoiu, D. Sohler, Z. Dombrádi, S. K. Bogner, B. A. Brown, H. Hergert, J. D. Holt, A. Schwenk, F. Azaiez, B. Bastin, C. Borcea, R. Borcea, C. Bourgeois, Z. Elekes, Z. Fülöp, S. Grévy, L. Gaudefroy, G. F. Grinyer, D. Guillemaud-Mueller, F. Ibrahim, A. Kerek, A. Krasznahorkay, M. Lewitowicz, S. M. Lukyanov, J. Mrázek, F. Negoita, F. de Oliveira, Y.-E. Penionzhkevich, Z. Podolyák, M. G. Porquet, F. Rotaru, P. Roussel-Chomaz, M. G. Saint-Laurent, H. Savajols, G. Sletten, J. C. Thomas, J. Timar, C. Timis, Z. Vajta, Nuclear structure studies of  $^{24}\text{F}$ , *Phys. Rev. C* 92 (2015) 014327. doi:10.1103/PhysRevC.92.014327.
- [327] B. Ishkhanov, I. Kapitonov, E. Lileeva, E. Shirokov, V. Erokhova, M. Elkin, A. Izotova, Cross sections of photon absorption by nuclei with nucleon numbers 12 - 65, Tech. Rep. MSU-INP-2002-27/711 (Institute of Nuclear Physics, Moscow State University, 2002).
- [328] J. Ahrens, H. Borchert, K. Czock, H. Eppler, H. Gimm, H. Gundrum, M. Kröning, P. Riehn, G. S. Ram, A. Zieger, B. Ziegler, Total Nuclear Photon Absorption Cross-Sections for Some Light Elements, *Nucl. Phys. A* 251 (1975) 479. doi:10.1016/0375-9474(75)90543-6.
- [329] M. Miorelli, S. Bacca, N. Barnea, G. Hagen, G. R. Jansen, G. Orlandini, T. Papenbrock, Electric dipole polarizability from first principles calculations, *Phys. Rev. C* 94 (2016) 034317. doi:10.1103/PhysRevC.94.034317.
- [330] J. Erler, N. Birge, M. Kortelainen, W. Nazarewicz, E. Olsen, A. M. Perhac, M. Stoitsov, The limits of the nuclear landscape, *Nature* 486 (2012) 509. doi:10.1038/nature11188.
- [331] D. Steppenbeck, S. Takeuchi, N. Aoi, P. Doornenbal, M. Matsushita, H. Wang, H. Baba, N. Fukuda, S. Go, M. Honma, J. Lee, K. Matsui, S. Michimasa, T. Motobayashi, D. Nishimura, T. Otsuka, H. Sakurai, Y. Shiga, P.-A. Söderström, T. Sumikama, H. Suzuki, R. Taniuchi, Y. Utsuno, J. J. Valiente-Dobón, K. Yoneda, Evidence for a new nuclear 'magic number' from the level structure of  $^{34}\text{Ca}$ , *Nature* 502 (2013) 207. doi:10.1038/nature12522.

- [332] B. A. Brown, Neutron radii in nuclei and the neutron equation of state, *Phys. Rev. Lett.* 85 (2000) 5296. doi:10.1103/PhysRevLett.85.5296.
- [333] J. Zenihiro, H. Sakaguchi, T. Murakami, M. Yosoi, Y. Yasuda, S. Terashima, Y. Iwao, H. Takeda, M. Itoh, H. P. Yoshida, M. Uchida, Neutron density distributions of  $^{204,206,208}\text{Pb}$  deduced via proton elastic scattering at  $E_p = 295$  MeV, *Phys. Rev. C* 82 (2010) 044611. doi:10.1103/PhysRevC.82.044611.
- [334] C. M. Tarbert, D. P. Watts, D. I. Glazier, P. Aguar, J. Ahrens, J. R. M. Annand, H. J. Arends, R. Beck, V. Bekrenev, B. Boillat, A. Braghieri, D. Branford, W. J. Briscoe, J. Brudvik, S. Cherepnaya, R. Codling, E. J. Downie, K. Foehl, P. Grabmayr, R. Gregor, E. Heid, D. Hornidge, O. Jahn, V. L. Kashevarov, A. Knezevic, R. Kondratiev, M. Korolija, M. Kotulla, D. Krambrich, B. Krusche, M. Lang, V. Lisin, K. Livingston, S. Lugert, I. J. D. MacGregor, D. M. Manley, M. Martinez, J. C. McGeorge, D. Mekterovic, V. Metag, B. M. K. Nefkens, A. Nikolaev, R. Novotny, R. O. Owens, P. Pedroni, A. Polonski, S. N. Prakhov, J. W. Price, G. Rosner, M. Rost, T. Rostomyan, S. Schadmand, S. Schumann, D. Sober, A. Starostin, I. Supek, A. Thomas, M. Unverzagt, T. Walcher, L. Zana, F. Zehr, Neutron skin of  $^{208}\text{Pb}$  from Coherent Pion Photoproduction, *Phys. Rev. Lett.* 112 (2014) 242502. doi:10.1103/PhysRevLett.112.242502.
- [335] S. Abrahamyan, Z. Ahmed, H. Albataineh, K. Aniol, D. S. Armstrong, W. Armstrong, T. Averett, B. Babineau, A. Barbieri, V. Bellini, R. Beminiwattha, J. Benesch, F. Benmokhtar, T. Bielarski, W. Boeglin, A. Camsonne, M. Canan, P. Carter, G. D. Cates, C. Chen, J.-P. Chen, O. Hen, F. Cusanno, M. M. Dalton, R. De Leo, K. de Jager, W. Decoinck, P. Decowski, X. Deng, A. Deur, D. Dutta, A. Etile, D. Flay, G. B. Franklin, M. Friend, S. Frullani, E. Fuchey, F. Garibaldi, E. Gasser, R. Gilman, A. Giusa, A. Glamazdin, J. Gomez, J. Grames, C. Gu, O. Hansen, J. Hansknecht, D. W. Higinbotham, R. S. Holmes, T. Holmstrom, C. J. Horowitz, J. Hoskins, J. Huang, C. E. Hyde, F. Itard, C.-M. Jen, E. Jensen, G. Jin, S. Johnston, A. Kelleher, K. Kliakhandler, P. M. King, S. Kowalski, K. S. Kumar, J. Leacock, J. Leckey, J. H. Lee, J. J. LeRose, R. Lindgren, N. Liyanage, N. Lubinsky, J. Mammei, F. Mammoliti, D. J. Margaziotis, P. Markowitz, A. McCreary, D. McNulty, L. Mercado, Z.-E. Meziani, R. W. Michaels, M. Mihovilovic, N. Muangma, C. Muñoz Camacho, S. Nanda, V. Nelyubin, N. Nuruzzaman, Y. Oh, A. Palmer, D. Parno, K. D. Paschke, S. K. Phillips, B. Poelker, R. Pomatsalyuk, M. Posik, A. J. R. Puckett, B. Quinn, A. Rakhman, P. E. Reimer, S. Riordan, P. Rogan, G. Ron, G. Russo, K. Saenboonruang, A. Saha, B. Sawatzky, A. Shahinyan, R. Silwal, S. Sirca, K. Slifer, P. Solvignon, P. A. Souder, M. L. Sperduto, R. Subedi, R. Suleiman, V. Sulkosky, C. M. Sutura, W. A. Tobias, W. Troth, G. M. Urciuoli, B. Waidyawansa, D. Wang, J. Wexler, R. Wilson, B. Wojtsekhowski, X. Yan, H. Yao, Y. Ye, Z. Ye, V. Yim, L. Zana, X. Zhan, J. Zhang, Y. Zhang, X. Zheng, P. Zhu, Measurement of the Neutron Radius of  $^{208}\text{Pb}$  Through Parity-Violation in Electron Scattering, *Phys. Rev. Lett.* 108 (2012) 112502. doi:10.1103/PhysRevLett.108.112502.
- [336] C. J. Horowitz, K. S. Kumar, R. Michaels, Electroweak Measurements of Neutron Densities in CREX and PREX at JLab, USA, *Eur. Phys. J. A* 50 (2014) 48. doi:10.1140/epja/i2014-14048-3.
- [337] J. Piekarewicz, B. K. Agrawal, G. Colo, W. Nazarewicz, N. Paar, P. G. Reinhard, X. Roca-Maza, D. Vretenar, Electric dipole polarizability and the neutron skin, *Phys. Rev. C* 85 (2012) 041302(R). doi:10.1103/PhysRevC.85.041302.
- [338] J. Simonis, S. Bacca, G. Hagen, First principles electromagnetic responses in medium-mass nuclei, *Eur. Phys. J. A* 55 (2019) 241. doi:10.1140/epja/i2019-12825-0.
- [339] A. Tamii, I. Poltoratska, P. von Neumann-Cosel, Y. Fujita, T. Adachi, C. A. Bertulani, J. Carter, M. Dozono, H. Fujita, K. Fujita, K. Hatanaka, D. Ishikawa, M. Itoh, T. Kawabata, Y. Kalmykov, A. M. Krumbholz, E. Litvinova, H. Matusubara, K. Nakanishi, R. Neveling, H. Okamura, H. J. Ong, B. Özel-Tashenov, V. Y. Ponomarev, A. Richter, B. Rubio, H. Sakaguchi, Y. Sakemi, Y. Sasamoto, Y. Shimbara, Y. Shimizu, F. D. Smit, T. Suzuki, Y. Tameshige, J. Wambach, R. Yamada, M. Yosoi, J. Zenihiro, Complete electric dipole response and the neutron skin in  $^{208}\text{Pb}$ , *Phys. Rev. Lett.* 107 (2011) 062502. doi:10.1103/PhysRevLett.107.062502.
- [340] T. Hashimoto, A. M. Krumbholz, P.-G. Reinhard, A. Tamii, P. von Neumann-Cosel, T. Adachi, N. Aoi, C. A. Bertulani, H. Fujita, Y. Fujita, E. Ganioglu, K. Hatanaka, E. Ideguchi, C. Iwamoto, T. Kawabata, N. T. Khai, A. Krugmann, D. Martin, H. Matusubara, K. Miki, R. Neveling, H. Okamura, H. J. Ong, I. Poltoratska, V. Y. Ponomarev, A. Richter, H. Sakaguchi, Y. Shimbara, Y. Shimizu, J. Simonis, F. D. Smit, G. Süsoy, T. Suzuki, J. H. Thies, M. Yosoi, J. Zenihiro, Dipole polarizability of  $^{120}\text{Sn}$  and nuclear energy density functionals, *Phys. Rev. C* 92 (2015) 031305(R). doi:10.1103/PhysRevC.92.031305.
- [341] D. M. Rossi, P. Adrich, F. Aksouh, H. Alvarez-Pol, T. Aumann, J. Benlliure, M. Böhmer, K. Boretzky, E. Casarejos, M. Chartier, A. Chatillon, D. Cortina-Gil, U. Datta Pramanik, H. Emling, O. Ershova, B. Fernandez-Dominguez, H. Geissel, M. Gorska, M. Heil, H. T. Johansson, A. Junghans, A. Kelic-Heil, O. Kiselev, A. Klimkiewicz, J. V. Kratz, R. Krücken, N. Kurz, M. Labiche, T. Le Bleis, R. Lemmon, Y. A. Litvinov, K. Mahata, P. Maierbeck, A. Movsesyan, T. Nilsson, C. Nociforo, R. Palit, S. Paschalis, R. Plag, R. Reifarh, D. Savran, H. Scheit, H. Simon, K. Sümmerer, A. Wagner, W. Waluś, H. Weick, M. Winkler, Measurement of the Dipole Polarizability of the Unstable Neutron-Rich Nucleus  $^{68}\text{Ni}$ , *Phys. Rev. Lett.* 111 (2013) 242503. doi:10.1103/PhysRevLett.111.242503.
- [342] V. D. Efros, W. Leidemann, G. Orlandini, Response functions from integral transforms with a Lorentz kernel, *Phys. Lett. B* 338 (1994) 130. doi:10.1016/0370-2693(94)91355-2.
- [343] V. D. Efros, W. Leidemann, G. Orlandini, N. Barnea, The Lorentz Integral Transform (LIT) method and its applications to perturbation induced reactions, *J. Phys. G* 34 (2007) R459-2456. doi:10.1088/0954-3899/34/12/R02.
- [344] R. Schiavilla, V. G. J. Stoks, W. Glöckle, H. Kamada, A. Nogga, J. Carlson, R. Machleidt, V. R. Pandharipande, R. B. Wiringa, A. Kievsky, S. Rosati, M. Viviani, Weak capture of protons by protons, *Phys. Rev. C* 58 (1998) 1263. doi:10.1103/PhysRevC.58.1263.
- [345] S. Raman, C. A. Houser, T. A. Walkiewicz, Mixed Fermi and Gamow-Teller  $\beta$ -Transitions and Isoscalar Magnetic Moments, Atomic Data and Nuclear Data Tables 21 (1978) 567. doi:10.1016/0092-640X(78)90008-6.
- [346] T. S. Park, L. E. Marcucci, R. Schiavilla, M. Viviani, A. Kievsky, S. Rosati, K. Kubodera, D. P. Min, M. Rho, Parameter free effective field theory calculation for the solar proton fusion and hep processes, *Phys. Rev. C* 67 (2003) 055206.

- [doi:10.1103/PhysRevC.67.055206](https://doi.org/10.1103/PhysRevC.67.055206).
- [347] M. Hoferichter, P. Klos, A. Schwenk, Chiral power counting of one- and two-body currents in direct detection of dark matter, *Phys. Lett. B* 746 (2015) 410. [doi:10.1016/j.physletb.2015.05.041](https://doi.org/10.1016/j.physletb.2015.05.041).
- [348] A. Baroni, L. Girlanda, S. Pastore, R. Schiavilla, M. Viviani, Nuclear Axial Currents in Chiral Effective Field Theory, *Phys. Rev. C* 93 (2016) 015501. [doi:10.1103/PhysRevC.93.049902](https://doi.org/10.1103/PhysRevC.93.049902), [doi:10.1103/PhysRevC.93.015501](https://doi.org/10.1103/PhysRevC.93.015501).
- [349] S. Raman, C. W. G. Nestor, Jr, P. Tikkanen, Transition probability from the ground to the first-excited  $2^+$  state of even-even nuclides, *Atom. Data Nucl. Data Tabl.* 78 (2001) 1. [doi:10.1006/adnd.2001.0858](https://doi.org/10.1006/adnd.2001.0858).
- [350] B. Pritychenko, M. Birch, B. Singh, M. Horoi, Tables of E2 Transition Probabilities from the first  $2^+$  States in Even-Even Nuclei, *Atom. Data Nucl. Data Tabl.* 107 (2016) 1. [doi:10.1016/j.adt.2015.10.001](https://doi.org/10.1016/j.adt.2015.10.001).
- [351] P. Maris, J. P. Vary, P. Navrátil, W. E. Ormand, H. Nam, D. J. Dean, Origin of the anomalous long lifetime of  $^{14}\text{C}$ , *Phys. Rev. Lett.* 106 (2011) 202502. [doi:10.1103/PhysRevLett.106.202502](https://doi.org/10.1103/PhysRevLett.106.202502).
- [352] J. M. Yao, B. Bally, J. Engel, R. Wirth, T. R. Rodríguez, H. Hergert, Ab Initio Treatment of Collective Correlations and the Neutrinoless Double Beta Decay of  $^{48}\text{Ca}$ , *Phys. Rev. Lett.* 124 (2020) 232501. [doi:10.1103/PhysRevLett.124.232501](https://doi.org/10.1103/PhysRevLett.124.232501).
- [353] A. Ekström, G. R. Jansen, K. A. Wendt, G. Hagen, T. Papenbrock, S. Bacca, B. Carlsson, D. Gazit, Effects of three-nucleon forces and two-body currents on Gamow-Teller strengths, *Phys. Rev. Lett.* 113 (2014) 262504. [doi:10.1103/PhysRevLett.113.262504](https://doi.org/10.1103/PhysRevLett.113.262504).
- [354] P. Gysbers, G. Hagen, J. D. Holt, G. R. Jansen, T. D. Morris, P. Navrátil, T. Papenbrock, S. Quaglioni, A. Schwenk, S. R. Stroberg, K. A. Wendt, Discrepancy between experimental and theoretical  $\beta$ -decay rates resolved from first principles, *Nature Phys.* 15 (2019) 428. [doi:10.1038/s41567-019-0450-7](https://doi.org/10.1038/s41567-019-0450-7).
- [355] N. Holden, Total half-lives for selected nuclides, *Pure and Applied Chemistry* 62 (1990) 941. [doi:10.1351/pac199062050941](https://doi.org/10.1351/pac199062050941).
- [356] W. F. Libby, E. C. Anderson, J. R. Arnold, Age determination by radiocarbon content: World-wide assay of natural radiocarbon, *Science* 109 (1949) 227. [doi:10.1126/science.109.2827.227](https://doi.org/10.1126/science.109.2827.227).
- [357] A. Negret, T. Adachi, B. R. Barrett, C. Bäumer, A. M. van den Berg, G. P. A. Berg, P. von Brentano, D. Frekers, D. De Frenne, H. Fujita, K. Fujita, Y. Fujita, E.-W. Grewe, P. Haefner, M. N. Harakeh, K. Hatanaka, K. Heyde, M. Hunyadi, E. Jacobs, Y. Kalmykov, A. Korff, K. Nakanishi, P. Navrátil, P. von Neumann-Cosel, L. Popescu, S. Rakers, A. Richter, N. Ryezayeva, Y. Sakemi, A. Shevchenko, Y. Shimbara, Y. Shimizu, Y. Tameshige, A. Tamii, M. Uchida, J. Vary, H. J. Wörtche, M. Yosoi, L. Zamick, Gamow-Teller Strengths in the  $A=14$  Multiplet: A Challenge to the Shell Model, *Phys. Rev. Lett.* 97 (2006) 062502. [doi:10.1103/PhysRevLett.97.062502](https://doi.org/10.1103/PhysRevLett.97.062502).
- [358] D. H. Wilkinson, Renormalization of the axial-vector coupling constant in nuclear  $\beta$ -decay (II), *Nucl. Phys. A* 209 (1973) 470. [doi:10.1016/0375-9474\(73\)90840-3](https://doi.org/10.1016/0375-9474(73)90840-3).
- [359] B. A. Brown, B. H. Wildenthal, Experimental and Theoretical Gamow-Teller Beta-Decay Observables for the sd-Shell Nuclei, *Atom. Data Nucl. Data Tabl.* 33 (1985) 347. [doi:10.1016/0092-640X\(85\)90009-9](https://doi.org/10.1016/0092-640X(85)90009-9).
- [360] W. T. Chou, E. K. Warburton, B. A. Brown, Gamow-Teller beta-decay rates for  $A \leq 18$  nuclei, *Phys. Rev. C* 47 (1993) 163. [doi:10.1103/PhysRevC.47.163](https://doi.org/10.1103/PhysRevC.47.163).
- [361] G. Martínez-Pinedo, A. Poves, E. Caurier, A. P. Zuker, Effective  $g_A$  in the pf-shell, *Phys. Rev. C* 53 (1996) R2602. [doi:10.1103/PhysRevC.53.R2602](https://doi.org/10.1103/PhysRevC.53.R2602).
- [362] I. S. Towner, Quenching of spin matrix elements in nuclei, *Phys. Rept.* 155 (1987) 263. [doi:10.1016/0370-1573\(87\)90138-4](https://doi.org/10.1016/0370-1573(87)90138-4).
- [363] J. Menéndez, D. Gazit, A. Schwenk, Chiral two-body currents in nuclei: Gamow-Teller transitions and neutrinoless double-beta decay, *Phys. Rev. Lett.* 107 (2011) 062501. [doi:10.1103/PhysRevLett.107.062501](https://doi.org/10.1103/PhysRevLett.107.062501).
- [364] A. S. Barabash, Average and recommended half-life values for two neutrino double beta decay, *Nucl. Phys. A* A935 (2015) 52. [doi:10.1016/j.nuclphysa.2015.01.001](https://doi.org/10.1016/j.nuclphysa.2015.01.001).
- [365] F. T. Avignone, III, S. R. Elliott, J. Engel, Double Beta Decay, Majorana Neutrinos, and Neutrino Mass, *Rev. Mod. Phys.* 80 (2008) 481. [doi:10.1103/RevModPhys.80.481](https://doi.org/10.1103/RevModPhys.80.481).
- [366] M. Agostini, M. Allardt, A. M. Bakalyarov, M. Balata, I. Barabanov, L. Baudis, C. Bauer, E. Bellotti, S. Belogurov, S. T. Belyaev, G. Benato, A. Bettini, L. Bezrukov, T. Bode, D. Borowicz, V. Brudanin, R. Brugnera, A. Caldwell, C. Cattadori, A. Chernogorov, V. D'Andrea, E. V. Demidova, N. Di Marco, A. di Vacri, A. Domula, E. Doroshkevich, V. Egorov, R. Falkenstein, O. Fedorova, K. Freund, N. Frodyma, A. Gangapshev, A. Garfagnini, C. Gooch, P. Grabmayr, V. Gurentsov, K. Gusev, J. Hakenmüller, A. Hegai, M. Heisel, S. Hemmer, W. Hofmann, M. Hult, L. V. Inzhechik, J. Janicskó Csáthy, J. Jochum, M. Junker, V. Kazalov, T. Kihm, I. V. Kirpichnikov, A. Kirsch, A. Kish, A. Klimenko, R. Kneiβl, K. T. Knöpfle, O. Kochetov, V. N. Kornoukhov, V. V. Kuzminov, M. Laubenstein, A. Lazzaro, V. I. Lebedev, B. Lehnert, H. Y. Liao, M. Lindner, I. Lippi, A. Lubashevskiy, B. Lubsandorzhiev, G. Lutter, C. Macolino, B. Majorovits, W. Maneschg, E. Medinaceli, M. Miloradovic, R. Mingazheva, M. Misiaszek, P. Moseev, I. Nemchenok, D. Palioselitis, K. Panas, L. Pandola, K. Pelczar, A. Pullia, S. Riboldi, N. Rumyantseva, C. Sada, F. Salamida, M. Salathe, C. Schmitt, B. Schneider, S. Schönert, J. Schreiner, O. Schulz, A.-K. Schütz, B. Schwingenheuer, O. Selivanenko, E. Shevchik, M. Shirchenko, H. Simgen, A. Smolnikov, L. Stanco, L. Vanhoefler, A. A. Vasenko, A. Veresnikova, K. von Sturm, V. Wagner, M. Walter, A. Wegmann, T. Wester, C. Wiesinger, M. Wojcik, E. Yanovich, I. Zhitnikov, S. V. Zhukov, D. Zinatulina, K. Zuber, G. Zuzel, Background-free search for neutrinoless double- $\beta$  decay of  $^{76}\text{Ge}$  with GERDA, *Nature* 544 (2017) 47. [doi:10.1038/nature21717](https://doi.org/10.1038/nature21717).
- [367] A. Gando, Y. Gando, T. Hachiya, A. Hayashi, S. Hayashida, H. Ikeda, K. Inoue, K. Ishidoshiro, Y. Karino, M. Koga, S. Matsuda, T. Mitsui, K. Nakamura, S. Obara, T. Ooura, H. Ozaki, I. Shimizu, Y. Shirahata, J. Shirai, A. Suzuki, T. Takai, K. Tamae, Y. Teraoka, K. Ueshima, H. Watanabe, A. Kozlov, Y. Takemoto, S. Yoshida, K. Fushimi, T. I. Banks, B. E. Berger, B. K. Fujikawa, T. O'Donnell, L. A. Winslow, Y. Efremenko, H. J. Karwowski, D. M. Markoff, W. Tornow, J. A. Detwiler, S. Enomoto, M. P. Decowski, Search for Majorana Neutrinos near the Inverted Mass Hierarchy

- Region with KamLAND-Zen, Phys. Rev. Lett. 117 (2016) 082503, [Addendum: Phys. Rev. Lett. 117 (2016) 109903]. doi:10.1103/PhysRevLett.117.109903, 10.1103/PhysRevLett.117.082503.
- [368] J. B. Albert, D. J. Auty, P. S. Barbeau, E. Beauchamp, D. Beck, V. Belov, C. Benitez-Medina, J. Bonatt, M. Breidenbach, T. Brunner, A. Burenkov, G. F. Cao, C. Chambers, J. Chaves, B. Cleveland, M. Coon, A. Craycraft, T. Daniels, M. Danilov, S. J. Daugherty, C. G. Davis, J. Davis, R. DeVoe, S. Delaquis, T. Didberidze, A. Dolgolenko, M. J. Dolinski, M. Dunford, W. Fairbank Jr, J. Farine, W. Feldmeier, P. Fierlinger, D. Fudenberg, G. Giroux†, R. Gornea, K. Graham, G. Gratta, C. Hall, S. Herrin, M. Hughes, M. J. Jewell, X. S. Jiang, A. Johnson, T. N. Johnson, S. Johnston, A. Karelin, L. J. Kaufman, R. Killick, T. Koffas, S. Kravitz, A. Kuchenkov, K. S. Kumar, D. S. Leonard, F. Leonard, C. Licciardi, Y. H. Lin, R. MacLellan, M. G. Marino, B. Mong, D. Moore, R. Nelson, A. Odian, I. Ostrovskiy, C. Ouellet, A. Piepke, A. Pocar, C. Y. Prescott, A. Rivas, P. C. Rowson, M. P. Roza, J. J. Russell, A. Schubert, D. Sinclair, S. Slutsky, E. Smith, V. Stekhanov, M. Tarka, T. Tolba, D. Tosi, K. Twelker, P. Vogel, J.-L. Vuilleumier, A. Waite, J. Walton, T. Walton, M. Weber, L. J. Wen, U. Wichoski, J. D. Wright, L. Yang, Y.-R. Yen, O. Ya. Zeldovich, Y. B. Zhao, Search for Majorana neutrinos with the first two years of EXO-200 data, Nature 510 (2014) 229. doi:10.1038/nature13432.
- [369] E. Caurier, F. Nowacki, A. Poves, Shell Model description of the  $\beta\beta$  decay of  $^{136}\text{Xe}$ , Phys. Lett. B 711 (2012) 62. doi:10.1016/j.physletb.2012.03.076.
- [370] J. D. Vergados, H. Ejiri, F. Simkovic, Theory of Neutrinoless Double Beta Decay, Rept. Prog. Phys. 75 (2012) 106301. doi:10.1088/0034-4885/75/10/106301.
- [371] J. Engel, J. Menéndez, Status and Future of Nuclear Matrix Elements for Neutrinoless Double-Beta Decay: A Review, Rept. Prog. Phys. 80 (2017) 046301. doi:10.1088/1361-6633/aa5bc5.
- [372] J. M. Yao, J. Engel, L. J. Wang, C. F. Jiao, H. Hergert, Generator-coordinate reference states for spectra and  $0\nu\beta\beta$  decay in the in-medium similarity renormalization group, Phys. Rev. C 98 (2018) 054311. doi:10.1103/PhysRevC.98.054311.
- [373] K. Sekiguchi, H. Sakai, H. Witala, W. Glockle, J. Golak, M. Hatano, H. Kamada, H. Kato, Y. Maeda, J. Nishikawa, A. Nogga, T. Ohnishi, H. Okamura, N. Sakamoto, S. Sakoda, Y. Satou, K. Suda, A. Tamii, T. Uesaka, T. Wakasa, K. Yako, Complete set of precise deuteron analyzing powers at intermediate energies: comparison with modern nuclear force predictions, Phys. Rev. C 65 (2002) 034003. doi:10.1103/PhysRevC.65.034003.
- [374] K. Ermisch, H. R. Amir-Ahmadi, A. M. van den Berg, R. Castelijns, B. Davids, E. Epelbaum, E. van Garderen, W. Glöckle, J. Golak, M. N. Harakeh, M. Hunyadi, M. A. de Huu, N. Kalantar-Nayestanaki, H. Kamada, M. Kis, M. Mahjour-Shafiei, A. Nogga, R. Skibiński, H. Witala, H. J. Wörtche, Systematic investigation of the elastic proton deuteron differential cross-section at intermediate-energies, Phys. Rev. C 68 (2003) 051001. doi:10.1103/PhysRevC.68.051001.
- [375] W. Tornow, R. C. Byrd, C. R. Howell, R. S. Pedroni, R. L. Walter, Measurements of analyzing power for  $^2\text{H}(\vec{n}, n)^2\text{H}$  scattering at 14.1 MeV and comparisons to  $^2\text{H}(\vec{p}, p)^2\text{H}$ , Phys. Rev. C 27 (1983) 2439. doi:10.1103/PhysRevC.27.2439.
- [376] H. Witala, J. Golak, R. Skibiński, K. Topolnicki, E. Epelbaum, K. Hebeler, H. Kamada, H. Krebs, U. G. Meißner, A. Nogga, Application of Semilocal Coordinate-Space Regularized Chiral Forces to Elastic Nd Scattering and Breakup, Few Body Syst. 60 (2019) 19. doi:10.1007/s00601-019-1485-0.
- [377] S. Giorgini, L. P. Pitaevskii, S. Stringari, Theory of ultracold atomic Fermi gases, Rev. Mod. Phys. 80 (2008) 1215. doi:10.1103/RevModPhys.80.1215.
- [378] W. E. Zwirger, The BCS-BEC Crossover and the Unitary Fermi Gas, Lecture Notes in Physics, Volume 836, Springer, Berlin, 2012. doi:10.1007/978-3-642-21978-8.
- [379] E. Pian, P. D'Avanzo, S. Benetti, M. Branchesi, E. Brocato, S. Campana, E. Cappellaro, S. Covino, V. D'Elia, J. P. U. Fynbo, F. Getman, G. Ghirlanda, G. Ghisellini, A. Grado, G. Greco, J. Hjorth, C. Kouveliotou, A. Levan, L. Limatola, D. Malesani, P. A. Mazzali, A. Melandri, P. Möller, L. Nicastro, E. Palazzi, S. Piranomonte, A. Rossi, O. S. Salafia, J. Selsing, G. Stratta, M. Tanaka, N. R. Tanvir, L. Tomasella, D. Watson, S. Yang, L. Amati, L. A. Antonelli, S. Ascenzi, M. G. Bernardini, M. Boër, F. Bufano, A. Bulgarelli, M. Capaccioli, P. Casella, A. J. Castro-Tirado, E. Chassande-Mottin, R. Ciolfi, C. M. Copperwheat, M. Dadina, G. De Cesare, A. Di Paola, Y. Z. Fan, B. Gendre, G. Giuffrida, A. Giunta, L. K. Hunt, G. L. Israel, Z.-P. Jin, M. M. Kasliwal, S. Klose, M. Lisi, F. Longo, E. Maiorano, M. Mapelli, N. Masetti, L. Nava, B. Patricelli, D. Perley, A. Pescalli, T. Piran, A. Possenti, L. Pulone, M. Razzano, R. Salvaterra, P. Schipani, M. Spera, A. Stameria, L. Stella, G. Tagliaferri, V. Testa, E. Troja, M. Turatto, S. D. Vergani, D. Vergani, Spectroscopic identification of r-process nucleosynthesis in a double neutron star merger, Nature 551 (2017) 67. doi:10.1038/nature24298.
- [380] T. Klähn, D. Blaschke, S. Typel, E. N. E. van Dalen, A. Faessler, C. Fuchs, T. Gaitanos, H. Grigorian, A. Ho, E. E. Kolomeitsev, M. C. Miller, G. Röpke, J. Trümper, D. N. Voskresensky, F. Weber, H. H. Wolter, Constraints on the high-density nuclear equation of state from the phenomenology of compact stars and heavy-ion collisions, Phys. Rev. C 74 (2006) 035802. doi:10.1103/PhysRevC.74.035802.
- [381] M. Leonhardt, M. Pospiech, B. Schallmo, J. Braun, C. Drischler, K. Hebeler, A. Schwenk, Symmetric nuclear matter from the strong interaction, Phys. Rev. Lett. 125 (14) (2020) 142502. doi:10.1103/PhysRevLett.125.142502.
- [382] K. Hebeler, J. M. Lattimer, C. J. Pethick, A. Schwenk, Equation of state and neutron star properties constrained by nuclear physics and observation, Astrophys. J. 773 (2013) 11. doi:10.1088/0004-637X/773/1/11.
- [383] I. Tews, J. Carlson, S. Gandolfi, S. Reddy, Constraining the speed of sound inside neutron stars with chiral effective field theory interactions and observations, Astrophys. J. 860 (2018) 149. doi:10.3847/1538-4357/aac267.
- [384] P. Bedaque, A. W. Steiner, Sound velocity bound and neutron stars, Phys. Rev. Lett. 114 (2015) 031103. doi:10.1103/PhysRevLett.114.031103.
- [385] S. K. Greif, G. Raaijmakers, K. Hebeler, A. Schwenk, A. L. Watts, Equation of state sensitivities when inferring neutron star and dense matter properties, Mon. Not. Roy. Astron. Soc. 485 (2019) 5363. doi:10.1093/mnras/stz654.
- [386] C. Drischler, J. Melendez, R. Furnstahl, D. Phillips, Quantifying uncertainties and correlations in the nuclear-matter



- equation of state (2020). [arXiv:2004.07805](https://arxiv.org/abs/2004.07805).
- [387] C. Drischler, R. Furnstahl, J. Melendez, D. Phillips, How well do we know the neutron-matter equation of state at the densities inside neutron stars? A Bayesian approach with correlated uncertainties (2020). [arXiv:2004.07232](https://arxiv.org/abs/2004.07232).
- [388] G. Baym, C. Pethick, P. Sutherland, The Ground state of matter at high densities: Equation of state and stellar models, *Astrophys. J.* 170 (1971) 299. [doi:10.1086/151216](https://doi.org/10.1086/151216).
- [389] J. W. Negele, D. Vautherin, Neutron star matter at subnuclear densities, *Nucl. Phys. A*207 (1973) 298. [doi:10.1016/0375-9474\(73\)90349-7](https://doi.org/10.1016/0375-9474(73)90349-7).
- [390] K. Hebeler, J. M. Lattimer, C. J. Pethick, A. Schwenk, Constraints on Neutron Star Radii Based on Chiral Effective Field Theory Interactions, *Phys. Rev. Lett.* 105 (2010) 161102. [doi:10.1103/PhysRevLett.105.161102](https://doi.org/10.1103/PhysRevLett.105.161102).
- [391] J. S. Read, B. D. Lackey, B. J. Owen, J. L. Friedman, Constraints on a phenomenologically parameterized neutron-star equation of state, *Phys. Rev. D* 79 (2009) 124032. [doi:10.1103/PhysRevD.79.124032](https://doi.org/10.1103/PhysRevD.79.124032).
- [392] J. Antoniadis, P. C. C. Freire, N. Wex, T. M. Tauris, R. S. Lynch, M. H. van Kerkwijk, M. Kramer, C. Bassa, V. S. Dhillon, T. Driebe, J. W. T. Hessels, V. M. Kaspi, V. I. Kondratiev, N. Langer, T. R. Marsh, M. A. McLaughlin, T. T. Pennucci, S. M. Ransom, I. H. Stairs, J. van Leeuwen, J. P. W. Verbiest, D. G. Whelan, A Massive Pulsar in a Compact Relativistic Binary, *Science* 340 (2013) 1233232. [doi:10.1126/science.1233232](https://doi.org/10.1126/science.1233232).
- [393] G. Raaijmakers, T. E. Riley, A. L. Watts, S. K. Greif, S. M. Morsink, K. Hebeler, A. Schwenk, T. Hinderer, S. Nissanke, S. Guillot, Z. Arzoumanian, S. Bogdanov, D. Chakrabarty, K. C. Gendreau, W. C. G. Ho, J. M. Lattimer, R. M. Ludlam, M. T. Wolff, A NICER view of PSR J0030+0451: Implications for the dense matter equation of state, *Astrophys. J. Lett.* 887 (2019) 22. [doi:10.3847/2041-8213/ab451a](https://doi.org/10.3847/2041-8213/ab451a).
- [394] T. E. Riley, A. L. Watts, S. Bogdanov, P. S. Ray, R. M. Ludlam, S. Guillot, Z. Arzoumanian, C. L. Baker, A. V. Bilous, D. Chakrabarty, K. C. Gendreau, A. K. Harding, W. C. G. Ho, J. M. Lattimer, S. M. Morsink, T. E. Strohmayer, A NICER View of PSR J0030+0451: Millisecond Pulsar Parameter Estimation, *Astrophys. J. Lett.* 887 (2019) 21. [doi:10.3847/2041-8213/ab481c](https://doi.org/10.3847/2041-8213/ab481c).
- [395] C. D. Capano, I. Tews, S. M. Brown, B. Margalit, S. De, S. Kumar, D. A. Brown, B. Krishnan, S. Reddy, GW170817: Stringent constraints on neutron-star radii from multimessenger observations and nuclear theory, *Nature Astron.* 4 (2020) 625. [doi:10.1038/s41550-020-1014-6](https://doi.org/10.1038/s41550-020-1014-6).
- [396] G. Raaijmakers, S. Greif, T. Riley, T. Hinderer, K. Hebeler, A. Schwenk, A. Watts, S. Nissanke, S. Guillot, J. Lattimer, R. Ludlam, Constraining the dense matter equation of state with joint analysis of NICER and LIGO/Virgo measurements, *Astrophys. J. Lett.* 893 (2020) L21. [doi:10.3847/2041-8213/ab822f](https://doi.org/10.3847/2041-8213/ab822f).
- [397] B. P. Abbott, et al., GW170817: Measurements of neutron star radii and equation of state, *Phys. Rev. Lett.* 121 (2018) 161101. [doi:10.1103/PhysRevLett.121.161101](https://doi.org/10.1103/PhysRevLett.121.161101).
- [398] A. L. Watts, N. Andersson, D. Chakrabarty, M. Feroci, K. Hebeler, G. Israel, F. K. Lamb, M. C. Miller, S. Morsink, F. Özel, A. Patruno, J. Poutanen, D. Psaltis, A. Schwenk, A. W. Steiner, L. Stella, L. Tolos, M. van der Klis, Colloquium: Measuring the neutron star equation of state using x-ray timing, *Rev. Mod. Phys.* 88 (2016) 021001. [doi:10.1103/RevModPhys.88.021001](https://doi.org/10.1103/RevModPhys.88.021001).
- [399] Z. Arzoumanian, K. C. Gendreau, C. L. Baker, T. Cazeau, P. Hestnes, J. W. Kellogg, S. J. Kenyon, R. P. Kozon, K.-C. Liu, S. S. Manthripragada, C. B. Markwardt, A. L. Mitchell, J. W. Mitchell, C. A. Monroe, T. Okajima, S. E. Pollard, D. F. Powers, B. J. Savadkin, L. B. Winternitz, P. T. Chen, M. R. Wright, R. Foster, G. Prigozhin, R. Remillard, J. Doty, The neutron star interior composition explorer (NICER): mission definition, *Space Telescopes and Instrumentation 2014: Ultraviolet to Gamma Ray* 9144 (2014) 579. [doi:10.1117/12.2056811](https://doi.org/10.1117/12.2056811).
- [400] K. C. Gendreau, Z. Arzoumanian, P. W. Adkins, C. L. Albert, J. F. Anders, A. T. Aylward, C. L. Baker, E. R. Balsamo, W. A. Bamford, S. S. Benegalrao, D. L. Berry, S. Bhalwani, J. K. Black, C. Blarrock, G. M. Bronke, G. L. Brown, J. G. Budinoff, J. D. Cantwell, T. Cazeau, P. T. Chen, T. G. Clement, A. T. Colangelo, J. S. Coleman, J. D. Coopersmith, W. E. Dehaven, J. P. Doty, M. D. Egan, T. Enoto, T. W.-M. Fan, D. M. Ferro, R. Foster, N. M. Galassi, L. D. Gallo, C. M. Green, D. Grosh, K. Q. Ha, M. A. Hasouneh, K. B. Heefner, P. Hestnes, L. J. Hoge, T. M. Jacobs, J. L. Järzgensen, M. A. Kaiser, J. W. Kellogg, S. J. Kenyon, R. G. Koenecke, R. P. Kozon, B. LaMarr, M. D. Lambertson, A. M. Larson, S. Lentine, J. H. Lewis, M. G. Lilly, K. A. Liu, A. Malonis, S. S. Manthripragada, C. B. Markwardt, B. D. Matonak, I. E. Mcginnis, R. L. Miller, A. L. Mitchell, J. W. Mitchell, J. S. Mohammed, C. A. Monroe, K. M. M. de Garcia, P. D. MulÃ©, L. T. Nagao, S. N. Ngo, E. D. Norris, D. A. Norwood, J. Novotka, T. Okajima, L. G. Olsen, C. O. Onyeachu, H. Y. Orosco, J. R. Peterson, K. N. Pevear, K. K. Pham, S. E. Pollard, J. S. Pope, D. F. Powers, C. E. Powers, S. R. Price, G. Y. Prigozhin, J. B. Ramirez, W. J. Reid, R. A. Remillard, E. M. Rogstad, G. P. Rosecrans, J. N. Rowe, J. A. Sager, C. A. Sanders, B. Savadkin, M. R. Saylor, A. F. Schaeffer, N. S. Schweiss, S. R. Semper, P. J. Serlemitsos, L. V. Shackelford, Y. Soong, J. Struebel, M. L. Vezie, J. S. Villasenor, L. B. Winternitz, G. I. Wofford, M. R. Wright, M. Y. Yang, W. H. Yu, The Neutron star Interior Composition Explorer (NICER): design and development, *Space Telescopes and Instrumentation 2016: Ultraviolet to Gamma Ray* 9905 (2016) 420. [doi:10.1117/12.2231304](https://doi.org/10.1117/12.2231304).
- [401] M. C. Miller, F. K. Lamb, A. J. Dittmann, S. Bogdanov, Z. Arzoumanian, K. C. Gendreau, S. Guillot, A. K. Harding, W. C. G. Ho, J. M. Lattimer, R. M. Ludlam, S. Mahmoodifar, S. M. Morsink, P. S. Ray, T. E. Strohmayer, K. S. Wood, T. Enoto, R. Foster, T. Okajima, G. Prigozhin, Y. Soong, PSR J0030+0451 Mass and Radius from NICER Data and Implications for the Properties of Neutron Star Matter, *Astrophys. J. Lett.* 887 (2019) 24. [doi:10.3847/2041-8213/ab50c5](https://doi.org/10.3847/2041-8213/ab50c5).
- [402] H. T. Cromartie, E. Fonseca, S. M. Ransom, P. B. Demorest, Z. Arzoumanian, H. Blumer, P. R. Brook, M. E. DeCesar, T. Dolch, J. A. Ellis, R. D. Ferdman, E. C. Ferrara, N. Garver-Daniels, P. A. Gentile, M. L. Jones, M. T. Lam, D. R. Lorimer, R. S. Lynch, M. A. McLaughlin, C. Ng, D. J. Nice, T. T. Pennucci, R. Spiewak, I. H. Stairs, K. Stovall, J. K. Swiggum, W. W. Zhu, Relativistic Shapiro delay measurements of an extremely massive millisecond pulsar, *Nat. Astron.* 4 (2019) 72. [doi:10.1038/s41550-019-0880-2](https://doi.org/10.1038/s41550-019-0880-2).

- [403] A. Carbone, A. Schwenk, Ab initio constraints on thermal effects of the nuclear equation of state, *Phys. Rev. C* 100 (2019) 025805. doi:10.1103/PhysRevC.100.025805.
- [404] A. Burrows, J. M. Lattimer, The birth of neutron stars, *Astrophys. J.* 307 (1986). doi:10.1086/164405.
- [405] C. Wellenhofer, J. W. Holt, N. Kaiser, W. Weise, Nuclear thermodynamics from chiral low-momentum interactions, *Phys. Rev. C* 89 (2014) 064009. doi:10.1103/PhysRevC.89.064009.
- [406] N. Kaiser, Quartic isospin asymmetry energy of nuclear matter from chiral pion-nucleon dynamics, *Phys. Rev. C* 91 (2015) 065201. doi:10.1103/PhysRevC.91.065201.
- [407] C. Wellenhofer, J. W. Holt, N. Kaiser, Divergence of the isospin-asymmetry expansion of the nuclear equation of state in many-body perturbation theory, *Phys. Rev. C* 93 (2016) 055802. doi:10.1103/PhysRevC.93.055802.
- [408] M. B. Tsang, J. R. Stone, F. Camera, P. Danielewicz, S. Gandolfi, K. Hebeler, C. J. Horowitz, J. Lee, W. G. Lynch, Z. Kohley, R. Lemmon, P. Möller, T. Murakami, S. Riordan, X. Roca-Maza, F. Sammarruca, A. W. Steiner, I. Vidaña, S. J. Yennello, Constraints on the symmetry energy and neutron skins from experiments and theory, *Phys. Rev. C* 86 (2012) 015803. doi:10.1103/PhysRevC.86.015803.
- [409] J. M. Lattimer, Y. Lim, Constraining the Symmetry Parameters of the Nuclear Interaction, *Astrophys. J.* 771 (2012) 51. doi:10.1088/0004-637X/771/1/51.
- [410] K. Hebeler, A. Schwenk, Symmetry energy, neutron skin, and neutron star radius from chiral effective field theory interactions, *Eur. Phys. J. A* 50 (2014) 11. doi:10.1140/epja/i2014-14011-4.
- [411] P. Klos, J. Menéndez, D. Gazit, A. Schwenk, Large-scale nuclear structure calculations for spin-dependent WIMP scattering with chiral effective field theory currents, *Phys. Rev. D* 88 (2013) 083516, [Erratum: *Phys. Rev. D* 89 (2014) 029901]. doi:10.1103/PhysRevD.88.083516.
- [412] M. Hoferichter, P. Klos, J. Menéndez, A. Schwenk, Nuclear structure factors for general spin-independent WIMP-nucleus scattering, *Phys. Rev. D* 99 (2019) 055031. doi:10.1103/PhysRevD.99.055031.
- [413] A. Fieguth, M. Hoferichter, P. Klos, J. Menéndez, A. Schwenk, C. Weinheimer, Discriminating WIMP-nucleus response functions in present and future XENON-like direct detection experiments, *Phys. Rev. D* 97 (2018) 103532. doi:10.1103/PhysRevD.97.103532.
- [414] A. A. Filin, V. Baru, E. Epelbaum, H. Krebs, D. Möller, P. Reinert, Extraction of the neutron charge radius from a precision calculation of the deuteron structure radius, *Phys. Rev. Lett.* 124 (2020) 082501. doi:10.1103/PhysRevLett.124.082501.
- [415] A. Tichai, R. Schutski, G. E. Scuseria, T. Duguet, Tensor-decomposition techniques for ab initio nuclear structure calculations. From chiral nuclear potentials to ground-state energies, *Phys. Rev. C* 99 (2019) 034320. doi:10.1103/PhysRevC.99.034320.
- [416] A. Ekström, Ab initio models of atomic nuclei: challenges and new ideas, *Front. in Phys.* 8 (2020) 29. doi:10.3389/fphy.2020.00029.
- [417] S. König, A. Ekström, K. Hebeler, D. Lee, A. Schwenk, Eigenvector Continuation as an Efficient and Accurate Emulator for Uncertainty Quantification, *Phys. Lett. B* 810 (2020) 135814. doi:10.1016/j.physletb.2020.135814.
- [418] A. Ekström, G. Hagen, Global sensitivity analysis of bulk properties of an atomic nucleus, *Phys. Rev. Lett.* 123 (2019) 252501. doi:10.1103/PhysRevLett.123.252501.
- [419] E. G. Hohenstein, R. M. Parrish, T. J. Martínez, Tensor hypercontraction density fitting. I. Quartic scaling second- and third-order Møller-Plesset perturbation theory, *The Journal of Chemical Physics* 137 (2012) 044103. doi:10.1063/1.4732310.
- [420] E. G. Hohenstein, R. M. Parrish, C. D. Sherrill, T. J. Martínez, Communication: Tensor hypercontraction. iii. least-squares tensor hypercontraction for the determination of correlated wavefunctions, *The Journal of Chemical Physics* 137 (2012) 221101. doi:10.1063/1.4768241.
- [421] R. Schutski, J. Zhao, T. M. Henderson, G. E. Scuseria, Tensor-structured coupled cluster theory, *The Journal of Chemical Physics* 147 (2017) 184113. doi:10.1063/1.4996988.
- [422] A. Tichai, J. Ripoche, T. Duguet, Pre-processing the nuclear many-body problem: Importance truncation versus tensor factorization techniques, *Eur. Phys. J. A* 55 (2019) 90. doi:10.1140/epja/i2019-12758-6.
- [423] S. Schulz, Four-Nucleon Forces in Ab Initio Nuclear Structure, Doctoral thesis, Technische Universität Darmstadt (2018), <https://tuprints.ulb-tu-darmstadt.de/7384/>.
- [424] Nogga, A., Rozpedzik, D., Epelbaum, E., Glöckle, W., Golak, J., Kamada, H., Skibiński, R., Witala, H., Four-nucleon force contribution to the binding energy of  $^4\text{He}$ , *EPJ Web of Conferences* 3 (2010) 05006. doi:10.1051/epjconf/20100305006.
- [425] T. Krüger, Chiral four-nucleon forces in nucleonic matter, Master's thesis, Technische Universität Darmstadt (2012).
- [426] P. W. Shor, Polynomial-time algorithms for prime factorization and discrete logarithms on a quantum computer, *SIAM Journal on Computing* 26 (1997) 1484. doi:10.1137/s0097539795293172.
- [427] M. Nielsen, I. Chuang, *Quantum Computation and Quantum Information: 10th Anniversary Edition*, Cambridge University Press, 2010.
- [428] F. Arute, K. Arya, R. Babbush, D. Bacon, J. C. Bardin, R. Barends, R. Biswas, S. Boixo, F. G. S. L. Brandao, D. A. Buell, B. Burkett, Y. Chen, Z. Chen, B. Chiaro, R. Collins, W. Courtney, A. Dunsworth, E. Farhi, B. Foxen, A. Fowler, C. Gidney, M. Giustina, R. Graff, K. Guerin, S. Habegger, M. P. Harrigan, M. J. Hartmann, A. Ho, M. Hoffmann, T. Huang, T. S. Humble, S. V. Isakov, E. Jeffrey, Z. Jiang, D. Kafri, K. Kechedzhi, J. Kelly, P. V. Klimov, S. Knysh, A. Korotkov, F. Kostritsa, D. Landhuis, M. Lindmark, E. Lucero, D. Lyakh, S. Mandrà, J. R. McClean, M. McEwen, A. Megrant, X. Mi, K. Michielsen, M. Mohseni, J. Mutus, O. Naaman, M. Neeley, C. Neill, M. Y. Niu, E. Ostby, A. Petukhov, J. C. Platt, C. Quintana, E. G. Rieffel, P. Roushan, N. C. Rubin, D. Sank, K. J. Satzinger, V. Smelyanskiy, K. J. Sung, M. D. Trevithick, A. Vainsencher, B. Villalonga, T. White, Z. J. Yao, P. Yeh, A. Zalcman, H. Neven,

- J. M. Martinis, Quantum supremacy using a programmable superconducting processor, *Nature* 574 (2019) 505. [doi:10.1038/s41586-019-1666-5](https://doi.org/10.1038/s41586-019-1666-5).
- [429] B. P. Lanyon, J. D. Whitfield, G. G. Gillett, M. E. Goggin, M. P. Almeida, I. Kassal, J. D. Biamonte, M. Mohseni, B. J. Powell, M. Barbieri, A. Aspuru-Guzik, A. G. White, Towards quantum chemistry on a quantum computer, *Nature Chemistry* 2 (2010) 106. [doi:10.1038/nchem.483](https://doi.org/10.1038/nchem.483).
- [430] A. Peruzzo, J. McClean, P. Shadbolt, M.-H. Yung, X.-Q. Zhou, P. J. Love, A. Aspuru-Guzik, J. L. O'Brien, A variational eigenvalue solver on a photonic quantum processor, *Nature Communications* 5 (2014) 4213. [doi:10.1038/ncomms5213](https://doi.org/10.1038/ncomms5213).
- [431] P. J. J. O'Malley, R. Babbush, I. D. Kivlichan, J. Romero, J. R. McClean, R. Barends, J. Kelly, P. Roushan, A. Tranter, N. Ding, B. Campbell, Y. Chen, Z. Chen, B. Chiaro, A. Dunsworth, A. G. Fowler, E. Jeffrey, E. Lucero, A. Megrant, J. Y. Mutus, M. Neeley, C. Neill, C. Quintana, D. Sank, A. Vainsencher, J. Wenner, T. C. White, P. V. Coveney, P. J. Love, H. Neven, A. Aspuru-Guzik, J. M. Martinis, Scalable Quantum Simulation of Molecular Energies, *Physical Review X* 6 (2016) 031007. [doi:10.1103/PhysRevX.6.031007](https://doi.org/10.1103/PhysRevX.6.031007).
- [432] A. Kandala, A. Mezzacapo, K. Temme, M. Takita, M. Brink, J. M. Chow, J. M. Gambetta, Hardware-efficient variational quantum eigensolver for small molecules and quantum magnets, *Nature* 549 (2017) 242. [doi:10.1038/nature23879](https://doi.org/10.1038/nature23879).
- [433] E. F. Dumitrescu, A. J. McCaskey, G. Hagen, G. R. Jansen, T. D. Morris, T. Papenbrock, R. C. Pooser, D. J. Dean, P. Lougovski, Cloud Quantum Computing of an Atomic Nucleus, *Phys. Rev. Lett.* 120 (2018) 210501. [doi:10.1103/PhysRevLett.120.210501](https://doi.org/10.1103/PhysRevLett.120.210501).
- [434] R. Babbush, N. Wiebe, J. McClean, J. McClain, H. Neven, G. K.-L. Chan, Low-depth quantum simulation of materials, *Phys. Rev. X* 8 (2018) 011044. [doi:10.1103/PhysRevX.8.011044](https://doi.org/10.1103/PhysRevX.8.011044).
- [435] H.-H. Lu, N. Klco, J. M. Lukens, T. D. Morris, A. Bansal, A. Ekström, G. Hagen, T. Papenbrock, A. M. Weiner, M. J. Savage, P. Lougovski, Simulations of Subatomic Many-Body Physics on a Quantum Frequency Processor, *Phys. Rev. A* 100 (2019) 012320. [doi:10.1103/PhysRevA.100.012320](https://doi.org/10.1103/PhysRevA.100.012320).
- [436] N. Klco, E. F. Dumitrescu, A. J. McCaskey, T. D. Morris, R. C. Pooser, M. Sanz, E. Solano, P. Lougovski, M. J. Savage, Quantum-classical computation of Schwinger model dynamics using quantum computers, *Phys. Rev. A* 98 (2018) 032331. [doi:10.1103/PhysRevA.98.032331](https://doi.org/10.1103/PhysRevA.98.032331).
- [437] R. H. Landau, *Quantum Mechanics II: A Second Course in Quantum Theory*, 2nd Edition, John Wiley and Sons, 1995.